

Copyright

by

Rachelle Lee Howell

2013

The Dissertation Committee for Rachelle Lee Howell
certifies that this is the approved version of the following dissertation:

**The Performance of Lateral Spread Sites
Treated with Prefabricated Vertical Drains:
Physical and Numerical Models**

Committee:

Ellen M. Rathje, Supervisor

Ross W. Boulanger

Robert B. Gilbert

Loukas F. Kallivokas

Clark R. Wilson

Jorge G. Zornberg

**The Performance of Lateral Spread Sites
Treated with Prefabricated Vertical Drains:
Physical and Numerical Models**

by

Rachelle Lee Howell, B.A.; B.S.C.E.; M.A.; M.S.E.

Dissertation

Presented to the Faculty of the Graduate School of

The University of Texas at Austin

in Partial Fulfillment

of the Requirements

for the Degree of

Doctor of Philosophy

The University of Texas at Austin

May 2013

To S.R.

Acknowledgments

Doctoral research is a monumental undertaking, and I am grateful to the many people in my life who made this undertaking possible.

I would first and foremost like to thank my advisor, Dr. Ellen Rathje. Her enthusiasm for her research is infectious, and it was she who started me on this journey seven years ago. I still have my copy of the 1964 Niigata earthquake video that she burned for me when I was an undergraduate in her geotechnical engineering class. She has encouraged me, guided me, and supported me throughout, and I am truly grateful.

I was honored to spend time at the University of California, Davis with an amazing group of people. I would like to thank Dr. Ross Boulanger for acting as my advisor while I was away from home, for continuing to offer assistance after I returned to Texas, for providing the occasional sanity check, and for giving me a much needed push when I stalled. I would like to thank Ronnie Kamai for assisting me in the construction and testing of my centrifuge model and for always answering her Skype messages. I would also like to thank Carolyn Conlee, Dan Wilson, Chad Justice, Ray Gerhard, Lars Pederson, Nick Sinikas, and Peter Rojas for their assistance in the construction and testing of my centrifuge model.

I would like to thank my committee members, Dr. Robert Gilbert, Dr. Loukas Kallivokas, Dr. Clark Wilson, and Dr. Jorge Zornberg, for their guidance, wisdom, and thoughtful suggestions. I have learned so much from each of you.

Funding for the first part of this research was provided by the NEES Grand Challenge Project for Seismic Risk Management of Port Systems (Award No. CMS-0530478), directed by Glenn Rix. Funding for the second half of this research was provided through the George E. Brown, Jr. Network for Earthquake Engineering Simulation (NEES). I would like to thank Dawn Weisman, Director of NEEScomm IT, for her support and encouragement over these past few years. I am honored to have had the opportunity to work with the NEEScomm IT team; they are an outstanding group of people.

I would especially like to thank my friends Antonio Marinucci, Albert Kottke, Sara Navidi, Menzer Pehlivan, Yiorgos Zalachoris, Onur Kaçar, and Matt LeBlanc. I have enjoyed our time together in and out of the classroom. Your constant support and encouragement have meant a lot to me.

Last, but certainly not least, I would like to thank my partner and my family. Sabine - I know it is not easy being the partner of a graduate student. You have probably spent more time staring at the back of my head while I was working than my face. Thank you for keeping me fed and watered and for making sure that our household was taken care of. Your love and support mean the world to me, and I could not have done this without you. My parents - I have never doubted myself because you have never doubted me. Thank you for believing in me and for not calling me crazy when I decided to start over on a new career path after already having two degrees and a job.

RACHELLE LEE HOWELL

The University of Texas at Austin
May 2013

The Performance of Lateral Spread Sites Treated with Prefabricated Vertical Drains: Physical and Numerical Models

Publication No. _____

Rachelle Lee Howell, Ph.D.

The University of Texas at Austin, 2013

Supervisor: Ellen M. Rathje

Drainage methods for liquefaction remediation have been in use since the 1970's and have traditionally included stone columns, gravel drains, and more recently prefabricated vertical drains. The traditional drainage techniques such as stone columns and gravel drains rely upon a combination of drainage and densification to mitigate liquefaction and thus, the improvement observed as a result of these techniques cannot be ascribed solely to drainage. Therefore, uncertainty exists as to the effectiveness of pure drainage, and there is some hesitancy among engineers to use newer drainage methods such as prefabricated vertical drains, which rely primarily on drainage rather than the combination of drainage and densification.

Additionally, the design methods for prefabricated vertical drains are based on the design methods developed for stone columns and gravel drains even though the primary mechanisms for remediation are not the same. The objectives of this research are to use physical and numerical models to assess the effectiveness of drainage as a liquefaction remediation technique and to identify the controlling behavioral mechanisms that most influence the performance of sites treated with prefabricated vertical drains.

In the first part of this research, a suite of three large-scale dynamic centrifuge tests of untreated and drain-treated sloping soil profiles was performed. Acceleration, pore pressure, and deformation data was used to evaluate the effectiveness of drainage in reducing liquefaction-induced lateral deformations. The results showed that the drains reduced the generated peak excess pore pressures and expedited the dissipation of pore water pressures both during and after shaking. The influence of the drains on the excess pore pressure response was found to be sensitive to the characteristics of the input motion. The drainage resulted in a 30 to 60% reduction in the horizontal deformations and a 20 to 60% reduction in the vertical settlements.

In the second part of this research, the data and insights gained from the centrifuge tests was used to develop numerical models that can be used to investigate the factors that most influence the performance of untreated and drain-treated lateral spread sites. Finite element modeling was performed using the OpenSees platform. Three types of numerical models were developed - 2D infinite slope unit cell models of the area of influence around a single drain, 3D infinite slope unit cell models of the area of influence around a single drain, and a full 2D plane strain model of the centrifuge tests that included both the untreated and drain-treated slopes as well as the centrifuge container. There was a fairly good match between the experimental and simulated excess pore

pressures. The unit cell models predicted larger horizontal deformations than were observed in the centrifuge tests because of the infinite slope geometry. Issues were identified with the constitutive model used to represent the liquefiable sand. These issues included a coefficient of volumetric compressibility that was too low and a sensitivity to low level accelerations when the stress path is near the failure surface.

In the final part of this research, the simulated and experimental data was used to examine the relationship between the generated excess pore water pressures and the resulting horizontal deformations. It was found that the deformations are directly influenced by both the excess pore pressures and the intensity of shaking. There is an excess pore pressure threshold above which deformations begin to become significant. The horizontal deformations correlate well to the integral of the average excess pore pressure ratio-time history above this threshold. They also correlate well to the Arias intensity and cumulative absolute velocity intensity measures.

Contents

Acknowledgments	v
Abstract	vii
List of Tables	xiii
List of Figures	xiv
Chapter 1 Introduction	1
1.1 Background	1
1.2 Objectives of Research	5
1.3 Organization of the Dissertation	7
Chapter 2 Previous Research	9
2.1 Introduction	9
2.2 Drainage for Liquefaction Remediation	10
2.2.1 History of Drainage for Liquefaction Remediation	10
2.2.2 Prefabricated Vertical Drains	18
2.2.3 FEQDrain	21
2.3 Centrifuge Testing	22
2.3.1 Principles of Geotechnical Centrifuge Testing	22
2.3.2 Centrifuge Testing of Drain-Treated Sites	24
2.3.3 Centrifuge Testing of Lateral Spread Sites	27
2.4 Numerical Modeling	29
2.4.1 Numerical Modeling of Lateral Spread Sites	29
2.4.2 Numerical Model Validation	32
2.5 Summary	41
Chapter 3 Centrifuge Testing of Lateral Spread Sites Treated with Prefabricated Vertical Drains	43
3.1 Introduction	43
3.2 Relationship between Centrifuge Models and Field Sites	44

3.3	Centrifuge Test SSK01	46
3.3.1	Model Construction	46
3.3.2	Test Results	50
3.4	Centrifuge Test RNK01	52
3.4.1	Model Construction	52
3.4.2	Test Results	55
3.5	Centrifuge Test RLH01	58
3.5.1	Model Construction	58
3.5.2	Test Results	63
3.6	Assessment of Centrifuge Results	81
3.7	Summary	84

Chapter 4 Numerical Models of Lateral Spread Sites Treated with PVDs 87

4.1	Introduction	87
4.2	Constitutive Models	88
4.2.1	OpenSees Finite Element Modeling Platform	88
4.2.2	Sand	89
4.2.3	Clay	107
4.3	Numerical Models	110
4.3.1	2D Unit Cell Infinite Slope Model	110
4.3.2	3D Unit Cell Infinite Slope Model	117
4.3.3	2D Centrifuge Model	121
4.4	Selection of Appropriate Hydraulic Conductivity using Data from Centrifuge Test SSK01	124
4.5	Summary	129

Chapter 5 Comparison of Numerical Models and Data from Centrifuge Test SSK01 131

5.1	Introduction	131
5.2	Comparison of Untreated 2D and 3D Unit Cell Models	132
5.3	Comparison of Untreated Numerical Models and Centrifuge Data	136
5.4	Comparison of the Treated 2D and 3D Unit Cell Models	150
5.5	Comparison of the Treated Numerical Models and Centrifuge Data	156
5.6	Comparison of Treated and Untreated Numerical Models	163
5.7	Summary	173

Chapter 6 Comparison of Numerical Models and Data from Centrifuge Test RNK01 175

6.1	Introduction	175
6.2	Comparison of Untreated Numerical Models and Centrifuge Data	176

6.3	Comparison of the Treated 2D and 3D Unit Cell Models	188
6.4	Comparison of Treated Numerical Models and Centrifuge Data	191
6.5	Comparison of Treated and Untreated Numerical Models	203
6.6	Summary	213
Chapter 7 Comparison of Numerical Models and Data from Centrifuge test RLH01		215
7.1	Introduction	215
7.2	Influence of Shaking Direction on the Untreated 3D Unit Cell Models	216
7.3	Comparison of Untreated Numerical Model and Centrifuge Data	229
7.4	Influence of Shaking Direction on the Treated 3D Unit Cell Models	238
7.5	Comparison of Treated Numerical Model and Centrifuge Data	246
7.6	Comparison of Treated and Untreated Numerical Models	252
7.7	Summary	266
Chapter 8 Investigation of the Pore Pressure - Deformation Relationship		269
8.1	Introduction	269
8.2	Characteristics of Pore Pressure and Deformation Responses	270
8.3	Correlating Pore Pressures and Deformations	282
8.4	Summary	292
Chapter 9 Summary, Conclusions, and Recommendations		293
9.1	Summary	293
9.2	Conclusions	296
9.3	Recommendations for Future Work	298
Appendices		301
Appendix A Scaling the hydraulic conductivity for the 2D models		301
Bibliography		307

List of Tables

2.1	Centrifuge Scaling Laws Relevant to Earthquake Engineering Experiments Modeling Flow Problems.	24
4.1	Parameters for the PDMY02 model (Yang et al., 2008).	92
4.2	Suggested (Yang et al., 2008) and final values for the PDMY02 model parameters.	98
4.3	Parameters for the PIMY model (Yang et al., 2008).	107
4.4	Suggested Parameters for a Medium Clay (Yang et al., 2008). . .	109
4.5	Model geometries for the 2D unit cell models corresponding to the mid-slope geometries of centrifuge tests SSK01, RNK01, and RLH01.	113
4.6	Parameters for Container elements.	123
5.1	Untreated and treated horizontal deformations from centrifuge test SSK01 and the 2D and 3D unit cell models	172
6.1	PDMY02 model parameters for sands at relative densities of 40%, 60%, and 75%.	183
6.2	Treated 2D and 3D horizontal deformations from centrifuge test RNK01 for shaking events with a PGA greater than 0.4 g.	190
6.3	Untreated and treated horizontal deformations from centrifuge test RNK01 and the 3D unit cell models for shaking events with a PGA greater than 0.4 g.	212
7.1	Untreated and treated horizontal deformations from centrifuge test RLH01 for all shaking events.	265

List of Figures

1.1	Cross section of a typical lateral spread site.	2
1.2	Aerial photograph of a lateral spread site in Port Au Prince, Haiti, taken by the U.S. Geological Survey after the 2010 earthquake (USGS, 2013).	3
1.3	Photo of a prefabricated vertical drain.	5
2.1	Drainage paths in an (a) untreated and (b) drain-treated soil deposit.	11
2.2	Relationship between the greatest pore pressure ratio and drain parameters for $\frac{N}{N_L} = 2$ (Seed and Booker, 1977).	13
2.3	Relationship between the greatest average pore pressure ratio and drain parameters for $\frac{N}{N_L} = 2$ (Seed and Booker, 1977).	13
2.4	Relationship between the coefficient of well resistance and the drain spacing ratio (Onoue, 1988).	16
2.5	Photograph of a PVD and an example of a triangular installation grid.	19
2.6	Example of a Drain Spacing Design Chart for PVDs with $\frac{N}{N_L} = 4$ (JGS, 1998).	20
2.7	Vertical Distribution of Excess Pore Pressures near the Drain (Left) and at 6 m (prototype) from the Drain (Right) (Brennan and Madabhushi, 2002).	26
2.8	Drawings of different centrifuge model geometries used to simulate lateral spread sites ((a) Abdoun et al., 2003; (b) Boulanger et al., 2003; (c) Haigh and Madabhushi, 2002; (d) Taboada-Urtuzuastegui and Dobry, 1998).	28
2.9	Drawings of different numerical models used to simulate lateral spreading ((a) Seid-Karbasi and Byrne, 2007; (b) Mayoral et al., 2009; (c) Cheng and Jeremić, 2009; (d) Phillips et al., 2012).	30
2.10	Centrifuge test and associated finite element model of a structure underlain by liquefiable soil used by Popescu and Prevost (1993).	34
2.11	Finite element model of a quay wall used by Madabhushi and Zeng (1998).	35

2.12	Centrifuge test and associated finite element models of a soil-structure system used by Pitilakis et al. (2004).	35
2.13	Centrifuge test and associated finite element model of untreated and drain-treated lateral spread sites used by Kamai and Boulanger (2012).	37
2.14	Centrifuge test and associated finite element model of a mildly sloping sand site used by Yang et al. (2003).	39
2.15	Centrifuge test and associated finite element model of liquefiable flat ground used by Byrne et al. (2004).	39
2.16	Centrifuge test and associated finite element model of a stiff sand site used by Elgamal et al. (2005).	40
2.17	Finite element models of undrained and drained stratified soil deposits used by Seid-Karbasi and Byrne (2007).	40
3.1	Model geometry of centrifuge test SSK01.	47
3.2	Schematic of a flexible shear beam container (Pedersen, 2004).	48
3.3	Instrumentation locations for SSK01.	49
3.4	Excess pore pressure development with depth and time in the treated and untreated zones for shaking event SSK01.12 (PGA = 0.30 g) (Marinucci et al., 2008).	51
3.5	Cumulative horizontal and vertical displacements in the treated and untreated zones for SSK01 (Marinucci et al., 2008).	52
3.6	Photo of centrifuge model RNK01 with instrumentation locations.	53
3.7	RNK01 input motions.	55
3.8	Cumulative horizontal displacements for RNK01.	57
3.9	Cumulative vertical displacements for RNK01.	57
3.10	Model geometry of centrifuge test RLH01.	59
3.11	Photo of the RLH01 centrifuge model.	60
3.12	Bentonite slurry in the RLH01 centrifuge model.	60
3.13	Instrumentation placement in the drain-treated area of the RLH01 centrifuge model.	61
3.14	Post-shaking photo of the RLH01 centrifuge model.	62
3.15	Comparison of pore pressure responses at the base of the untreated area and untreated area with non-draining tubes for shaking events PAC03 and PSL03.	63
3.16	Comparison of deformation responses for the untreated area and untreated area with non-draining tubes for shaking events PAC03 and PSL03.	64
3.17	Excess pore water pressure ratio, r_u , vs. time for the PAC04 (PGA = 0.95 g), PSL04 (PGA = 0.90 g), and SIN01 (PGA = 0.60 g) events.	66

3.18	Development of excess pore water pressure versus depth with time for the PAC04 (PGA = 0.95 g), PSL04 (PGA = 0.90 g), and SIN01 (PGA = 0.60 g) events.	68
3.19	Calculation of r_u , \bar{r}_u , and $\bar{r}_{u,max}$ in RLH01.	71
3.20	$\bar{r}_{u,max}$ as a function of PGA.	72
3.21	Cumulative horizontal (a) and vertical (b) displacements at mid-slope in the untreated and treated areas for all shaking events. . .	74
3.22	Colored sand markers in the untreated and treated areas after shaking.	75
3.23	(a) Horizontal displacement and (b) Vertical displacement versus $\bar{r}_{u,max}$	77
3.24	The $\bar{r}_{u,max}$ threshold shown in relation to a stress path.	77
3.25	Horizontal displacement, vertical settlement, \bar{r}_u , and acceleration - time histories for the PAC04 event (PGA = 0.95 g).	79
3.26	(a) Horizontal displacement and (b) Vertical displacement as a function of the time between the first and last exceedance of $\bar{r}_u = 0.5$	80
3.27	(a) Displacement profile typical of a lateral spread site with an impervious surface layer (Rauch, 1997). (b) Colored sand markers from the untreated area of the RLH01 centrifuge model	82
3.28	The RLH01 centrifuge model (a) before shaking and (b) after shaking.	84
4.1	Relationship between the backbone curve and the yield surfaces generated for the PDMY02 model (Khosravifar, 2011).	90
4.2	A plot of the failure surface defined by the friction angle, the phase transformation surface defined by the phase transformation angle, and the transition from contractive to dilative behavior.	91
4.3	Cyclic resistance ratio curve for the simulated sand compared to lab data for Nevada sand from Kano (2008), Doygun (2009), and Arumoli et al. (1992).	97
4.4	Volumetric strain vs. peak pore pressure ratio ($r_{u,max}$) for Monterey Sand (Lee and Albaisa, 1974)	101
4.5	Normalized relationships between peak pore pressure ratios ($r_{u,max}$) and m_v of sands from Seed et al. (1975).	102
4.6	Volumetric strain vs. peak pore pressure ratio ($r_{u,max}$) for the simulated sand and the Monterey Sand from Lee and Albaisa (1974)	104
4.7	Coefficient of volumetric compressibility (m_v) vs. peak pore pressure ratio ($r_{u,max}$) for the simulated sand and the Monterey Sand from Lee and Albaisa (1974)	105
4.8	Cross sectional view of a lateral spread site with an example of where an infinite slope model would be appropriate.	111

4.9	(a) PPT locations in the treated area of the RLH01 centrifuge model, and (b) r_u -time histories for PPTs located at similar depths (shown in red in (a)) for shaking event PSL03 (PGA = 0.46 g).	112
4.10	Drawing of the drain-treated 2D unit cell model.	116
4.11	Triangular and square drain spacing equivalency (Civil Engineering Portal, 2012).	118
4.12	Drawing of the drain-treated 3D unit cell model.	120
4.13	Drawing of the 2D centrifuge model.	122
4.14	Excess pore water pressure-time histories at different depths within the treated 3D unit cell model for shaking event SSK01_10 (PGA = 0.07 g) and a range of hydraulic conductivities.	125
4.15	Excess pore water pressure time histories at different depths within the treated 3D unit cell model for shaking event SSK01_11 (PGA = 0.11 g) and a range of hydraulic conductivities.	127
5.1	Excess pore water pressure-time histories at three different depths within the untreated 2D and 3D unit cell models for shaking events SSK01_09 (PGA = 0.03 g) through SSK01_12 (PGA = 0.30 g).	133
5.2	Horizontal and vertical displacement-time histories at the top of the clay layer and horizontal displacement vs. depth profiles for the untreated 2D and 3D unit cell models for shaking events SSK01_09 (PGA = 0.03 g) through SSK01_12 (PGA = 0.30 g).	135
5.3	Excess pore water pressure-time histories at three different depths within the untreated unit cell models vs. centrifuge data at comparable depths for shaking events SSK01_09 (PGA = 0.03 g) through SSK01_12 (PGA = 0.30 g).	138
5.4	Excess pore water pressure-time histories at three different depths for the untreated unit cell models, the untreated area of the full 2D model, and the untreated area of the SSK01 centrifuge model for shaking events SSK01_09 (PGA = 0.03 g) and SSK01_12 (PGA = 0.30 g).	139
5.5	Horizontal and vertical displacement-time histories at the top of the clay layer for the untreated unit cell models vs. mid-slope data from the centrifuge model for shaking events SSK01_09 (PGA = 0.11 g) through SSK01_12 (PGA = 0.30 g).	141
5.6	Displacement-time histories for the untreated area of full 2D model vs. mid-slope data from the untreated area of the SSK01 centrifuge model for shaking events SSK01_09 (PGA = 0.11 g) through SSK01_12 (PGA = 0.30 g).	143
5.7	Deformed mesh and countours of displacement for the full 2D model for shaking event SSK01_12 (PGA = 0.30 g).	144

5.8	Acceleration-time histories at depths of 2.4 m and 3.7 m for the untreated 2D unit cell model, the untreated area of the full 2D model, and the untreated area of the centrifuge model for shaking events (a) SSK01_10 (PGA = 0.07 g) and (b) SSK01_12 (PGA = 0.30 g).	146
5.9	(a) Peak average excess pore water pressure ($\bar{r}_{u,max}$) vs. PGA and (b) Horizontal displacement vs. PGA for the untreated unit cell models and the untreated area of the SSK01 centrifuge model.	149
5.10	Excess pore water pressure-time histories for the treated 2D and 3D unit cell models for shaking events SSK01_09 (PGA = 0.11 g) through SSK01_12 (PGA = 0.30 g).	152
5.11	Excess pore pressures across the treated 2D and 3D unit cell models at a depth of 1.30 m for shaking event SSK01_12 (PGA = 0.30 g) at time = 10 seconds.	153
5.12	Horizontal displacement-time histories at the top of the clay layer and horizontal displacement vs. depth data at the end of shaking for the treated 2D and 3D unit cell models for shaking events SSK01_09 (PGA = 0.11 g) through SSK01_12 (PGA = 0.3 g).	154
5.13	(a) 3D and (b) 2D drainage conditions for the unit cell models.	155
5.14	Excess pore water pressure-time histories for the treated 2D and 3D unit cell models and the treated area of the SSK01 centrifuge model for shaking events SSK01_09 (PGA = 0.11 g) through SSK01_12 (PGA = 0.30 g).	158
5.15	Pore pressure recorder location for the treated unit cell models and PPT array location for the SSK01 centrifuge model.	159
5.16	Excess pore water pressure-time histories at three different depths for the treated 3D unit cell model, the treated area of the full 2D model, and the treated area of the SSK01 centrifuge model for shaking event SSK01_12 (PGA = 0.30 g).	160
5.17	Horizontal displacement-time histories at the top of the clay layer for the treated 2D and 3D unit cell models and the treated area of the SSK01 centrifuge model for shaking events SSK01_09 (PGA = 0.11 g) through SSK01_12 (PGA = 0.3 g).	162
5.18	Excess pore water pressure-time histories for the untreated and treated 3D unit cell models at three different depths within the model for shaking events SSK01_09 (PGA = 0.11 g) through SSK01_12 (PGA = 0.3 g).	165
5.19	Peak average excess pore water pressure ($\bar{r}_{u,max}$) vs. PGA for (a) the untreated and treated unit cell models and (b) the untreated and treated areas of the SSK01 centrifuge model.	166

5.20	(a) \bar{r}_u vs. time for the untreated and treated unit cell models for SSK01_12, (b) Treated and untreated \bar{r}_u data for time = 15 to 16 s, (c) r_u data at every node along the vertical centerline of the untreated unit cell model for time = 15 to 16 s, (d) r_u data at every node along the upslope boundary of the treated unit cell model for time = 15 to 16 s.	167
5.21	Horizontal displacement-time histories at the top of the clay layer and horizontal displacement vs. depth for the untreated and treated 3D unit cell models for shaking events SSK01_09 (PGA = 0.11 g) through SSK01_12 (PGA = 0.3 g).	169
6.1	Excess pore water pressure-time histories for the untreated unit cell models and the untreated area of the RNK01 centrifuge model for shaking events RNK01_PAC06 (PGA = 0.41 g) through RNK01_PAC08 (PGA = 0.88 g).	179
6.2	Excess pore water pressure-time histories for the untreated unit cell models and the RNK01 centrifuge model for shaking events RNK01_PSL06 (PGA = 0.46 g) and RNK01_PSL07 (PGA = 0.88 g).	180
6.3	Excess pore water pressure-time histories for the untreated unit cell models and the RNK01 centrifuge model for shaking events RNK01_SIN01 (PGA = 0.28 g) and RNK01_SIN02 (PGA = 0.56 g).	181
6.4	Excess pore water pressure-time histories for the untreated unit cell models, the full 2D model, and the RNK01 centrifuge model for shaking event RNK01_PAC06 (PGA = 0.41 g) for $D_R = 40\%$, 60% , and 75%	184
6.5	Peak average excess pore water pressures ($\bar{r}_{u,max}$) vs. PGA for the untreated unit cell models and the untreated area of the RNK01 centrifuge model for (a) the PAC and (b) the PSL motions.	187
6.6	(a) Average excess pore pressure (\bar{r}_u)-time histories and (b) Horizontal deformation time histories for the treated 2D and 3D unit cell models for shaking event RNK01_PAC08 (PGA = 0.88 g).	189
6.7	Excess pore water pressure-time histories for the treated 3D unit cell model and the treated area of the RNK01 centrifuge model at three different depths for shaking events PAC06 (PGA = 0.41 g) through PAC08 (PGA = 0.88 g).	192
6.8	Excess pore water pressure-time histories for the treated 3D unit cell model and the treated area of the RNK01 centrifuge model at three different depths for shaking events PSL06 (PGA = 0.46 g) and PSL07 (PGA = 0.88 g).	193

6.9	Excess pore water pressure-time histories for the treated 3D unit cell model and the treated area of the RNK01 centrifuge model at three different depths for shaking events SIN01 (PGA = 0.28 g) and SIN02 (PGA = 0.56 g).	194
6.10	Input acceleration-time history for (a) the RNK01_PAC08 shaking event and (b) the RNK01_PSL06 shaking event.	197
6.11	Excess pore pressure-time histories at three different depths for (a) the treated 2D unit cell model for the PSL06 shaking event with and without low-level accelerations in the input motion, and (b) the treated 2D unit cell model and the full 2D model for the PSL06 shaking event.	198
6.12	Octahedral shear stress (τ_{oct}) vs. mean effective stress (p') for (a) PAC08 and (b) PSL06.	199
6.13	Excess pore water pressure-time histories for the treated 3D unit cell model, the treated area of the full 2D model, and the treated area of the RNK01 centrifuge model at relative densities of 40% and 75% for shaking events PAC06 (PGA = 0.41 g) and PSL06 (PGA = 0.46 g).	202
6.14	Excess pore water pressure-time histories for the untreated and treated 3D unit cell models at three different depths for shaking events PAC06 (PGA = 0.41 g) through PAC08 (PGA = 0.88 g).	205
6.15	Excess pore water pressure-time histories for the untreated and treated 3D unit cell models at three different depths for shaking events PSL06 (PGA = 0.46 g) and PSL07 (PGA = 0.88 g).	206
6.16	Excess pore water pressure-time histories for the untreated and treated 3D unit cell models at three different depths for shaking events SIN01 (PGA = 0.28 g) and SIN02 (PGA = 0.56 g).	207
6.17	Peak average excess pore water pressures ($\bar{r}_{u,max}$) vs. PGA for the untreated and treated unit cell models for (a) the PAC shaking events and (b) the PSL shaking events.	208
6.18	Horizontal displacement-time histories at the top of the clay layer for the untreated and treated 3D unit cell models for RNK01 shaking events with PGA > 0.4 g.	210
7.1	Excess pore water pressure-time histories for the untreated 3D unit cell models at three different depths for shaking events RLH01_PAC01 (PGA = 0.11 g) through RLH01_PAC04 (PGA = 0.95 g).	218
7.2	Excess pore water pressure-time histories for the untreated 3D unit cell models at three different depths for shaking events RLH01_PSL01 (PGA = 0.10 g) through RLH01_PSL04 (PGA = 0.90 g).	219

7.3	Excess pore water pressure-time histories for the untreated 3D unit cell models at three different depths for the RLH01_SIN01 shaking event (PGA = 0.60 g).	220
7.4	Excess pore pressure-time history and octahedral shear stress vs. mean effective stress for an element at a depth of 2.05 m in the untreated 3D unit cell models for shaking orthogonal and parallel to the slope for the SIN01 shaking event.	222
7.5	Stress paths at a depth of 6.45 m for simulations of the PSL03 shaking event for a 10° slope and flat ground.	224
7.6	Horizontal displacement-time histories at the top of the clay layer and horizontal displacement vs. depth profiles for the untreated 3D unit cell models for shaking events RLH01_PAC01 (PGA = 0.11 g) through RLH01_PAC04 (PGA = 0.95 g).	226
7.7	Horizontal displacement-time histories at the top of the clay layer and horizontal displacement vs. depth profiles for the untreated 3D unit cell models for shaking events RLH01_PSL01 (PGA = 0.10 g) through RLH01_PSL04 (PGA = 0.90 g).	227
7.8	Horizontal displacement-time histories at the top of the clay layer and horizontal displacement vs. depth profiles for the untreated 3D unit cell models for the RLH01_SIN01 shaking event (PGA = 0.60 g).	228
7.9	Excess pore water pressure-time histories for the untreated 3D unit cell model with shaking orthogonal to the slope and the untreated area of the RLH01 centrifuge model for shaking events RLH01_PAC01 (PGA = 0.11 g) through RLH01_PAC04 (PGA = 0.95 g).	231
7.10	Excess pore water pressure-time histories for the untreated 3D unit cell model with shaking orthogonal to the slope and the untreated area of the RLH01 centrifuge model for shaking events RLH01_PSL01 (PGA = 0.10 g) through RLH01_PSL04 (PGA = 0.90 g).	232
7.11	Excess pore water pressure-time histories for the untreated 3D unit cell model with shaking orthogonal to the slope and the untreated area of the RLH01 centrifuge model for the RLH01_SIN01 shaking event (PGA = 0.60 g).	233
7.12	Peak average excess pore water pressures ($\bar{r}_{u,max}$) for the untreated 3D unit cell model with shaking orthogonal to the slope and the untreated area of the RLH01 centrifuge model for (a) the PAC shaking events and (b) the PSL shaking events.	235

7.13	Horizontal displacement-time histories for the untreated 3D unit cell model with shaking orthogonal to the slope and the untreated area of the RLH01 centrifuge model for shaking events RLH01_PAC01 (PGA = 0.11 g) through RLH01_PAC04 (PGA = 0.95 g) and RLH01_PSL01 (PGA = 0.10 g) through RLH01_PSL03 (PGA = 0.46 g).	237
7.14	Excess pore water pressure-time histories for the treated 3D unit cell models at three different depths for shaking events RLH01_PAC01 (PGA = 0.11 g) through RLH01_PAC04 (PGA = 0.95 g).	239
7.15	Excess pore water pressure-time histories for the treated 3D unit cell models at three different depths for shaking events RLH01_PSL01 (PGA = 0.10 g) through RLH01_PSL04 (PGA = 0.90 g).	240
7.16	Excess pore water pressure-time histories for the treated 3D unit cell models at three different depths for the RLH01_SIN01 shaking event (PGA = 0.60 g).	241
7.17	Horizontal displacement-time histories at the top of the clay layer and horizontal displacement vs. depth profiles for the treated 3D unit cell models for shaking events RLH01_PAC01 (PGA = 0.11 g) through RLH01_PAC04 (PGA = 0.95 g).	243
7.18	Horizontal displacement-time histories at the top of the clay layer and horizontal displacement vs. depth profiles for the treated 3D unit cell models for shaking events RLH01_PSL01 (PGA = 0.10 g) through RLH01_PSL04 (PGA = 0.90 g).	244
7.19	Horizontal displacement-time histories at the top of the clay layer and horizontal displacement vs. depth profiles for the treated 3D unit cell models for the RLH01_SIN01 shaking event (PGA = 0.60 g).	245
7.20	Excess pore water pressure-time histories for the treated 3D unit cell model with shaking orthogonal to the slope and the treated area of the RLH01 centrifuge model for shaking events RLH01_PAC01 (PGA = 0.11 g) through RLH01_PAC04 (PGA = 0.95 g).	247
7.21	Excess pore water pressure-time histories for the treated 3D unit cell model with shaking orthogonal to the slope and the treated area of the RLH01 centrifuge model for shaking events RLH01_PSL01 (PGA = 0.10 g) through RLH01_PSL04 (PGA = 0.90 g).	248
7.22	Excess pore water pressure-time histories for the treated 3D unit cell model with shaking orthogonal to the slope and the treated area of the RLH01 centrifuge model for the RLH01_SIN01 shaking event (PGA = 0.60 g).	249

7.23	Horizontal displacement-time histories for the treated 3D unit cell model with shaking orthogonal to the slope and the treated area of the RLH01 centrifuge model for shaking events RLH01_PAC01 (PGA = 0.11 g) through RLH01_PAC04 (PGA = 0.95 g), RLH01_PSL01 (PGA = 0.10 g) through RLH01_PSL04 (PGA = 0.90 g), and RLH01_SIN01 (PGA = 0.60 g).	251
7.24	Excess pore water pressure-time histories for the untreated and treated 3D unit cell models with shaking orthogonal to the slope for shaking events RLH01_PAC01 (PGA = 0.11 g) through RLH01_PAC04 (PGA = 0.95 g).	253
7.25	Excess pore water pressure-time histories for the untreated and treated 3D unit cell models with shaking orthogonal to the slope for shaking events RLH01_PSL01 (PGA = 0.10 g) through RLH01_PSL04 (PGA = 0.90 g).	254
7.26	Excess pore water pressure-time histories for the untreated and treated 3D unit cell models with shaking orthogonal to the slope for the RLH01_SIN01 shaking event (PGA = 0.60 g).	255
7.27	Excess pore water pressure vs. depth profiles at selected times for the untreated and treated 3D unit cell models with shaking orthogonal to the slope for the RLH01_PAC04, PSL04, and SIN01 shaking events.	257
7.28	Peak average excess pore water pressures ($\bar{r}_{u,max}$) vs. PGA for the untreated and treated 3D unit cell models with shaking orthogonal to the slope for (a) the PAC shaking events and (b) the PSL shaking events.	259
7.29	Horizontal displacement-time histories at the top of the clay layer and horizontal displacement vs. depth profiles for the untreated and treated 3D unit cell models with shaking orthogonal to the slope for shaking events RLH01_PAC01 (PGA = 0.11 g) through RLH01_PAC04 (PGA = 0.95 g).	261
7.30	Horizontal displacement-time histories at the top of the clay layer and horizontal displacement vs. depth profiles for the untreated and treated 3D unit cell models with shaking orthogonal to the slope for shaking events RLH01_PSL01 (PGA = 0.10 g) through RLH01_PSL04 (PGA = 0.90 g).	262
7.31	Horizontal displacement-time histories at the top of the clay layer and horizontal displacement vs. depth profiles for the untreated and treated 3D unit cell models with shaking orthogonal to the slope for the RLH01_SIN01 shaking event (PGA = 0.60 g).	263

8.1	\bar{r}_u , horizontal deformation, and input acceleration-time histories for the untreated and treated areas of the RLH01 centrifuge model for the PAC shaking events.	271
8.2	\bar{r}_u , horizontal deformation, and input acceleration-time histories for the untreated and treated areas of the RLH01 centrifuge model for the PSL shaking events.	272
8.3	\bar{r}_u , horizontal deformation, and input acceleration-time histories for the untreated and treated areas of the RLH01 centrifuge model for the SIN01 shaking event.	273
8.4	\bar{r}_u , horizontal deformation, and input acceleration-time histories for the RLH01 untreated and treated orthogonal 3D unit cell models for the PAC shaking events.	278
8.5	\bar{r}_u , horizontal deformation, and input acceleration-time histories for the RLH01 untreated and treated orthogonal 3D unit cell models for the PSL shaking events.	279
8.6	\bar{r}_u , horizontal deformation, and input acceleration-time histories for the RLH01 untreated and treated orthogonal 3D unit cell models for the SIN01 shaking event.	280
8.7	Horizontal displacement vs. peak average excess pore water pressures ($\bar{r}_{u,max}$) for (a) the RLH01 centrifuge model for all shaking events, (b) the untreated and treated orthogonal 3D unit cell models for all shaking events, and (c) the untreated and treated orthogonal 3D unit cell models in which there was less than 18 cm of deformation.	284
8.8	Horizontal deformation vs. $\bar{r}_uInt0.4$ for the untreated and treated areas of the RLH01 centrifuge model.	286
8.9	Horizontal deformation vs. (a) Arias intensity (I_a) and (b) cumulative absolute velocity (CAV_5) for the untreated and treated areas of the RLH01 centrifuge model.	287
8.10	Horizontal deformation vs. $\bar{r}_uInt0.25$ for the RLH01 (a) untreated and (b) treated 3D orthogonal unit cell models.	289
8.11	Horizontal deformation vs. (a) Arias intensity (I_a) and (b) cumulative absolute velocity (CAV_5) for the RLH01 untreated and treated 3D orthogonal unit cell models.	291
A.1	Axisymmetric and plane strain models from Hird et al. (1992).	302
A.2	Average degree of consolidation on a horizontal plane for an axisymmetric model and geometry-matched and permeability-matched plane strain models (Hird et al., 1992).	302
A.3	Pore pressure variation along a horizontal plane for an axisymmetric model and a geometry-matched model (Hird et al., 1992).	303

Chapter 1

Introduction

1.1 Background

Liquefaction is a phenomenon in which saturated, loose sandy soils lose their strength and stiffness due to pore water pressure generation during undrained cyclic loading. Under drained cyclic loading, loose saturated sand tends to contract. However, if the same sand is undrained, only minimal volume changes can occur and the normal stresses resulting from the sand's tendency to contract are transferred from the soil matrix to the pore water, which generates excess pore water pressures. These generated excess pore water pressures reduce the effective stresses and strength of the soil. Liquefaction occurs when the magnitude of the generated excess pore water pressures is equal or nearly equal to the magnitude of the initial vertical effective stresses of the soil. A liquefied soil has little or no strength and little resistance to deformation.

One damaging consequence of liquefaction is lateral spreading. Lateral spread sites are generally characterized by gently sloping or nearly flat ground

(small static shear stresses) located near water such as rivers, bays, oceans, etc (Figure 1.1). Lateral spread deformations can be significant (up to several meters) and they can cause substantial damage to nearby structures and infrastructure. An example of lateral spread deformations and associated cracking, as observed in the 2010 Haiti earthquake, is shown in Figure 1.2. According to the National Research Council (1985), lateral spread deformations have caused more cumulative damage than any other type of liquefaction-induced ground failure. The economic losses due to the 2010 - 2011 Christchurch, New Zealand earthquakes, in which liquefaction and lateral spreading were prevalent, are currently estimated to be between 25 to 30 billion NZ dollars (Cubrinovski et al., 2012).

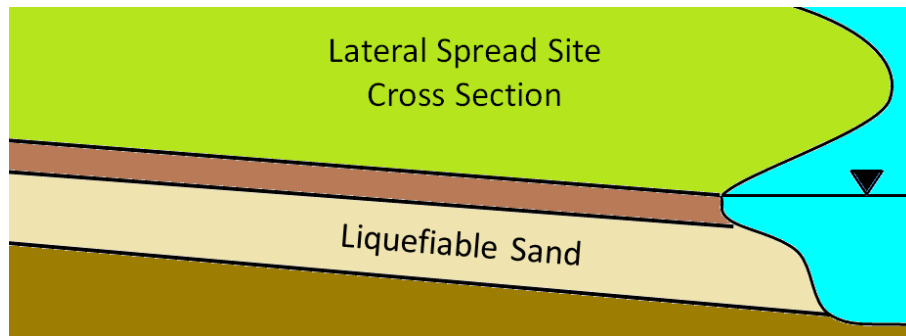


Figure 1.1: Cross section of a typical lateral spread site.

There are several soil improvement methods that can be used to reduce deformations due to liquefaction and lateral spreading. These methods include densification, grouting, drainage, soil mixing, and removal and replacement of the liquefiable soil (Kramer, 1996). This research focuses on the use of drainage for mitigating liquefaction-induced deformations at lateral spread sites.



Figure 1.2: Aerial photograph of a lateral spread site in Port Au Prince, Haiti, taken by the U.S. Geological Survey after the 2010 earthquake (USGS, 2013).

Drainage methods were first introduced in the 1970's (Seed and Booker, 1977). Drains reduce the magnitude of the generated excess pore water pressures, expedite the dissipation of generated pore water pressures, and provide drainage paths through low-permeability soil layers. Traditional drains such as gravel drains and stone columns are installed using vibratory methods and rely on a combination of densification and drainage to mitigate liquefaction. The drainage capacity of traditional drains can be negatively impacted by soil mixing during drain installation, the migration of native soil into the drain over time, and clogging due to previous liquefaction events. Therefore, although gravel drains and stone columns may expedite drainage, their drainage capacity is generally not relied upon and their primary mechanism for mitigating liquefaction stems from the densification that accompanies their installation.

Prefabricated vertical drains (PVDs) are a more recently introduced drainage method. PVDs are hollow, perforated, plastic pipes ranging from 75 to 100 mm in diameter (Figure 1.3). PVDs can be installed using non-vibratory methods, meaning that their installation is not necessarily accompanied by densification; their primary mechanism for mitigating liquefaction is drainage. PVDs are wrapped in filter fabric to prevent problems experienced by traditional drains such as native soil migrating into drains over time and the clogging of drains during liquefaction events. Prefabricated vertical drains have been installed in liquefiable sites in the United States, but as yet have not been subjected to a design-level earthquake. Therefore, field verification of their effectiveness in reducing deformations during earthquakes is lacking.



Figure 1.3: Photo of a prefabricated vertical drain.

1.2 Objectives of Research

The objective of this research is to use physical and numerical models to investigate the effectiveness of drainage as a liquefaction remediation technique and to identify the controlling behavioral mechanisms that most influence the performance of lateral spread sites treated with prefabricated vertical drains.

This research will focus on lateral spread sites in the general sense; there is no particular site associated with this project. Thus, the physical and numerical models used in this research will be designed to model a hypothetical, idealized lateral spread site. The soil profile at this idealized site will be homogeneous across the site, consisting of a relatively thin layer of clean, loose sand overlain by a clay crust. PVDs are most effective in clean sands where the soil has a large enough hydraulic conductivity to allow the pore water to flow to the drains during the short time of earthquake shaking. The clay crust slows the dissipation of excess pore water near the low-permeability interface, which can result in pore water accumulation and localized shearing, particularly in sloping soil profiles, at

that interface. Additionally, most lateral spread sites have some sort of crust of unsaturated material; thus including a crust in the models will make them more representative of field conditions.

The idealized lateral spread site represented by the physical and numerical models used in this research will not capture all aspects of a field lateral spread site. A lateral spread site in the field will have material properties that vary spatially throughout the site. Additionally, the geometry of a field lateral spread site will be larger than modeled in this research. However, these issues make the material and geometrical characterization of a field lateral spread site difficult and thus, validation of numerical models relative to a field site difficult. Therefore, physical models with more precise control of material properties and site geometry will be used to investigate the general mechanisms of behavior and numerical models will be created to further study the important behavioral mechanisms.

In the first part of this research, large-scale dynamic centrifuge tests are performed to assess the performance of untreated and drain-treated sloping ground subjected to sinusoidal and earthquake input motions. The centrifuge tests performed as part of this research allow the effects of drainage to be isolated, the relationship between excess pore pressures and deformations to be investigated, and the influence of ground motion characteristics to be examined.

Although dynamic centrifuge tests are very useful, only a small number of variables can be investigated due to the time and expense of performing the experiments. For parametric studies in which a large number of variables are to be investigated, the use of large-scale centrifuge tests is not feasible. Similarly, large-scale centrifuge tests are not feasible to evaluate the performance of a field lateral spread site. In these cases, numerical modeling is the more appropriate

approach. In the second part of this research, the data and insights gained from the centrifuge tests are used to develop and evaluate numerical models of untreated and drain-treated lateral spread sites. Ultimately, these models can be used for future parametric or field design studies.

1.3 Organization of the Dissertation

The following dissertation consists of nine chapters:

Chapter 2 summarizes previous research. Specifically, the chapter introduces the concepts associated with the use of drainage as a liquefaction remediation measure, the use of centrifuge testing as a means of modeling drains and lateral spread sites, the use of numerical modeling as a means of modeling lateral spread sites and drains, and the use of data from centrifuge tests to validate numerical models,.

Chapter 3 presents the design of the large-scale centrifuge models and the results of the dynamic centrifuge testing.

Chapter 4 describes the numerical models, including a discussion of the finite element modeling platform used, the constitutive models, and the calibration of the numerical models.

Chapter 5 describes the numerical simulations of the SSK01 centrifuge test. The simulated and experimental excess pore pressure and horizontal deformation data are compared, and the numerical data is analyzed with emphasis given to identifying the behavioral trends that were observed in the centrifuge test.

Chapter 6 describes the numerical simulations of the RNK01 centrifuge test. The simulated and experimental excess pore pressure and horizontal defor-

mation data are compared, and the numerical data is analyzed with emphasis given to identifying the behavioral trends that were observed in the centrifuge test.

Chapter 7 describes the numerical simulations of the RLH01 centrifuge test. The simulated and experimental excess pore pressure and horizontal deformation data are compared, and the numerical data is analyzed with emphasis given to identifying the behavioral trends that were observed in the centrifuge test.

Chapter 8 investigates the relationship between pore pressure generation/dissipation and horizontal deformations using the centrifuge data and numerical simulation data. The development of pore pressures and deformations will be examined in relation to shaking intensity and time of shaking, and then the correlation between the pore pressures and deformations will be examined.

Chapter 9 summarizes the findings of this dissertation and provides recommendations for future research.

Chapter 2

Previous Research

2.1 Introduction

This research uses physical and numerical models to assess the effectiveness of drainage in minimizing ground deformation due to liquefaction-induced lateral spreading. The following chapter details the history of gravel drains and prefabricated vertical drains for liquefaction remediation. This chapter also discusses the general principles of centrifuge testing and the use of centrifuge testing to investigate drainage techniques and lateral spread sites. Finally, this chapter discusses numerical modeling of lateral spread sites and the validation of numerical models using centrifuge data. Specific examples are provided of centrifuge tests used to model lateral spread sites, numerical models used to simulate lateral spreading, and centrifuge tests used to validate numerical models.

2.2 Drainage for Liquefaction Remediation

2.2.1 History of Drainage for Liquefaction Remediation

Traditional drainage systems consist of gravel/stone columns spaced regularly across a site. Drainage systems can reduce the magnitude of the generated excess pore water pressures, modify the flow patterns within the soil, and expedite the dissipation of the excess pore water pressures at a liquefiable site such that the earthquake-induced deformations are significantly reduced. In a drain-treated soil deposit, the shortest drainage path is radial toward the drains rather than upward (Figure 2.1). The shortened drainage paths in conjunction with the relatively high permeability of the drains increase the rate of excess pore water pressure dissipation. If the characteristics of the seismic shaking are such that the pore water has time to reach the drains during shaking and the drain capacity is not overloaded, the drains can reduce the magnitude of the generated excess pore water pressures (Sasaki and Taniguchi, 1982; Iai et al., 1988). The drains also create a pathway through an overlying low-permeability layer, should one exist, that helps prevent the accumulation of pore water and localization of deformation at the low-permeability interface (Idriss and Boulanger, 2008).

The effectiveness of a drainage system for liquefaction resistance depends on the soil characteristics (cyclic liquefaction resistance, compressibility, hydraulic conductivity, and layer thickness), the characteristics of earthquake shaking (intensity and duration of shaking), and the drain characteristics (drain radius, drain-to-drain spacing, and hydraulic resistance of the drain). Drainage system design is primarily concerned with selecting a drain diameter and drain spacing that will keep the peak excess pore water pressures below a specified threshold

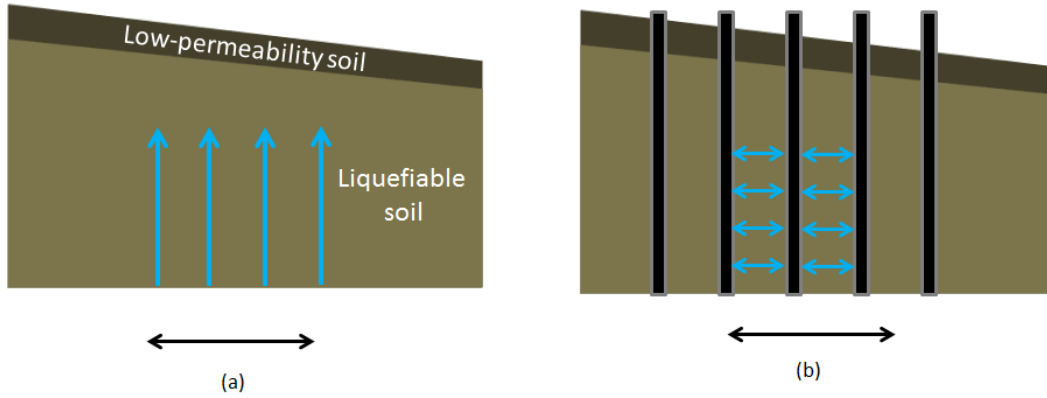


Figure 2.1: Drainage paths in an (a) untreated and (b) drain-treated soil deposit.

level for the design earthquake (Seed and Booker, 1977). This threshold level is defined in terms of an excess pore water pressure ratio (r_u , where $r_u = \frac{\Delta u}{\sigma'_{vo}}$, Δu = excess pore water pressure, and σ'_{vo} = initial vertical effective stress) or an average excess pore water pressure ratio ($\bar{r}_u = r_u$ averaged over space at any time). Generally, a threshold of less than 0.6 for $\bar{r}_{u,max}$ is used, where $\bar{r}_{u,max}$ is the largest average excess pore pressure ratio at any time during earthquake shaking (Onoue, 1988; Japanese Geotechnical Society, 1998).

Seed and Booker (1977) developed an analytical procedure that predicts the development of pore water pressures in drain-treated liquefiable soil as a function of drain spacing, the hydraulic conductivity and compressibility of the soil, and the characteristics of earthquake loading. In this approach, pore pressure generation is modeled through a simple expression that relates r_u to the cycle ratio ($\frac{N}{N_L}$, where N = the number of uniform loading cycles and N_L = the number of uniform cycles to cause liquefaction) using the following equation:

$$\frac{\Delta u}{\sigma'_{vo}} = \frac{2}{\pi} \arcsin\left(\frac{N}{N_L}\right)^{\frac{1}{2\alpha}} \quad (2.1)$$

where α is an empirical constant generally taken to be 0.7 (Seed et al., 1975). Pore pressure dissipation is modeled using Darcy's Law and radial flow. The hydraulic conductivity (k) and volumetric compressibility (m_v) of the soil are required to model the dissipation. The number of loading cycles at a given amplitude (N), the number of cycles to cause liquefaction at the same amplitude (N_L), and the loading duration (t_d) are required to model pore pressure generation. This approach assumes perfect drainage (i.e., that the drain is infinitely permeable), meaning the pore water pressures at the drain remain at their hydrostatic levels throughout loading.

Seed and Booker (1977) used a finite element program (LARF - Liquefaction Analysis for Radial Flow) to solve the differential equations governing the pore pressure generation/dissipation process. They summarized their results in design charts that relate the excess pore pressure ratio to the drain spacing ($\frac{a}{b}$, a = drain radius, b = half of the effective spacing between drains), a time factor that accounts for the hydraulic properties of the soil and the duration of loading ($T_{ad} = \frac{k}{\gamma_w} \frac{t_d}{m_v a^2}$), and the cycle ratio $\frac{N}{N_L}$.

Two design charts from Seed and Booker (1977) are provided in Figures 2.2 and 2.3. Figure 2.2 predicts r_g , which is the largest excess pore pressure ratio (i.e., $r_{u,max}$), at any point in space in the soil deposit at any time during earthquake shaking, while Figure 2.3 predicts \bar{r}_g , which is the largest, average excess pore pressure ratio (i.e., $\bar{r}_u = r_u$ averaged over space at any time, \bar{r}_g = largest value of \bar{r}_u). In this dissertation we will call this $\bar{r}_{u,max}$). Generally, r_g is larger than \bar{r}_g because it is the largest value within the soil deposit.

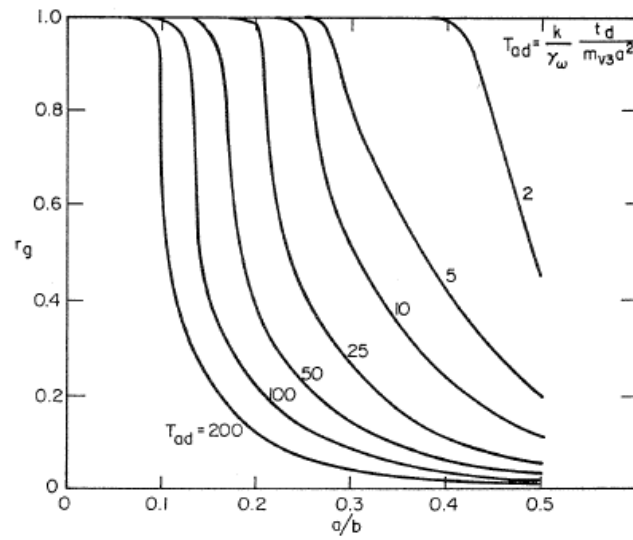


Figure 2.2: Relationship between the greatest pore pressure ratio and drain parameters for $\frac{N}{N_L} = 2$ (Seed and Booker, 1977).

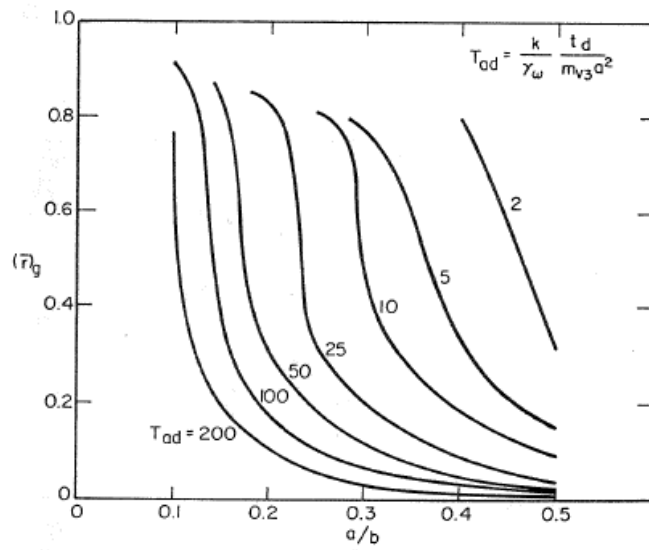


Figure 2.3: Relationship between the greatest average pore pressure ratio and drain parameters for $\frac{N}{N_L} = 2$ (Seed and Booker, 1977).

Figures 2.2 and 2.3 indicate that the excess pore pressure ratio decreases with increasing T_{ad} and increasing $\frac{a}{b}$. T_{ad} is similar to the time factor used in consolidation analysis, and relates the drainage properties of the soil, the duration of shaking, and the geometric properties of the drain. Larger values of T_{ad} represent more efficient drainage of water and thus smaller values of excess pore pressure. Larger values of T_{ad} are associated with more permeable soils (larger k), less compressible soils (smaller m_v), longer duration motions that allow for more pore pressure dissipation, or larger diameter drains. Larger values of $\frac{a}{b}$ for a given radius represent smaller values of the effective spacing between the drains, which decreases the drainage path length and leads to smaller pore pressure ratios. The ratio $\frac{N}{N_L}$ is essentially a measure of the cyclic resistance of the soil relative to the cyclic loading. An $\frac{N}{N_L}$ equal to 1.0 indicates that the number of loading cycles is just enough to cause liquefaction under undrained conditions (i.e., factor of safety ~ 1.0), while larger values of $\frac{N}{N_L}$ indicate that liquefaction will occur earlier during cyclic loading (i.e., factor of safety less than 1.0). As the $\frac{N}{N_L}$ ratio increases, the r_g versus $\frac{a}{b}$ curves for the varying T_{ad} values shift to the right, meaning that for a given spacing ratio and a given T_{ad} , the excess pore water pressure increases because the factor of safety against liquefaction is smaller.

Seed and Booker (1977) made two critical assumptions when developing their drain spacing design charts: (1) the drain is infinitely permeable and (2) purely radial flow. Seed and Booker (1977) asserted that as long as the permeability of the drain was more than 200 times greater than that of the surrounding soil, the permeability of the drain could be neglected. Gravel drains, however, are not infinitely permeable. Onoue (1987) performed in-situ dynamic tests on gravel drains in sandy soil and found that even if the permeability of the gravel drain

is more than 400 times greater than that of the sand, the well/drain resistance associated with water flowing in the drain is still substantial and must be taken into consideration. Onoue (1987) concluded that there is no limit at which the well resistance of a gravel drain can be considered negligible. Onoue (1988) also evaluated the assumption of purely radial flow and found that as the time factor for horizontal flow (T_d) increases, the effects of vertical water flow increase. The effects of vertical water flow were determined to be particularly significant for the case where $\frac{N}{N_L} = 1$. The effects of vertical water flow are less important when $\frac{N}{N_L} = 2$.

Onoue (1988) created a new set of design charts that incorporate the well resistance of the drain. Well resistance can be quantified based on the hydraulic conductivities of the drain and soil materials, as well as the drain dimensions, using the following equation:

$$L_w = \frac{32}{\pi^2} \frac{k_s}{k_w} \left(\frac{H}{d_w} \right)^2 \quad (2.2)$$

where k_s is the hydraulic conductivity of the soil, k_w is the hydraulic conductivity of the drain, H is the drain length, and d_w is the diameter of the drain. Figure 2.4 represents the Onoue (1988) design chart for $\frac{N}{N_L} = 2$. The Onoue (1988) charts predict the spacing ratio required to achieve a given $\bar{r}_{u,\max}$ (i.e., the same \bar{r}_g from Seed and Booker, 1977) as a function of well resistance. The spacing ratio in Figure 2.4 ($\frac{d_w}{d_e}$, where d_w = drain diameter, d_e = effective drain spacing) is the same as $\frac{a}{b}$ in the Seed and Booker (1977) charts. The chart in Figure 2.4 indicates that as well resistance increases, the spacing ratio must increase (i.e., drain spacing decrease) to maintain the same pore pressure ratio.

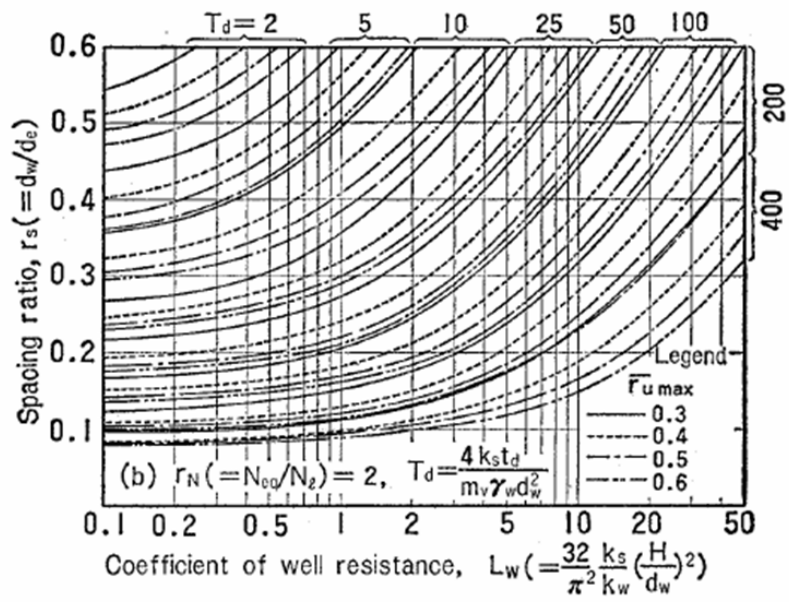


Figure 2.4: Relationship between the coefficient of well resistance and the drain spacing ratio (Onoue, 1988).

Ohkita (1986) proposed a third method of determining the design spacing for gravel drains. The Ohkita method uses the Seed and Booker (1977) design charts, but modifies the time factor, T_{ad} , to take into account the well resistance of the drain (JGS, 1998).

Although drainage system design focuses on limiting the induced excess pore water pressures, traditional gravel drains do not rely solely on drainage to remediate liquefaction. Traditional drains composed of gravel or crushed stone are commonly installed using vibratory installation methods (e.g., Adalier and Elgamal, 2004). The vibrations are known to produce a considerable degree of densification and increase in lateral stresses in the soil deposit, which strengthens the soil's resistance to liquefaction. In Japanese practice, a combined auger-casing/compaction-rod type installation method is used to densify the soil adjacent to the drain without inducing significant vibrations (Oishi and Tanaka, 1993; Adalier and Elgamal, 2004). Sites treated with drains installed via vibratory or densification methods have generally performed well in earthquakes (e.g., Mitchell and Wentz, 1991; Hayden and Baez, 1994; Iai et al., 1994; Adalier and Elgamal, 2004), but because of the associated densification of the soil during drain installation, the improved performance cannot be definitively ascribed to drainage.

With traditional gravel drains, there have been some concerns that soil mixing (particularly as a result of the vibratory installation methods) and migration of soil into the drain over time reduce the drain's permeability and thus its effectiveness (Boulanger et al., 1998). It has also been shown that the permeability of drains previously subjected to a liquefaction event may be decreased by as much 60% due to clogging (Onoue et al., 1987). As a result of the concerns about decreased drain permeability and the lack of confidence in pure drainage as a soil

improvement technique, engineers tend to rely more on the densification resulting from the drain installation rather than the drain's drainage capacity to mitigate liquefaction.

2.2.2 Prefabricated Vertical Drains

PVDs provide an alternative to traditional drains. PVDs are hollow, perforated, plastic pipes ranging in diameter from 75 to 100 mm that can be installed in a triangular or square pattern using either an auger-casing or vibratory method (Figure 2.5). PVDs are wrapped in filter fabric in an effort to prevent issues related to soil mixing and clogging. As is the case with traditional gravel drains, there may be some degree of densification associated with PVD installation; however, it is believed that the primary benefit of PVDs stems from drainage rather than densification. If the primary benefit of PVDs stems from drainage rather than densification, then it is important to isolate the effects of drainage alone on the performance of liquefiable sites in order to evaluate the potential effectiveness of PVDs.

The drain spacing design procedure for PVDs is identical to that of gravel drains. The same parameters are used, but the time factor parameter ($T_{ad} = \frac{k}{\gamma_w} \frac{t_d}{m_v a^2}$) is much larger because a PVD has a much smaller diameter than a gravel drain and the drain radius is in the denominator of the time factor. Neither the Seed and Booker (1977) nor the Onoue (1987) charts show design curves for the large values of T_{ad} associated with PVDs. The Japanese Geotechnical Society (1998) has provided new charts (Figure 2.6) that have been expanded to incorporate the large T_d values ($T_d = m \cdot T_{d0}$, where m = a correction factor

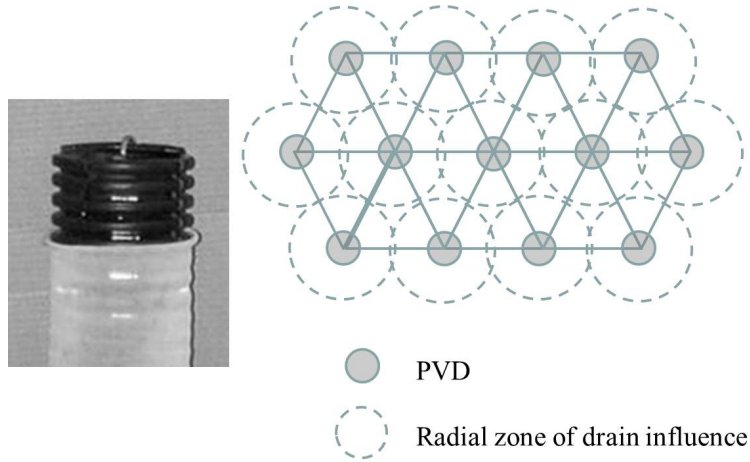


Figure 2.5: Photograph of a PVD and an example of a triangular installation grid.

and $T_{d0} = T_{ad}$ as defined by Seed and Booker, 1977). The JGS charts plot the maximum average pore pressure ratio, $\bar{r}_{u,max}$, versus the ratio of the effective drain spacing to drain radius, $\frac{b}{a}$, for specified $\frac{N}{N_L}$ ratios and T_d values ranging from 200 to 3000. The T_d values in the JGS charts pick up where the T_d values in the Seed and Booker (1977) and Onoue (1987) charts leave off. Additionally, the JGS charts invert the $\frac{b}{a}$ ratio used by Seed and Booker (1977) and Onoue (1987), which is reasonable given that $\frac{b}{a}$ is very small for PVDs (i.e., less than 1) as compared to the typical values for gravel drains. The relationship between $\bar{r}_{u,max}$, the hydraulic conductivity and compressibility of the soil, and the drain spacing remains the same; $\bar{r}_{u,max}$ decreases with increasing hydraulic conductivity, decreasing compressibility, and decreasing drain spacing. One issue that is a concern for PVDs and not gravel drains is smearing of the soil at the drain/soil interface during drain installation. This issue is important for PVDs in clay, but it is generally ignored in sands.

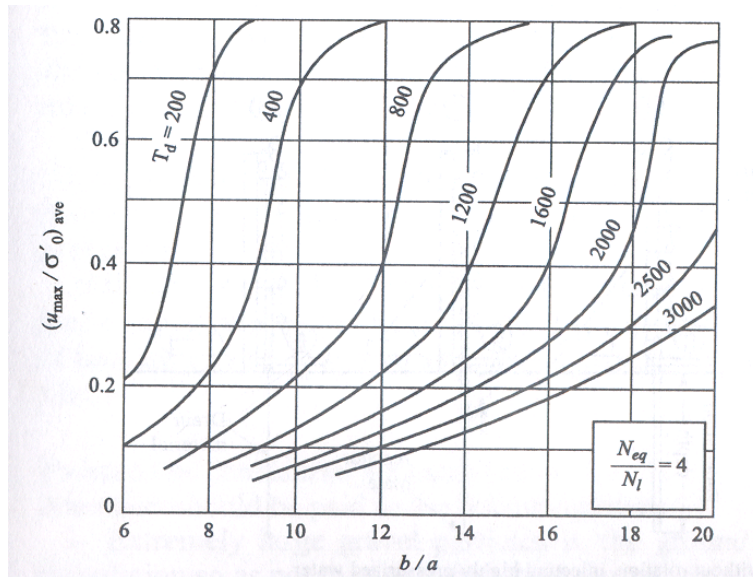


Figure 2.6: Example of a Drain Spacing Design Chart for PVDs with $\frac{N}{N_L} = 4$ (JGS, 1998).

PVDs have been installed at sites across the United States, but as yet none of these sites has been subjected to a design-level earthquake; therefore, field verification of their effectiveness in reducing deformations during earthquakes is lacking. Full-scale field tests performed by Rollins et al. (2003) showed that (1) significant settlements may accompany the installation of the drains if a vibratory installation method is employed, (2) PVDs are effective in dissipating excess pore water pressures, and (3) PVDs are effective in reducing settlements during a post-installation event. However, these field tests were performed using controlled blasting, which does not mimic the dynamic loading applied by an earthquake.

2.2.3 FEQDrain

FEQDrain is a finite element program developed by Pestana et al. (1997) that models the generation and dissipation of earthquake-induced pore water pressures, as well as liquefaction-induced settlement, in level ground soil deposits treated with drains. For the soil, FEQDrain uses the same pore pressure generation and dissipation models as Seed and Booker (1977) and Onoue (1988). However, FEQDrain includes modifications to the drain elements and boundary conditions that allow it to more accurately represent the drain resistance and account for drain storage capacity. FEQDrain is capable of modeling an untreated condition, a “perfect drain” condition in which well resistance is ignored, an equivalent gravel drain, or a prefabricated vertical drain.

FEQDrain requires input parameters to describe the soil profile, the earthquake loading conditions, the time step, and the drainage type. While most of these parameters are fairly common and easy to determine with some measure of accuracy (e.g., hydraulic conductivity, unit weight, and relative density), some of the parameters are not as easily characterized. These difficult parameters are not unique to FEQDrain, but are also used by the design charts described previously. These parameters stem from the models used for pore pressure generation and dissipation. For example, a coefficient of volumetric compressibility (m_v) must be specified for each soil layer and it is used along with k to model the coefficient of consolidation (c_v) for pore pressure dissipation. This is not a commonly measured parameter, its value varies with the applied stresses, and even relatively small variations in m_v can significantly impact pore pressure generation and dissipation. Other examples of parameters that are difficult to estimate include the number

of equivalent uniform cycles and the time duration of shaking, which are used to characterize the earthquake loading. There are more than 50 different cycle counting techniques (Hancock and Bommer, 2005) and there are multiple ways to define the duration of loading (e.g., significant duration measures such as D_{5-75} , D_{5-95} , bracketed duration measures, uniform duration measures, etc.). Moreover, it is known that the effectiveness of drainage elements depends on the specific ground motion characteristics (Sasaki and Taniguchi, 1982; Iai et al., 1988); thus, characterizing the ground motion in terms of equivalent cycles of harmonic loading is not the best representation of the seismic loading.

In addition to having multiple parameters that may be difficult to characterize, FEQDrain is also limited in that it only models the area of influence around a single drain and therefore cannot model complex geometries such as sloping soil profiles or embankments, and it cannot predict lateral deformations. Rollins et al. (2003) found FEQDrain to be adequate for modeling pore pressure generation and dissipation for drain treated sites subjected to controlled blasting events. However, for more complex loading conditions (i.e., earthquake loading) and site geometries, FEQDrain may not be as adequate.

2.3 Centrifuge Testing

2.3.1 Principles of Geotechnical Centrifuge Testing

Testing small-scale models is a common practice in civil engineering; however, the use of small-scale models in geotechnical engineering is problematic. The properties of soil are stress-dependent, meaning that the soil response that develops in a small-

scale model at 1g does not accurately reflect the response that develops in the field at full scale. Centrifuge testing allows geotechnical engineers to test relatively small-scale models in an enhanced gravity field that produces prototype-level stresses and therefore prototype-level soil properties and responses. Geotechnical centrifuge testing has existed since the 1930's although early geotechnical centrifuges did not have dynamic testing capabilities (Schofield, 1998). Centrifuges with shake tables were developed and refined in the late 1980's and early 1990's, and since the early 1990's, dynamic centrifuge testing has become an increasingly important tool in geotechnical earthquake engineering (Kutter, 1995).

Scaling laws are used to relate model (i.e. small-scale) behavior to prototype (i.e. field-scale or full-scale) behavior and can be derived from dimensional analysis (Schofield, 1980). The earliest scaling laws were put forth by Bucky (1931) and Pokrovsky (1934). Since then, much research has been performed regarding the scaling of phenomena such as heat transfer, fluid flow, particle size effects, strain rate effects, etc. The Technical Committee for Physical Modelling in Geotechnics (TC2) of the International Society for Soil Mechanics and Geotechnical Engineering has published a catalogue of geotechnical centrifuge model scaling laws (Garnier and Gaudin, 2007). These scaling laws represent a compilation of all current geotechnical centrifuge modeling research. The most relevant scaling laws for earthquake engineering experiments that consider flow problems are provided in Table 2.1. The scale factor, N , is the centrifugal acceleration.

The scaling laws in Table 2.1 indicate that scale factors for time differ when dealing with dynamic events versus consolidation/flow problems. The scaling of time for consolidation is significantly larger because it scales with N^2 , which means that consolidation occurs very quickly. This effect becomes significant when the

Table 2.1: Centrifuge Scaling Laws Relevant to Earthquake Engineering Experiments Modeling Flow Problems.

Property	Prototype Scale / Model Scale
Acceleration	1 / N
Length	N / 1
Time (Dynamic)	N / 1
Time (Consolidation)	N ² / 1
Pressure	1
Stress, σ	1
Strain, ε	1
Density (Identical Materials), ρ	1

time scale for consolidation is of similar magnitude to the time scale for dynamic events, i.e., when the time required for reconsolidation of the sand is roughly the same as the duration of shaking. In cases where consolidation is important, the differing time factors become important and the hydraulic conductivity of the model soil may be modified (i.e., reduced) so that the consolidation time scales similarly to the dynamic time. It is possible to modify the hydraulic conductivity in one of two ways, either a more viscous pore fluid (e.g., methyl cellulose) can be used or a finer grained sand can be used that has a smaller hydraulic conductivity (Kutter, 1995).

2.3.2 Centrifuge Testing of Drain-Treated Sites

A small number of centrifuge tests have been performed previously to assess the performance of drain-treated sites. Brennan and Madabhushi (2002) performed a dynamic centrifuge test to explore the effectiveness of gravel drains in mitigating liquefaction. The centrifuge model consisted of a loose sand with a single sand drain, constructed of coarser material, extending the full depth of the liquefiable sand. The model was spun at a centrifugal acceleration of 50 g and three sinusoidal

shaking events were applied at 1 Hz for 25 seconds. The peak input accelerations of the shaking events ranged from 0.14 to 0.24 g. Results showed that the drains did not significantly reduce the peak pore pressure ratios. However, during the drain process it was observed that pore water drains first from the deeper strata, meaning that the shallower strata remain liquefied longer while the pore fluid from the deeper strata utilizes the capacity of the drains (Figure 2.7). Brennan and Madabhushi (2002) concluded that when dealing with thick liquefiable strata, the drainage capacity of the drain should be increased (i.e., by doubling the drain radius). In a separate set of centrifuge tests, Brennan and Madabhushi (2006) showed that in order for drains to be effective, they have to penetrate the full depth of the liquefiable soil layer. Partial drains were found to have little or no dissipative effects at all.

Brennan and Madabhushi (2005) performed additional centrifuge tests to further research gravel drains, evaluating the effects of soil stratification. Two of the models, one containing a single drain and the other containing a small grouping of drains, were tested with and without an overlying silt layer. The models were spun at a centrifugal acceleration of 50 g and sinusoidal shaking events were applied at 1 Hz for 25 seconds. From these tests, Brennan and Madabhushi (2005) concluded that in stratified soil deposits, drains could prevent the formation of water films at the interfaces between high- and low-permeability soil layers.

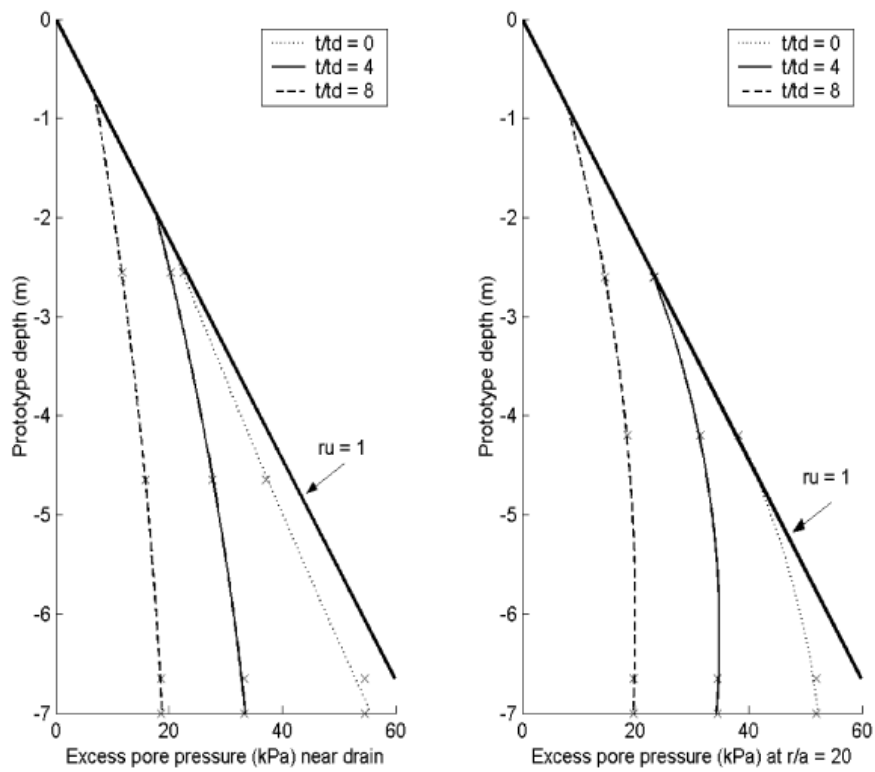


Figure 2.7: Vertical Distribution of Excess Pore Pressures near the Drain (Left) and at 6 m (prototype) from the Drain (Right) (Brennan and Madabhushi, 2002).

2.3.3 Centrifuge Testing of Lateral Spread Sites

Over the past 20 years, there have been a multitude of dynamic centrifuge tests designed to represent the lateral spreading of sites due to liquefaction (e.g. Fiegel and Kutter, 1994; Taboada et al., 1996; Taboada-Urtuzuastegui and Dobry, 1998; Haigh et al., 2000; Madabhushi et al., 2001; Haigh and Madabhushi, 2002; Sharp and Dobry, 2002; Abdoun et al., 2003; Boulanger et al., 2003; Brandenberg et al., 2005). These models can be divided into three basic categories: centrifuge models of lateral spreading used to evaluate soil-structure interaction (Abdoun et al., 2003; Boulanger et al., 2003; Brandenberg et al., 2005; Haigh and Madabhushi, 2002), centrifuge models used to evaluate the phenomena of lateral spreading itself (Fiegel and Kutter, 1994; Haigh et al., 2000; Madabhushi et al., 2001; Taboada-Urtuzuastegui and Dobry, 1998), and centrifuge models of lateral spreading used to calibrate relatively simple (sliding block) numerical analyses for predicting deformations (Sharp and Dobry, 2002; Taboada et al., 1996).

Centrifuge models used to simulate lateral spread sites generally consist of a single slope in either a laminar or shear beam model container subjected to a horizontal excitation. This excitation may be harmonic or an earthquake acceleration-time history, and the excitation is applied parallel to the slope. Drawings of various model configurations from the aforementioned centrifuge studies are shown in Figure 2.8. These models represent plane strain simulations of typical lateral spread sites (e.g., infinite slopes or sloping ground with a free face) in which the geometry depicted in the model is assumed to extend infinitely in the out-of-plane direction.

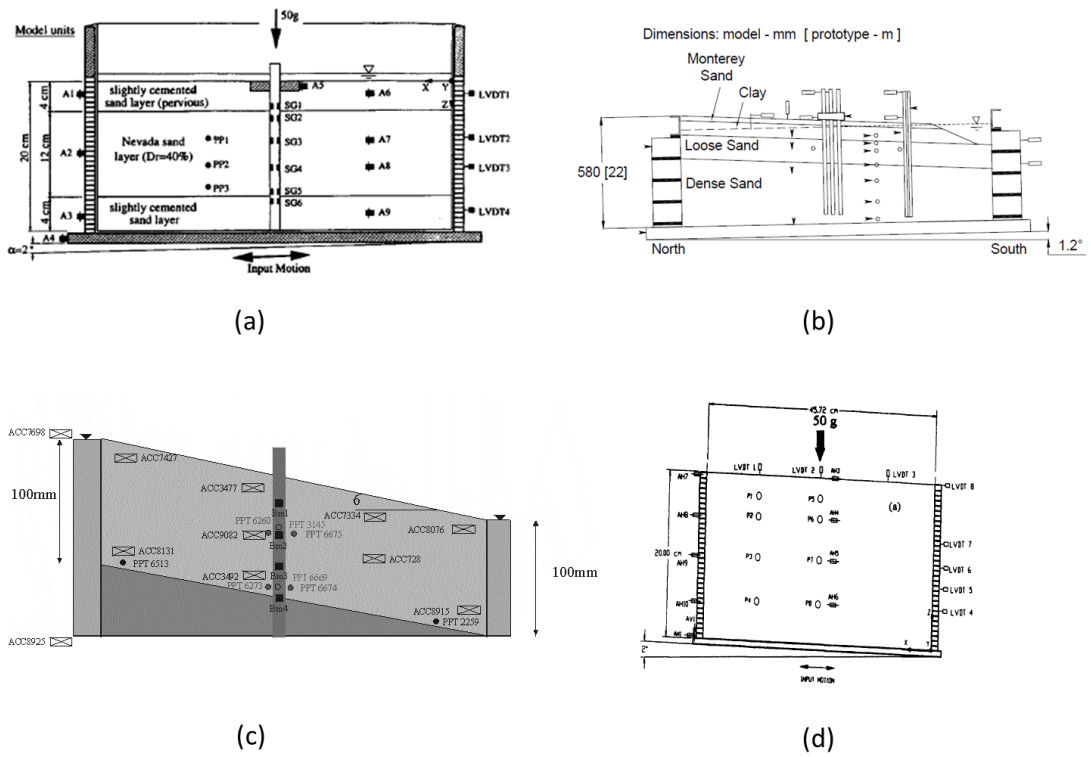


Figure 2.8: Drawings of different centrifuge model geometries used to simulate lateral spread sites ((a) Abdoun et al., 2003; (b) Boulanger et al., 2003; (c) Haigh and Madabhushi, 2002; (d) Taboada-Urtuzuastegui and Dobry, 1998).

2.4 Numerical Modeling

2.4.1 Numerical Modeling of Lateral Spread Sites

Lateral spread sites are generally characterized by gently sloping ground or nearly flat ground near water. It is common for lateral spread sites to cover a large areal extent and the numerical models used to predict the performance of a lateral spread site generally used simplified geometries of the field site. Some examples of numerical models with simplified geometries are Seid-Karbasi and Byrne, 2007; Mayoral et al., 2009; Cheng and Jeremić, 2009; and Phillips et al., 2012. These models (Figure 2.9), though they vary in dimensionality and complexity, are all simplifications that do not reflect the full geometry of the field site or centrifuge test that they are modeling.

Seid-Karbasi and Byrne (2009) examined the effects of low permeability layers in stratified soil deposits that are subjected to earthquake shaking, and the use of drains to stabilize such soil deposits. They used simplified 2D models for both the untreated and drain-treated simulations (Figure 2.9a) and only modeled the zone of influence around a single drain. The input motion was applied as an acceleration-time history at the base of the model and the deformations at the left and right boundaries of the soil column were linked to create a shear beam type condition. The drain column is modeled using soil elements with a permeability 100 times greater than that of the surrounding soil, and the 3D drain effects are represented using an equivalent drain area approach.

Mayoral et al. (2009) used 1D finite element modeling to predict the performance of liquefiable soil deposits (Figure 2.9b). The goal of their study was to produce a simple, practice-oriented model with relatively few parameters that

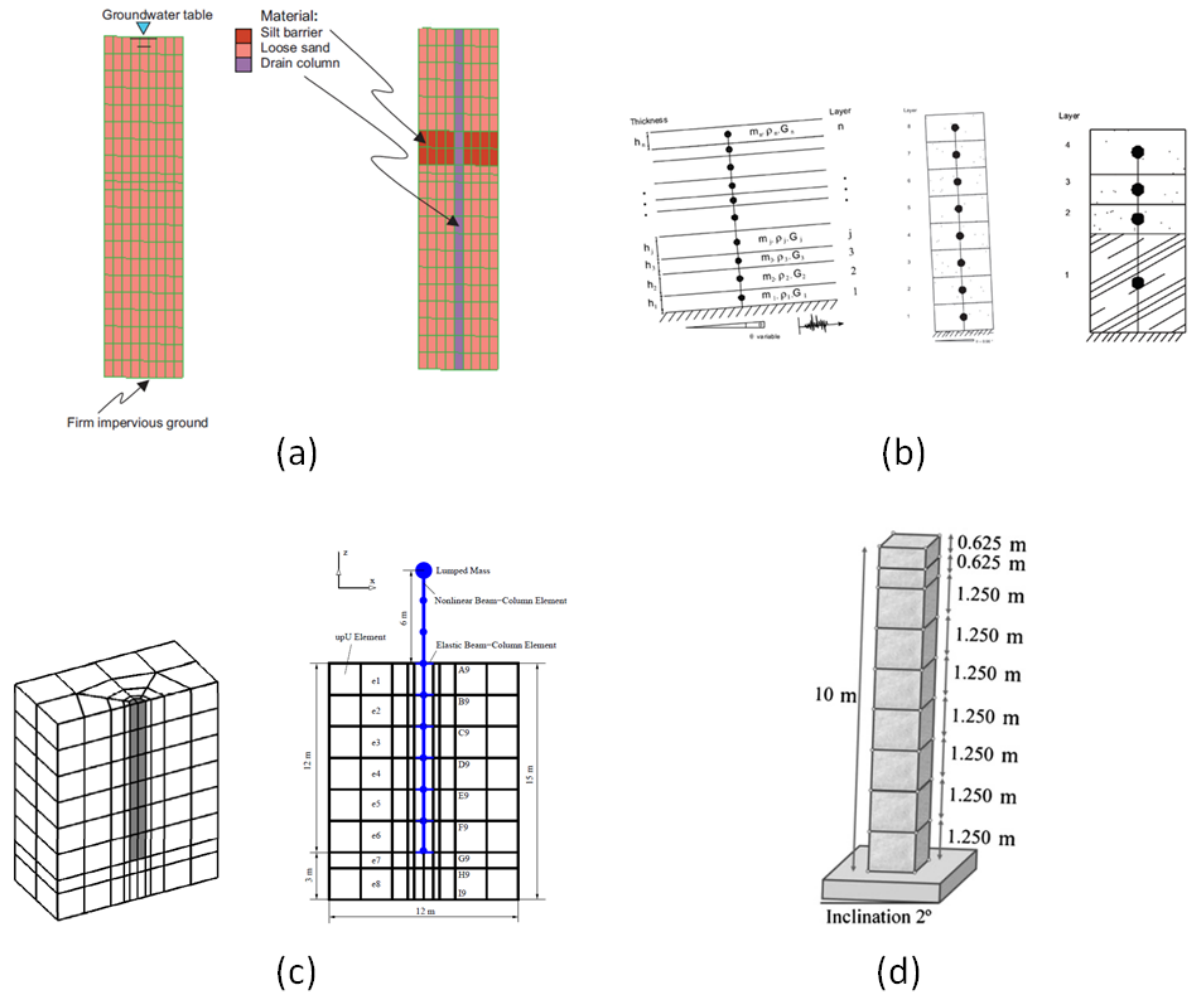


Figure 2.9: Drawings of different numerical models used to simulate lateral spreading ((a) Seid-Karbasi and Byrne, 2007; (b) Mayoral et al., 2009; (c) Cheng and Jeremić, 2009; (d) Phillips et al., 2012).

could be used to generate representative estimates of liquefaction-induced lateral deformations. This model can accommodate a slight slope, but for sites where the slope inclination is important, a 2D modeling approach is required (Mayoral et al., 2009). The model's performance was evaluated using three well-documented case histories from the 1979 Imperial Valley, 1987 Superstition Hills, and 1999 Koacaeli earthquakes, and it was found that the displacements predicted by the finite element model were closer to the observed displacements than were the displacements predicted using empirical relationships. Thus, although this model is very simple, it was shown to develop realistic predictions of lateral deformations.

Cheng and Jeremić (2009) simulated piles in laterally spreading liquefiable ground to investigate the effects of pile pinning (Figure 2.9c). This work is part of a larger effort to develop models and simulation tools for use in the performance-based design of infrastructure. Cheng and Jeremić (2009) opted for a 3D model of a region around a single pile, which allowed them to explore different constraints on the pile head and capture, as fully as possible, the complexities of soil-pile interaction.

Phillips et al. (2012) simulated an infinite slope lateral spreading centrifuge test (Figure 2.9d) in order to determine whether their numerical model can reproduce the behavior of soils undergoing lateral spreading. They constructed two numerical models in order to compare the performance of simplified and more complex numerical models. Their complex model was a full 3D model of the centrifuge test. Their simplified model was a 3D shear beam type model (Figure 2.9d). For the simplified model, equal displacement constraints were applied at each depth in the x, y, and z directions, creating a shear beam effect. Phillips et al. (2012) determined that the simplified shear beam type model and the full 3D model had nearly identical responses when modeling free-field liquefaction.

2.4.2 Numerical Model Validation

In the absence of robust field data, is not uncommon to use data from centrifuge tests to validate numerical models (e.g., Popescu and Prevost, 1993; Madabhushi and Zen, 1998; Yang et al., 2003; Pitilakis et al., 2004; Byrne et al., 2004; Elgamal et al., 2005; Seid-Karbasi and Byrne, 2007; Phillips et al., 2012, Kamai and Boulanger, 2012). Centrifuge models are highly instrumented and test conditions are tightly controlled, making them ideal for testing a numerical model. Additionally, centrifuge tests produce a significant amount of data that is not generally available from field observations, and these data are created under known test conditions. While the centrifuge models may not be exact representations of particular sites, the controlling behavioral mechanisms and observed behavioral trends are still valid and are therefore useful in calibrating and validating numerical models (Dobry and Liu, 1994; Madabhushi and Zeng, 1998).

Because centrifuge tests are not exact representations of field conditions, the agreement between the centrifuge data and the numerical data may vary depending on how closely the numerical model mimics the centrifuge test. In particular there are various manners in which the centrifuge container may be taken into account in the numerical model. From the examples cited previously, Popescu and Prevost (1993), Madabhushi and Zeng (1998), Pitilakis et al. (2004), and Kamai and Boulanger (2012) use numerical models that include the effects of the centrifuge container in some way, while Yang et al. (2003), Byrne et al. (2004), Elgamal et al. (2005), Seid-Karbasi and Byrne (2007), and Phillips et al. (2012) use simplified numerical models that do not model the centrifuge container.

Popescu and Prevost (1993), Madabhushi and Zeng (1998), and Pitilakis

et al. (2004) used various boundary conditions to replicate the conditions created by the container. For example, the Popescu and Prevost (1993) numerical models (Figure 2.10) have impervious lateral boundaries and the base of the model is fixed to prevent vertical motion. The Madabhushi and Zeng (1998) numerical models (Figure 2.11) use artificial non-reflecting boundaries developed by Madabhushi (1993) at the lateral edges of the numerical model to prevent stress waves from re-entering the main soil mesh. Pitilakis et al. (2004) created three models, each with different boundary conditions (Figure 2.12). Model A uses extended lateral boundaries and viscous dampers to reduce refracted waves. Model B assumes that the soil and container are tied at the lateral boundaries and so fixities are applied at these boundaries to prevent the soil from moving in the vertical direction. Model C uses the same fixities as Model B, but also includes a zone of material with a low shear modulus in between the soil and the lateral boundary. This zone allows for some vertical soil movement and allows for debonding and recontact of the soil and container. For all three of the Pitilakis et al. (2004) numerical models, the horizontal deformations of the lateral boundaries at each depth are constrained such that they equal.

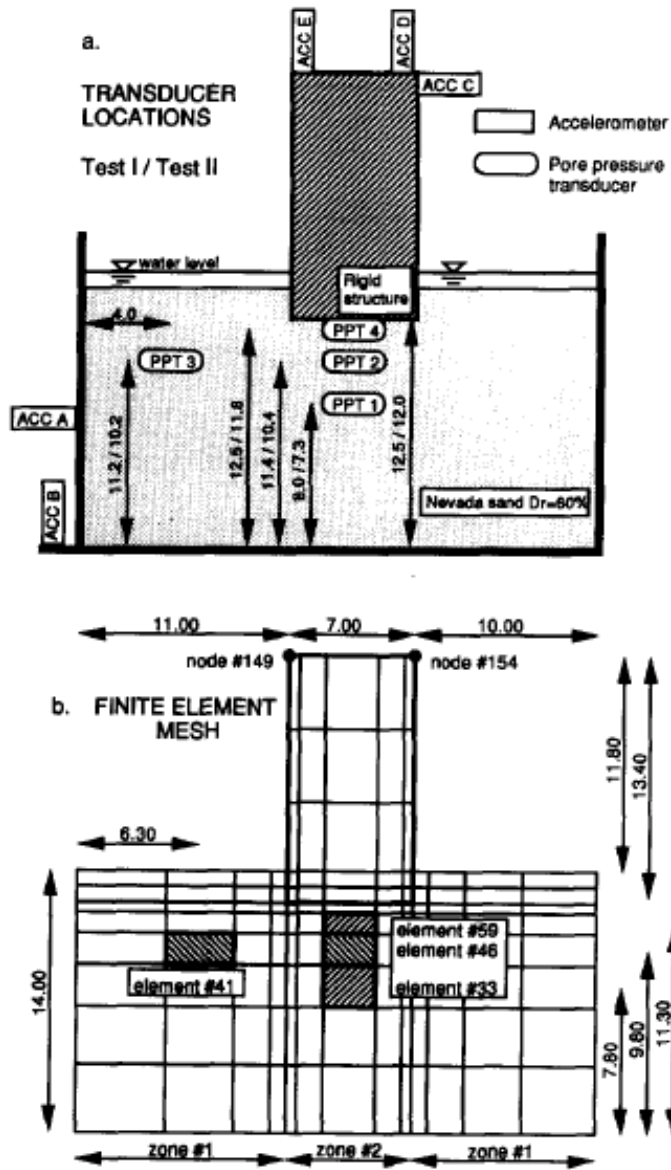


Figure 2.10: Centrifuge test and associated finite element model of a structure underlain by liquefiable soil used by Popescu and Prevost (1993).

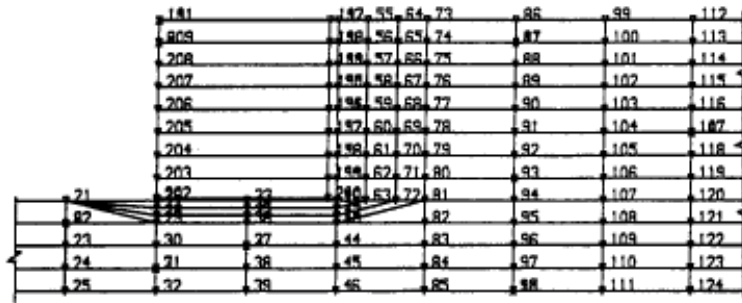


Figure 2.11: Finite element model of a quay wall used by Madabhushi and Zeng (1998).

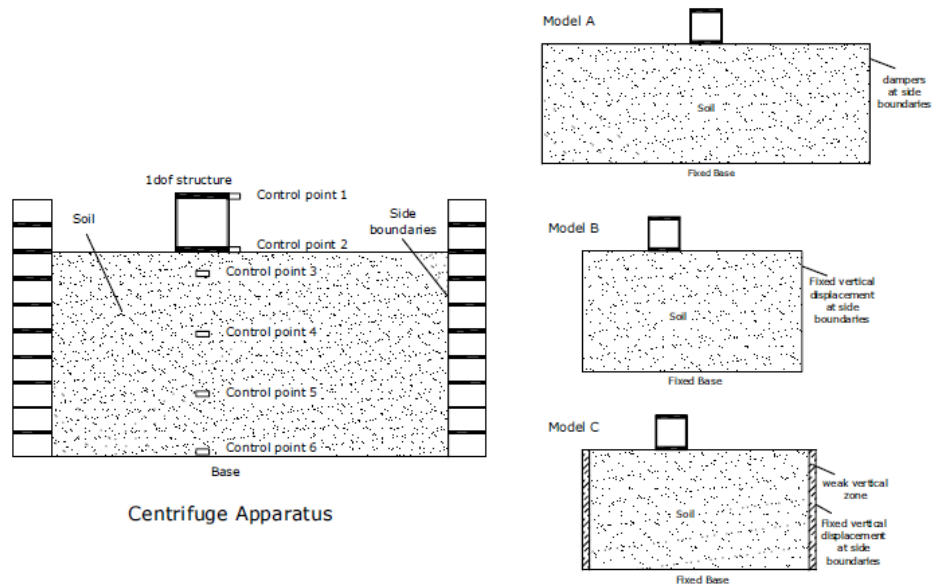


Figure 2.12: Centrifuge test and associated finite element models of a soil-structure system used by Pitilakis et al. (2004).

Kamai and Boulanger (2012) represents one of the few studies available in which the numerical model explicitly models the centrifuge container (Figure 2.13). The aluminum and rubber rings of the centrifuge container are modeled as elastic materials. The masses applied to the aluminum rings in the numerical model take into account the fact that the physical rings are hollow. The container is constrained horizontally during the construction phases of loading, and it is constrained vertically, but not horizontally, during shaking. There is a frictional interface and an impervious boundary between the soil and the container. Vertical deformations at the base of the model are prevented.

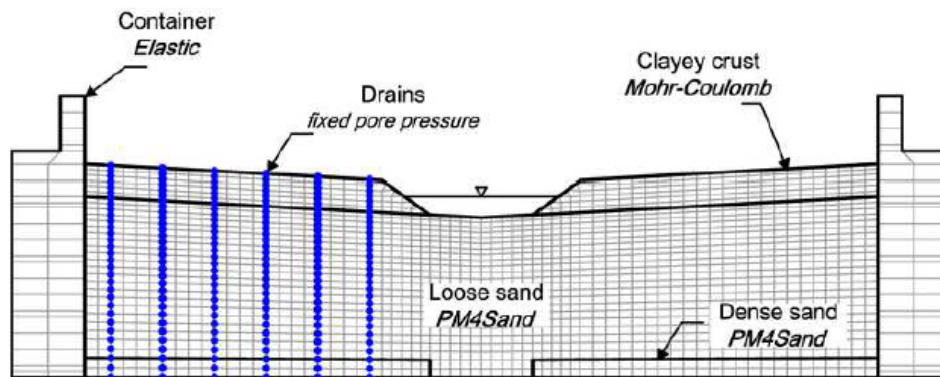
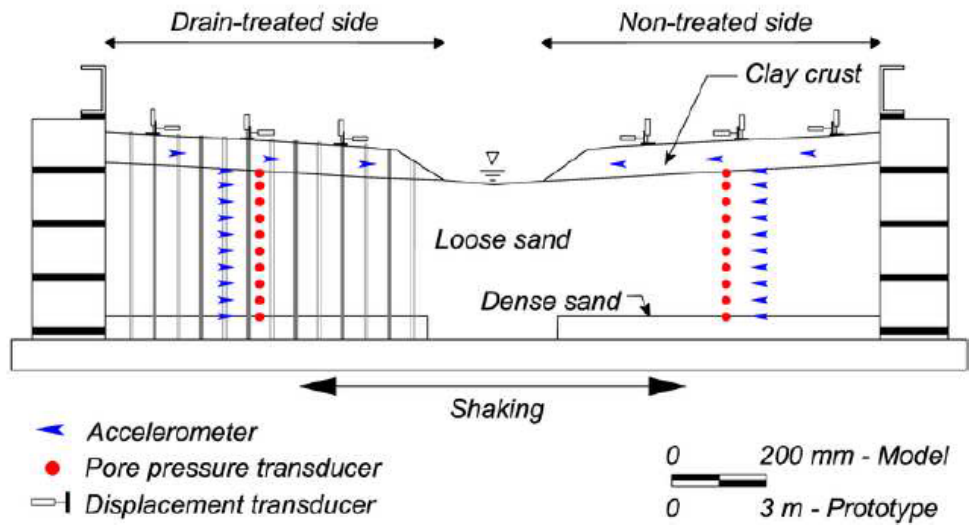


Figure 2.13: Centrifuge test and associated finite element model of untreated and drain-treated lateral spread sites used by Kamai and Boulanger (2012).

The studies by Yang et al. (2003), Byrne et al. (2004), Elgamal et al. (2005), Seid-Karbasi and Byrne (2007), and Phillips et al. (2012) use simplified numerical models that do not explicitly model the centrifuge container, but rather use various boundary conditions to account for some of the effects of the centrifuge container. Yang et al. (2003) used impervious lateral boundaries (Figure 2.14). Byrne et al. (2004) applied constraints such that the width of the model remained constant and the top of each element remained horizontal (Figure 2.15), and for one of the Byrne et al. (2004) models, interface elements were added on either side of the sand column to account for the presence of side friction present in the laminar centrifuge model container. Elgamal et al. (2005) used impervious lateral boundaries and the horizontal and vertical deformations at each depth were constrained to create a shear beam type effect (Figure 2.16). Seid-Karbasi and Byrne (2007) (Figure 2.17) and Phillips et al. (2012) (Figure 2.9d) also constrained the horizontal and vertical deformations at each depth to create a shear beam type effect.

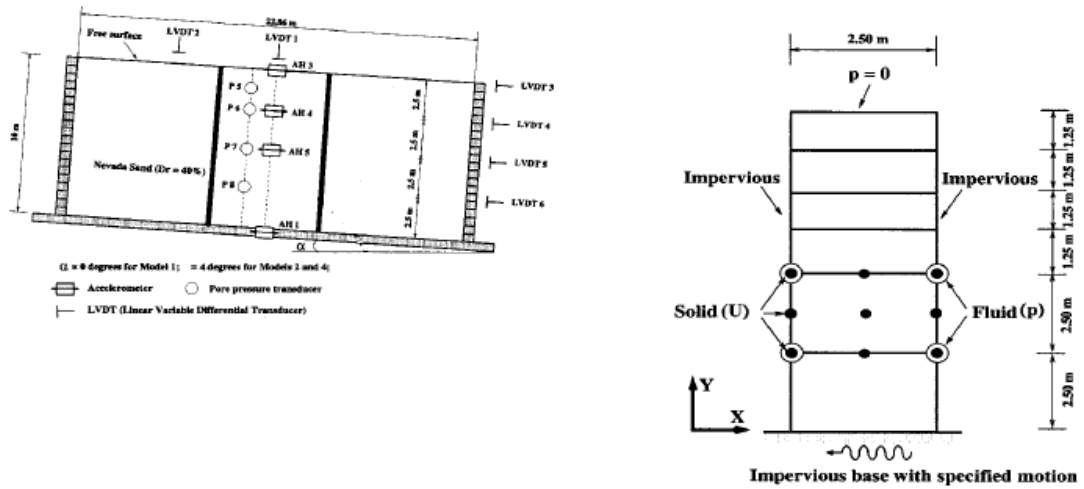


Figure 2.14: Centrifuge test and associated finite element model of a mildly sloping sand site used by Yang et al. (2003).

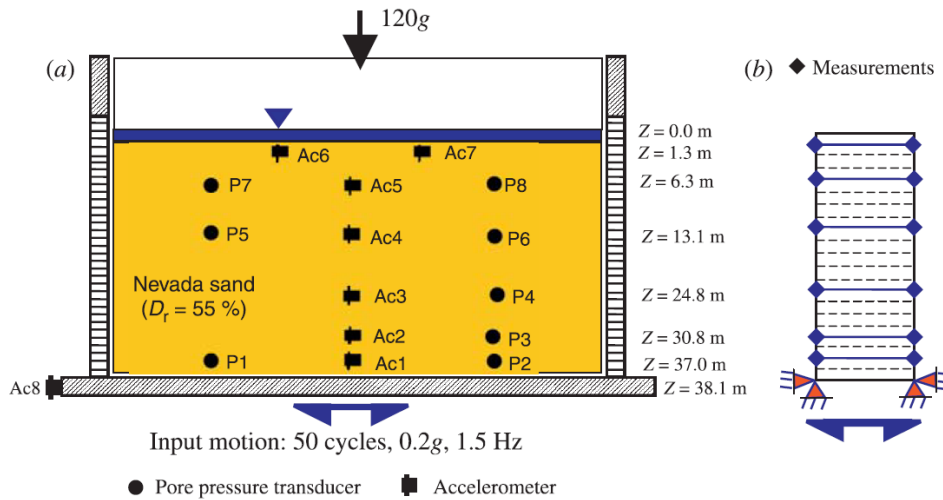


Figure 2.15: Centrifuge test and associated finite element model of liquefiable flat ground used by Byrne et al. (2004).

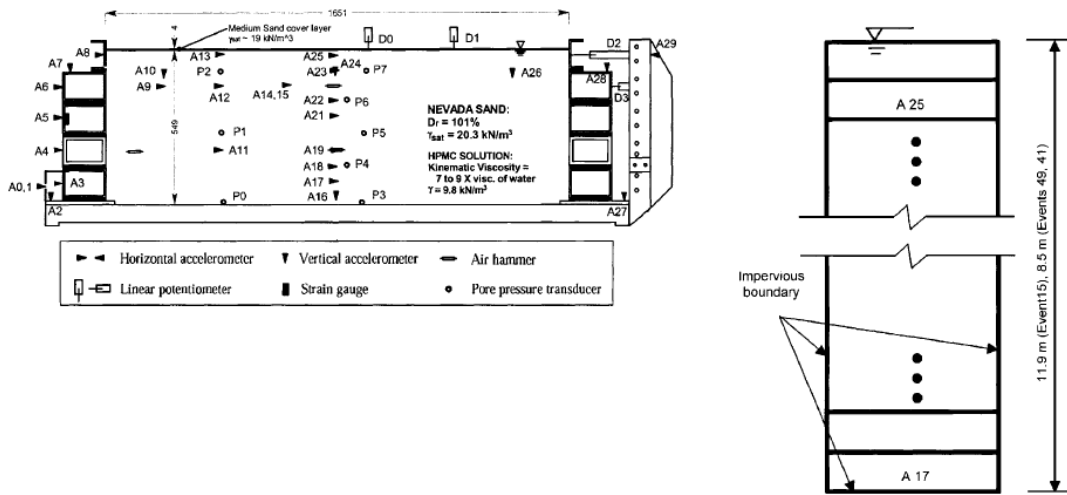


Figure 2.16: Centrifuge test and associated finite element model of a stiff sand site used by Elgamal et al. (2005).

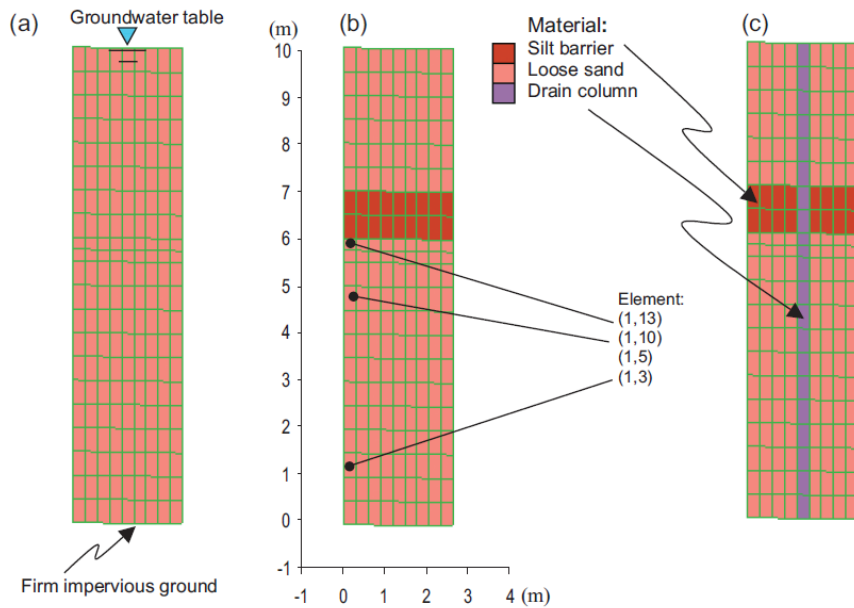


Figure 2.17: Finite element models of undrained and drained stratified soil deposits used by Seid-Karbasi and Byrne (2007).

2.5 Summary

This chapter provided background on drainage for liquefaction remediation, geotechnical centrifuge modeling, centrifuge tests that model lateral spread sites, and numerical models that simulate lateral spreading.

The use of drains as a liquefaction remediation technique began with gravel drains in the 1970's. More recently, prefabricated drains have been used for liquefaction remediation. The first design charts for drain spacing were developed by Seed and Booker (1977). However, the Seed and Booker (1977) design charts assumed that the drain was infinitely permeable. Onoue (1987 and 1988) showed that the permeability of the drain must be considered when determining drain spacing and developed new design charts that accounted for resistance in the drain. The Japanese Geotechnical Society (1998) provided new design charts for use with prefabricated drains that have been expanded to incorporate the large time factors that result due to the smaller drain radius. Alternatively, the finite element program FEQDrain can be used to select an appropriate drain spacing. However, neither FEQDrain nor the design charts can predict the deformation response of a lateral spread site treated with drains.

Centrifuges allow for the reproduction of prototype-scale stresses using relatively small-scale models. Although centrifuge models do not exactly replicate what happens in the field, the controlling behavioral mechanisms are still valid. Examples were provided of centrifuge tests used to model lateral spread sites. On the whole, these models consist of a single slope and they represent plane strain simulations of typical lateral spread sites. Numerical models of centrifuge tests of lateral spread sites often used simplified geometries and boundary conditions. These numerical models often capture the controlling behavioral mechanisms

present in the centrifuge tests and allow one to validate the numerical models against the centrifuge data.

Chapter 3

Centrifuge Testing of Lateral Spread Sites Treated with Prefabricated Vertical Drains

3.1 Introduction

A suite of three dynamic centrifuge tests are investigated and analyzed as part of this research. These tests are used to evaluate the performance of sloping ground treated with PVDs. All centrifuge testing was performed at the UC Davis Center for Geotechnical Modeling (CGM). The centrifuge at the CGM is 9 m in radius, can operate up to 75 g, and has a payload capacity of 340 g-tons. The centrifuge incorporates a large servo-hydraulic shaker that can be used to generate earthquake shaking (Kutter et al., 1994). Although the centrifuge models are small in scale compared to the field, the models used in this research, are considered large-scale centrifuge models, measuring 1.651 m (length) x 0.787 m (width) x

0.584 m (height). Each model was heavily instrumented with accelerometers, pore pressure transducers, and displacement transducers so that the model's responses could be evaluated. This chapter describes each of the centrifuge models and the observed responses from each model. Two of the centrifuge models (SSK01 and RNK01) were constructed and tested by others, and will be summarized here. The third centrifuge test (RLH01) was performed as part of this research and the results from this test will be investigated more fully in this chapter.

3.2 Relationship between Centrifuge Models and Field Sites

The centrifuge models used in this research are not modeled on a particular lateral spread site and do not capture all the characteristics of real lateral spread sites in the field. For instance, the centrifuge model container imposes boundary conditions that are not present in the field, and the centrifuge model lacks any spatial variability in material properties that would be present in a lateral spread site in the field. However, the objective of a centrifuge test is not to predict the response of a particular field site, but rather to enhance our understanding of the behavioral mechanisms controlling the general response of the phenomenon under consideration. The centrifuge test allows this phenomenon to be investigated under controlled conditions without the complexities and unknowns present at a field site. In this way, centrifuge tests complement field testing and field observations of behavior.

Centrifuge tests are particularly well-suited for studying mechanisms of

behavior under controlled conditions. The models are constructed with a known geometry and soil profile; shaking is applied in predetermined direction and at a selected intensity; and they are highly instrumented so their response can be recorded as fully as possible. Each of the centrifuge models used in this research contained over 80 instruments (accelerometers, pore pressure transducers, linear potentiometers), most of which were embedded in the model during construction. In most cases, installing such dense instrumentation within a field site is cost prohibitive and then there would be no guarantee that an earthquake would occur in a timely manner. An additional benefit associated with centrifuge testing for this project is that the drains were placed in the centrifuge model during construction and the sand was pluviated around the drains such that there were no densification effects associated with their placement. This approach to model construction allows the effects of drainage on the performance of liquefied ground to be investigated alone. There may be densification effects associated with the installation of drains in the field, but these centrifuge tests were designed to study the effects of drainage alone, not drainage with added densification, which will only increase the soil's resistance to liquefaction.

3.3 Centrifuge Test SSK01

3.3.1 Model Construction

The first dynamic centrifuge test, SSK01, was designed by Antonio Marinucci (Marinucci, 2010) and constructed by Seiji Kano. For more information on centrifuge test SSK01, please reference Kamai et al. (2007) and Kamai et al. (2013b). The SSK01 centrifuge model featured untreated and drain-treated mildly sloping (3°) soil profiles separated by a central channel (Figure 3.1). The model was designed for a centrifugal acceleration of 15 g, which makes the model dimension 15 times smaller than the prototype. Each slope was comprised of a 4 to 5 m thick (prototype scale) layer of liquefiable sand overlain by a 1 m thick (prototype scale) clay cap. The treatment areas were separated by a central channel that acted as a buffer between the two slopes such that the impact of the response of one area on the other area was minimized.

Nevada sand was used as the liquefiable sand in all three centrifuge models, and this sand is a relatively uniform, clean, fine sand. It has a specific gravity (G_s) of 2.64, a mean grain size (D_{50}) of 0.17 mm (model scale), a uniformity coefficient (C_u) of 1.64, and a hydraulic conductivity of 0.002 cm/s (at 1 g) (Howell et al., 2009a). The Nevada sand was placed in multiple layers using dry pluviation with the pluviator calibrated to the appropriate relative density for the layer (i.e., 40%). The model was saturated under vacuum with de-aired water (Howell et al., 2009a). Water was used as the pore fluid rather than a more viscous liquid (e.g., methyl cellulose) because there were concerns as to how well a more viscous fluid would flow through the model drains. The use of water meant that the scaling laws for consolidation and dynamic response were not simultaneously

satisfied (Section 2.3.1). The model’s response can still be interpreted using the scaling laws for dynamics, but with the hydraulic conductivity of the sand being effectively 15 times greater than that for the same sand at 1 g. The scaled hydraulic conductivity for fine Nevada sand corresponds to values that would be more typical of medium to coarse sands, which is realistic in terms of the type of soil in which drains would likely be installed. It should be noted that although the Catalogue of scaling laws and similitude questions in centrifuge modeling prepared by the International Technical Committee TC2 -Physical Modelling in Geotechnics (Garnier and Goudin, 2007) recommends scaling the hydraulic conductivity for dynamic flow in saturated centrifuge samples and this discussion references a scaled hydraulic conductivity, it can also be argued that the hydraulic conductivity does not scale directly but rather the flow is affected by the scaling of the length of the flow path and the applied head.

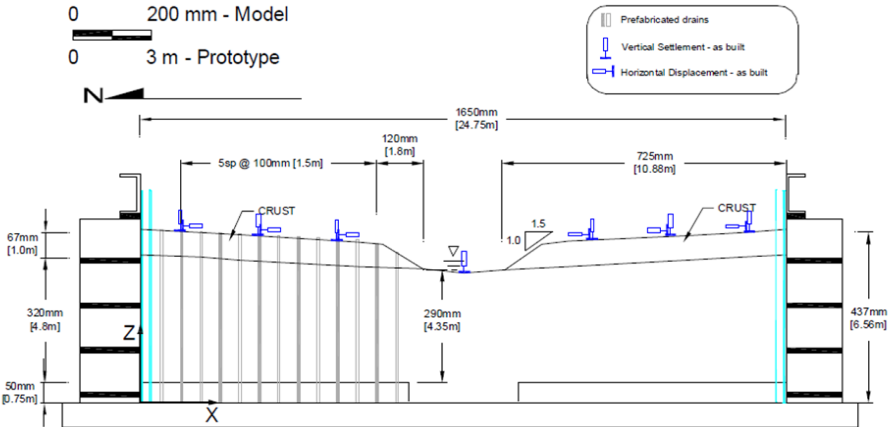


Figure 3.1: Model geometry of centrifuge test SSK01.

The model was built in a flexible shear beam container that consists of hollow aluminum rings separated by layers of neoprene rubber. The container is designed to be flexible enough to deform with the liquefied soil and minimize the reflection of stress waves off of the container walls (Kutter, 1995). There are shear rods on either end of the container that are designed to produce complementary shear stresses. A schematic of the container is shown in Figure 3.2.

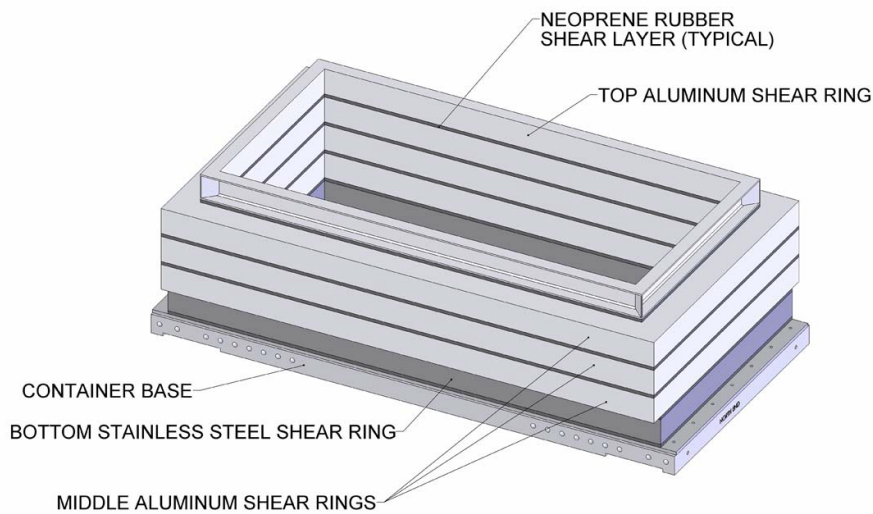


Figure 3.2: Schematic of a flexible shear beam container (Pedersen, 2004).

The treated area of the SSK01 model contained 58 model drains in a triangular pattern at a center-to-center spacing of 1.5 m (prototype scale). The drains were modeled using nylon tubes with an inside diameter of 7 mm (105 mm prototype scale). The drains were perforated along their lengths for the portion extending into the liquefiable soil layer. Each drain was wrapped in a precision woven polypropylene fabric mesh to prevent sand from entering the drain. The drains were placed in the model prior to the pluviation of the sand layers so there were no densification effects due to their placement.

Instrumentation in the model included vertical arrays of accelerometers and pore pressure transducers located at mid-slope within each treatment area, as well as vertical and horizontal deformation monitors along the surface of the model. The instrumentation embedded in the model was placed along the longitudinal mid-line of the slope where the response would be least affected by boundary effects (Figure 3.3).

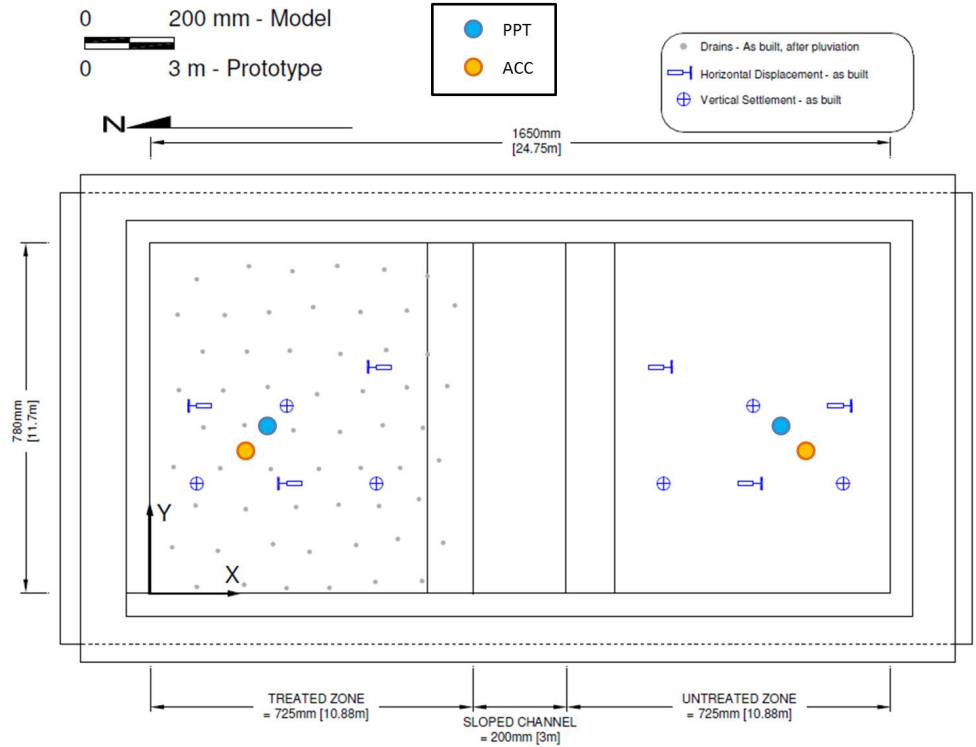


Figure 3.3: Instrumentation locations for SSK01.

The model was spun up to a centrifugal acceleration of 22 g to overconsolidate the soil ($\text{OCR} = 1.5$), and then the centrifugal acceleration was reduced to 15 g for the remainder of the test. The model was subjected to 12 sinusoidal input motions, each with 20 cycles of motion at a frequency of 2 Hz (prototype scale), and shaking was performed parallel to the slope. The amplitudes of the first three shaking events were too small to be captured by the sensors. The remaining shaking events ranged in PGA from 0.01 g to 0.3 g. The shaking events were spaced such that the generated excess pore water pressures from one event had fully dissipated before the next event was applied. The model was not rebuilt or modified between shaking events.

3.3.2 Test Results

The improved performance of the drain-treated area is evaluated based on the pore pressure and deformation responses. Figure 3.4 shows the measured excess pore pressures versus depth for the treated and untreated zones for shaking event SSK01.12 ($\text{PGA} = 0.30$ g). Drains are effective in reducing the peak excess pore water pressures and increasing the rate of pore water pressure dissipation. Figure 3.5 shows the cumulative horizontal and vertical deformation time series for the treated and untreated areas across the five main shaking events. For each shaking event, the treated zone experienced less deformation than the untreated zone, particularly in the horizontal direction. At the conclusion of the test, the permanent horizontal and vertical deformations in the drain-treated zone were 80% and 50% smaller, respectively, than those observed in the untreated zone.

The observed reduction in the horizontal deformations in the drain-treated area of this model was much larger than anticipated. It was hypothesized that the rigidity of the model drains, which were made of a stiff nylon plastic, reinforced the soil in the drain-treated area resulting in an exaggerated reduction in the horizontal deformations. For more information on the results of this test, please see Marinucci et al. (2008) and Marinucci (2010).

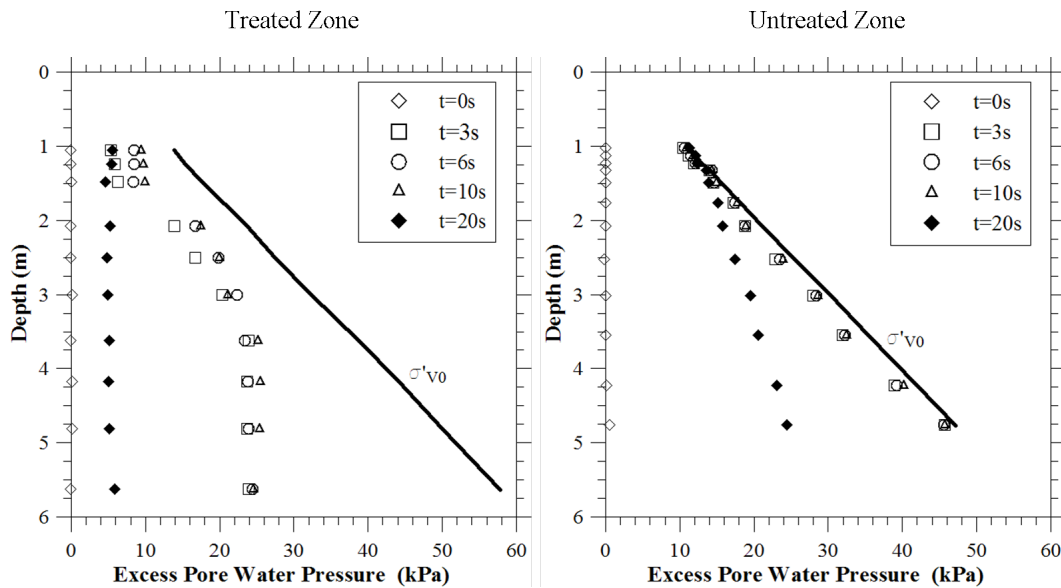


Figure 3.4: Excess pore pressure development with depth and time in the treated and untreated zones for shaking event SSK01.12 (PGA = 0.30 g) (Marinucci et al., 2008).

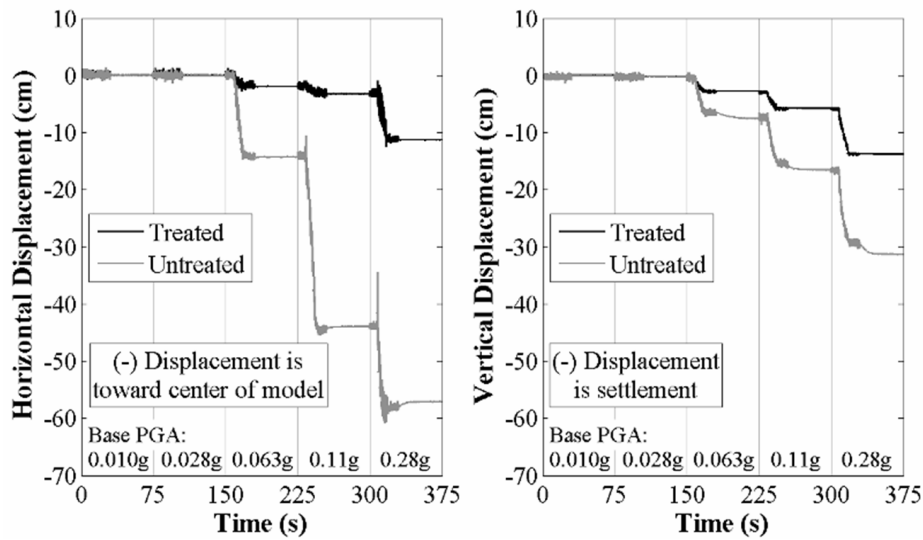


Figure 3.5: Cumulative horizontal and vertical displacements in the treated and untreated zones for SSK01 (Marinucci et al., 2008).

3.4 Centrifuge Test RNK01

3.4.1 Model Construction

The second centrifuge test, RNK01, used the same design as centrifuge test SSK01 (Marinucci, 2010) and was constructed and tested by Ronnie Kamai. For more information on centrifuge test RNK01, please reference Kamai et al. (2008) and Kamai et al. (2013a). The RNK01 model was designed to investigate the potential slope reinforcement issue identified in SSK01. Like the SSK01 centrifuge model, the RNK01 model featured untreated and drain-treated sloping (3°) soil profiles separated by a central channel. However, the untreated area in the RNK01 model contained non-draining tubes of a material identical to that of the drains so that

the effect of their stiffness on the untreated response could be evaluated. The RNK01 model was designed for a centrifugal acceleration of 15 g and the geometry of the model was identical to that of the SSK01 model. The RNK01 model was constructed in a flexible shear beam container (Figure 3.2), and instrumentation was placed along the longitudinal mid-line of the slope where the response would be least affected by boundary effects (Figure 3.6).

The treated and untreated areas of RNK01 each contained 58 model drains/tubes in a triangular pattern at a center-to-center spacing of 1.5 m (prototype scale). The model drains/tubes used in RNK01 were identical to those used in SSK01 (Section 3.3.1) and as before each drain was wrapped in a precision woven polypropylene fabric mesh to prevent sand from entering the drain. The drains/tubes were placed in the model prior to pluviation of the sand layers so that there were no densification effects due to their placement.

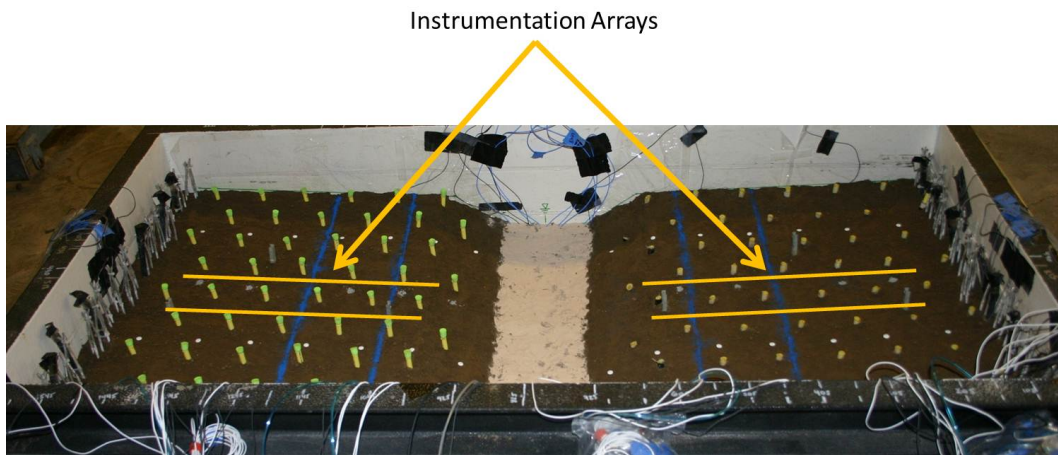


Figure 3.6: Photo of centrifuge model RNK01 with instrumentation locations.

Water was used as the pore fluid, and the model was saturated under vacuum over a period of 24 hours. The model was spun up to a centrifugal acceleration of 22 g to overconsolidate the soil ($OCR = 1.5$), and then the centrifugal acceleration was reduced to 15 g for the remainder of the test. The model was subjected to 18 shaking events. The first shaking event was a 0.05 g step wave. The next 15 shaking events were earthquake motions ranging in PGA from 0.018 to 0.88 g. Two earthquake acceleration-time histories (Figure 3.7) were used for these input motions. These are outcrop motions recorded during the 1994 Northridge earthquake (PAC175) and the 1974 San Fernando earthquake (PSL180). Finally, two sine wave input motions with 20 cycles of motion at a frequency of 2 Hz (prototype scale) with PGAs of 0.26 g and 0.56 g were applied to the model. The shaking events were spaced such that the generated excess pore water pressures from one event had fully dissipated before the next event was applied. The model was not rebuilt or modified between shaking events.

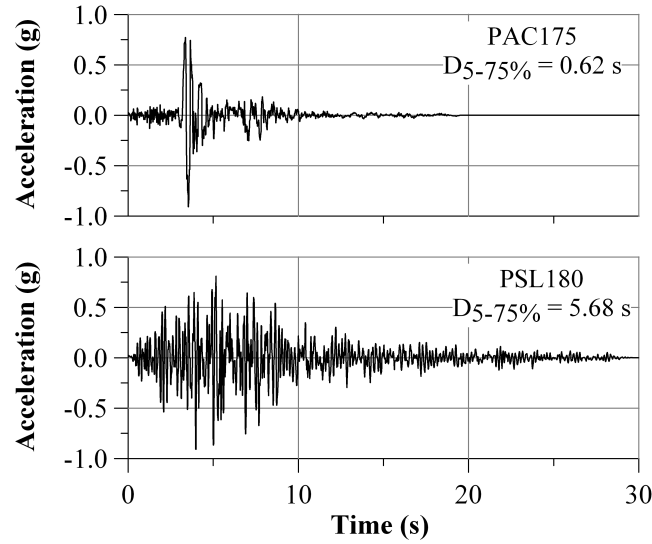


Figure 3.7: RNK01 input motions.

3.4.2 Test Results

The RNK01 model featured drains in the drain-treated area and non-draining tubes in the untreated area. Because both slopes in the RNK01 model contain drains/tubes, the only difference between the untreated and drain-treated areas in this model is drainage. Thus, it can be determined whether the improvement observed in RNK01 differs significantly from the SSK01 observations. Figures 3.8 and 3.9 show the cumulative horizontal and vertical displacements for the RNK01 centrifuge test. In the SSK01 centrifuge test, there was an 80% and 50% reduction observed in the horizontal and vertical deformations, respectively. In RNK01, the drain-treated zone still showed improvement in terms of the excess pore water pressures, but the cumulative horizontal and vertical deformations in the treated area and the untreated-tube area were very similar up until the

0.88 g shaking events (PAC08 and PSL07). At the conclusion of this test, the cumulative horizontal and vertical deformations in the drain-treated area were only 27% and 33% smaller, respectively, than those observed in the untreated area. The decrease in the observed improvement indicates that the stiffness of the tubes did affect the deformations of the drain-treated area in the SSK01 centrifuge test. Therefore, the improved performance observed in SSK01 cannot be solely attributed to the effects of drainage through the model PVDs.

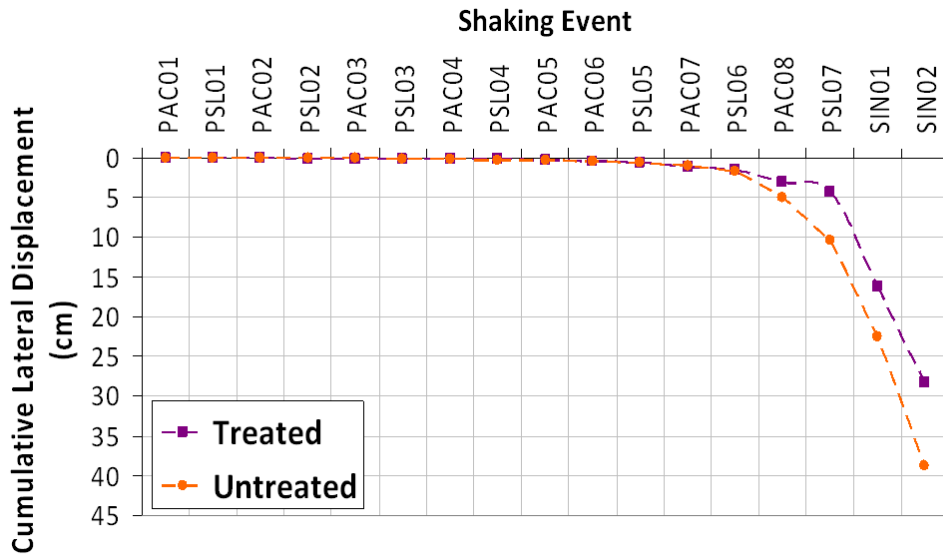


Figure 3.8: Cumulative horizontal displacements for RNK01.

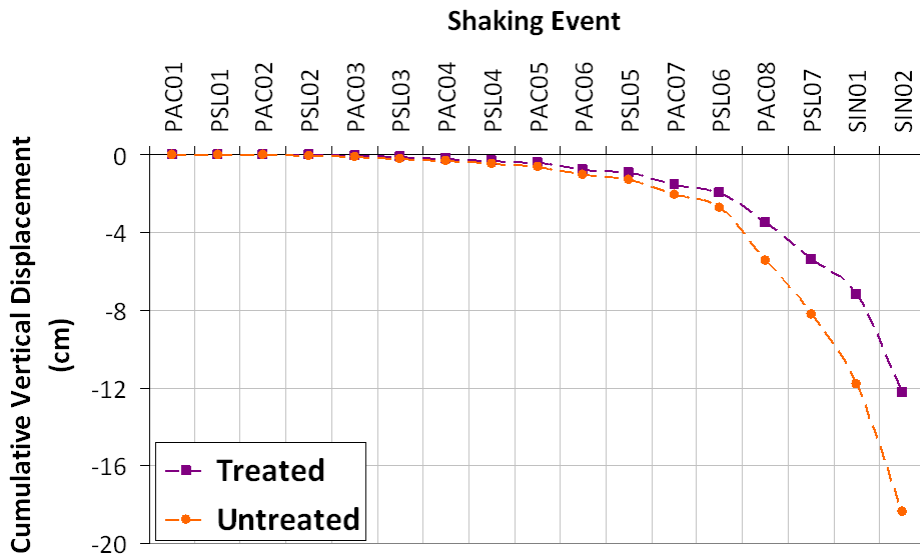


Figure 3.9: Cumulative vertical displacements for RNK01.

3.5 Centrifuge Test RLH01

3.5.1 Model Construction

The third centrifuge test, RLH01, was designed to investigate the slope reinforcement issue associated with the nylon drains, as well as to provide additional data regarding the beneficial effects of drains. To minimize the slope reinforcement effects, the nylon tubes were replaced by more flexible tubes made of a rubber-plastic blend. To further investigate the reinforcement issue, the slope consisted of three adjacent treatment areas: a drain-treated area, an untreated area, and an untreated area with non-draining tubes. In order to fit all three treatment areas in a single model, the orientation of the model was rotated such that it consisted of a single slope and a channel aligned with the longer dimension of the laminar box (Figures 3.10 and 3.11). As a result, shaking took place orthogonal to the direction of the slope. To compensate for the lack of inertial forces parallel to the slope and ensure that significant lateral deformations would occur, the slope angle was steepened from 3° (SSK01 and RNK01) to 10° and the clay layer was thickened from 1 m (SSK01 and RNK01) to 1.5 m.

The model for RLH01 was built in the same flexible shear beam container used in SSK01 and RNK01 (Section 3.3.1). Due to the rotated geometry, additional measures were taken to limit the boundary effects due to both the container and the close proximity of the treatment areas. The clay crust was separated from the container and bentonite slurry was placed between the clay and the container walls. Cuts were made in the clay cap between the treatment areas, and these cuts were also filled with bentonite slurry (Figure 3.12). The instrumentation was placed in the center of each treatment area to minimize the boundary effects on

the recorded data. Figure 3.13 shows the placements of the pore water pressure transducers and accelerometers in the drain-treated area. Post-shaking photos of the model indicate that although there was a zone of overlapping influence between the untreated and drain-treated areas, the instrumentation for each area was outside of this zone (Figure 3.14).

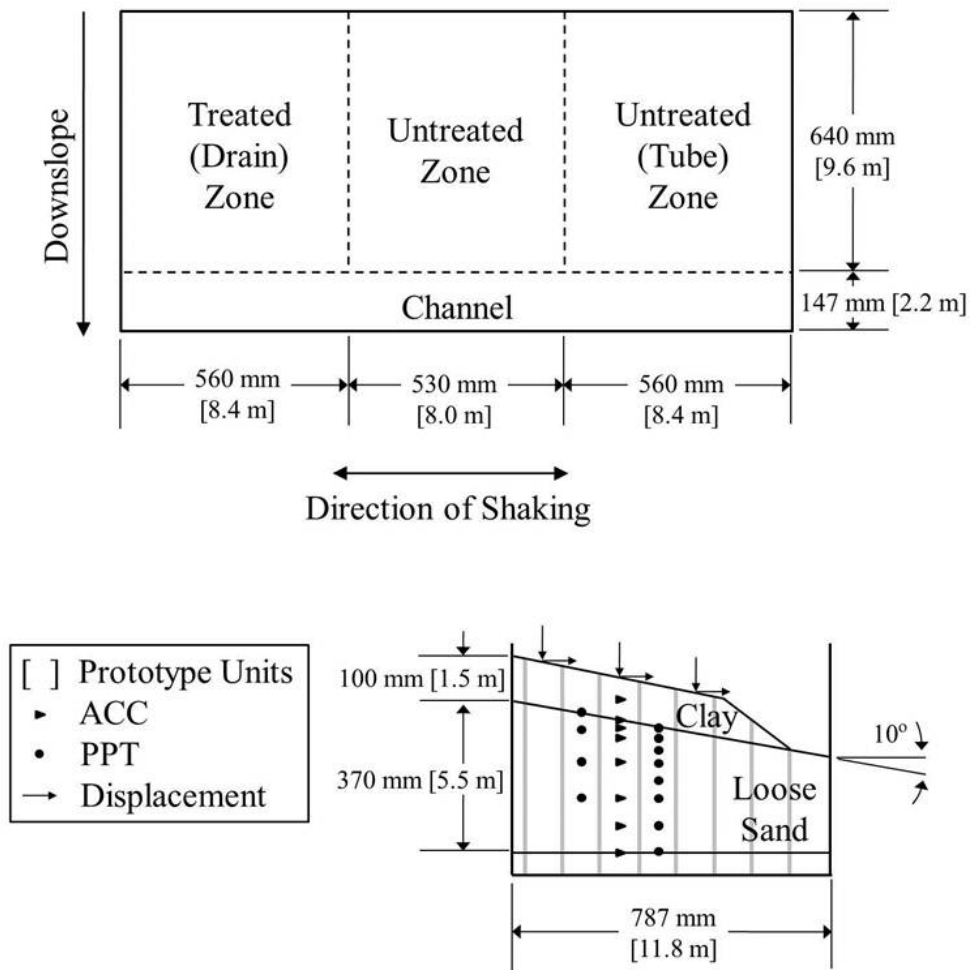


Figure 3.10: Model geometry of centrifuge test RLH01.

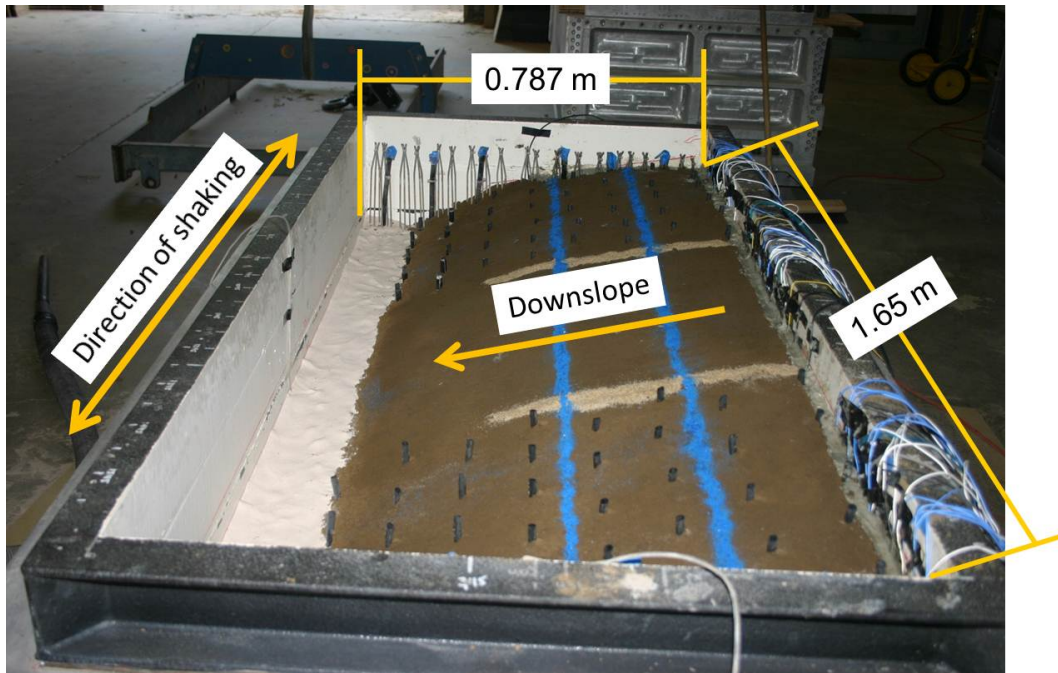


Figure 3.11: Photo of the RLH01 centrifuge model.

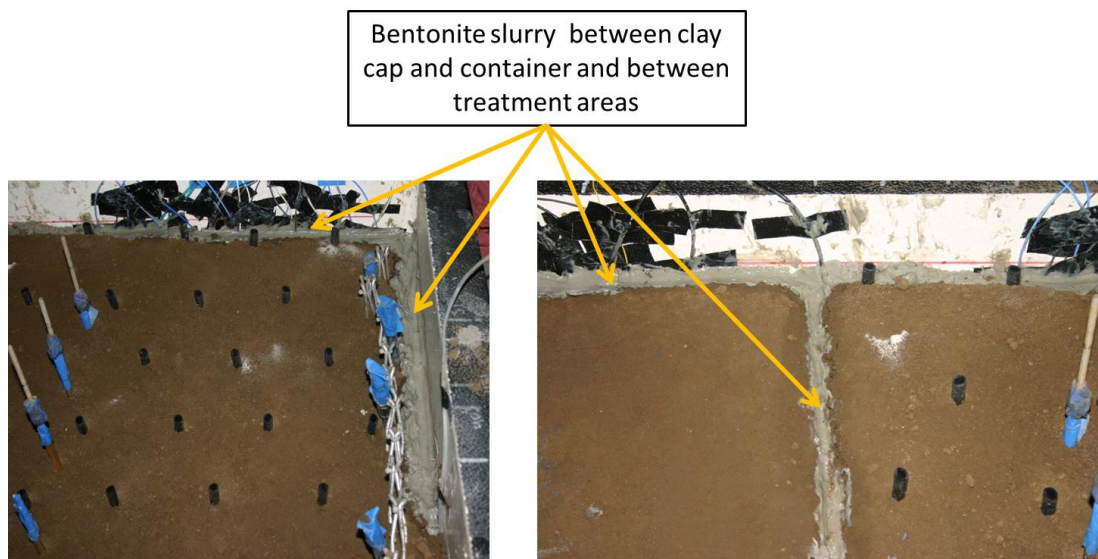


Figure 3.12: Bentonite slurry in the RLH01 centrifuge model.

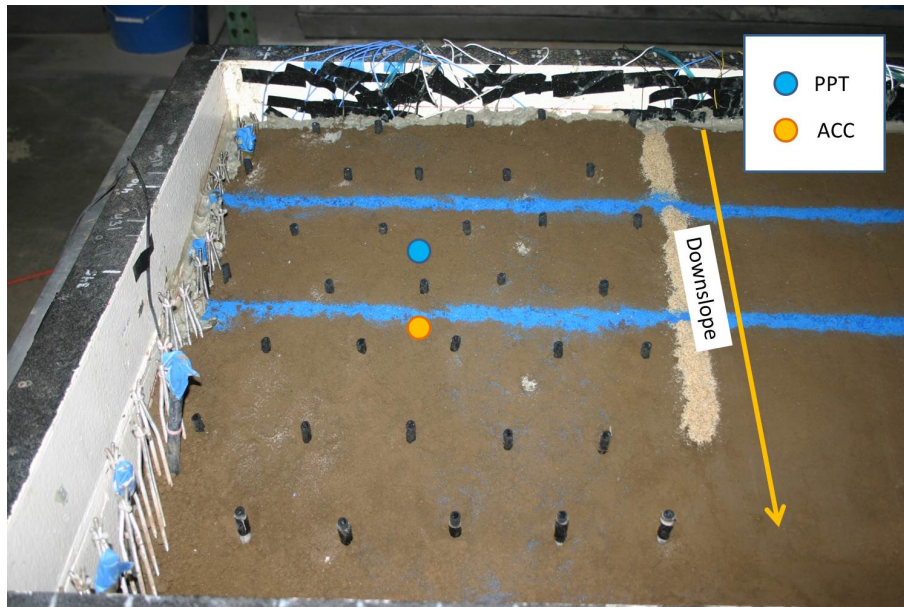


Figure 3.13: Instrumentation placement in the drain-treated area of the RLH01 centrifuge model.

The treated area and untreated area containing non-draining tubes each contained 40 model drains/tubes in a triangular pattern at a center-to-center spacing of 1.5 m (prototype scale). The drains/tubes were constructed of a rubber-plastic blend tubing. The drains were perforated along their lengths for the section of the drain located within the liquefiable layer. Each drain was wrapped in a precision woven polypropylene fabric mesh to prevent sand from entering the drains. The drains/tubes were placed prior to the pluviation of the sand layers so that there were no densification effects due to the placement of the drains.

Water was used as the pore fluid, and the model was saturated under vacuum. However, the saturation tubes in this model were clogged and the model had to be saturated from the top down rather than from the bottom up. The

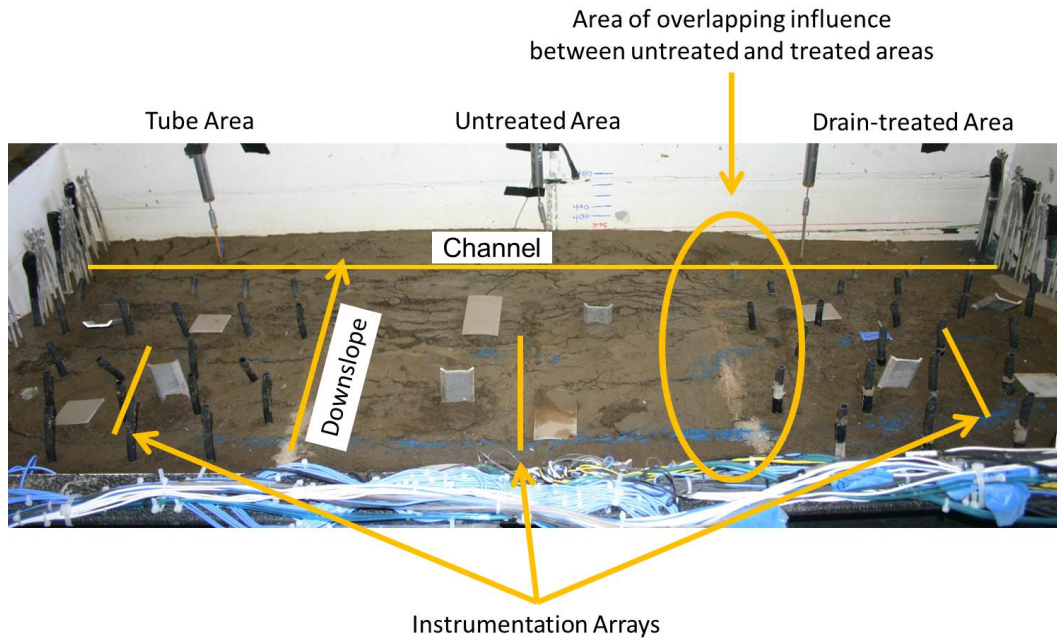


Figure 3.14: Post-shaking photo of the RLH01 centrifuge model.

model was spun up to a centrifugal acceleration of 22 g to overconsolidate the soil ($OCR = 1.5$) and stiffen up the clay layer, and then the centrifugal acceleration was reduced to 15 g for the remainder of the test. A total of 10 shaking events were applied to the model. The first shaking event was a step wave with a PGA of 0.016 g. The next eight shaking events were earthquake motions ranging in PGA from 0.1 to 0.95 g. The same input motions used in RNK01 were used again in RLH01 (Figure 3.7). The final shaking event was a sine wave with 20 cycles of motion at a frequency of 2 Hz (prototype scale) and a PGA of 0.6 g. As was the case with SSK01 and RNK01, the shaking events were spaced such that the generated excess pore water pressures from one event had fully dissipated before the next event was applied, and the model was not rebuilt or modified between shaking events.

3.5.2 Test Results

The RLH01 model contained two untreated areas (i.e. untreated and untreated with non-draining tubes) in an effort to investigate the influence of the stiffness of the tubing on the results. Figures 3.15 and 3.16 show measured excess pore pressure ratio (r_u) and displacement-time histories from the untreated area and the untreated area with non-draining tubes for selected shaking events. The untreated area and the untreated area with non-draining tubes had similar pore water pressure and deformation responses (e.g., Figures 3.15 and 3.16), indicating that the new tubing used to model the drains was flexible enough such that the presence of the tubes did not influence the behavior of the tube-treated area.

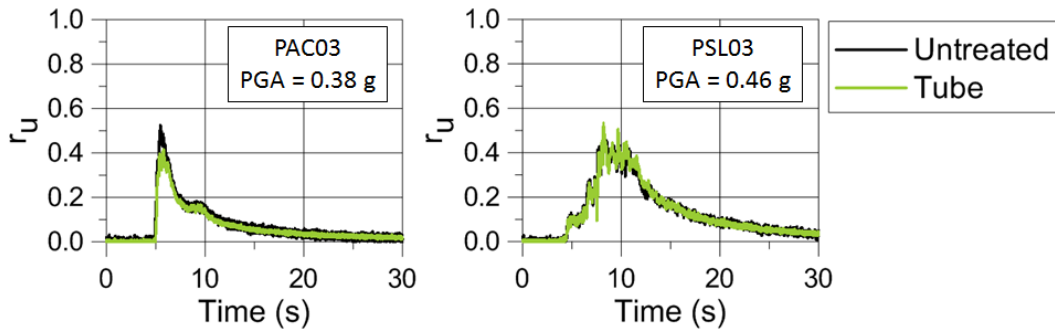


Figure 3.15: Comparison of pore pressure responses at the base of the untreated area and untreated area with non-draining tubes for shaking events PAC03 and PSL03.

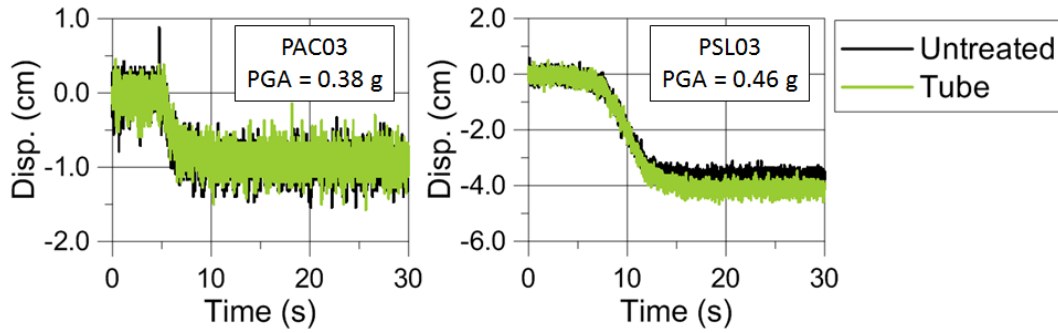


Figure 3.16: Comparison of deformation responses for the untreated area and untreated area with non-draining tubes for shaking events PAC03 and PSL03.

The pore pressure response in the untreated and treated areas of the RLH01 model was evaluated by means of the vertical array of PPTs located at mid-slope in each treatment area (Figure 3.10). The r_u -time histories for the untreated and treated areas at a depth of approximately 2.2 m (prototype scale) are shown in Figure 3.17 for the three highest intensity events (PAC04, PSL04, and SIN01). These data illustrate how the ground motion characteristics influence the pore pressure response.

The PAC04 event is dominated by a few, large intensity cycles within the first second of shaking, which cause the r_u levels in both the untreated and treated areas to increase rapidly towards 1.0. In the untreated area, r_u remains elevated throughout shaking and for several seconds afterwards, whereas in the treated area, r_u decreases after the initial high intensity cycles of shaking, increases again during later acceleration cycles, and then decreases quickly at the end of shaking (Figure 3.17).

The PSL04 motion is similar in PGA to the PAC04 motion, but the pore pressure response is different due to the characteristics of shaking. The PSL04 input motion builds up in intensity with the PGA occurring about five seconds after shaking begins. In the untreated area, r_u increases quickly at the start of shaking, continues to increase as larger cycles of shaking occur, and remains elevated for more than 10 seconds after shaking ends (Figure 3.17). In the treated area, the average r_u throughout shaking is smaller than that of the untreated area because the acceleration-time history evolves slowly enough over time to give the soil time to drain. While the r_u level in the untreated area remains elevated for more than after shaking ends, the r_u level in the treated area decreases to 0.2 within 5 seconds of the end of shaking (Figure 3.17).

The SIN01 motion is distinct from either the PAC or PSL motions because the amplitude and frequency content of shaking are constant throughout the 10 seconds of shaking. Large r_u levels are evident in both the untreated and treated areas during shaking. However there are significant dilation spikes in the pore pressure response for the treated area (i.e., cyclic reductions in r_u during shaking), and the r_u level in the treated area drops to 0.3 immediately after shaking ends. In the untreated area, r_u is still above 0.9 six seconds after shaking ends and above 0.4 sixteen seconds after shaking ends.

There are two key observations that can be made from Figure 3.17. The first observation is that the drains are effective in dissipating excess pore water pressures both during and after shaking. This is evident in the reduction in r_u after the initial high intensity acceleration cycles in the PAC04 event, the smaller average r_u levels throughout shaking in the PSL04 event, the large dilation spikes in the SIN01 event, and the rapid excess pore pressure dissipation at the end

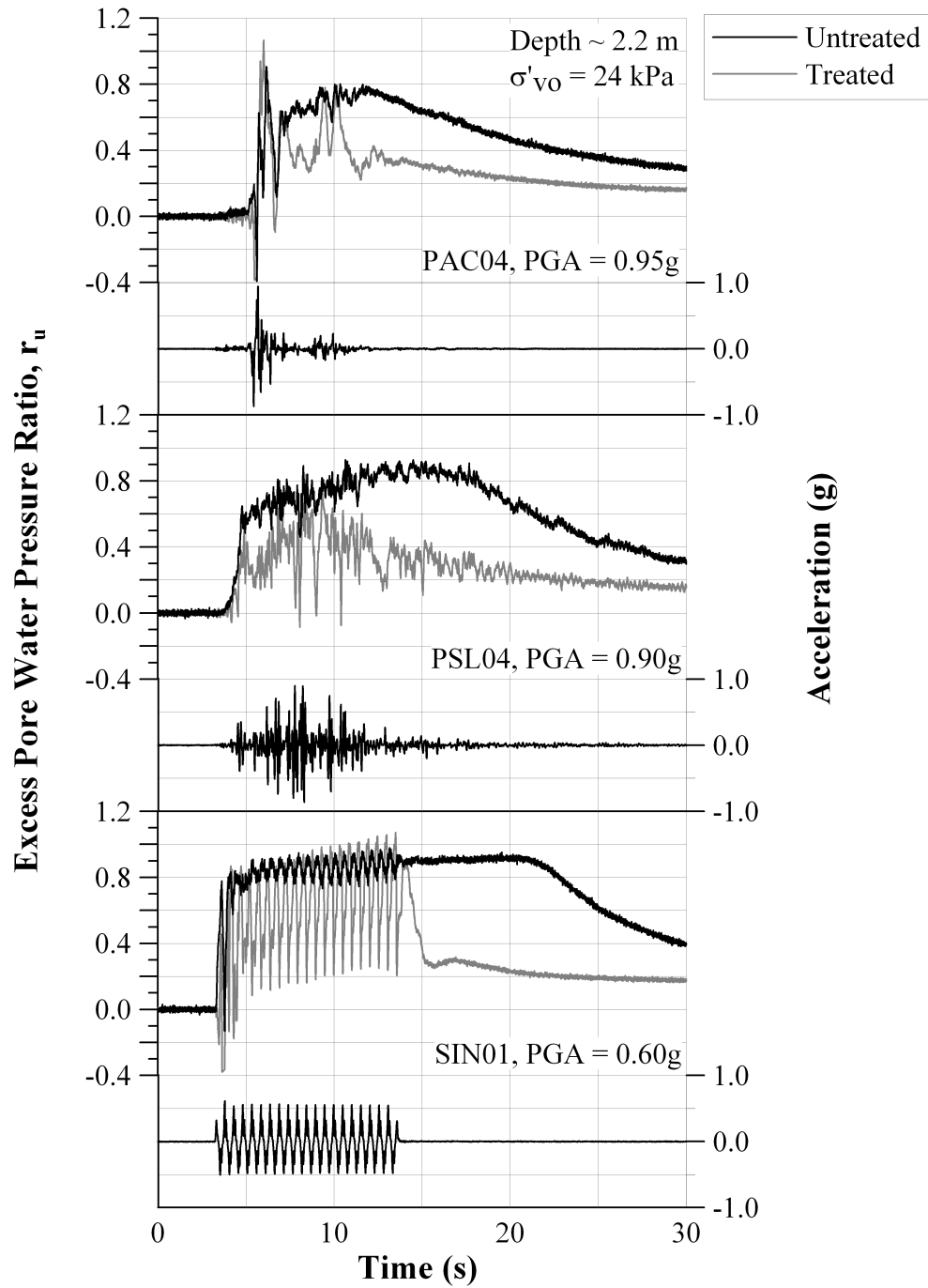


Figure 3.17: Excess pore water pressure ratio, r_u , vs. time for the PAC04 (PGA = 0.95 g), PSL04 (PGA = 0.90 g), and SIN01 (PGA = 0.60 g) events.

of shaking in all three events. The second observation that can be made from Figure 3.17 is that the impact of the drains on the excess pore pressure response is sensitive to the characteristics of the input motion, which is consistent with the observations made for gravel drains in previous studies by Sasaki and Taniguchi (1982) and Iai et al. (1988). In the PAC04 event, the highest intensity cycles occur almost immediately such that the pore water does not have time to flow to the drains. The impact of the drains is therefore not immediately realized and r_u approaches 1.0 in both the untreated and treated areas. In the PSL04 event, the highest intensity cycles occur near the middle of the shaking event such that the pore water has time to reach the drains. As a result, the average r_u level in the treated area is smaller than that in the untreated area. All of the acceleration cycles in the SIN01 event are of the same intensity, and without the smaller intensity cycles to allow time for drainage, the r_u level in the treated area remains high ($r_u > 0.8$) throughout shaking. For the SIN01 motion, the full impact of the drains cannot be realized until shaking has ended.

The results shown in Figure 3.17 are from a single depth in the liquefiable layer, whereas the drains impact the pore pressure response and flow patterns throughout the entire soil deposit. Figure 3.18 illustrates profiles of excess pore water pressure (Δu) versus depth for the untreated and treated areas at multiple instances in time for the PAC04, PSL04, and SIN01 events. These data are used to illustrate the influence of the drains on the flow patterns and dissipation mechanisms in treated soil.

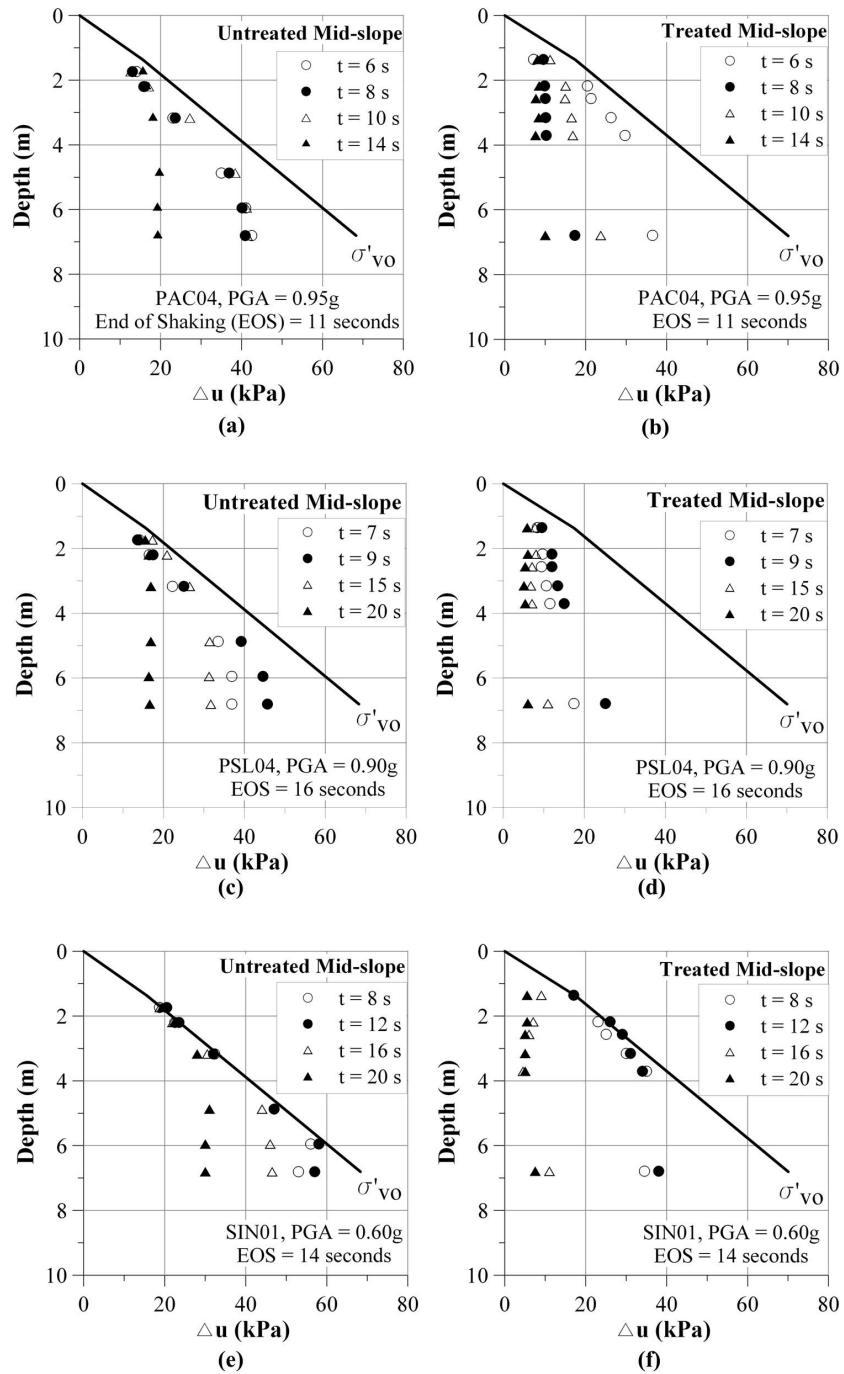


Figure 3.18: Development of excess pore water pressure versus depth with time for the PAC04 (PGA = 0.95 g), PSL04 (PGA = 0.90 g), and SIN01 (PGA = 0.60 g) events.

In the PAC04 event (Figure 3.18a and 3.18b) the Δu profiles near the start of shaking ($t = 6$ s) in the untreated and treated areas are similar, with $\Delta u \sim \sigma'_{vo}$ in the top 3 m and $\Delta u < \sigma'_{vo}$ at depths below 3 m. In the untreated area (Figure 3.18a), the Δu profile remains elevated throughout shaking ($t = 8$ s and 10 s). After shaking ends, dissipation in the untreated area is observed at the bottom of the liquefiable layer while Δu in the upper part of the layer remains elevated, indicating that there is an upward flow pattern. In the treated area (Figure 3.18b), the Δu profile indicates that dissipation begins earlier ($t \sim 8$ s) and a Δu profile develops that is generally uniform throughout the liquefiable layer for most of the shaking event. The shortened drainage path disrupts the upward flow pattern such that a uniform Δu profile develops due to radial drainage. The uniform Δu profile in the treated area (Figure 3.18b) at $t = 14$ s represents $r_u = 0.48$ at 1.4 m depth and $r_u = 0.14$ at 6.8 m depth.

In the PSL04 event (Figures 3.18c and 3.18d), the Δu profile in the untreated area (Figure 3.18c) follows the same pattern as it did in the PAC04 event - large Δu during strong shaking followed by dissipation and a decrease in Δu at the bottom of the liquefiable layer and little to no decrease in Δu for the upper part of the liquefiable layer. In the treated area, smaller values of Δu are realized at all times and Δu stays fairly uniform throughout shaking (Figure 3.18d).

In the SIN01 event (Figures 3.18e and 3.18f), the untreated area liquefies ($\Delta u = \sigma'_{vo}$) throughout most of the entire depth of the loose sand layer (Figure 3.18e). At the end of shaking ($t = 14$ to 16 s), dissipation begins and Δu decreases at the bottom of the liquefiable layer, but the upper part of the layer remains liquefied more than 6 seconds after shaking has ended ($t = 20$ s). In the treated

area (Figure 3.18f), only the upper ~ 3 m of the layer liquefies, and once dissipation begins at the end of shaking ($t > 14$ s), the Δu profile quickly becomes uniform throughout the layer.

While Figure 3.18 shows the excess pore water pressures at several depths in the liquefiable layer at multiple instances in time, it is more convenient to summarize the spatial and temporal excess pore water pressure responses with a single parameter. One such parameter that has been used in the past is $\bar{r}_{u,\max}$ (e.g., \bar{r}_g from Seed and Booker, 1977), where $\bar{r}_{u,\max}$ is defined as the peak of the \bar{r}_u - time history, and \bar{r}_u is the spatial average (over depth and radius) of r_u within the radius of the influence of the drain. The average excess pore pressure ratio, \bar{r}_u , is also recommended for use in slope stability calculations by Bishop and Morgenstern (1960) to characterize pore pressures in sections of slopes where r_u is not constant. Calculation of \bar{r}_u and $\bar{r}_{u,\max}$ for the centrifuge data is illustrated in Figure 3.19. \bar{r}_u was calculated from the point measurements of Δu along the vertical PPT array. Radial PPT arrays from the first centrifuge test (SSK01) indicated that pore pressures did not vary significantly with radial distance (Marinucci, 2010), and thus considering only vertical variations in the \bar{r}_u calculation is deemed appropriate. The \bar{r}_u calculation used a weighted average in which the r_u - time history for each PPT was weighted by the layer thickness (Δz) derived from the mid-points between the upper and lower adjacent PPTs. In the treated area of RLH01, there was a large area in the lower half of the liquefiable layer where no Δu - time histories were available due to the instrumentation failures. To compensate for the instrument failure and to fill this gap when computing \bar{r}_u , an interpolated data point of Δu was created between the bottom PPT and the next functional PPT (Figure 3.19). The interpolated data was created assuming

a linear variation of Δu with depth. The functional PPTs in the untreated area were more uniformly distributed; therefore, no data interpolation was needed for that treatment area. After computing \bar{r}_u at each time step, $\bar{r}_{u,\max}$ was taken as the maximum value in the \bar{r}_u time series.

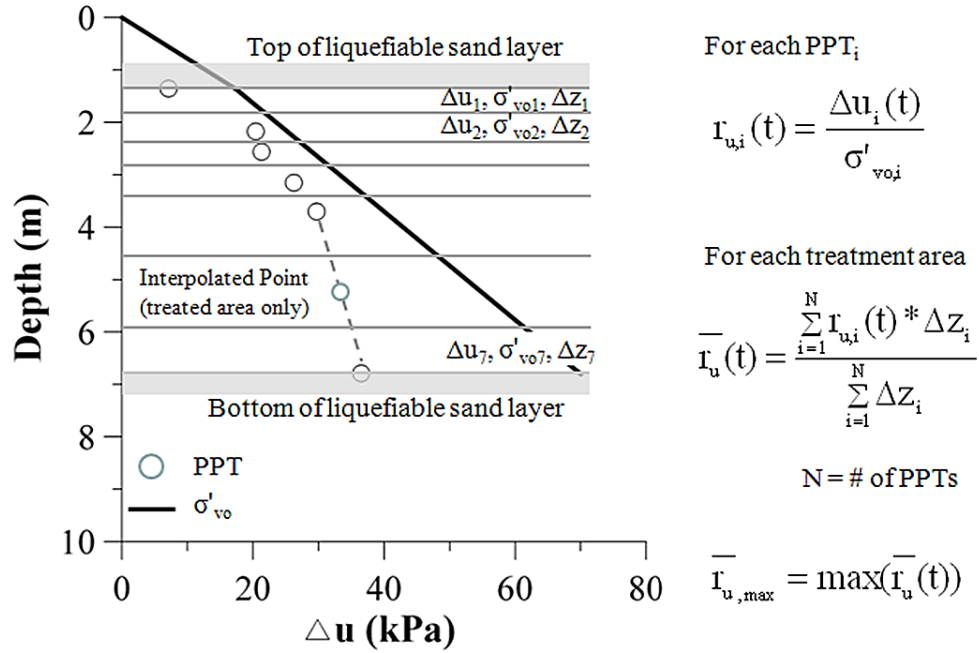


Figure 3.19: Calculation of r_u , \bar{r}_u , and $\bar{r}_{u,\max}$ in RLH01.

Figure 3.20 shows $\bar{r}_{u,\max}$ graphed as a function of input PGA for the RLH01 shaking events that induced excess pore water pressures. These data show that $\bar{r}_{u,\max}$ generally increases with increasing PGA and it is consistently smaller in the treated area than in the untreated area. For the untreated area, $\bar{r}_{u,\max}$ is slightly larger for the large intensity PSL event (PGA = 0.9 g) than for the large intensity PAC event (PGA = 0.95 g) because the PSL event has more cycles of motion. In contrast, values of $\bar{r}_{u,\max}$ in the treated area are larger for the PAC events than the PSL events because the short duration of the PAC input motion does not

provide much time for water to drain and thus there is a smaller reduction in the peak excess pore pressure ratios and $\bar{r}_{u,max}$. The $\bar{r}_{u,max}$ values for the SIN event are significantly larger than the $\bar{r}_{u,max}$ values for the PAC and PSL events because of its different ground motion characteristics.

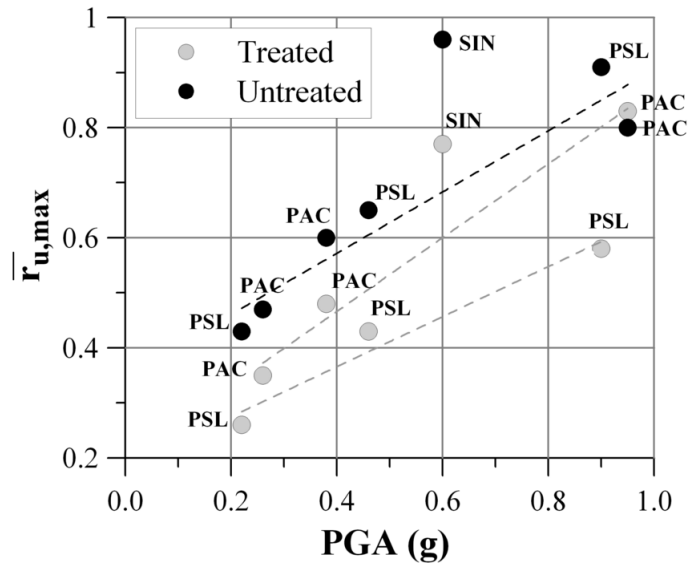


Figure 3.20: $\bar{r}_{u,max}$ as a function of PGA.

From the results presented, it is apparent that the 0.60 g SIN01 event produced larger excess pore pressures than either the 0.95 g PAC event or the 0.90 g PSL event. The fact that the sine waves and earthquake motions produced significantly different responses from the model illustrates that it is important to avoid overly generalizing observations from any one shaking event, whether sine waves or earthquake motions. Additionally, it is valuable to obtain model responses to a range of input motions for the purpose of providing a thorough test for the validation of numerical models.

PVDs affect the deformation response through their impact on the generated excess pore water pressures, the dissipation rate of excess pore pressures, and the flow patterns within the soil. By reducing the magnitude of the generated excess pore water pressures and increasing the rate of dissipation, drains decrease the amount of time that the soil spends in a low-strength or liquefied state, which in turn decreases the intensity of the resulting deformations. Additionally, drains can prevent the loosening of soil near the low-permeability interface and the resulting localized shear deformations.

The deformations of the surface of the centrifuge model were measured via three vertical and three horizontal displacement transducers located at the back, middle, and toe of the slope in each treatment area (Figure 3.10). The cumulative vertical and horizontal displacements at mid-slope in the untreated and treated areas for the eight earthquake shaking events are shown in Figure 3.21. The deformation measurement system began to malfunction in some locations due to excessive deformations after the PSL04 event, and therefore data from SIN01 are not shown. The results in Figure 3.21 show that there was a 30 to 60% reduction in the horizontal displacements and a 20 to 60% reduction in the vertical settlements in the treated area. The most significant improvements were observed for the most intense shaking events.

Additional deformation data was obtained from vertical colored sand markers that were located in each treatment area and surface measurements that were made before and after the test. The colored sand markers showed that the displacements in the untreated area distributed over a significant depth in the soil layer, while those in the treated area were concentrated mainly in the upper half of the layer (Figure 3.22). These displacement patterns reflect the fact that

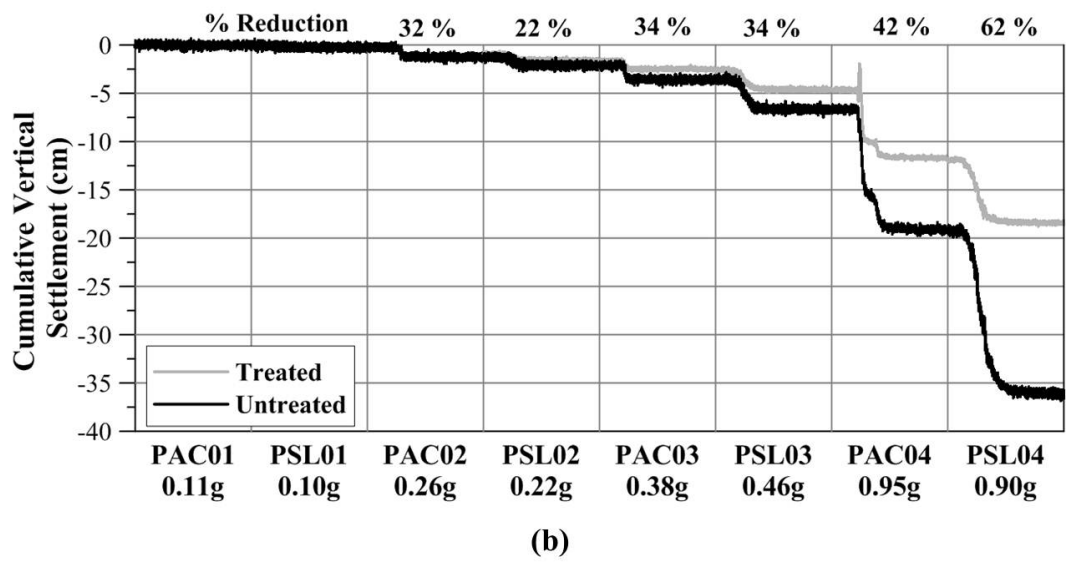
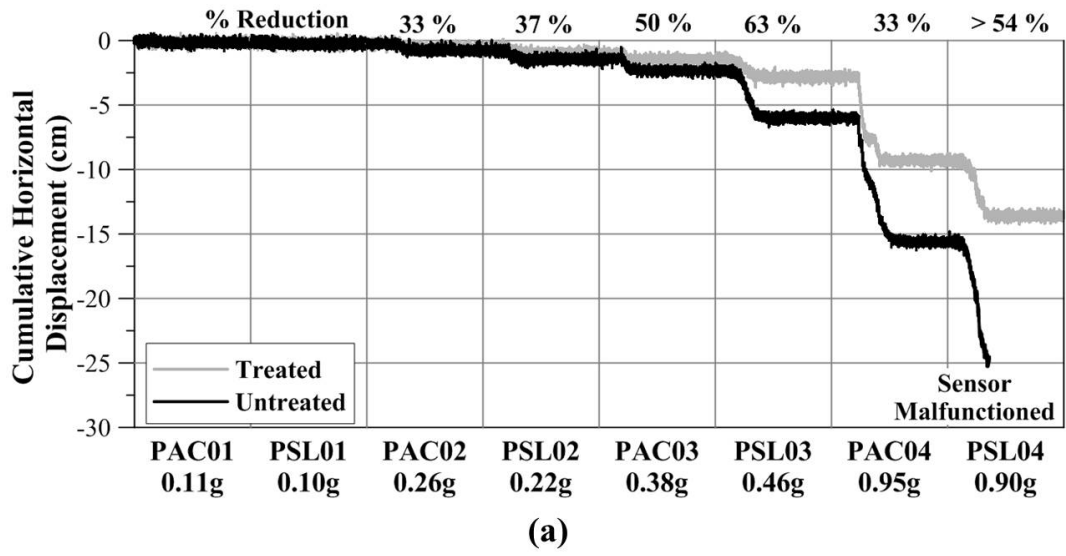


Figure 3.21: Cumulative horizontal (a) and vertical (b) displacements at mid-slope in the untreated and treated areas for all shaking events.

$r_u = 1.0$ was experienced through most of the layer in the untreated area, but only in the top half of the layer in the treated area (Figure 3.18). The colored sand markers in the untreated area also showed evidence of localized shearing at the interface between the liquefiable sand layer and the overlying clay layer, indicating that there was some accumulation of pore water and loosening of the soil at the low-permeability interface (Figure 3.22). There were no discernible areas of localized shear in the treated area. Additionally, sand vents (i.e., sand boils that did not reach the surface) formed in the untreated area but did not form in the treated area. Finally, it was determined from the surface measurements that the untreated area experienced more heave in the channel area and at the toe of the slope, as well as larger vertical settlements at the middle and back of the slope, than did the treated area (Howell et al., 2009b).

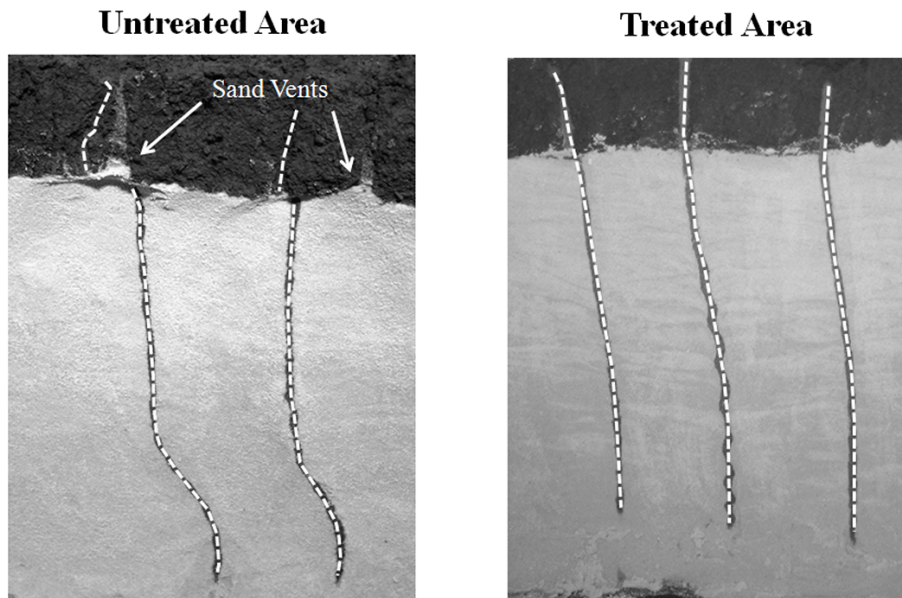


Figure 3.22: Colored sand markers in the untreated and treated areas after shaking.

As previously discussed, one potential parameter for characterizing the excess pore water pressure response for a soil deposit is $\bar{r}_{u,\max}$, which describes the Δu response over both space and time and is therefore a good indicator of overall excess pore water pressure response. Figure 3.23 shows the untreated and treated mid-slope horizontal and vertical deformations as a function of $\bar{r}_{u,\max}$. The data shown in Figure 3.23 indicate that deformations become significant and increase dramatically for $\bar{r}_{u,\max}$ greater than about 0.5, which agrees well with previous observations that large deformations generally begin to occur when r_u exceeds 0.5 to 0.6 (e.g., as summarized in Adalier and Elgamal, 2004). As r_u increases, the vertical effective stress (σ'_v) decreases, and the stress path moves towards the failure surface. As r_u exceeds about 0.5 and the stress path nears the failure surface, plastic yielding increases, and the deformations become more significant (Figure 3.24). However, the deformation data for $\bar{r}_{u,\max}$ greater than 0.5 show significant scatter (Figure 3.23). For example, the untreated area in PAC04, the treated area in PAC04, and the treated area in SIN01 all recorded an $\bar{r}_{u,\max}$ of ~ 0.8 , but the resulting horizontal deformations ranged from 6.5 cm to 16 cm. These results illustrate that while $\bar{r}_{u,\max} \sim 0.5$ is a good indicator of whether or not the displacements will be significant, other factors control the resulting magnitude of the deformation.

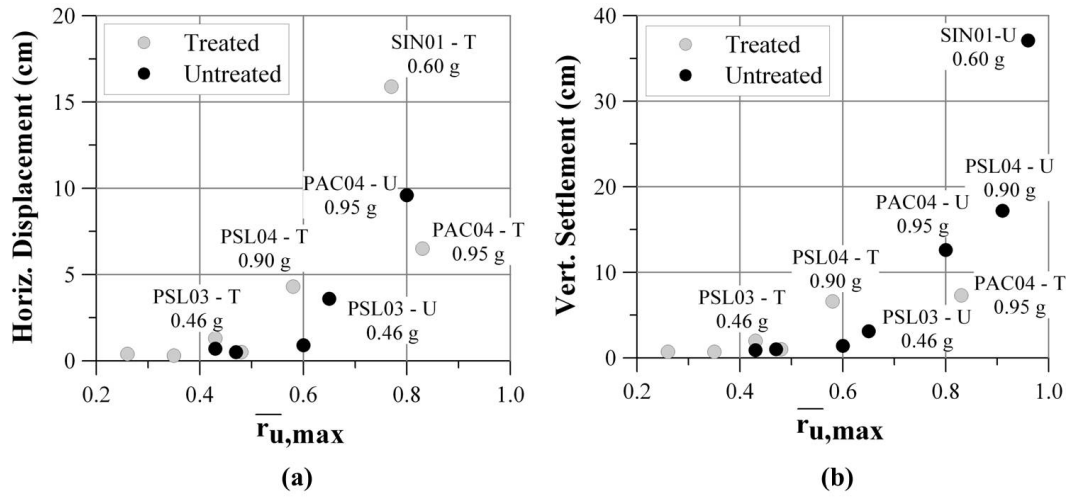


Figure 3.23: (a) Horizontal displacement and (b) Vertical displacement versus $\bar{r}_{u,max}$.

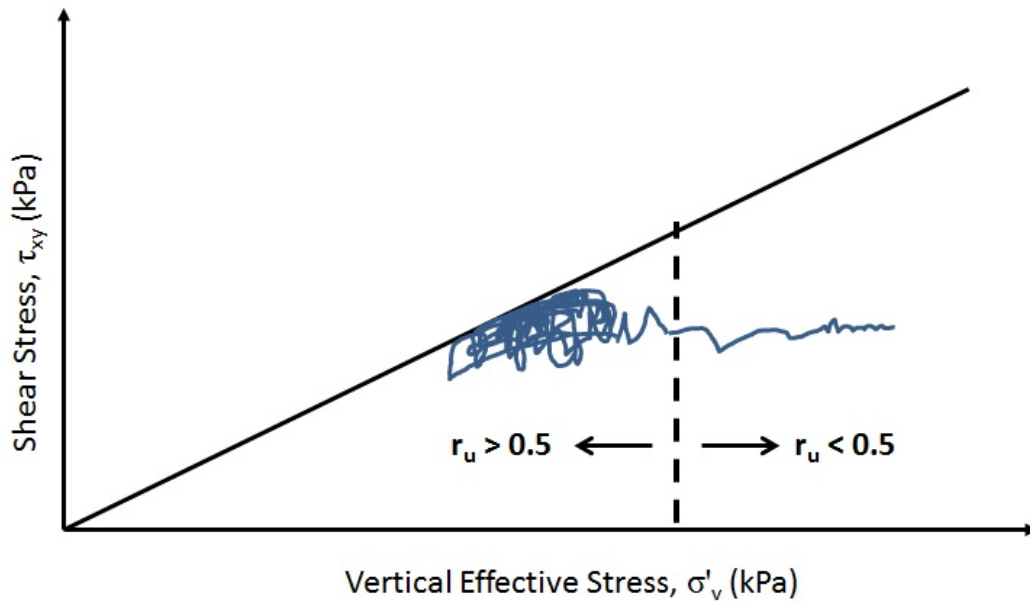


Figure 3.24: The $\bar{r}_{u,max}$ threshold shown in relation to a stress path.

The relationship between the evolution of excess pore pressures and deformations over time is illustrated in Figure 3.25, which shows time histories for acceleration, r_u , mid-slope vertical settlement, and mid-slope horizontal displacement for the PAC04 event. For this motion, the peak r_u values in the untreated and treated areas are similar (~ 0.8), but the treated-area displacements are 30 to 40% smaller. Considering $r_u = 0.5$ as being the threshold for deformation development, let us define $t_{\overline{r_u} > 0.5}$ as the time between the first and last exceedance of $r_u = 0.5$. In the treated area $t_{\overline{r_u} > 0.5} = 5.6$ seconds while in the untreated area $t_{\overline{r_u} > 0.5} = 8.4$ seconds. This 3.8 second difference equates to a 44% reduction in $t_{\overline{r_u} > 0.5}$, which directly relates to the 30 - 40% reduction in the induced displacements.

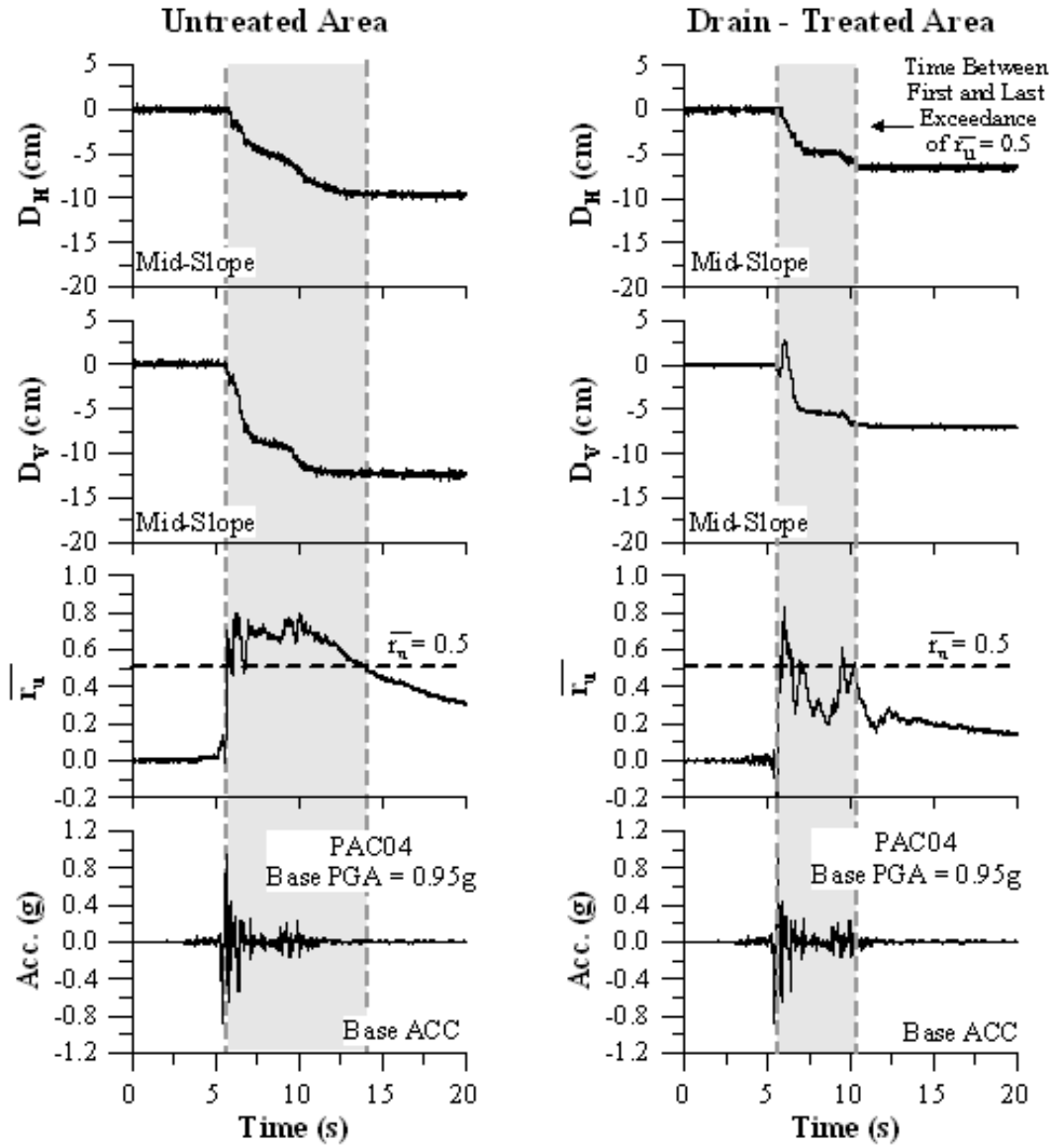


Figure 3.25: Horizontal displacement, vertical settlement, \bar{r}_u , and acceleration - time histories for the PAC04 event (PGA = 0.95 g).

Figure 3.26 plots the horizontal and vertical deformations at mid-slope in the untreated and treated areas versus $t_{\bar{r}_u > 0.5}$ for all events in which $r_u = 0.5$ was exceeded. It can be seen that larger values of $t_{\bar{r}_u > 0.5}$ correspond with larger deformations. It can also be seen that the results for the SIN01 event now follow the same trend as the results for the PAC and PSL events, which was not the case when $\bar{r}_{u, \max}$ was related to the deformations (Figure 3.23). These results indicate that a relationship exists between deformations and $t_{\bar{r}_u > 0.5}$, and that the relationship appears to hold true regardless of the individual characteristics of the input motions. It should be noted that these results are based on a data set from only a single centrifuge test and that further studies are needed to determine if this relationship holds true for other cases.

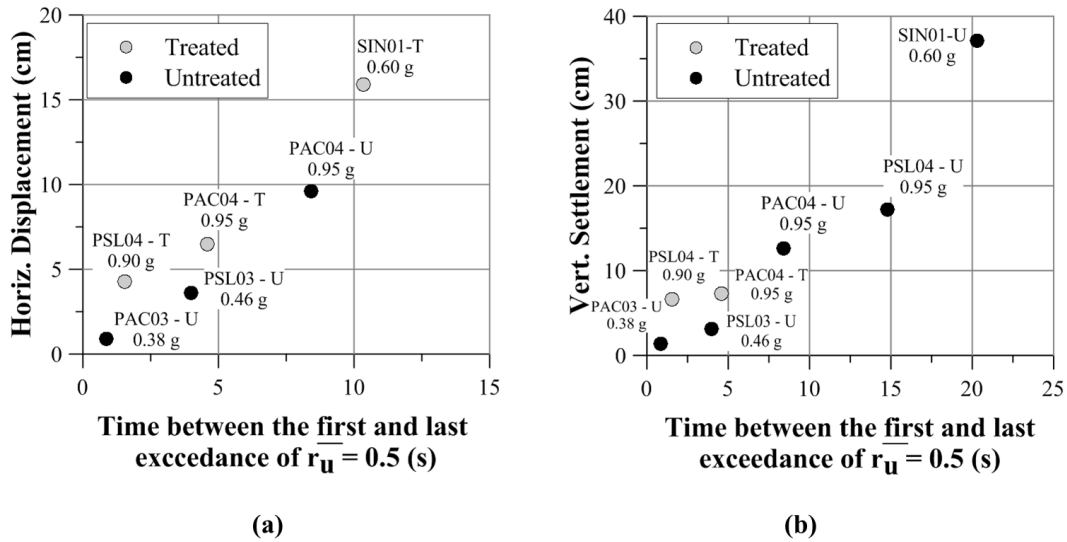


Figure 3.26: (a) Horizontal displacement and (b) Vertical displacement as a function of the time between the first and last exceedance of $\bar{r}_u = 0.5$.

3.6 Assessment of Centrifuge Results

In general, the centrifuge tests used in this research were successful. Liquefaction was triggered in the untreated areas of all three models. The clay crust slowed the dissipation of excess pore water at shallow depths and there was pore water accumulation at the sand/clay interface in the untreated areas as evidenced by localized shearing. The drains worked and did not clog; water was observed flowing from the drains for all shaking events in which liquefaction was triggered. Finally, the drain-treated area of the RLH01 model, which was not subject to reinforcement effects, had smaller peak average excess pore pressures, faster pore pressure dissipation, and smaller horizontal deformations than did the untreated area, which showed definitively that drainage is successful in mitigating, at least to some degree, damaging deformations due to liquefaction.

The pore pressure and deformation responses recorded in the centrifuge models are assumed to be a representative reflection of the general behavior that would be observed in the field. Without field data for comparison, there is no formal quantitative confirmation of this assumption; however, there are some behavioral markers from the centrifuge tests that compare well with observations made in the field. For example, the centrifuge models exhibit cracking in the clay crust and sand ejecta, both of which are observed in the field at lateral spread sites. The displacement profiles that developed at mid-slope in the untreated area are similar to the displacement vs. depth profile expected of a lateral spread site with an impervious surface layer (Figure 3.27). Horizontal deformations start to become significant when $\bar{r}_{u,\max}$ exceeds 0.5, which agrees well with the previous research showing that large deformations generally begin to occur when r_u exceeds

0.5 to 0.6 (e.g., as summarized by Adalier and Elgamal, 2004). While there is no field data with which to compare the centrifuge data, the models' behavior is consistent with the behavior expected of a lateral spread site and thus, the models' responses are assumed to be accurate reflections of the responses that would develop in a comparable field site.

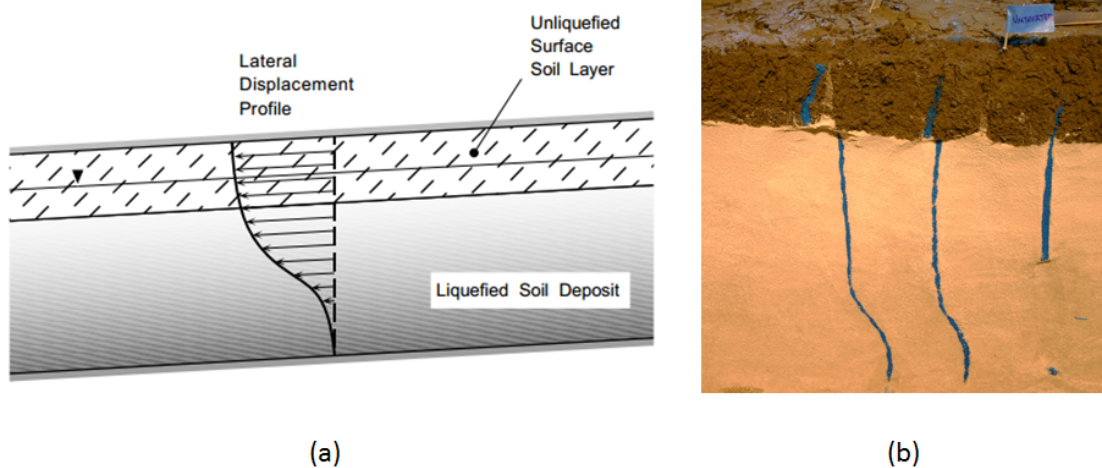


Figure 3.27: (a) Displacement profile typical of a lateral spread site with an impervious surface layer (Rauch, 1997). (b) Colored sand markers from the untreated area of the RLH01 centrifuge model

Successful though they were, the centrifuge tests were not without their issues and limitations that influenced the results. The most important issues to consider are the container effects, boundary effects, potential interaction between the treatment areas, and changes to the model geometry during testing. Where possible, steps were taken to minimize the impact of these issues.

The centrifuge container produces boundary effects related to the interface between the container and the soil. Wilson (1998) examined boundary effects in flexible shear beam containers and found that while the container and soil move together during shaking, the lateral deformations are restricted near the container edges. The instrumentation in the SSK01, RNK01, and RLH01 centrifuge models was concentrated in the central part of the models to minimize boundary effects on the data (Figures 3.3, 3.6, and 3.13).

Other boundary condition effects are related to the geometry of the centrifuge models. The centrifuge models all contained more than one slope; this was necessary in order for the treated and untreated areas to be constructed and tested under identical conditions. However, this geometry resulted in models where either the treatment areas were deforming in opposition to each other (SSK01 and RNK01) or the performance of one area was affected by that of an adjacent area (RLH01). The central channel was used to minimize these effects in SSK01 and RNK01, and other steps were taken to minimize these effects (e.g., cutting the clay crust between adjacent zones, placing the instrumentation in the center of the treatment area) in the RLH01 model.

Finally, one of the limitations of using large-scale centrifuge models is that it takes three to five weeks to build a model, meaning that the model cannot be re-built or put back in its original state before each shaking event. The shaking events in the SSK01, RNK01, and RLH01 centrifuge tests were applied in order of increasing intensity (i.e., the smallest events which would have the least significant impact were applied first), but as the intensity of shaking increased, permanent changes resulted (e.g., the slope flattened, the sand liquefied and reconsolidated, cracks developed in the clay crust, etc.). By the end of the test, the model had

been significantly transformed (e.g., Figure 3.28), and certain changes, such as the flattening of the slope, most likely had a significant impact on the horizontal deformations that developed.



Figure 3.28: The RLH01 centrifuge model (a) before shaking and (b) after shaking.

3.7 Summary

In the first phase of this research, a suite of three dynamic centrifuge tests was performed on specimens of liquefiable soil treated with PVDs. Centrifuge test SSK01 was designed by Antonio Marinucci (Marinucci, 2010) and constructed and tested by Seiji Kano. Centrifuge test RNK01 used the same design as centrifuge test SSK01 and was constructed and tested by Ronnie Kamai. Centrifuge test RLH01 used a modification of the SSK01 design and was constructed and tested as part of this dissertation research. The objective of these tests was to assess

the effectiveness of PVDs in mitigating liquefaction-induced deformations and to identify behavioral trends for drain-treated sites.

The first test, SSK01, compared the performance of an untreated slope to that of a drain treated slope. The results of SSK01 showed that the drains were effective in reducing excess pore water pressures and increasing the rate of excess pore water pressure dissipation. At the end of testing, the drain treated slope had 80% smaller horizontal deformations than those observed in the untreated slope; however, it was suspected that the stiffness of the model tubes was influencing the response of the drain-treated slope.

The second test, RNK01, compared the performance of a drain-treated slope to that of an untreated slope containing non-draining tubes. The goal of RNK01 was to investigate the effect of the stiffness of the model tubes used in SSK01 on the performance (i.e., deformations) of the slope. The results of RNK01 confirmed that the stiffness of the model tubes affected the deformations of the drain-treated slopes such that the improved performance that was observed in SSK01 could not be solely attributed to the effects of drainage.

The third test, RLH01, compared the performance of a drain-treated slope, an untreated slope, and an untreated slope containing non-draining tubes. This test used more flexible tubes to model the drains than the previous tests. The goals of RLH01 were to confirm that the new model tubes had no impact on the performance of the slope, and to assess the effectiveness of the drains in mitigating liquefaction-induced deformations. The results of RLH01 indicated that the new model tubes were flexible enough such that their presence did not impact the response of the drain-treated slope. Thus, the 30 to 60% reduction in horizontal deformations observed in this test could be ascribed solely to the

effects of drainage. It was also observed in this test that the impact of the drains on the excess pore water pressure response is sensitive to the characteristics of the input motion. For certain motions (e.g., PAC motions), the untreated and treated areas had similar $\bar{r}_{u,\max}$ values even though the influence of the drains was still evident in the excess pore water pressure dissipation patterns. Deformations in RLH01 become significant when $\bar{r}_{u,\max}$ exceeds a threshold of about 0.5 and the magnitude of the deformations corresponds more strongly to the time the soil spends at an \bar{r}_u that exceeds this threshold rather than the peak \bar{r}_u value.

Chapter 4

Numerical Models of Lateral Spread Sites Treated with PVDs

4.1 Introduction

Three types of numerical models of varying complexity are developed for this research: 2D unit cell models of the area of influence around a drain, 3D unit cell models of the area of influence around a drain, and a full 2D model of the centrifuge model geometry and container. These models will be used to analyze the centrifuge tests and the results from these models will be compared with the centrifuge data. As previously noted, lateral spread sites are commonly modeled as infinite slopes and the unit cell models fit well within this approach. The full 2D model is used to investigate the various aspects of the centrifuge model (e.g., 2D geometry, container mass, etc.) that may influence the comparison between the unit cell models and the centrifuge data. This chapter discusses the characteristics of the constitutive models used to represent the soil materials and the different numerical models.

4.2 Constitutive Models

4.2.1 OpenSees Finite Element Modeling Platform

Numerical simulations of untreated and drain-treated sites are being performed using the Open System for Earthquake Engineering Simulation (OpenSees). OpenSees is an open-source software framework intended for use in simulating the seismic response of structural and geotechnical systems (Mazzoni et al., 2004). OpenSees is capable of modeling the nonlinear dynamic response of systems, making it an appropriate choice for modeling the response of a liquefiable soil subjected to earthquake loading. Additionally, because OpenSees is open source, the code is easily accessible and the inner workings of the individual constitutive models, elements, and solution algorithms are relatively transparent to the user.

Within the OpenSees framework, there are three constitutive models available for modeling soil. For sands, there are the PressureDependMultiYield and PressureDependMultiYield02 material models. For clays, there is the PressureIndependentMultiYield material model. The PressureDependMultiYield02 model is a modification of the PressureDependMultiYield model with additional parameters to account for the $K\sigma$ effect and the effect of dilation on the contraction phases, and modified logic for the permanent accumulation of shear strain (Mazzoni et al., 2004). The models used in this research have both sand and clay layers. The PressureDependMultiYield02 and PressureIndependentMultiYield constitutive models are used to simulate these materials.

4.2.2 Sand

The PressureDependentMultiYield02 (PDMY02) constitutive model has been chosen to represent the behavior of the liquefiable sand. The PDMY02 model is an elasto-plastic model used to simulate the cyclic response of soils whose behavior is sensitive to applied stresses (i.e., sands and silts). The model includes characteristics such as dilatancy, non-flow liquefaction, and permanent shear strain accumulation, which are critical for modeling the response of sands subjected to cyclic loading (Yang et al., 2008).

The PDMY02 model's response can be either elastic or elasto-plastic, and is controlled by a user-defined setting. For these analyses, the model is set to behave elastically during the gravity loading stage, and elasto-plastically during the dynamic loading stage. The plasticity model uses nested Drucker-Prager yield surfaces that are automatically generated by the model. The number of yield surfaces can vary from 20 to 100, and is set by the user. Each yield surface represents a linear piecewise approximation of a segment of the nonlinear, stress-dependent, shear stress-shear strain backbone curve, which is defined by a hyperbola (Yang et al., 2003; Yang et al., 2008):

$$\tau = \frac{G_{\max}\gamma}{1 + \frac{\gamma}{\gamma_r}\left(\frac{p'_r}{p'}\right)^d} \quad (4.1)$$

Where τ is the octahedral shear stress, G_{\max} is the small-strain shear modulus, γ is the octahedral shear strain, γ_r is a reference shear strain, p'_r is the user-defined reference mean effective confining pressure, p' is the current effective confinement, and d is the user-defined stress dependency coefficient (for more detailed descriptions of these parameters see Table 4.1). Each nonlinear segment is

represented by a linear piecewise approximation that is then used in determining the bounds of the yield surface (Figure 4.1). The failure criterion is defined by the outermost yield surface, the size of which is determined by the friction angle, while the inner yield surfaces make up the the hardening region (Khosravifar, 2011). Plastic strain is divided into deviatoric and volumetric components with the deviatoric strain component following an associative flow rule and the volumetric strain component following a non-associative flow rule (Khosravifar, 2011). The use of the non-associative flow rule for the volumetric strain component enables the PDMY02 model to capture the dilatancy behavior of the soil (Yang et al., 2008).

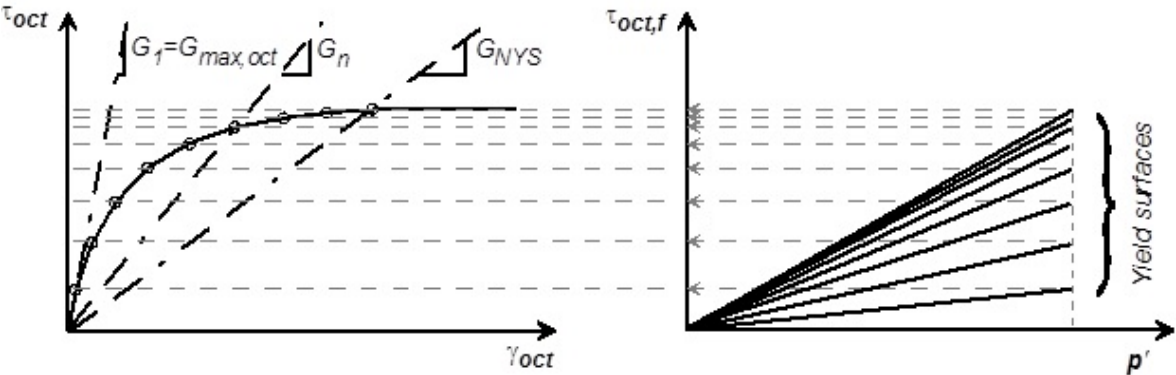


Figure 4.1: Relationship between the backbone curve and the yield surfaces generated for the PDMY02 model (Khosravifar, 2011).

The PDMY02 model has 25 user-defined parameters. These parameters are presented in Table 4.1. Of these parameters, the most critical parameters in determining the behavior of the model are the G_r , B_r , ϕ , ϕ_{PT} , volumetric contraction parameters (contrac1 , contrac2 , contrac3), and volumetric dilation parameters (dilata1 , dilata2 , dilata3). The friction angle parameter (ϕ) is used to define the size of the outermost yield surface (i.e., the failure surface). The phase transformation angle parameter (ϕ_{PT}) is used to define the phase transformation surface, which is the point at which the soil transitions from contractive to dilative behavior (Figure 4.2). The contraction parameters (contrac1 , contrac2 , contrac3) and dilation parameters (dilata1 , dilata2 , dilata3) are used in the flow rules for contractive and dilative volumetric plastic strains, respectively.

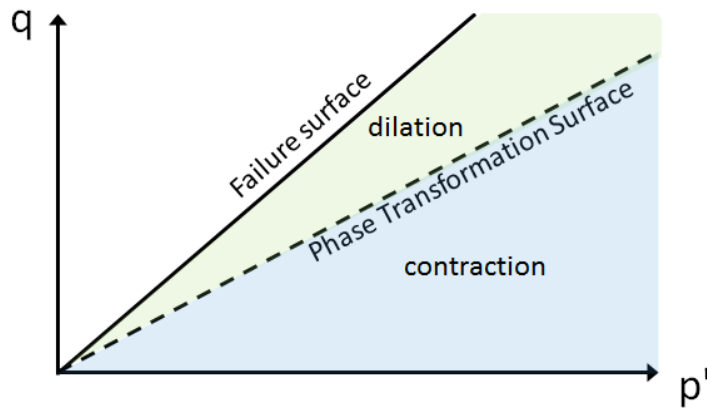


Figure 4.2: A plot of the failure surface defined by the friction angle, the phase transformation surface defined by the phase transformation angle, and the transition from contractive to dilative behavior.

Table 4.1: Parameters for the PDMY02 model (Yang et al., 2008).

Parameter	Definition
$\$nd$	Number of dimensions, 2 for plane-strain, 3 for 3D.
$\$rho$	Saturated soil mass density.
$\$refShearModul (G_r)$	Reference low-strain, octahedral shear modulus defined at a reference mean effective confining pressure ($\$refPress$). The octahedral shear strain is related to normal shear strain (G_{reg}) as follows:
$G_{oct} = \frac{3 p'_r}{(1 + 2k_0)\sigma_y} G_{reg} \quad (4.2)$	
$\$refBulkModul (B_r)$	Reference bulk modulus defined at a reference mean effective confining pressure ($\$refPress$).
$\$frictionAng (\phi)$	Friction angle.
$\$peakShearStra (\gamma_{max})$	The octahedral shear strain at which the maximum shear strength is reached, defined at a reference mean effective confining pressure ($\$refPress$).
$\$refPress (p'_r)$	Reference mean effective confining pressure.

Table 4.1 – Continued

Parameter	Definition
\$pressDependCoe (d)	<p>A positive constant defining variations of G and B as a function of instantaneous effective confinement, p':</p> $G = G_r \left(\frac{p'}{p'_r} \right)^d \quad (4.3)$ $B = B_r \left(\frac{p'}{p'_r} \right)^d \quad (4.4)$
\$PTAng (ϕ_{PT})	Phase transformation angle.
\$contrac1	A non-negative constant defining the rate of shear-induced volume decrease or pore pressure buildup. A larger value corresponds to a faster contraction rate.
\$contrac2	A non-negative constant reflecting the influence of the dilation history on the contraction tendency.
\$contrac3	A non-negative constant reflecting the K_σ effect.
\$dilat1	A non-negative constant defining the rate of shear-induced volume increase. A larger value corresponds to a stronger dilation rate.
\$dilat2	A non-negative constant defining the rate of shear-induced volume increase. A larger value corresponds to a stronger dilation rate.

Table 4.1 – Continued

Parameter	Definition
$\$dilat3$	A non-negative constant reflecting the K_σ effect.
$\$liquefac1$	A damage parameter to define the accumulated permanent shear strain as a function of dilation history.
$\$liquefac2$	A damage parameter to define the biased accumulated permanent shear strain as a function of load reversal history.
$\$noYieldSurf$	The number of yield surfaces.
$\$e$	Initial void ratio.
$\$cs1, \$cs2, \$cs3, \pa	Parameters defining a straight critical-state line (e_c) in e - p' space. If $\$cs3 = 0$,
	$e_c = cs1 - cs2 \log\left(\frac{p'}{p_a}\right) \quad (4.5)$
	else
	$e_c = cs1 - cs2 \left(\frac{p'}{p_a}\right)^{cs3} \quad (4.6)$
	This critical-state line does not appear to be fully implemented or is disabled at this time.
$\$c$	Numerical constant (cohesion).

The authors of the PDMY02 model have provided default parameters for sands with relative densities (D_R) of 30%, 40%, 50%, 60%, and 75% (Yang et al., 2008). The parameters for the $D_R = 40\%$ soil were chosen as a starting point for the liquefiable sand, and these parameters were then modified to match the properties of the Nevada Sand used in the centrifuge tests. The mass density was changed from the suggested 1.8 ton/m^3 to 1.99 ton/m^3 , which equates to a unit weight of 19.5 kN/m^3 (Kamai et al., 2007). The shear modulus was reduced from the suggested $9.e4 \text{ kPa}$ to $7.5e4 \text{ kPa}$ to achieve a $V_{s,1}$ of 175 m/s at 1 atm of confining pressure (Kamai and Boulanger, 2012). This value of $V_{s,1}$ equates to shear wave velocities of 120 to 161 m/s at the confining stress levels in the sand layer of the RLH01 model, which agrees well with the values of 120 to 165 m/s measured in the RLH01 centrifuge model after the consolidation phase of the test (Howell et al, 2009a). The bulk modulus was changed to match the new shear modulus, assuming a Poisson's ratio of 0.333 . The void ratio was increased from 0.77 to 0.8 , although this parameter does not seem to impact on the results.

OpenSees was used to simulate simple cyclic shear tests using the model parameters. Simulations were performed for several values of cyclic stress ratio ($\text{CSR} = \frac{\tau}{\sigma'_v}$) at a vertical effective stress of 40 kPa , which is the average overburden pressure in the liquefiable sand layer in the centrifuge models, and the results were used to develop cyclic resistance ratio (CRR) curves for the modeled liquefiable sand, where the CRR is the CSR required to trigger liquefaction in a specified number of uniform loading cycles. The simulated CRR curves along with the measured CRR curves from lab data for Nevada Sand from Kano (2008), Doygun

(2009), and Arumoli et al. (1992), are shown in Figure 4.3. The lab data were adjusted to a K_o of 0.575, an OCR of 1.5, and a σ'_v of 40 kPa. The $\$contract1$ parameter was adjusted until the simulated CRR curve was within the upper and lower bound limits for the lab data at 10 to 20 cycles. Most of the shaking events used in this research (SIN and PSL180) will have somewhere between 10 and 20 cycles, so this range was determined to be the most critical range for matching the CRR data. The PAC175 shaking events have less than 10 cycles of motion. For these shaking events the CRR of the simulated liquefiable sand is larger than indicated by the lab data, meaning that liquefaction resistance of the simulated sand is larger than Nevada sand. It is evident in Figure 4.3 that the CRR curve for the simulated sand is much steeper than the lab data. No set of PDMY02 parameters was found that could make the simulated CRR curve match the lab data; it was overly steep for all combinations of parameters that were tried. These results are consistent with the findings of Ziotopoulou and Boulanger (2012) and Karamitros (2010) for other, similar constitutive models for liquefiable sand (e.g., Dafalias and Manzari, 2004 and Andrianopolous et al., 2010).

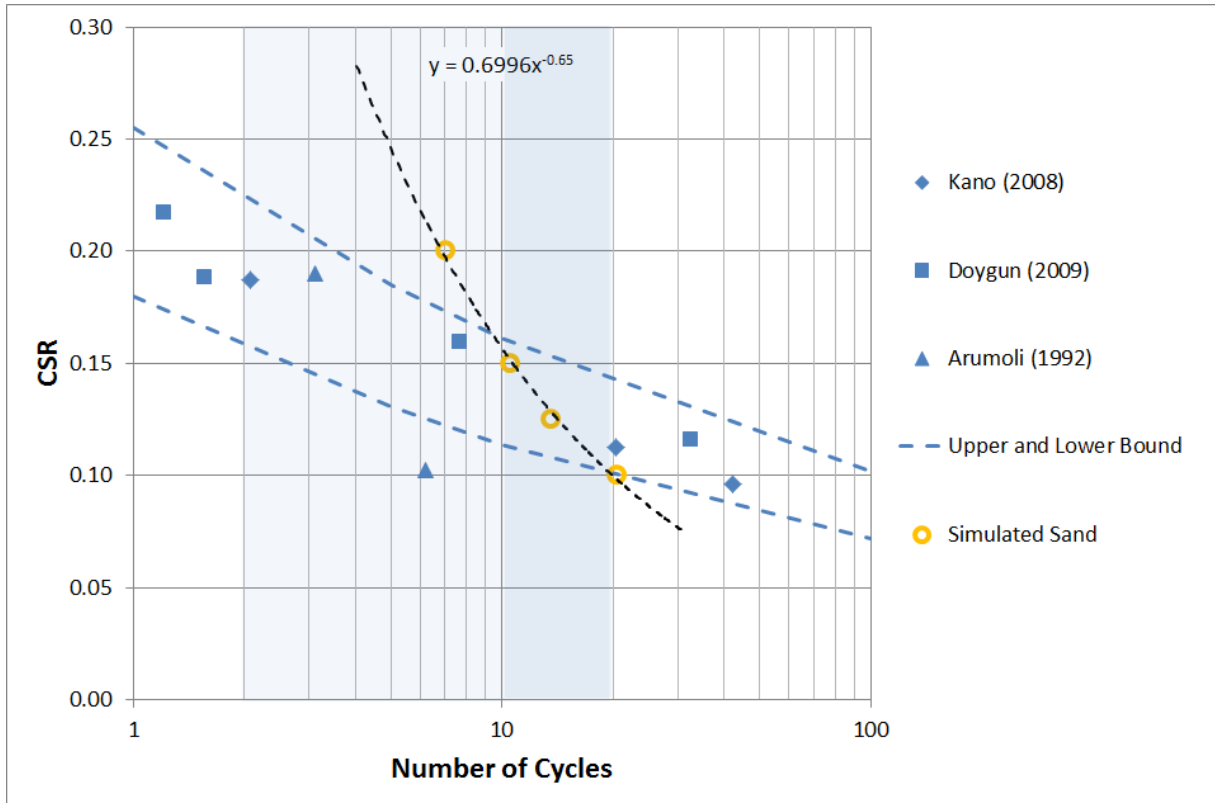


Figure 4.3: Cyclic resistance ratio curve for the simulated sand compared to lab data for Nevada sand from Kano (2008), Doygun (2009), and Arumoli et al. (1992).

The suggested value for the $\$contrac1$ parameter for a $D_R = 40\%$ soil is 0.067 (Yang et al., 2008). This value was decreased to 0.057 during the simulated simple cyclic shear tests to decrease the rate of pore pressure build up and better match the cyclic resistance of Nevada sand. The suggested values for the PDMY02 parameters from Yang et al. (2003) and final values for the PDMY02 model parameters for the liquefiable sand are shown in Table 4.2. For all parameters not shown in Table 4.2, the Yang et al. (2003) suggested values were used.

Table 4.2: Suggested (Yang et al., 2008) and final values for the PDMY02 model parameters.

Parameter	Suggested for $D_R = 40\%$	Final
$\$rho$ (ton/m ³)	1.8	1.99
$\$refShearModul$ (G_r) (kPa)	9e4	7.5e4
$\$refBulkModul$ (B_r) (kPa)	22e4	20.e4
$\$frictionAng$ (ϕ) (deg)	32	32
$\$PTAng$ (ϕ_{PT}) (deg)	26	26
$\$contrac1$	0.067	0.057
$\$contrac3$	0.23	0.23
$\$dilat1$	0.06	0.06
$\$dilat3$	0.27	0.27
$\$e$	0.77	0.80

The PDMY02 constitutive model parameters were determined using laboratory data and simulated cyclic direct simple shear tests, but the hydraulic conductivity of the liquefiable sand is an independent parameter that does not influence the cyclic direct simple shear simulations. While the measured hydraulic conductivity of Nevada sand, scaled appropriately based on the centrifugal acceleration (Section 3.3.1) could be used, the drainage properties of the sand are so critical in evaluating drain performance that it is important to confirm an appropriate value.

For the untreated condition, the hydraulic conductivity is not generally of concern as long as it is small enough to ensure that the soil remains undrained during dynamic loading. The hydraulic conductivity is most important when evaluating the drain-treated condition as it affects the flow of pore water towards the drains during dynamic loading. The pore pressure dissipation response of soil is controlled by the coefficient of consolidation (c_v), which is related to both k and the coefficient of volumetric compressibility (m_v) of the soil through:

$$c_v = \frac{k}{m_v \gamma_w} \quad (4.7)$$

By definition, the volumetric compressibility is the ratio of the volumetric strain to the effective stress.

The Nevada sand used in the centrifuge models is a relatively uniform, clean, fine sand. It has a specific gravity (G_s) of 2.64, a mean grain size (D_{50}) of 0.17 mm (model scale), a uniformity coefficient (C_u) of 1.64, and a hydraulic conductivity of 0.002 cm/s at 1 g (Kamai et al., 2007). For a centrifugal acceleration of 15 g and with water as the pore fluid, the scaled hydraulic conductivity is 0.03 cm/s, which is typical of a medium sand ($D_{50} = 0.25$ to 0.5 mm). For a medium sand,

typical values of m_v are generally on the order of $4 \cdot 10^{-5}$ to $10 \cdot 10^{-5}$ 1/kPa (Pestana et al., 1997) and vary based on relative density, confining pressure, and the peak excess pore pressures in the soil (Lee and Albaisa, 1974). The m_v of liquefiable soil can be calculated from cyclic laboratory tests by measuring the volumetric strain during consolidation after generation of excess pore pressure. In this case, the change in the effective stress associated with the volumetric strain is $r_u \cdot \sigma'_{v,o}$, where $\sigma'_{v,o}$ is the initial vertical effective stress. Figure 4.4 shows volumetric strain vs. peak pore pressure ratio ($r_{u,max}$) data for Monterey sand (Lee and Albaisa, 1974). Each point on this graph represents the measured volumetric strain upon consolidation, after reaching a given peak pore pressure ratio in an undrained cyclic test. In this figure m_v is related to the slope of the volumetric strain vs. peak pore pressure ratio line, and it is clear from these data that m_v is not constant. Most importantly, m_v increases with increasing r_u because of the increased volumetric strain that occurs as r_u approaches 1.0. For a loose sand ($D_R = 30$ to 40%), m_v can increase by as much as a factor of 10 as liquefaction is approached (Figure 4.5).

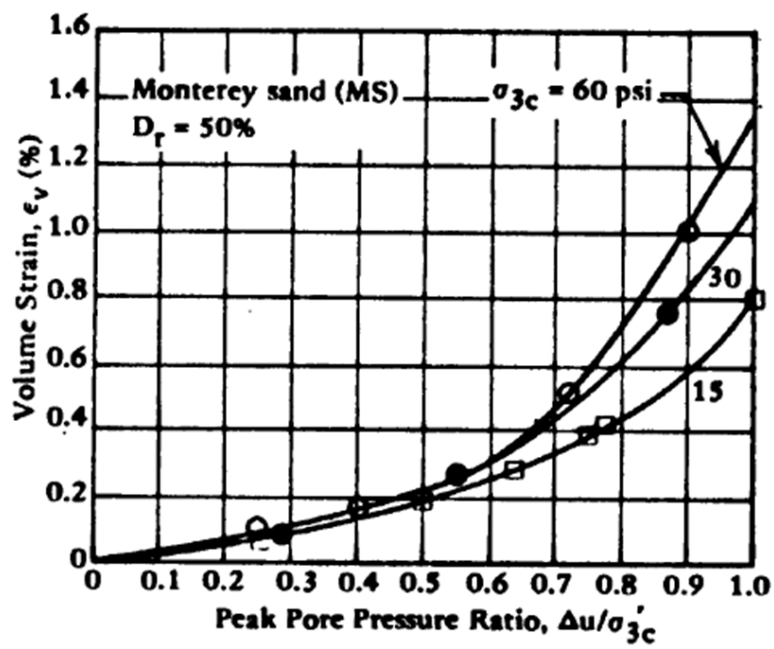


Figure 4.4: Volumetric strain vs. peak pore pressure ratio ($r_{u,max}$) for Monterey Sand (Lee and Albaisa, 1974)

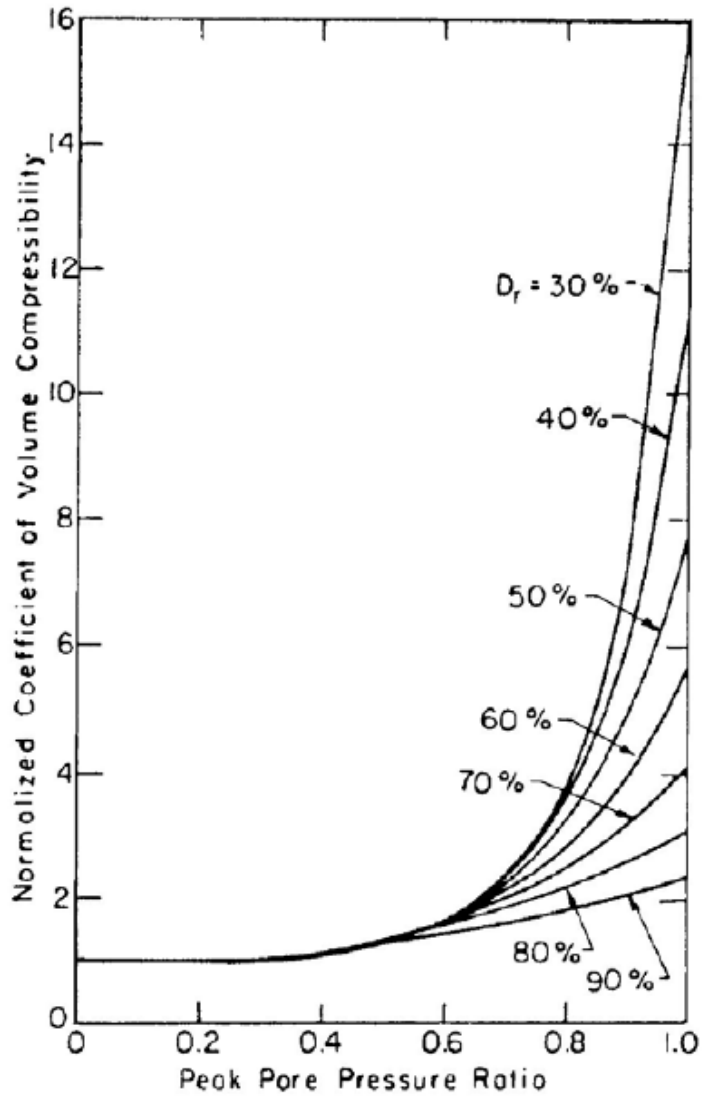


Figure 4.5: Normalized relationships between peak pore pressure ratios ($r_{u,max}$) and m_v of sands from Seed et al. (1975).

The volumetric compressibility of the liquefiable sand in the numerical model is controlled by the PDMY02 constitutive model, although in this case not explicitly. The equivalent volumetric compressibility of the PDMY02 constitutive model was evaluated by modeling cyclic simple shear tests and computing the predicted volumetric strain for different levels of pore pressure generation. The simulated cyclic simple shear tests were performed on a single element with a CSR of 0.15 and an initial vertical effective stress of 40 kPa, which is the average vertical effective stress in the centrifuge models. The applied number of cycles ranged from 1 to 11 and the induced peak r_u ranged from 0.19 to 0.95. After cyclic loading was stopped, the element was allowed to drain (consolidate), and m_v was calculated as $\epsilon_v/\Delta\sigma'_v$, where ϵ_v is the volumetric strain and $\Delta\sigma'_v$ is the change in σ'_v during consolidation calculated as $r_u * \sigma'_{v,o}$.

Figure 4.6 plots the simulated values of ϵ_v vs. r_u . In comparison to the Lee and Albaisa (1974) data for Monterey Sand, the volumetric strains exhibited by the simulated sand are very small and the slope of the ϵ_v vs. r_u curve is relatively constant (Figure 4.6), indicating that the m_v for the simulated sand is too small and remains relatively constant even as r_u increases. Figure 4.7 shows the m_v values associated with the data in Figure 4.6. The m_v values from Lee and Albaisa range from $3e-5$ to $8e-5$ 1/kPa, which agrees well with the range of $4e-5$ to $10e-5$ 1/kPa reported by Pestana et al. (1997). The m_v values for the simulated sand range from $0.7e-5$ 1/kPa to $1.5e-5$ 1/kPa and are much smaller than expected (Figure 4.7). Additionally, the m_v values for the simulated sand only change by a factor of about 2 for an increase in $r_{u,max}$ from 0.19 to 0.95. The smaller m_v associated with the PDMY02 model will influence the equivalent c_v associated with the model.

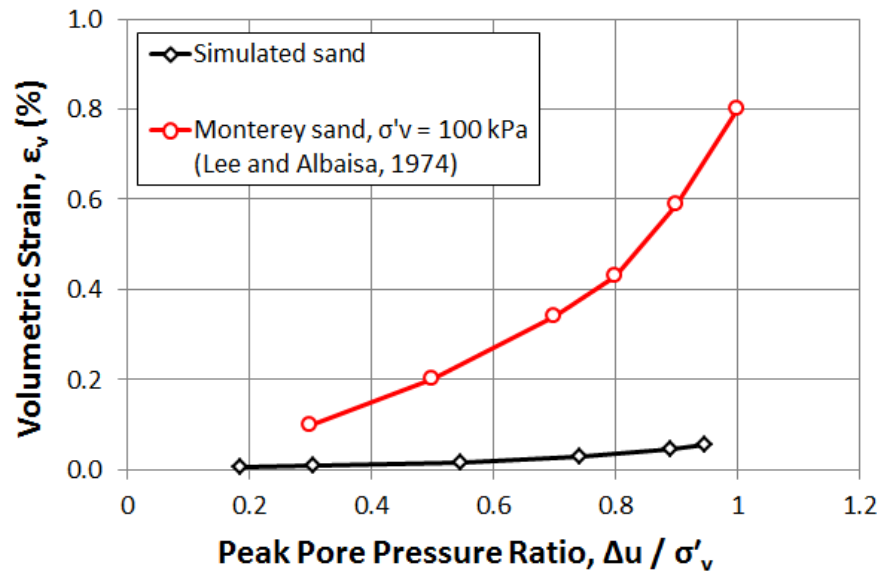


Figure 4.6: Volumetric strain vs. peak pore pressure ratio ($r_{u,max}$) for the simulated sand and the Monterey Sand from Lee and Albaisa (1974)

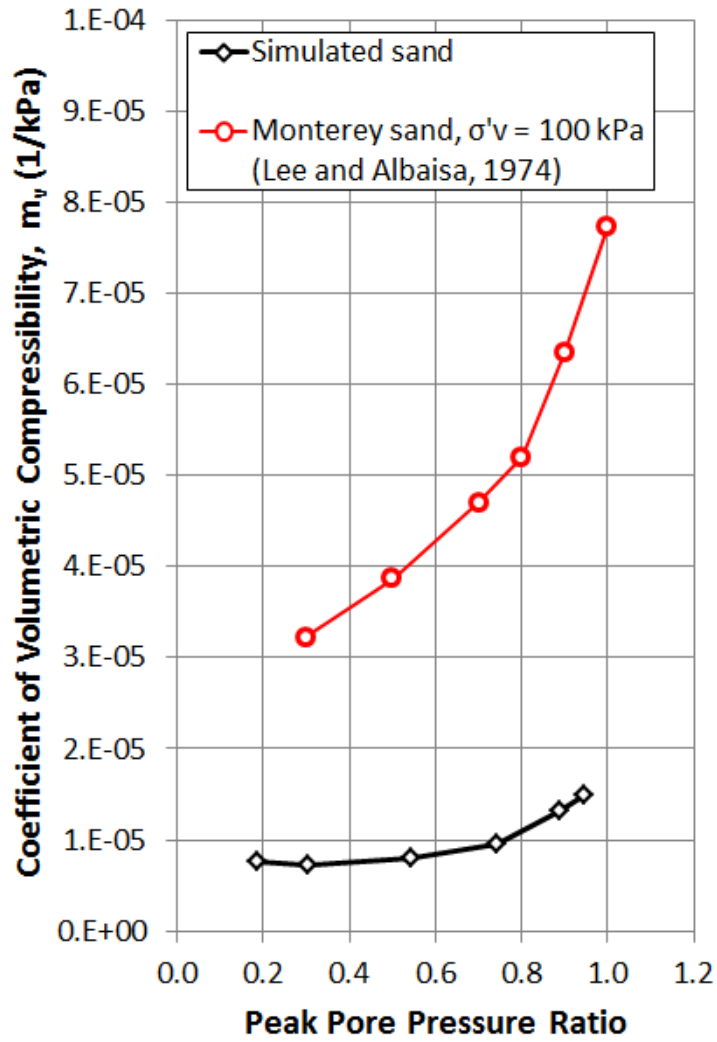


Figure 4.7: Coefficient of volumetric compressibility (m_v) vs. peak pore pressure ratio ($r_{u,max}$) for the simulated sand and the Monterey Sand from Lee and Albaisa (1974)

A range of c_v values for the prototype sand from the centrifuge tests was computed using $k = 0.03$ cm/s and assuming m_v values of $4.0e-5$ 1/kPa and $10.e-5$ 1/kPa (the lower and upper values of the range provided by Pestana et al. (1997)). The resulting range of prototype c_v values is 0.31 m²/s to 0.76 m²/s. These values are slightly larger than the 0.25 m²/s c_v of a uniformly graded fraction E silica sand calculated by Brennan and Madabushi (2011) using experimental data. If one simply uses the prototype k of 0.03 cm/s with the equivalent m_v modeled by the PDMY02 constitutive model, the resulting c_v values range from 2.0 to 4.3 m²/s. These values are approximately 3 to 15 times larger than the magnitudes of the prototype values. The larger c_v values indicate that the model soil will consolidate (or drain) faster than the prototype soil. Because we cannot control the equivalent m_v for the PDMY02 constitutive model, we must modify the specified k to achieve the desired c_v . Using the PDMY02 equivalent m_v range of $0.7e-5$ to $1.5e-5$ 1/kPa and the prototype c_v range of 0.31 to 0.76 m²/s, the resulting hydraulic conductivity values are between $.002$ and $.01$ cm/s. Therefore to appropriately model the drainage properties (i.e., c_v) of a sand with a prototype $k \sim 0.03$ cm/s using the PDMY02 constitutive model, we must use a k between $.002$ and $.01$ cm/s. The modified k range is quite large (0.002 to 0.01 cm/s); a single value for the hydraulic conductivity was determined during the calibration phase of this research and will be discussed in a later section.

4.2.3 Clay

The PressureIndependentMultiYield (PIMY) constitutive model was chosen to represent the behavior of the clay cap. The PIMY model is an elasto-plastic model used to simulate the cyclic response of soils whose behavior is insensitive to applied stresses (i.e., undrained clays). The response of the PIMY model can be either elastic or elasto-plastic, and is controlled by a user-defined setting. For these analyses, the model's behavior is elastic during the gravity loading stage, and elasto-plastic during the dynamic loading stage. The plasticity model uses nested Von Mises yield surfaces and an associative flow rule. Plasticity is exhibited in the deviatoric stress-strain response, while the volumetric stress-strain response is linear-elastic and independent of the deviatoric response (Yang et al., 2008).

The PIMY model has 10 user-defined parameters. These parameters are presented in Table 4.3. The critical parameters defined by the user are G_r , which is the reference shear modulus at small strains and c , which is the apparent cohesion or undrained shear strength.

Table 4.3: Parameters for the PIMY model (Yang et al., 2008).

Parameter	Definition
n_d	Number of dimensions, 2 for plane-strain, 3 for 3D.
ρ	Saturated soil mass density.

Table 4.3 – Continued

Parameter	Definition
$\$refShearModul$ (G_r)	Reference low-strain shear modulus defined at a reference mean effective confining pressure ($\$refPress$).
$\$refBulkModul$ (B_r)	Reference bulk modulus defined at a reference mean effective confining pressure ($\$refPress$).
$\$cohesi$ (c)	Apparent cohesion at zero confinement.
$\$frictionAng$ (ϕ)	Friction angle.
$\$peakShearStra$ (γ_{max})	The octahedral shear strain at which the maximum shear strength is reached, defined at a reference mean effective confining pressure ($\$refPress$).
$\$refPress$ (p'_r)	Reference mean effective confining pressure.
$\$pressDependCoe$ (d)	A positive constant defining variations of G and B as a function of initial effective confinement, p'_i :
	$G = G_r \left(\frac{p'_i}{p'_r} \right)^d \quad (4.8)$
	$B = B_r \left(\frac{p'_i}{p'_r} \right)^d \quad (4.9)$
	If $\phi = 0$, this parameter is reset to 0.
$\$noYieldSurf$	The number of yield surfaces.

The authors of the PIMY model have provided default parameters for soft, medium, and stiff clays (Yang et al., 2008). The clay cap in the centrifuge test was placed in layers and compacted well using metal cylinders and miniature sheepsfoot rollers. The suggested parameters for a medium clay have been used to model this material. The dynamic response of the clay cap is not critical to these analyses, therefore no attempt has been made to improve upon the suggested parameters, which are presented in Table 4.4.

Table 4.4: Suggested Parameters for a Medium Clay (Yang et al., 2008).

Parameter	Value
ρ (ton/m ³)	1.5
G_r (kPa)	6.0e4
B_r (kPa)	3.0e5
c (kPa)	37
ϕ (deg)	0.0
γ_{max}	0.1
p'_r (kPa)	101
d	0.0
$noYieldSurf$	20

To facilitate the achievement of hydrostatic conditions during the application of gravity, the hydraulic conductivity of the clay layer is set equal to the hydraulic conductivity of the sand layer, making it a drained material. Prior to dynamic loading, the hydraulic conductivity of the clay layer is reduced to 1.e-10 m/s, making it an undrained material. Although the clay layer is above the

groundwater table, the bulk modulus of water is used as the combined undrained bulk modulus for the clay elements, meaning that these elements are saturated. This approach facilitates the generation of excess pore water pressures at the sand/clay interface. If the clay elements are modeled as “dry” or unsaturated elements, pore water pressures do not develop at the sand/clay interface, even though the clay is modeled as a low-permeability material and pore water should get trapped below this layer. It should be noted that this model will resist tension without cracking and thus, pore water trapped at the low-permeability interface will not be able to dissipate through cracks in the crust as was the case in the centrifuge models.

4.3 Numerical Models

4.3.1 2D Unit Cell Infinite Slope Model

The least complex type of numerical model that is used for this research is the 2D unit cell, infinite slope model. This is a plane strain model of the area of influence around a single drain (or, in the case of the untreated model, a free-field untreated area equal to the area of influence around a single drain). This model assumes an infinite slope condition. In slope stability, an infinite slope assumption is often used in cases in which the soil profile consists of cohesionless soils or cases in which the length of the slope is much greater than the thickness of the soil profile being modeled and the soil profile is fairly consistent across the entire length slope (Duncan and Wright, 2005). This assumption would not strictly apply to the centrifuge models where the slopes were necessarily shortened in order to fit

more than one treatment area into each model, but it would be applicable to a lateral spread site in the field. Even though centrifuge data was used to validate the numerical models, the numerical model geometry is based on the geometry of the hypothetical field site. The circular failure surface that was observed in the centrifuge tests would only be applicable to the very edges (shorelines) of a lateral spread site in the field, the rest of the site would develop sliding deformations akin to those produced by an infinite slope (Figure 4.8).



Figure 4.8: Cross sectional view of a lateral spread site with an example of where an infinite slope model would be appropriate.

Using unit cell or single column models to simulate lateral spreading is not uncommon (e.g., Yang et al., 2003; Seid-Karbasi and Byrne, 2007; Mayoral et al., 2009; Cheng and Jeremić, 2009; Phillips et al., 2012). However, the unit cell approach assumes that what happens at one drain is indicative of what happens at all drains. Though only one set of PPT data was discussed when analyzing the RLH01 centrifuge data (Section 3.5), there were actually two PPT arrays in the RLH01 model. The pore pressure data for instruments at similar locations in these two arrays are in good agreement (Figure 4.9). While the deformation data for these two locations may not match because of the characteristics of the

circular failure surface that developed in the centrifuge model, the pore pressure data is comparable, indicating that the periodicity assumption of the unit cell model is valid. When modeling the field condition, this periodicity assumption would likely still be made, but it may be less accurate due to the spatial variability in the site geometry and material properties.

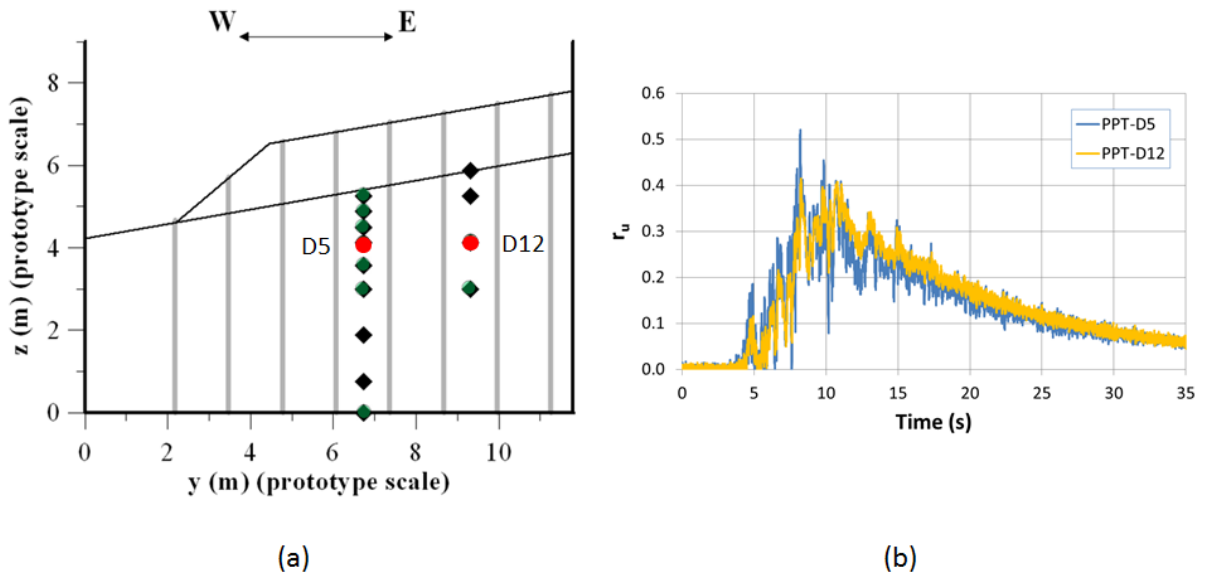


Figure 4.9: (a) PPT locations in the treated area of the RLH01 centrifuge model, and (b) r_u -time histories for PPTs located at similar depths (shown in red in (a)) for shaking event PSL03 (PGA = 0.46 g).

The 2D unit cell model consists of a 4.5 m (SSK01 and RNK01) or 5.5 m (RLH01) thick layer of liquefiable sand overlain by a 1 m (SSK01 and RNK01) or 1.5 m (RLH01) thick clay cap, which is consistent with the geometry of the mid-slope sections of the centrifuge models. A slope angle of 3° (SSK01 and RNK01) or 10° (RLH01) is applied using horizontal and vertical gravitational components applied as body forces on the elements (e.g., Lu et al., 2010; McGann

and Arduino, 2011; and Phillips et al., 2012). The ground water table was placed at the sand/clay interface. The 2D unit cell model geometries are summarized in Table 4.5.

Table 4.5: Model geometries for the 2D unit cell models corresponding to the mid-slope geometries of centrifuge tests SSK01, RNK01, and RLH01.

Centrifuge Test	Sand Thickness (m)	Clay Thickness (m)	Slope Angle (deg)	Centrifuge Shaking	Numerical Shaking
SSK01	4.5	1.0	3	parallel to slope	parallel to slope
RNK01	4.5	1.0	3	parallel to slope	parallel to slope
RLH01	5.5	1.5	10	orthogonal to slope	parallel to slope

In the treated 2D unit cell model, a perfect drain was created by holding the pore water pressures at hydrostatic levels during shaking at the nodes up the vertical centerline of the model. The hydraulic conductivity (k) of the liquefiable sand in the 2D unit cell models is adjusted based on scaling laws from Hird et al. (1992) to compensate for the fact that the drain acts as a wall drain in a 2D model. The Hird et al. (1992) scaling laws modify the drain spacing or soil hydraulic conductivity in order to equate the average degree of consolidation on a horizontal plane for an axisymmetric unit cell with a drain and a plane strain unit cell with a drain. For this research, the drain spacing is held constant and the soil hydraulic conductivity is modified. An axisymmetric unit cell model is a circular model with a drain in the center, and the radius of the model is equal to the radius of influence of the drain. In the centrifuge tests, the drains were placed in a triangular pattern at a center-to-center spacing of 1.5 m (prototype scale). Using equivalent areas, the 1.5 m center-to-center triangular spacing equates to

a circular area of influence with a 0.7 m radius (1.4 m diameter). Therefore the plane strain 2D unit cell model has a 1.4 m width. The determination and scaling of the hydraulic conductivity for the liquefiable sand will be detailed in Section 4.4.

The 2D unit cell model uses `Nine_Four_Node_QuadUP` elements, which are 9-node quadrilateral plane strain u - p elements in which the solid-fluid response is fully coupled based on Biot's theory of porous medium (Yang et al., 2008). The u - p formulation solves for the deformations of the soil skeleton (u) and the changes in excess pore water pressures (p), neglecting the relative accelerations between the pore fluid (U) and the soil skeleton (u) that would be solved for in a u - p - U or u - U formulation. The four corner nodes of the `Nine_Four_Node_QuadUP` element have three degrees of freedom (two for displacement and one for fluid pressure), while the other five nodes only have two degrees of freedom for solid displacement. A 9-node quadrilateral element was chosen over the 4-node quadrilateral element in order to prevent volumetric mesh locking, which can sometimes result when displacements take place under undrained conditions. The `SSK01` and `RNK01` unit cell models are divided into 10 elements in the horizontal direction and 38 elements in the vertical direction. The `RLH01` unit cell model is divided into 10 elements in the horizontal direction and 52 elements in the vertical direction.

The horizontal and vertical deformations at the outer nodes of the soil column at each depth within the model are tied together, the base of the column is fully fixed, and input acceleration-time histories are applied in the horizontal direction at all nodes as a uniform excitation (Figure 4.10). These boundary conditions produce a 1D shear beam type effect. Simplified shear beam type numerical models are commonly used to represent lateral spread sites when the model consists entirely of soil (i.e., there are no structures) (e.g., see Section 2.4.1:

Seid-Karbasi and Byrne (2007), Mayoral et al. (2009), Cheng and Jeremić (2009), and Phillips et al. (2012)). The use of simplified shear beam type models is one of the earliest approaches to dynamic analyses of 2D problems in geotechnical engineering (Kramer, 2006). This type of approach was first applied in the study of earth dams in the 1930's (Mononobe et al., 1936). The assumptions built into this model are that deformations occur in simple shear (i.e., purely horizontal deformations) and that the stresses and strains are uniform across the horizontal planes. The assumption of simple shear was verified by Hatanaka (1952) for earth dams with rigid foundations, and the assumption of uniform stresses and strains was verified, for earth dams, by Chopra (1996) and Dakoulas (1985). The shear beam approach has since been extended to cover a variety of geotechnical applications (as summarized by Gazetas, 1987).

There is no field data available for use with this research. The centrifuge data is the only data available with which to validate the numerical models and thus, the simulations need to be at least somewhat comparable to the centrifuge tests. To simulate the centrifuge conditions as closely as possible while modeling the infinite slope condition, the PDMY02 parameters are calibrated to match the Nevada sand material properties, the layer thicknesses of the sand and clay layers in the unit cell models match those of the mid-slope geometry in the centrifuge models, shear beam type constraints are applied (Zienkiewicz, 1999), and a rigid base is used. The material properties and layer thicknesses could be representative of any field site and are not particular to the centrifuge models, and the shear beam type constraints are necessary to prevent the unit cell models from falling over during shaking. The rigid base assumption is the only condition applied to the numerical model that is not applicable to a field site. If field data were being

used in place of centrifuge data for the model validation, a Lysmer-Kuhlemeyer (1969) absorbing boundary would be a more appropriate choice for the base of the model.

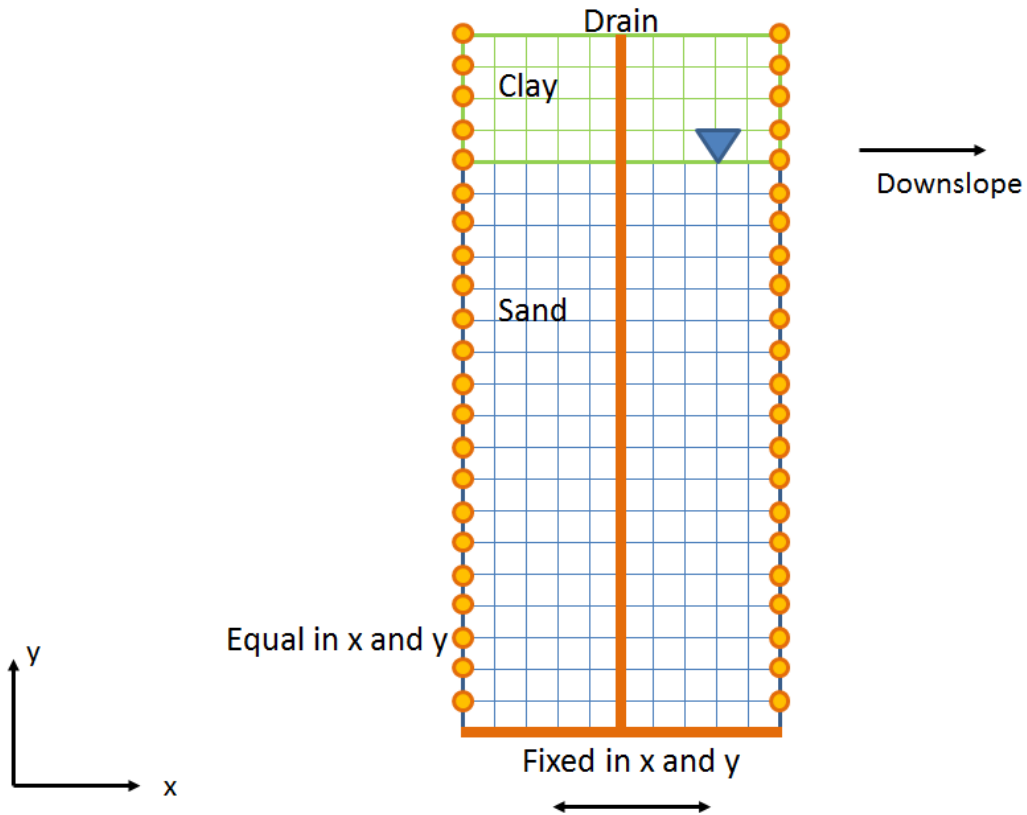


Figure 4.10: Drawing of the drain-treated 2D unit cell model.

4.3.2 3D Unit Cell Infinite Slope Model

The 3D unit cell infinite slope model is one step up in complexity from the 2D unit cell infinite slope model. Like the 2D unit cell model, this is a model of the area of influence around a single drain (or, in the case of the untreated model, a free-field untreated area equal to the area of influence around a single drain). The 3D unit cell model is a square model. Using equivalent areas, the 1.5 m center-to-center triangular drain spacing from the centrifuge test equates to a 1.578 m square spacing (Figure 4.11). Therefore, the 3D unit cell model is 1.578 m wide and extends 1.578 m into the page (Figure 4.12). With a 3 dimensional model, it was possible to shake the RLH01 unit cell model in the out-of-plane direction (i.e., orthogonal to the slope), which is the direction of shaking that was applied in the centrifuge test. Shaking was also applied parallel to the slope for some simulations so that the effects of parallel vs. orthogonal shaking could be studied.

The 3D unit cell model uses 8-node brickUP elements. These are hexahedral linear isoparametric u - p elements in which the solid-fluid response is fully coupled based on Biot's theory of porous medium (Yang et al., 2008). 8-node elements were chosen instead of 20-node elements due to concerns about computational cost and available memory. Additionally, preliminary results showed that the data for the untreated 2D and 3D unit cell models were nearly identical, indicating that mesh locking was not a problem and higher order elements were not necessary. Each node of the 8-node brickUP element has four degrees of freedom, 3 for solid displacement and one for fluid pressure. The SSK01 and RNK01 unit cell models are divided into 10 elements in the in-plane (x) and out-of-plane (y) horizontal

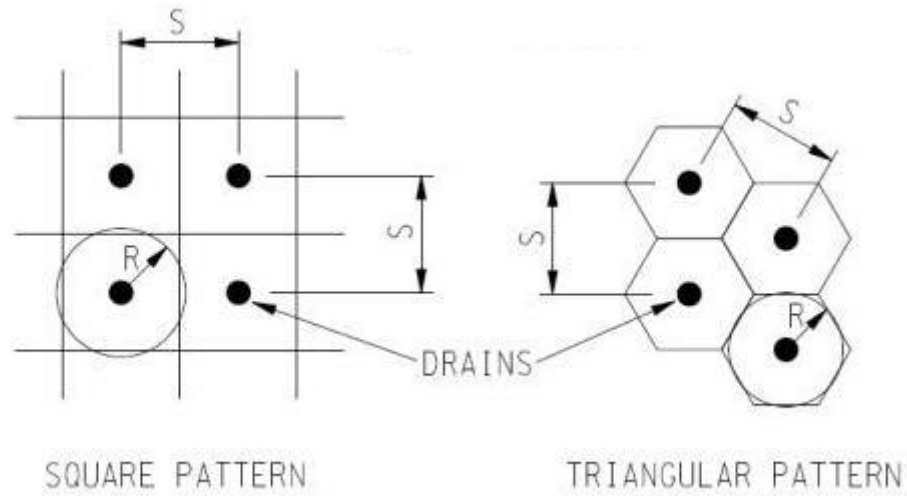


Figure 4.11: Triangular and square drain spacing equivalency (Civil Engineering Portal, 2012).

directions and 38 elements in the vertical direction (z). The RLH01 unit cell model is divided into 10 elements in the in-plane and out-of-plane horizontal directions and 52 elements in the vertical direction.

At each depth within the 3D unit cell model, the in-plane (x - z plane) horizontal and vertical deformations at the outer nodes of the model are constrained to be equal, the base is fully fixed, and input acceleration-time histories are applied at all nodes as a uniform excitation (Figure 4.12). Again, these boundary conditions produce a shear beam type effect. For the SSK01 and RNK01 numerical simulations, shaking was applied in the in-plane horizontal direction and all of the nodes in the model were fixed in the out-of-plane (x - y plane) direction to prevent out-of-plane deformations; the effects of this fixity on the pore pressure and in-plane horizontal deformation responses were examined and found to be negligible. For the RLH01 numerical simulation, shaking was applied orthogonal to the slope and the model was allowed to move in the out-of-plane direction. For

these simulations an additional constraint was added such that the out-of-plane horizontal deformations at each depth were equal.

In the treated 3D unit cell model, a perfect drain was created by holding the pore water pressures at hydrostatic levels during shaking at the nodes up the vertical centerline of the model. The k of the liquefiable sand was determined during the calibration phase of this research and will be discussed in Section 4.4. In the 2D models, the k of the liquefiable sand must be scaled to account for the fact that the drains act as wall drains. It is not necessary to scale the k of the liquefiable sand in the 3D unit cell models as the drains do not extend infinitely in the out-of-plane direction.

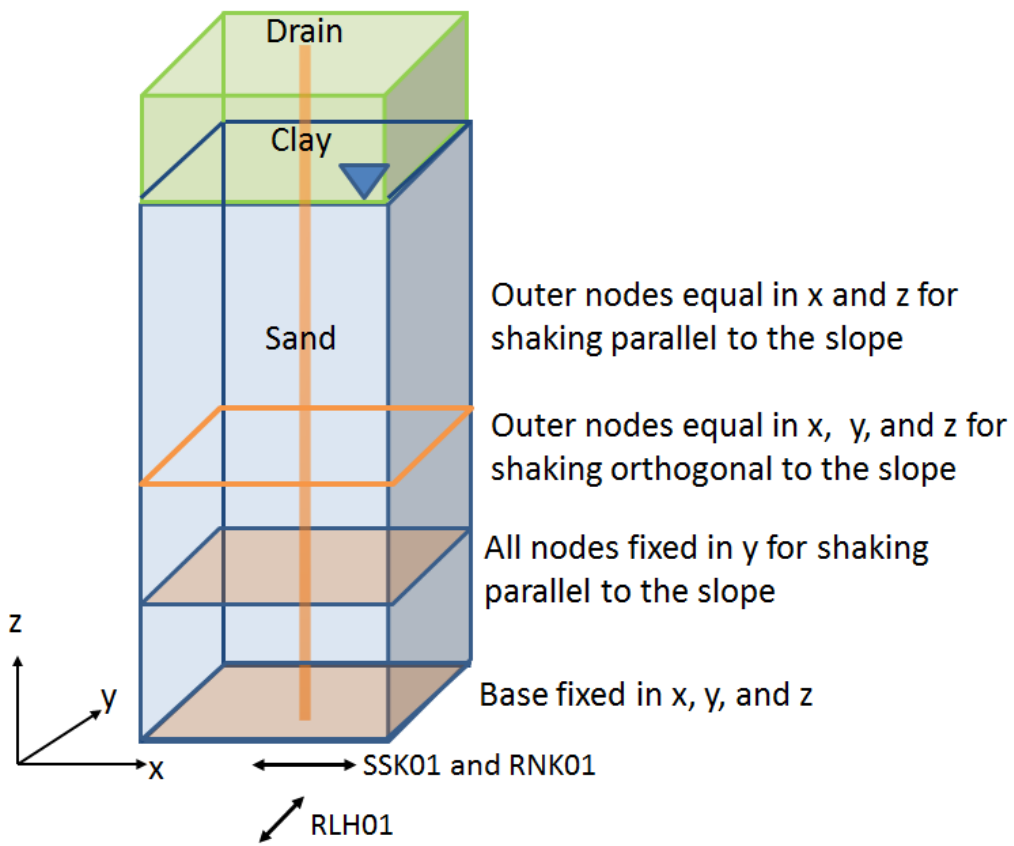


Figure 4.12: Drawing of the drain-treated 3D unit cell model.

4.3.3 2D Centrifuge Model

The final model that was constructed was a full 2D, plane strain model of the SSK01 and RNK01 centrifuge models, including the centrifuge model container. Because the data being used to validate the numerical models comes from the centrifuge tests, it is important to be able to identify those aspects of the centrifuge test that may influence the results. For example, the flexible shear beam container and the 2D geometry of the centrifuge models may affect the results of the tests; it is important to identify the effects these factors have on the results from the numerical models.

The 2D centrifuge model consists of an untreated slope and a drain-treated slope, each comprised of liquefiable sand overlain by a clay cap. The drain-treated slope contains perfect drains spaced approximately 1.5 m apart (Figure 4.13). The soil was modeled using four-node quadUP elements. These are bilinear isoparametric u - p elements in which the solid-fluid response is fully coupled based on Biot's theory of porous medium (Yang et al., 2008). Each node has two degrees of freedom for solid displacement and one degree of freedom for fluid pressure. The elements were of varying size depending on their location in the model. This model contains both untreated and treated slopes. A scaled k , the determination of which is discussed in Section 4.4, was necessary for the treated slope in order to account for the fact that the drains act as wall drains in a plane strain model. The scaled k was also used for the untreated slope in order to prevent having a discontinuity in the k across the model that may affect the flow patterns of the pore water.

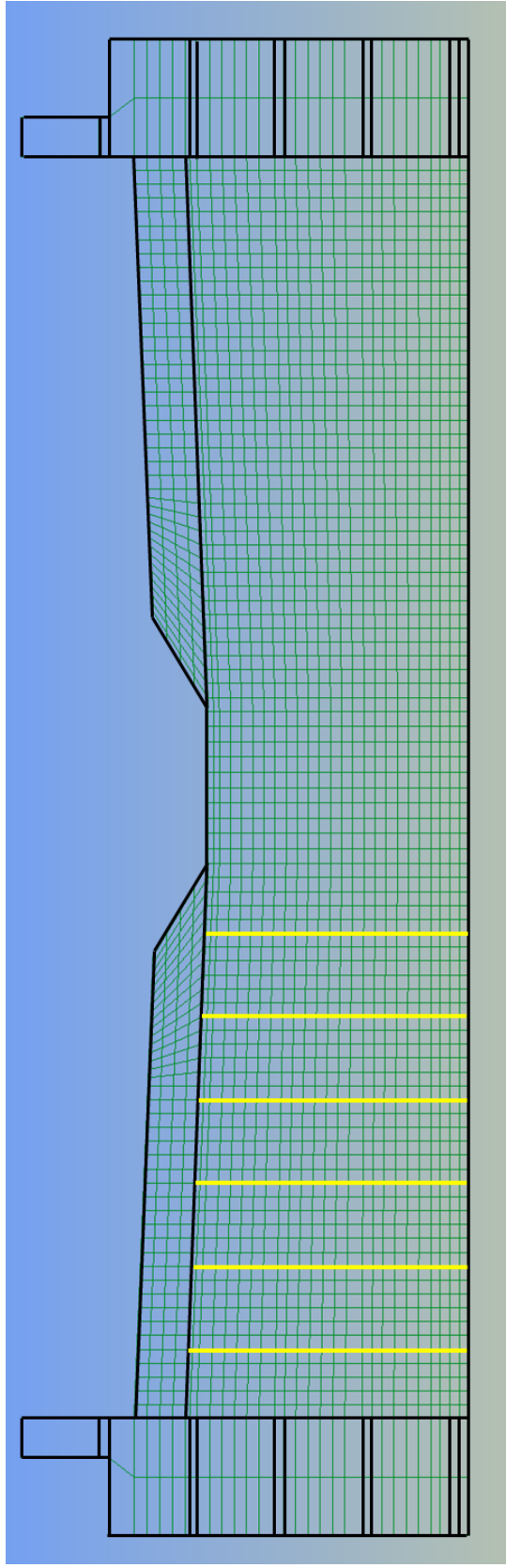


Figure 4.13: Drawing of the 2D centrifuge model.

Four-node bilinear isoparametric Quad elements were used to model the aluminum rings and rubber layers of the container. The aluminum rings of the flexible shear beam are hollow and the mass density of the elements is adjusted to reflect this. The aluminum and rubber are modeled using the ElasticIsotropic constitutive model and the properties for each ring, developed by Armstrong (2010), are listed in Table 4.6. The material properties for each ring vary according to the size and shape of the ring (Pedersen, 2004). The top ring of the container is referenced as Aluminum Ring 1. The soil and container elements are tied together using an equal degree of freedom constraint, and the container rings are constrained to move together in the horizontal and vertical directions. Shaking was performed by applying acceleration-time histories recorded during the centrifuge tests as a uniform excitation to all of the nodes in the model.

Table 4.6: Parameters for Container elements.

Element	Young's Modulus (kPa)	Poisson's Ratio	Mass Density (ton/m³)
Aluminum Ring 1	68900	0.3	1.623
Rubber Ring 1	4654	0.4	3.639
Aluminum Ring 2	68900	0.3	1.947
Rubber Ring 2	2605	0.4	2.065
Aluminum Ring 3	68900	0.3	1.947
Rubber Ring 3	3192	0.4	2.524
Aluminum Ring 4	68900	0.3	3.688
Rubber Ring 4	3192	0.4	2.524
Aluminum Ring 5	68900	0.3	4.123
Rubber Ring 5	1771	0.4	2.787
Container Base	68900	0.3	4.123

4.4 Selection of Appropriate Hydraulic Conductivity using Data from Centrifuge Test SSK01

A range of potential hydraulic conductivities (k) for the liquefiable sand was identified in Section 4.2.2. This range is quite large (0.002 to 0.01 cm/s), and 3D unit cell simulations of the drain-treated area of the SSK01 centrifuge model were used to select the most suitable k from the potential range of k . Two shaking events (SSK01_10 and SSK01_11) with moderate to large pore pressure generation were used. The analyses focused on hydraulic conductivities in the middle of the modified k range of 0.002 to 0.01 cm/s.

Figure 4.14 shows the excess pore water pressure-time histories at three different depths within the 3D unit cell model for shaking event SSK01_10 (PGA = 0.07 g) and three hydraulic conductivities. It can be seen in Figure 4.14 that when $k = 0.005$ cm/s, the excess pore water pressures near the sand/clay interface match the centrifuge data and the excess pore water pressures at mid-depth and near the base of the model are slightly higher at the end of shaking than in the centrifuge model. When $k = 0.006$ cm/s, the excess pore water pressures near the sand/clay interface are slightly lower than in the centrifuge model and the excess pore water pressures at mid-depth and near the base of the model are slightly higher at the end of shaking. When $k = 0.007$ cm/s the excess pore water pressures near the sand/clay interface are lower, but the excess pore water pressures at mid-depth and near the base of the model match the centrifuge data at the end of shaking. It should be noted that if the prototype k of 0.03 cm/s was used in these simulations, no excess pore water pressures would be generated because the soil would drain too quickly.

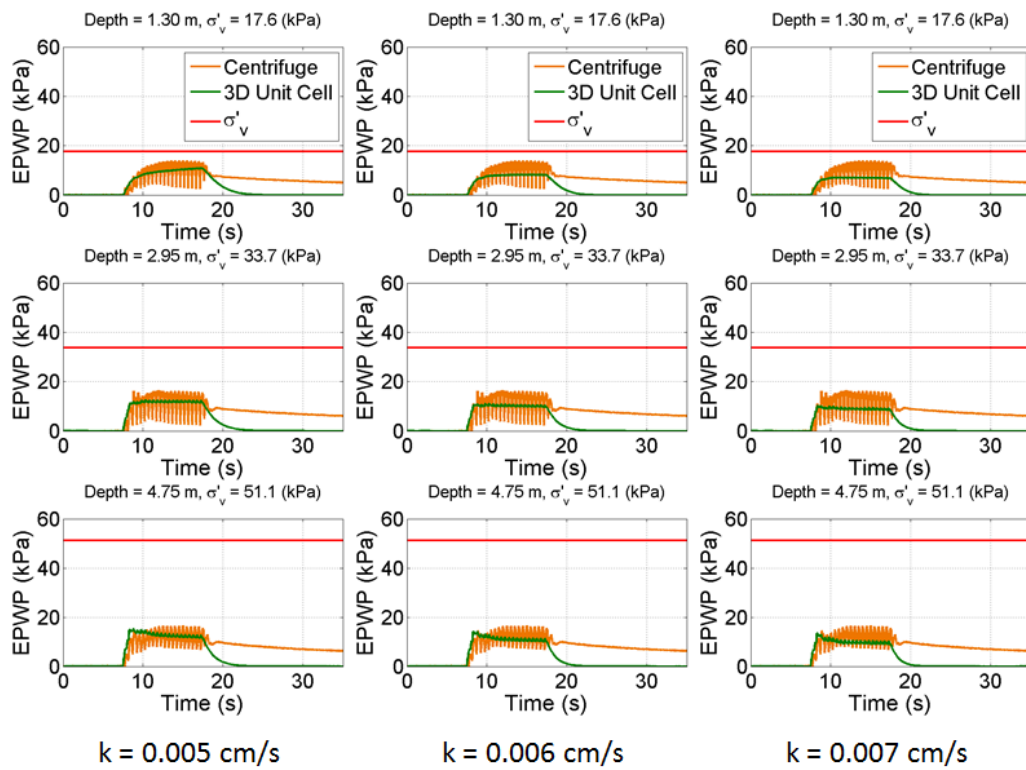


Figure 4.14: Excess pore water pressure-time histories at different depths within the treated 3D unit cell model for shaking event SSK01_10 (PGA = 0.07 g) and a range of hydraulic conductivities.

All of the excess pore water pressure-time history results shown in Figure 4.14 are fair to good matches to the centrifuge data. It would be difficult to choose a hydraulic conductivity from those shown based on these results alone. However, when the intensity of shaking increases, the differences between the different hydraulic conductivities becomes more apparent. Figure 4.15 shows the excess pore water pressure-time histories at three depths within the 3D unit cell model for shaking event SSK01_11 ($PGA = 0.11$ g) and the same range of hydraulic conductivities used previously. It can be seen in Figure 4.15 that when $k = 0.005$ cm/s, the excess pore water pressures near the sand/clay interface are slightly high compared to the centrifuge data and the excess pore water pressures at mid-depth and near the base of the model are very high compared to the centrifuge data at the end of shaking. When $k = 0.006$ cm/s, the excess pore water pressures at all three depths are still higher than in the centrifuge model. When $k = 0.007$ cm/s, the excess pore water pressures near the sand/clay interface, at mid-depth, and at the base of the model are still slightly higher than in the centrifuge model, but the overall match to the centrifuge data is good.

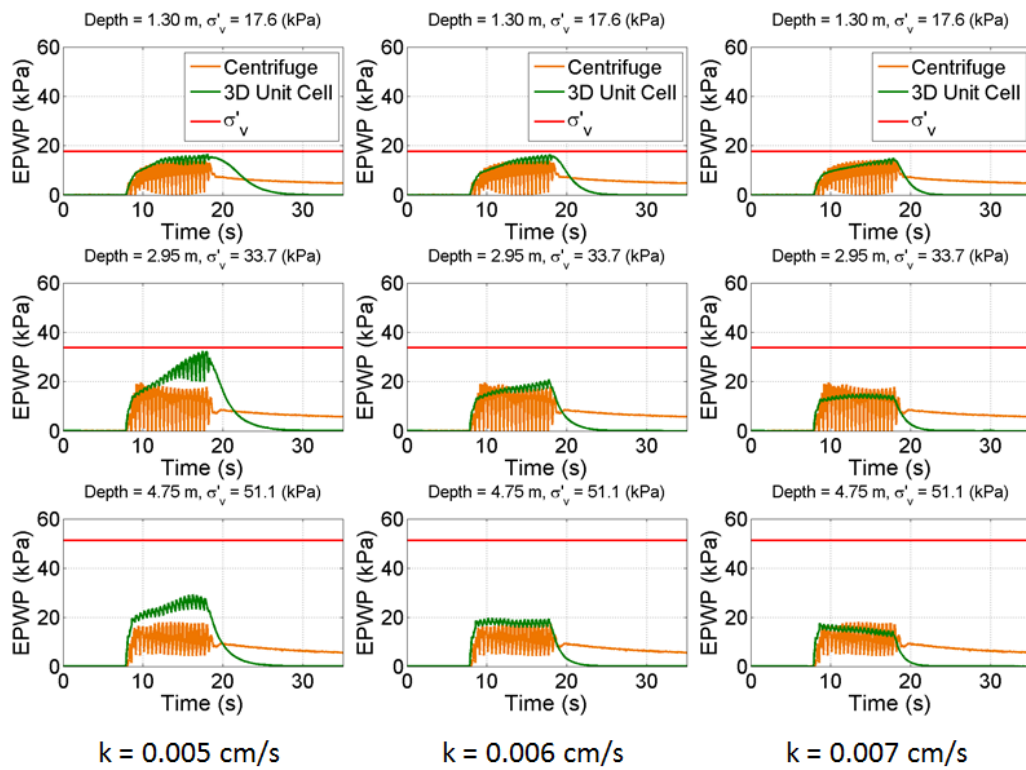


Figure 4.15: Excess pore water pressure time histories at different depths within the treated 3D unit cell model for shaking event SSK01_11 (PGA = 0.11 g) and a range of hydraulic conductivities.

Based on the results shown in Figures 4.14 and 4.15, a hydraulic conductivity of 0.007 cm/s was chosen for the liquefiable sand in the numerical model. Finding an exact match to the centrifuge model hydraulic conductivity is not critical since the numerical model is not an exact model of the centrifuge tests. However, having a comparable hydraulic conductivities does aid in the comparison of the data.

The 0.007 cm/s hydraulic conductivity chosen for the 3D model cannot directly be used in the 2D plane strain models. The 2D models effectively have wall drains that extend infinitely into the page, which significantly increases drainage within the model. Hird et al. (1992) introduced scaling laws that modify the drain spacing or soil hydraulic conductivity in a plane strain unit cell model in order to equate the average degree of consolidation on a horizontal plane for an axisymmetric unit cell with a drain and a plane strain unit cell with a drain. For this research, the soil hydraulic conductivity rather than the drain spacing was scaled. The Hird et al. (1992) scaling laws modify the hydraulic conductivity based on the radius of influence of the drain and the radius of the drain. Based on these scaling laws, the 0.007 cm/s hydraulic conductivity in the 3D unit cell model equates to a 0.0023 cm/s hydraulic conductivity in the 2D models. A complete derivation of the scaled hydraulic conductivity for the 2D unit cell models can be found in Appendix A.

4.5 Summary

This chapter described the development of the numerical models used in this research. Simulations have been performed using OpenSees, which is an open-source software framework intended for use in simulating the seismic response of structural and geotechnical systems. The PressureDependentMultiYield02 (PDMY02) constitutive model was chosen to represent the liquefiable sand. This is an elasto-plastic model used to simulate the cyclic response of soils whose behavior is sensitive to applied stresses. The PressureIndependentMultiYield (PIMY) constitutive model was chosen to represent the clay. This is an elasto-plastic model used to simulate the cyclic response of soils whose behavior is insensitive to applied stresses.

Three types of numerical models have been developed: a 2D unit cell model, a 3D unit cell model, and a full 2D, plane strain model of the centrifuge models. The 2D and 3D unit cell models are infinite slope, shear beam type models. These models are appropriate for modeling the free-field response of a lateral spread site where sliding deformations parallel to the slope dominate the displacements. These models are not appropriate for modeling the response of lateral spread sites in locations where circular failure surfaces would be expected to form (e.g., near shorelines).

The hydraulic conductivity of the simulated sand is most critical for the drain-treated condition as it affects the flow of pore water into the drains. A range of hydraulic conductivities for the simulated sand were identified such that the resulting coefficient of consolidation for the simulated sand was equivalent to the coefficient of consolidation of the prototype sand. A final hydraulic conductivity

was selected based on simulations of the mid-range intensity SSK01 shaking events performed using the treated 3D unit cell model. This hydraulic conductivity was then scaled again to account for the drainage effects in the 2D unit cell models using the Hird et al. (1992) scaling laws for equating an axisymmetric unit cell model with a drain to a 2D plane strain unit cell model with a drain. The hydraulic conductivity of the prototype sand was 0.03 cm/s and the hydraulic conductivity of the simulated sand is 0.007 cm/s; this is the hydraulic conductivity of the simulated sand in the 3D unit cell models. The hydraulic conductivity of the simulated sand in the 2D unit cell models is further reduced to 0.0023 cm/s to account for the improved drainage effects resulting from the fact that the drain in the 2D model acts as a wall drain instead of a line drain.

Chapter 5

Comparison of Numerical Models and Data from Centrifuge Test

SSK01

5.1 Introduction

This chapter describes the results of the numerical simulations of centrifuge test SSK01 and focuses on how well the numerical results compare with the observed behavioral trends from the SSK01 centrifuge test. Simulations of shaking events SSK01.09 (PGA = 0.03 g) through SSK01.12 (PGA = 0.30 g) were performed using the untreated and drain-treated 2D and 3D unit cell models. The numerical data is analyzed with emphasis given to identifying the behavioral trends that were observed in the centrifuge test.

5.2 Comparison of Untreated 2D and 3D Unit Cell Models

The first step in the evaluation of the numerical models is to confirm that the 2D and 3D unit cell models produce similar results for the untreated condition. Figure 5.1 shows the excess pore water pressure-time histories at three different depths within the untreated 2D and 3D unit cell models for shaking events SSK01.09 (PGA = 0.03 g) through SSK01.12 (PGA = 0.30 g). It can be seen in Figure 5.1 that the excess pore water pressure-time histories for the untreated 2D and 3D unit cell models are identical during shaking with only minor discrepancies. The unit cell models are completely undrained with impervious lateral boundaries and a clay crust. These boundary conditions are generally acceptable during shaking because the soil layer remains undrained. However, after shaking, the soil will drain vertically through cracks in the clay crust and horizontally to areas with smaller excess pore pressures. To model this behavior in the unit cell models, a manual drainage phase is included after shaking. This drainage phase is accomplished by increasing the hydraulic conductivity of the clay layer to simulate vertical drainage through the crust. If this drainage phase is not included in the numerical analyses, the excess pore water pressures do not dissipate and the lateral deformations continue, albeit at a slower pace, indefinitely.

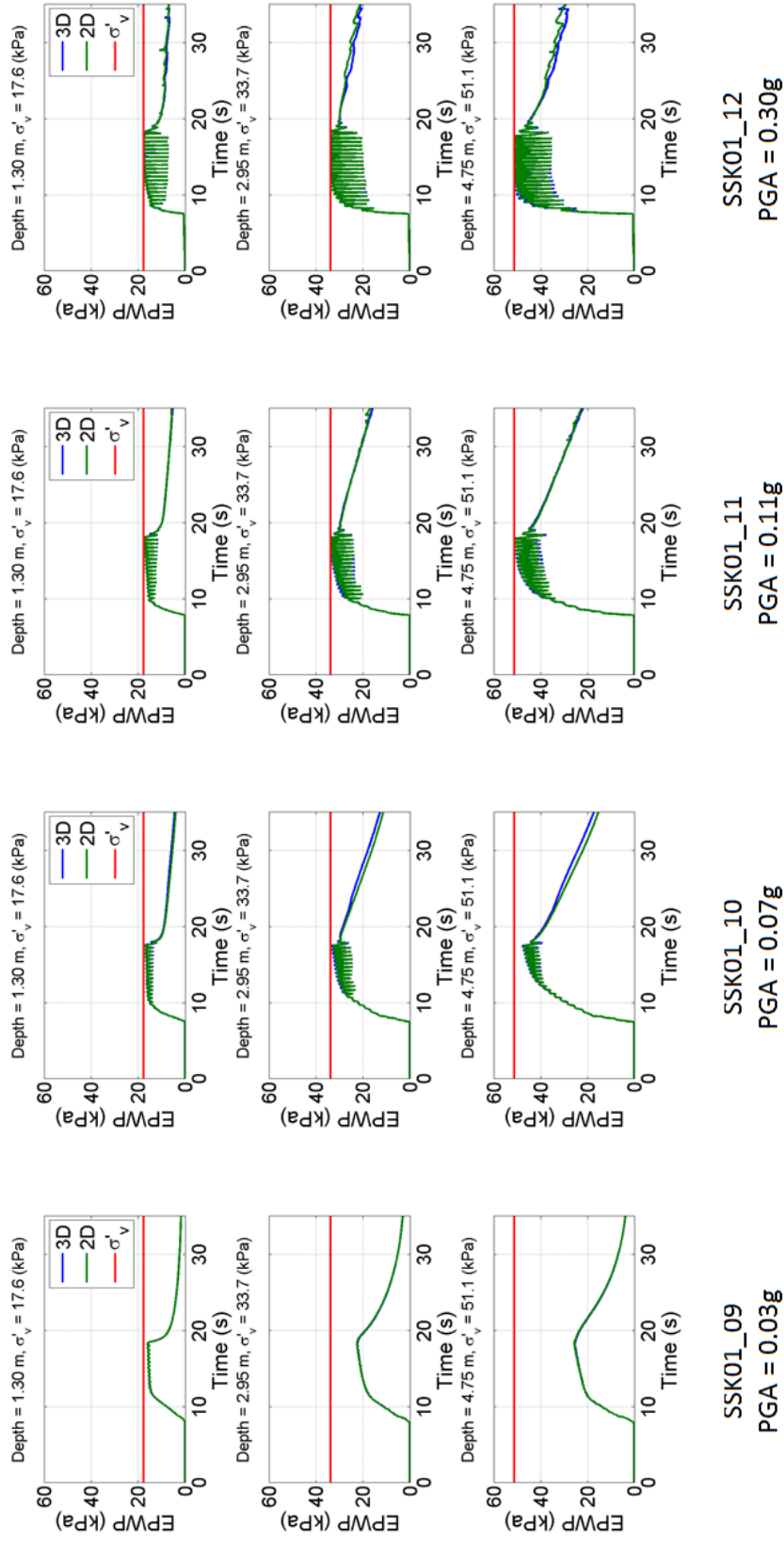


Figure 5.1: Excess pore water pressure-time histories at three different depths within the untreated 2D and 3D unit cell models for shaking events SSK01_09 (PGA = 0.03 g) through SSK01_12 (PGA = 0.30 g).

Given that the excess pore pressures for the untreated 2D and 3D unit cell models are nearly identical, the horizontal and vertical deformations for the untreated 2D and 3D unit cell models should also be similar. Figure 5.2 shows the horizontal and vertical deformation-time histories at top of the clay layer and the horizontal displacement vs. depth profiles for the untreated 2D and 3D unit cell models for shaking events SSK01_09 (PGA = 0.03 g) through SSK01_12 (PGA = 0.30 g). It can be seen that the horizontal and vertical deformation-time histories at the top of the clay layer for the untreated 2D and 3D unit cell models are nearly identical for all shaking events. The horizontal deformation vs. depth data for the untreated 2D and 3D unit cell models are also a good match for shaking events SSK01_09, 11, and 12. There are some slight differences evident in the 2D and 3D horizontal displacement vs. depth profiles for shaking event SSK01_10, but these differences are minor (2.5 cm or 7%) and are not evident in the other shaking events.

Boundary conditions have been applied to the untreated 2D and 3D unit cell models such that they both exhibit an infinite slope, shear beam type response. The data shown in Figures 5.1 and 5.2 confirm that the pore pressure and deformation responses of the untreated 3D unit cell model are identical or nearly identical to the untreated 2D unit cell model responses. For the remainder of this section, no distinction will be made between the 2D and 3D data when discussing the untreated unit cell models.

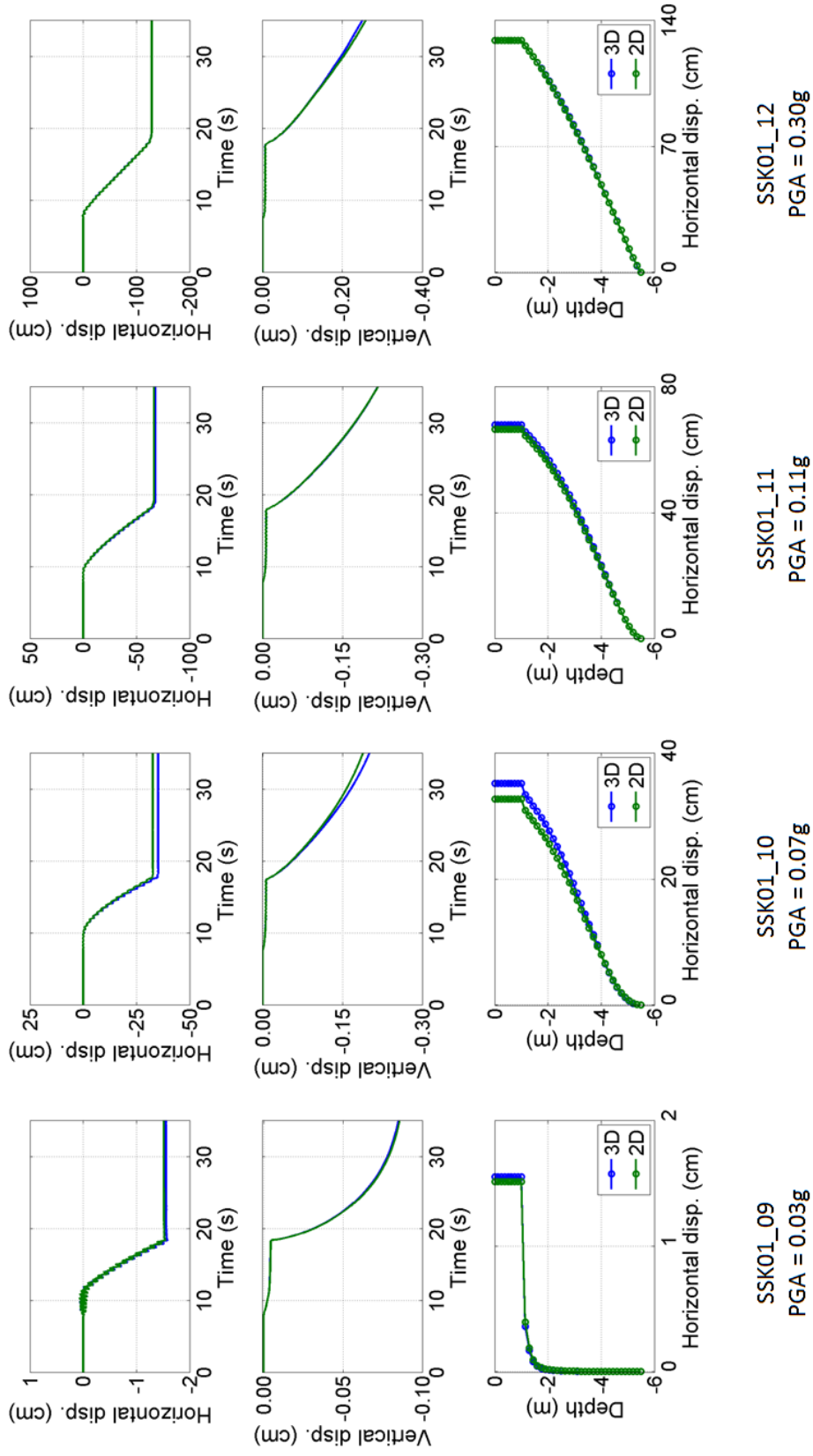


Figure 5.2: Horizontal and vertical displacement-time histories at the top of the clay layer and horizontal displacement vs. depth profiles for the untreated 2D and 3D unit cell models for shaking events SSK01_09 (PGA = 0.03 g) through SSK01_12 (PGA = 0.30 g).

5.3 Comparison of Untreated Numerical Models and Centrifuge Data

This section compares the excess pore pressure and deformation responses of the numerical models with the centrifuge data for the untreated condition. Figure 5.3 shows the excess pore water pressure-time histories at three different depths within the untreated unit cell models versus data from comparable depths within the SSK01 centrifuge model for shaking events SSK01_09 (PGA = 0.03 g) through SSK01_12 (PGA = 0.30 g). For the lowest intensity shake, SSK01_09 (PGA = 0.03 g), the untreated unit cell models significantly overestimate the excess pore water pressures in comparison to the centrifuge data. For SSK01_10 (PGA = 0.07 g) and SSK01_11 (PGA = 0.11 g), the numerical models do well near the sand/clay interface and at mid-depth, but still somewhat overestimate the excess pore water pressures near the base of the model. For SSK01_12 (PGA = 0.3 g), the numerical data matches well with the centrifuge data at all depths. For shaking events SSK01_10 through SSK01_12, the numerical models exhibit larger dilation spikes (i.e., cyclic reductions in r_u during shaking) than the centrifuge model during shaking, but the magnitudes of excess pore water pressures at the end of shaking are similar to the values observed in the centrifuge test.

Figure 5.3 illustrates that, with the exception of SSK01_09, there is a good match between the simulated and experimental excess pore water pressure data. The difference between the simulated and observed excess pore water pressures for shaking event SSK01_09 is likely due to the effects of the centrifuge container. The SSK01 centrifuge model was constructed in a flexible shear beam container that was designed to deform with the liquefiable sand. However, the container

has mass and this mass affects the centrifuge model's response, particularly for lower-intensity shaking events. To confirm that the container was affecting the pore pressure response, SSK01_09 was simulated using the full 2D plane strain model (the 2D numerical model of the full centrifuge model including the container described in Section 4.3.3), and the results are shown in Figure 5.4. The excess pore water pressure-time histories from the full 2D model, which takes into account the effects of the container, match very well with the centrifuge data for SSK01_09. As the intensity of shaking is increased, the effects of the container are less critical. In Figure 5.4, the pore pressure data from both the unit cell model and the full 2D model are a good match to the centrifuge data for the SSK01_12.

Taking into account that the centrifuge container is influencing the excess pore water pressure response from the centrifuge model for the low-intensity SSK01_09 shaking event, the untreated unit cell models do well in predicting the excess pore water pressures that developed in the untreated area of the SSK01 centrifuge model.

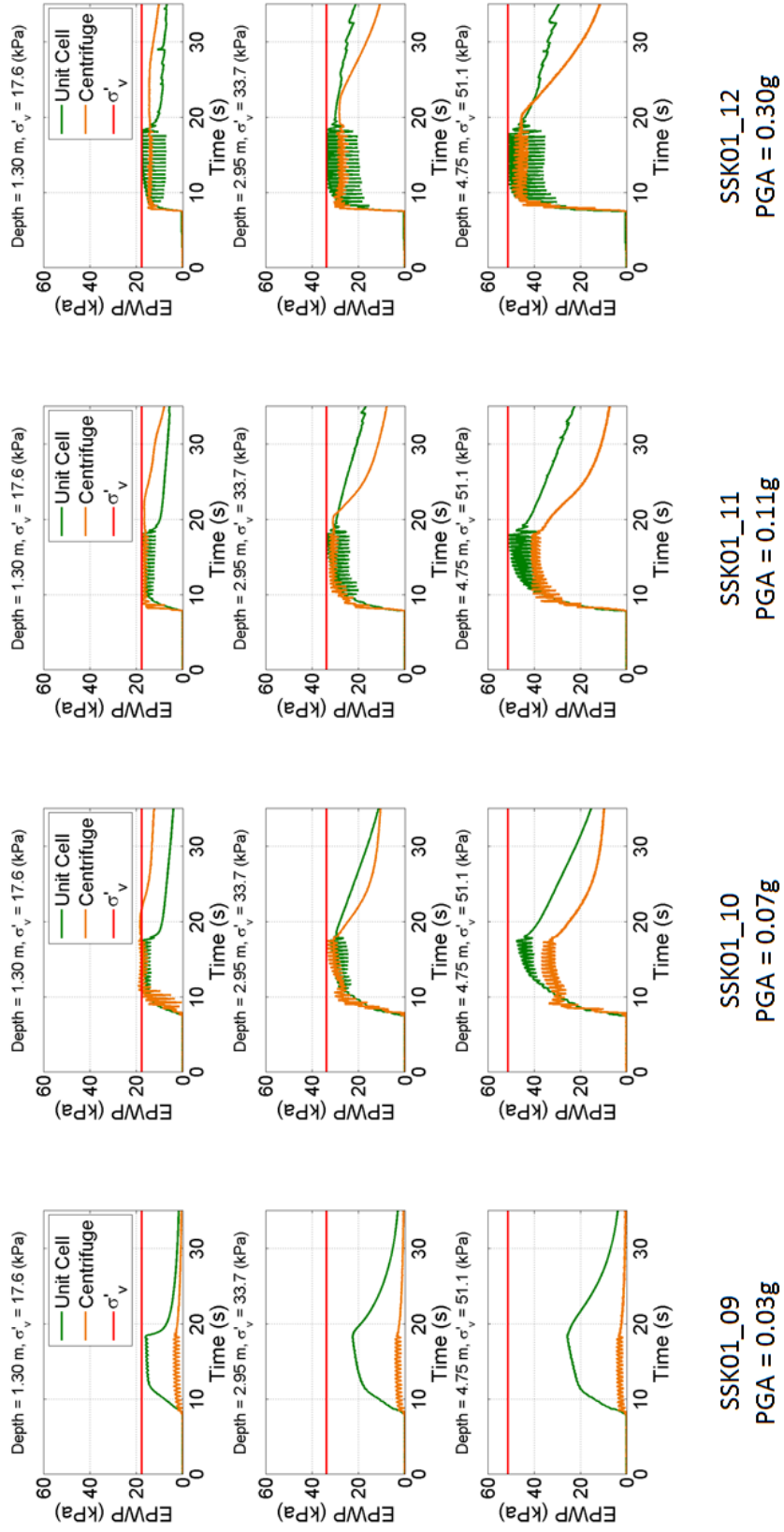


Figure 5.3: Excess pore water pressure-time histories at three different depths within the untreated unit cell models vs. centrifuge data at comparable depths for shaking events SSK01_09 (PGA = 0.03 g) through SSK01_12 (PGA = 0.30 g).

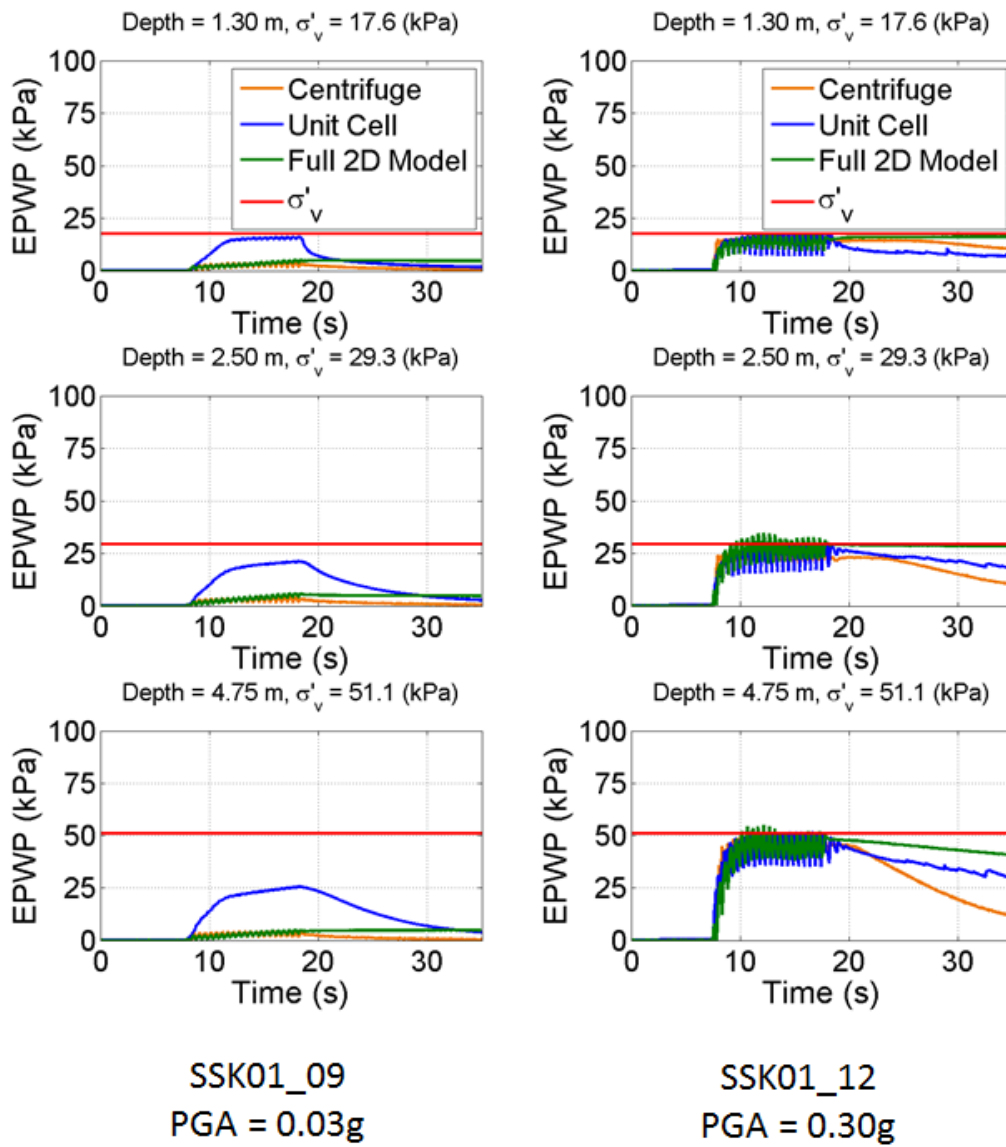


Figure 5.4: Excess pore water pressure-time histories at three different depths for the untreated unit cell models, the untreated area of the full 2D model, and the untreated area of the SSK01 centrifuge model for shaking events SSK01_09 (PGA = 0.03 g) and SSK01_12 (PGA = 0.30 g).

Figure 5.5 shows the horizontal and vertical displacement-time histories at the top of the clay layer for the untreated unit cell models compared with the mid-slope data from the untreated area of the SSK01 centrifuge model for shaking events SSK01_09 (PGA = 0.03 g) through SSK01_12 (PGA = 0.30 g). It can be seen the untreated unit cell models exhibit significant horizontal deformations and almost no vertical settlement for all shaking events. The largest overprediction is for SSK01_12, but the centrifuge model at this stage of shaking had flattened significantly due to deformation from previous shaking events such that the SSK01_12 deformations were actually smaller than the deformations for the lower-intensity SSK01_11 shake.

The larger horizontal deformations in the unit cell models are due to the fact that these models represent infinite slope conditions in which all deformations are translational and there is no passive resistance at the toe of the slope. As noted in Chapter 4, infinite slope models are most appropriate when the length of the slope is much greater than the thickness of the soil layer. The length of the slope in the centrifuge model was not significantly longer than its thickness and the presence of the treated area of the model provided passive resistance at the toe of the slope in the untreated area. As a result, the failure surface in the centrifuge model was more circular in nature and the lateral deformations in the centrifuge were smaller than in the numerical models. The smaller vertical deformations in the unit cell models are due to the fact that the infinite slope model does not capture vertical deformations associated with a circular failure surface, as well as the fact that the PDMY02 constitutive model does not accurately model volumetric strain due to liquefaction, as evidenced by the smaller equivalent volumetric compressibility in Section 4.2.2.

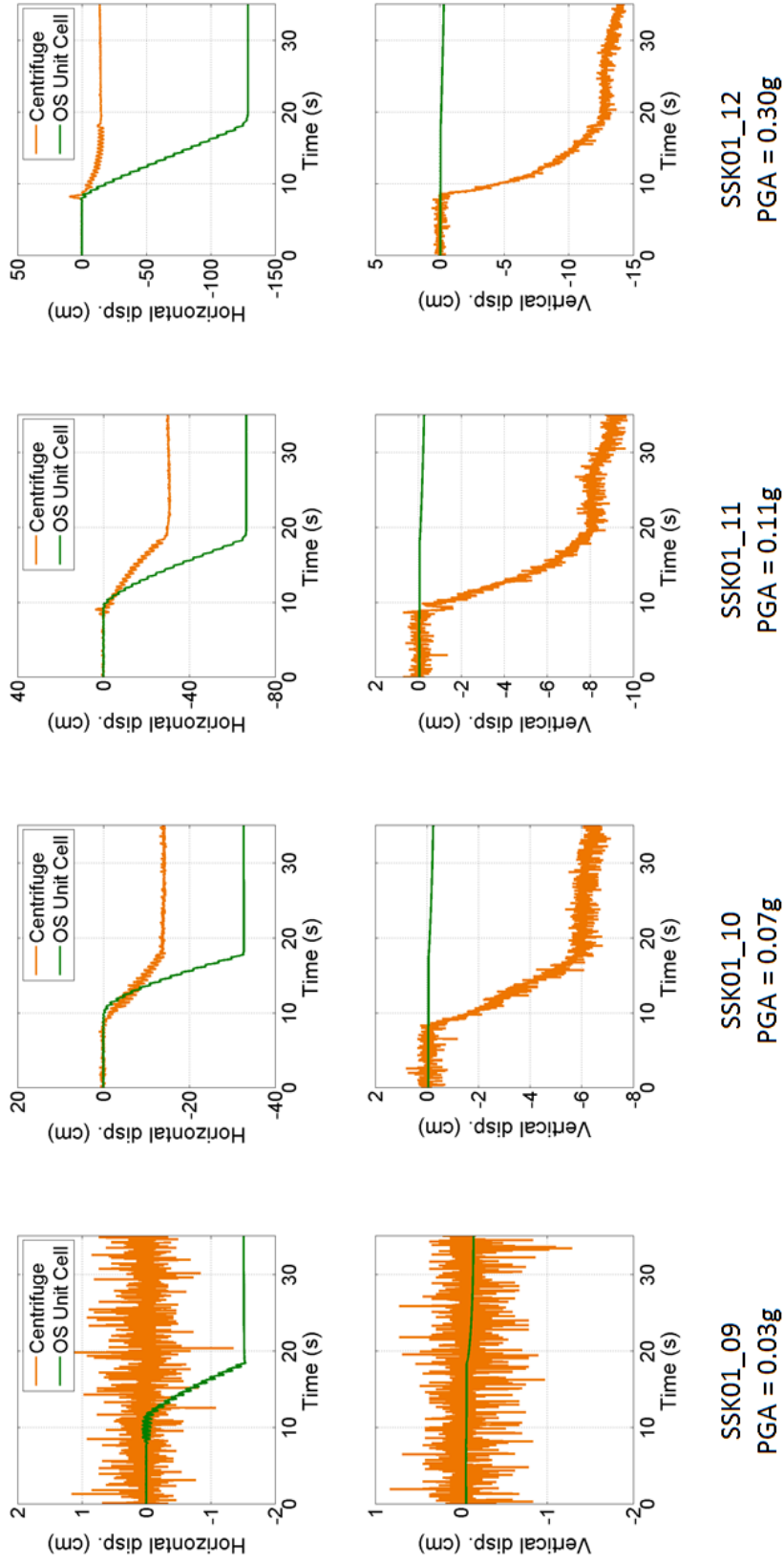


Figure 5.5: Horizontal and vertical displacement-time histories at the top of the clay layer for the untreated unit cell models vs. mid-slope data from the centrifuge model for shaking events SSK01_09 (PGA = 0.11 g) through SSK01.12 (PGA = 0.30 g).

To illustrate how the geometry of the centrifuge model is influencing the deformation response, simulations of shaking events SSK01_09 (PGA = 0.03 g) through SSK01_12 (PGA = 0.30 g) were performed using the full 2D plane strain model and the results are shown in Figure 5.6. The full 2D model accurately predicts no horizontal deformations for SSK01_09, it underpredicts the horizontal deformations for SSK01_10 and SSK01_11 by factors of 2 to 3, and predicts well the horizontal deformations for SSK01_12. The better agreement for SSK01_12 may simply be caused by the centrifuge experiencing smaller deformations due to flattening of the slope. Thus, in general the full 2D model underpredicts the centrifuge deformations. However, the full 2D model develops vertical deformations that are consistent with those from the centrifuge test. The full 2D model captures the vertical deformations better than the unit cell models because it can model a circular failure surface. Figure 5.7 shows the deformed mesh and contours of displacement for the full 2D model for shaking event SSK01_12. It is evident that a circular failure surface develops in the untreated area of the model.

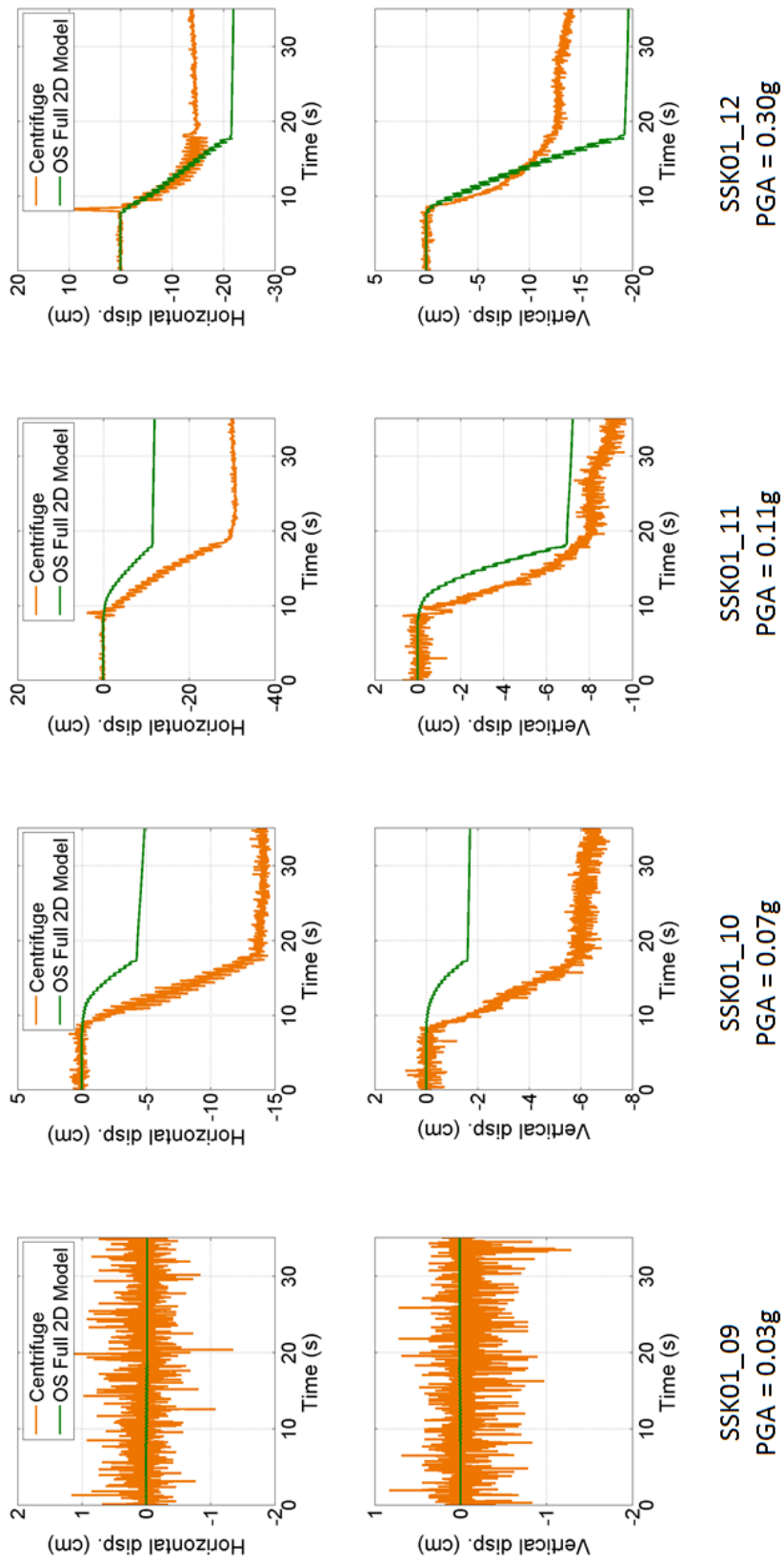


Figure 5.6: Displacement-time histories for the untreated area of full 2D model vs. mid-slope data from the untreated area of the SSK01 centrifuge model for shaking events SSK01_09 (PGA = 0.11 g) through SSK01_12 (PGA = 0.30 g).

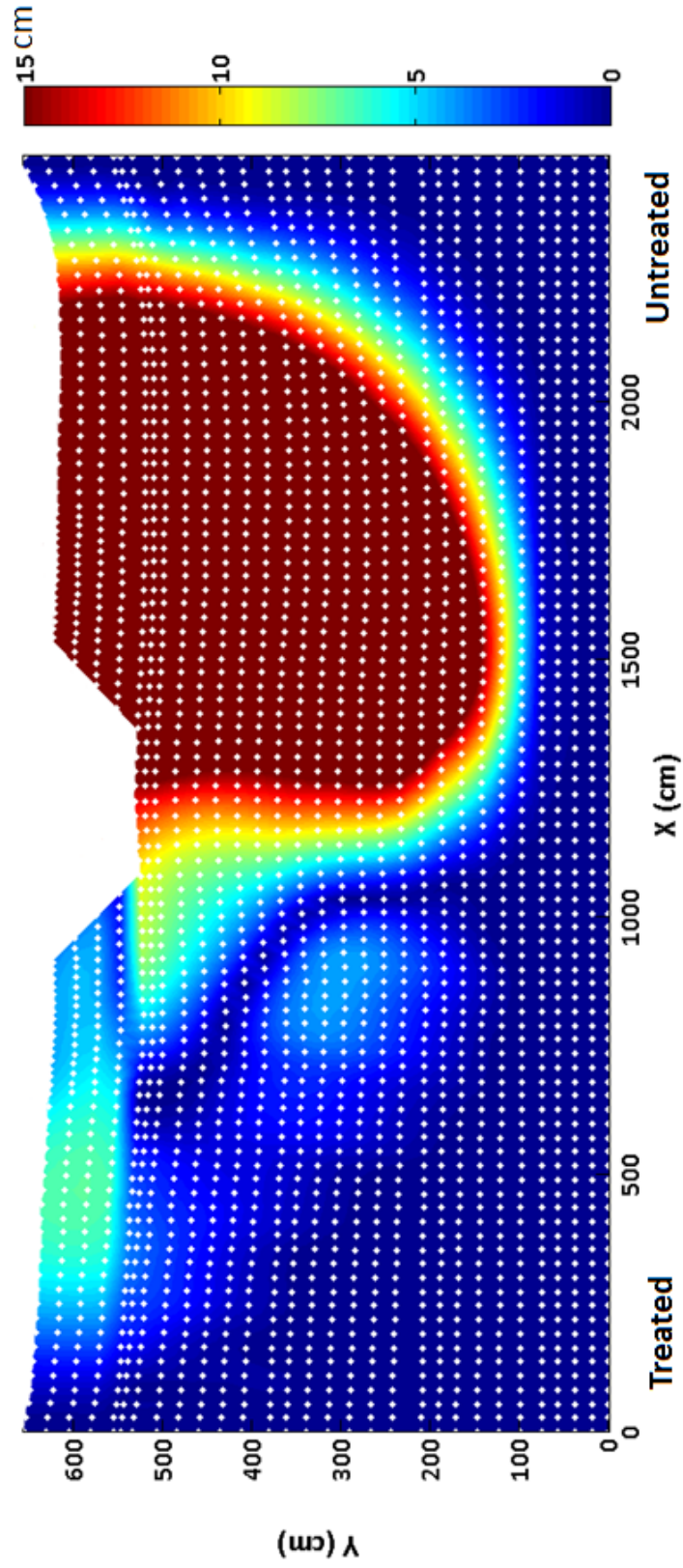


Figure 5.7: Deformed mesh and contours of displacement for the full 2D model for shaking event SSK01_12 (PGA = 0.30 g).

The differences between the numerical and experimental pore pressure and deformation responses may also be affected by differences between the simulated and experimental accelerations. The input acceleration-time histories used in the numerical models are the recorded acceleration-time histories from an accelerometer located at the base of the centrifuge container; however, the models' response to these accelerations over the depth of the soil profile may differ. Figure 5.8 shows the acceleration time histories at depths of 2.4 m and 3.7 m for the untreated unit cell model, the untreated area of the full 2D model, and the untreated area of the centrifuge model for shaking events SSK01_10 and SSK01_12. For SSK01_10 (Figure 5.8a), both the centrifuge model and the numerical models exhibit accelerations that are generally between ± 0.1 g at both the 2.4 m and 3.7 m depth. The accelerations at 2.4 m in the centrifuge increase slightly to ~ -1.5 g between time = 10 and 20 seconds, while those in the numerical models decrease, but the general agreement between the simulated and experimental accelerations for SSK01_10 are fairly decent. The differences are much more significant for shaking event SSK01_12 (Figure 5.8b). In the centrifuge model, the accelerations at both depths decrease dramatically after the initial cycles of shaking due to the liquefaction of the loose sand, whereas the accelerations in the numerical models cycle between ± 0.3 g throughout significant shaking. The accelerations decrease somewhat in the full 2D model, but that decrease is relatively insignificant in comparison to the decrease observed in accelerations from the centrifuge model. The larger accelerations in the numerical models may also contribute to larger deformation and pore pressure responses.

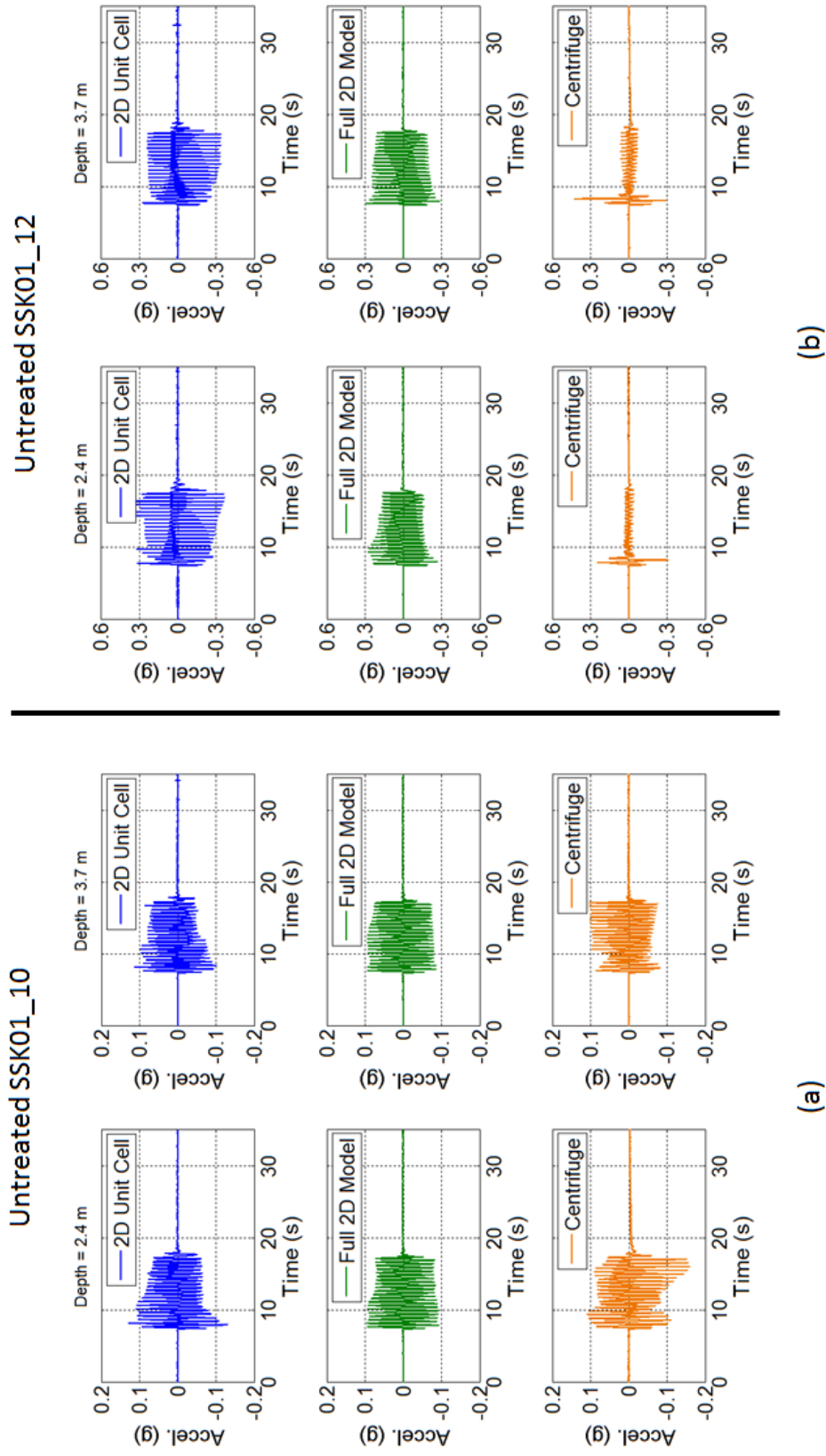


Figure 5.8: Acceleration-time histories at depths of 2.4 m and 3.7 m for the untreated 2D unit cell model, the untreated area of the full 2D model, and the untreated area of the centrifuge model for shaking events (a) SSK01_10 (PGA = 0.07 g) and (b) SSK01_12 (PGA = 0.30 g).

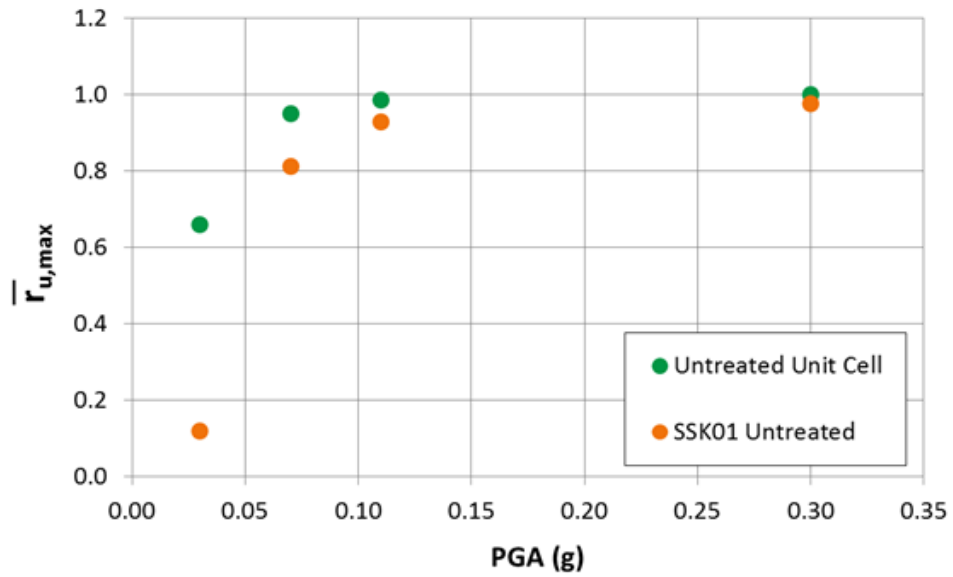
Regardless of how well the simulated and experimental data match for specific shaking events, there are behavioral trends related to both pore pressure generation and deformations that the numerical models are expected to capture. These trends include an increase in pore pressure generation and deformation with increasing input intensity.

To evaluate the spatial and temporal variation in the pore pressure response, $\bar{r}_{u,\max}$ is used (Section 3.5.2). For the numerical model, $\bar{r}_{u,\max}$ was computed from the excess pore pressures at each node along the vertical centerline of the model. Figure 5.9a shows $\bar{r}_{u,\max}$ as a function of the PGA of the input motion for the untreated unit cell models and the untreated area of the SSK01 centrifuge model. For both the unit cell models and the centrifuge model, $\bar{r}_{u,\max}$ increases with increasing PGA until $\bar{r}_{u,\max}$ reaches a maximum value of 1.0. The greatest difference between the experimental data and the simulated data exists for shaking event SSK01_09 (PGA = 0.03 g), but as illustrated in Figure 5.4, this is due the influence of the container. For the remaining shaking events, there is good agreement between the centrifuge and numerical data and the behavioral trend associated with the $\bar{r}_{u,\max}$ is consistent for both models.

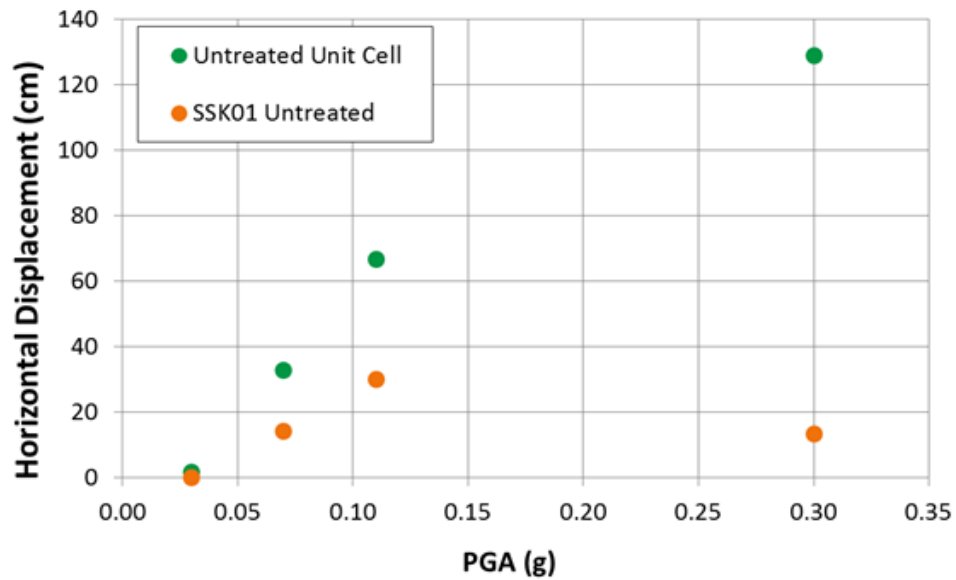
Figure 5.9b shows the horizontal displacements as a function of the PGA of the input motion for the untreated unit cell models and the untreated area of the SSK01 centrifuge model. While the simulated deformations are significantly larger than the deformations from the centrifuge test; the relationship between the PGA and the horizontal deformations is the same for both the numerical models and the centrifuge model. With the exception of the SSK01_12 (PGA = 0.30 g) data from the centrifuge test, the magnitudes of horizontal displacements for both the untreated unit cell models and the centrifuge model increase with

increasing input intensity. The smaller centrifuge deformations for SSK01_12 are most likely due to flattening of the slope during previous shakes.

Because the unit cell models do not capture vertical deformations, vertical deformations and the behavioral trends associated with the vertical deformations will not be evaluated further. Emphasis will instead be placed on the horizontal deformation response, the excess pore pressure response, and the relationship between the excess pore pressures and the horizontal deformations.



(a)



(b)

Figure 5.9: (a) Peak average excess pore water pressure ($\bar{r}_{u,max}$) vs. PGA and (b) Horizontal displacement vs. PGA for the untreated unit cell models and the untreated area of the SSK01 centrifuge model.

5.4 Comparison of the Treated 2D and 3D Unit Cell Models

This section focuses on the numerical modeling of the drain-treated condition. The most significant difference between the treated 2D and 3D unit cell models is the drainage around the drain at the center of the unit cell. In the treated 3D unit cell model, the drain acts as a vertical line drain, whereas in the 2D unit cell model, the drain acts as a wall drain because of the plane strain condition. The Hird et al. (1992) scaling laws for equating axisymmetric and plane strain unit cell models with drain elements were applied as discussed in Section 4.4. As a result of the scaling, the hydraulic conductivity of the 2D unit cell model is reduced from 0.007 cm/s to 0.00238 cm/s (See Appendix A) to account for the differences between the drainage conditions in the 2D and 3D unit cell models. However, the Hird et al. (1992) scaling laws are based on the average degree of consolidation on a horizontal plane; they do not consider horizontal deformations, nor do they consider the pore pressure variation along a horizontal plane (Figure A.3).

Figure 5.10 shows the excess pore water pressure-time histories at three different depths for the treated 2D and 3D unit cell models for shaking events SSK01_09 (PGA = 0.11 g) through SSK01_12 (PGA = 0.30 g). These excess pore pressures were recorded at the upslope edge of the unit cell, which represents the centerline between adjacent drains. This location is consistent with the location of the PPT array in the centrifuge tests. It can be seen in Figure 5.10 that the excess pore water pressures for the 2D and 3D unit cell models are similar, but, as expected, they are not identical and the differences are most evident at shallow

depths near the sand/clay interface. The 2D unit cell model exhibits somewhat smaller excess pore water pressures at these depths, indicating that it is draining faster than the 3D unit cell model. Figure 5.11 shows the excess pore pressures across the treated 2D and 3D unit cell models at a depth of 1.30 m for shaking event SSK01.09 (PGA = 0.03 g) at time = 10 seconds. The treated 2D unit cell model has smaller excess pore pressures than the treated 3D unit cell model at all locations, except at the drain where the excess pore pressures are set to zero.

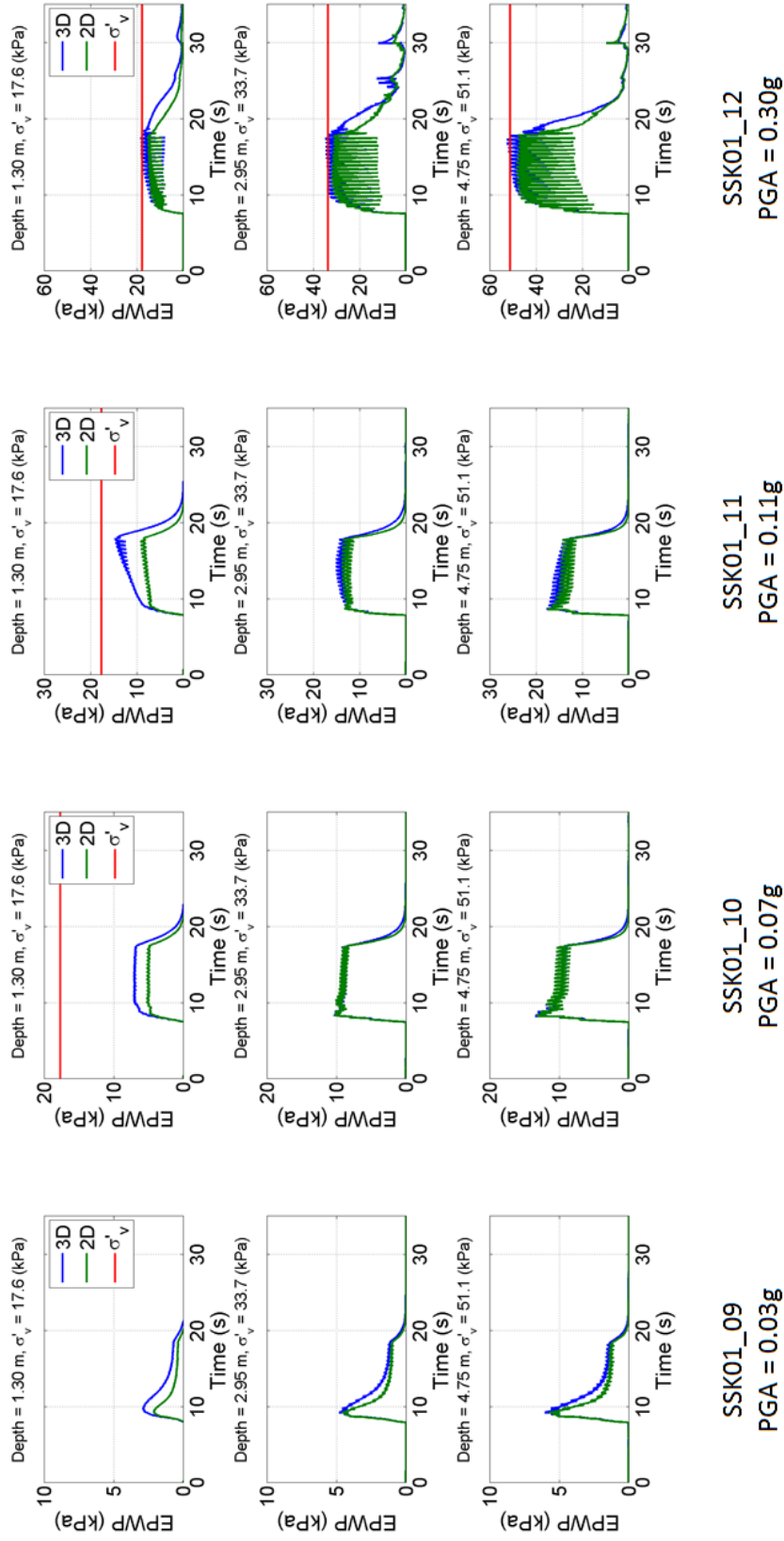


Figure 5.10: Excess pore water pressure-time histories for the treated 2D and 3D unit cell models for shaking events SSK01_09 (PGA = 0.11 g) through SSK01_12 (PGA = 0.30 g).

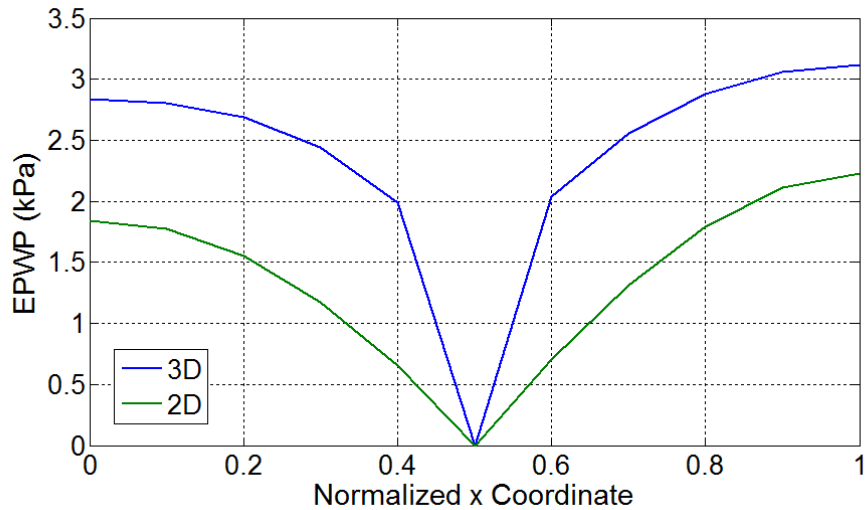


Figure 5.11: Excess pore pressures across the treated 2D and 3D unit cell models at a depth of 1.30 m for shaking event SSK01_12 (PGA = 0.30 g) at time = 10 seconds.

Figure 5.12 shows horizontal displacement-time histories at the top of the clay layer and the horizontal displacement vs. depth profiles at the end of shaking for the treated 2D and 3D unit cell models for shaking events SSK01_09 (PGA = 0.11 g) through SSK01_12 (PGA = 0.30 g). The horizontal displacements are minimal for shaking events SSK01_09 and SSK01_10 because the excess pore water pressures stay well below the vertical effective stress (Figure 5.10). The displacements are still less than 1.0 cm for SSK01_11, but there is some discrepancy between the 2D and 3D models due to the larger pore pressures predicted by the 3D model (Figure 5.10). For SSK01_12, the horizontal deformations predicted by the 3D model are 70% larger than those predicted by the 2D model, despite the fact that the 2D and 3D pore pressures are very similar (Figure 5.10).

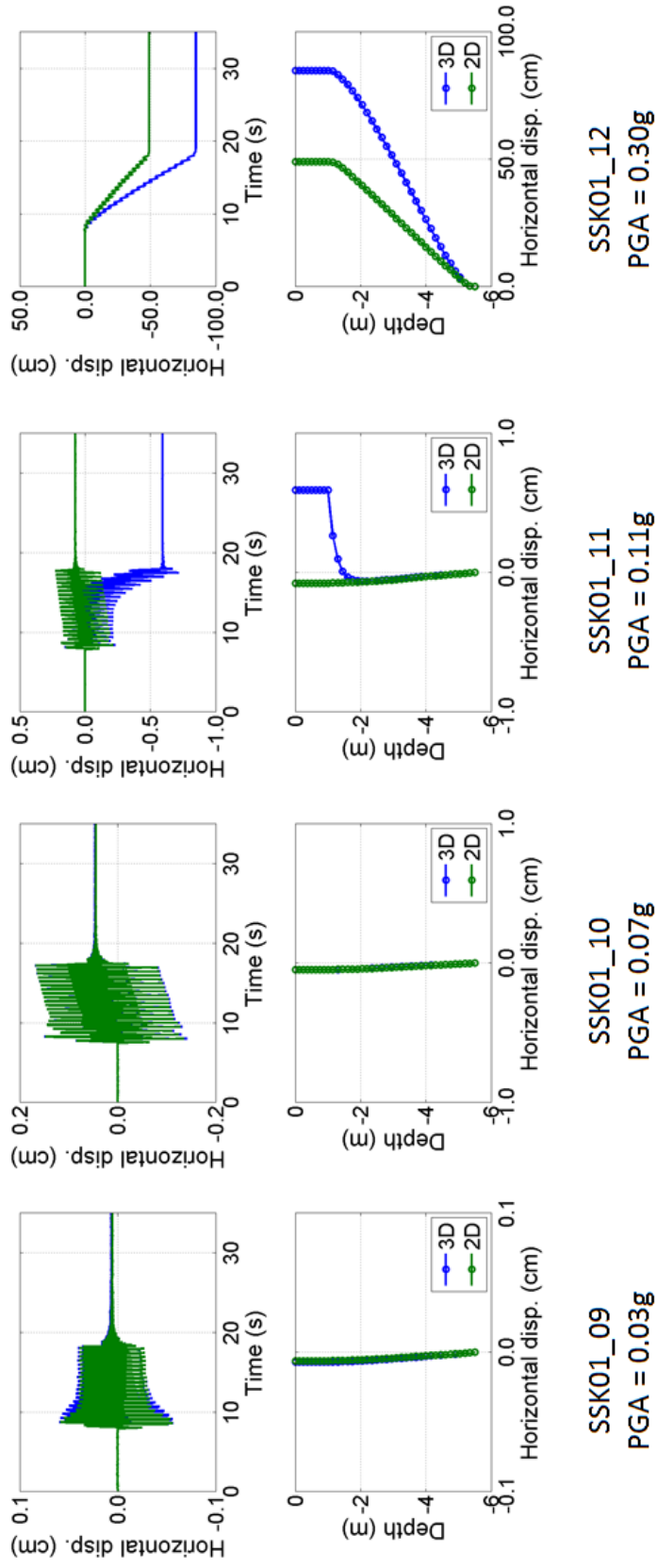


Figure 5.12: Horizontal displacement-time histories at the top of the clay layer and horizontal displacement vs. depth data at the end of shaking for the treated 2D and 3D unit cell models for shaking events SSK01_09 (PGA = 0.11 g) through SSK01_12 (PGA = 0.3 g).

For SSK01_12, the larger deformations in the 3D unit cell model are a result of the differences between the 2D and 3D drainage conditions, which are illustrated in Figure 5.13. The presence of a drain reduces the excess pore pressures in the adjacent soil and thus, the soil next to the drain retains more of its strength than the soil further away from the drain (i.e., at the edges of the model). In the 3D unit cell model (Figure 5.13a), the drain acts as a vertical line drain, and the excess pore pressures are reduced in a cone around the very center of the model while the pore pressures around the edges of the model remain elevated. In the 2D unit cell model (Figure 5.13b), the drain acts as a linear wall drain and the excess pore pressures are reduced along a wedge parallel to the drain. This effectively creates a wall of stronger soil across the center of the 2D unit cell model, which is much larger and more effective in reducing deformations than the small area of stronger soil along the centerline of the 3D unit cell model. If \bar{r}_u were calculated for the cross sectional planes shown in Figure 5.13, the 3D model have a larger average r_u than the 2D model, and larger excess pore pressures result in larger deformations.

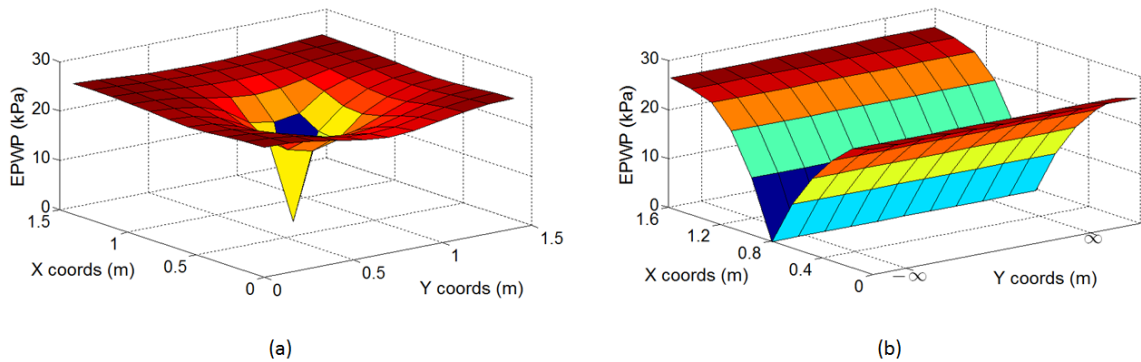


Figure 5.13: (a) 3D and (b) 2D drainage conditions for the unit cell models.

5.5 Comparison of the Treated Numerical Models and Centrifuge Data

Figure 5.14 shows the excess pore water pressure-time histories for the treated 2D and 3D unit cell models and the treated area of the SSK01 centrifuge model at three different depths for shaking events SSK01_09 (PGA = 0.11 g) through SSK01_12 (PGA = 0.30 g). The excess pore pressures for the numerical models were recorded at the left edge of the model, which is the upslope boundary at the edge of the area of influence for the drain. The excess pore pressures for the centrifuge model were recorded by a vertical array of PPTs located in line with and midway between two drains, putting them at the edges of the areas of influence around each drain and outside of the area of influence of any other drain (Figure 5.15). It can be seen in Figure 5.14 that the treated models overpredict the excess pore water pressures for shaking event SSK01_09. This result is due to the effects of the centrifuge container, which are not modeled in the unit cell models, and was similarly observed for the untreated models (Figures 5.3, 5.4). There is a good match between the simulated and experimental data for shaking events SSK01_10 and SSK01_11, but this is expected given that these are the shaking events that were used to calibrate the hydraulic conductivity of the numerical models. For SSK01_12, the numerical data compares well with the centrifuge data at shallow depths, but the numerical model overpredicts the excess pore pressures at depth. This too may be related to the container effects as the base shearing ring of the centrifuge container is actually steel, not aluminum (Figure 3.2), and thus, has a higher mass and more significant inertial effects. To investigate this effect, SSK01_12 was simulated using the full 2D model. All of the container rings

in the full 2D model are modeled as aluminum, but the base shearing ring and the container base have a higher mass density to account for the fact that they are actually made of steel. The pore pressure results for the full 2D simulation of SSK01_12 are shown in Figure 5.16. When modeling the container, liquefaction is still triggered at shallow and mid-depths, but the base of the model does not liquefy.

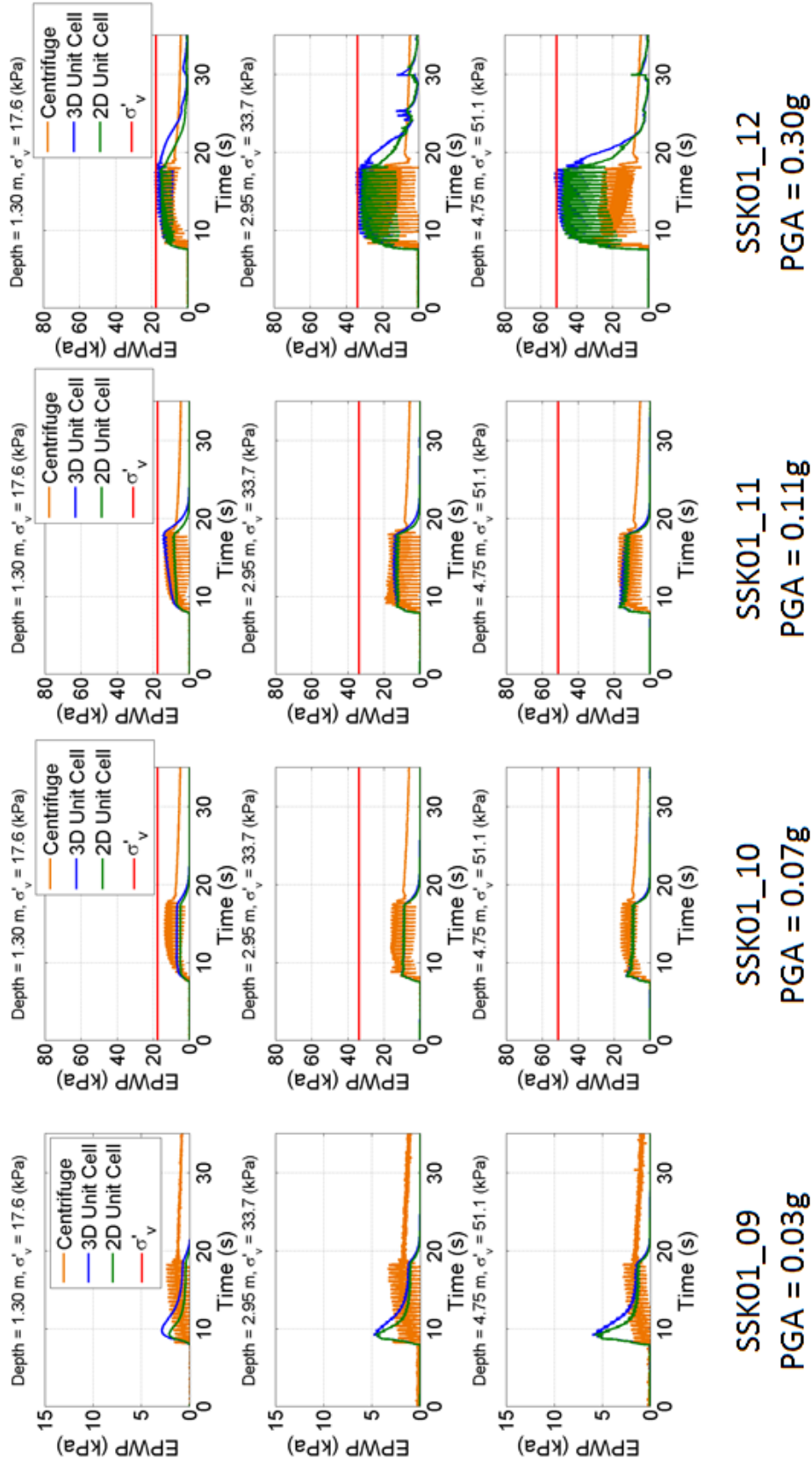


Figure 5.14: Excess pore water pressure-time histories for the treated 2D and 3D unit cell models and the treated area of the SSK01 centrifuge model for shaking events SSK01_09 (PGA = 0.11 g) through SSK01_12 (PGA = 0.30 g).

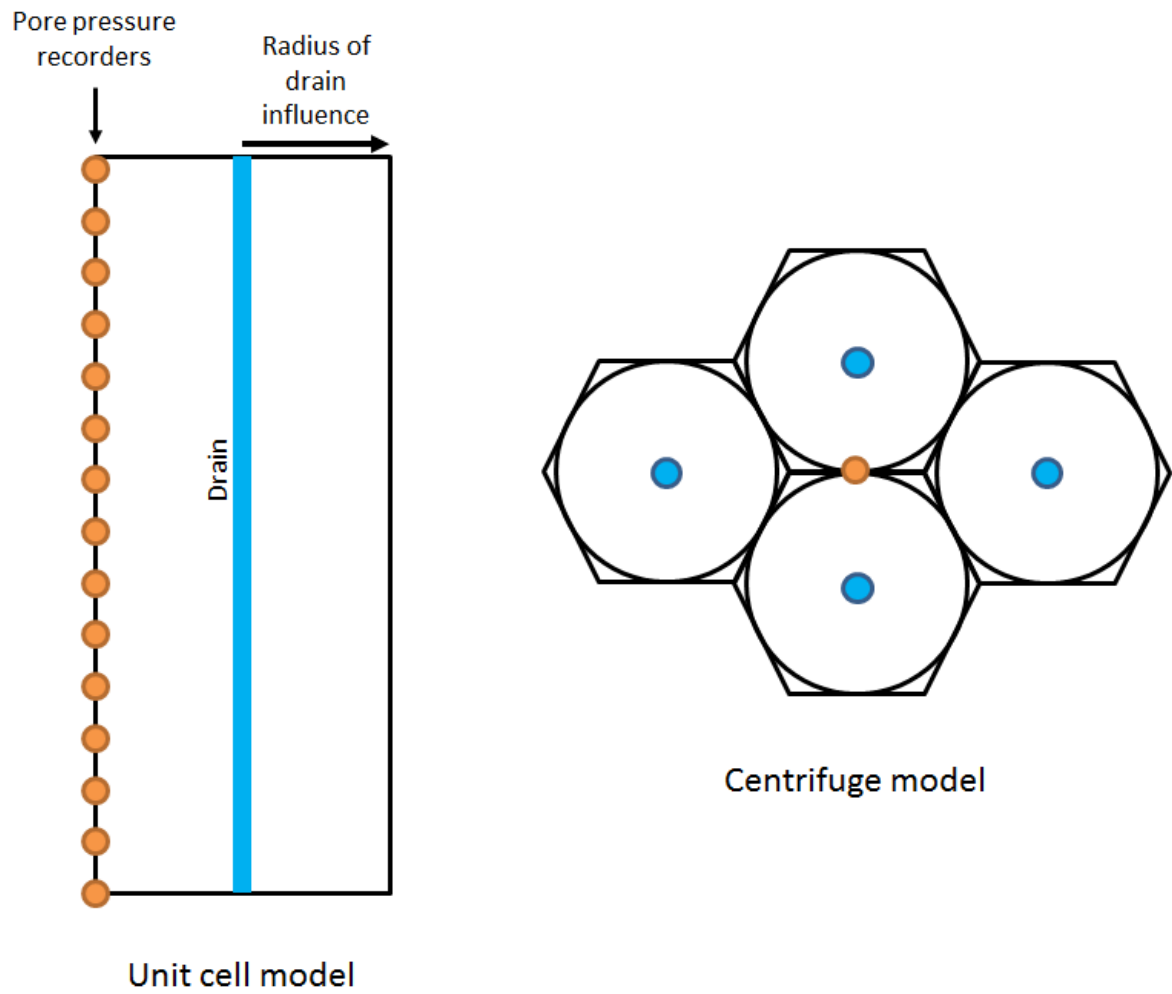


Figure 5.15: Pore pressure recorder location for the treated unit cell models and PPT array location for the SSK01 centrifuge model.

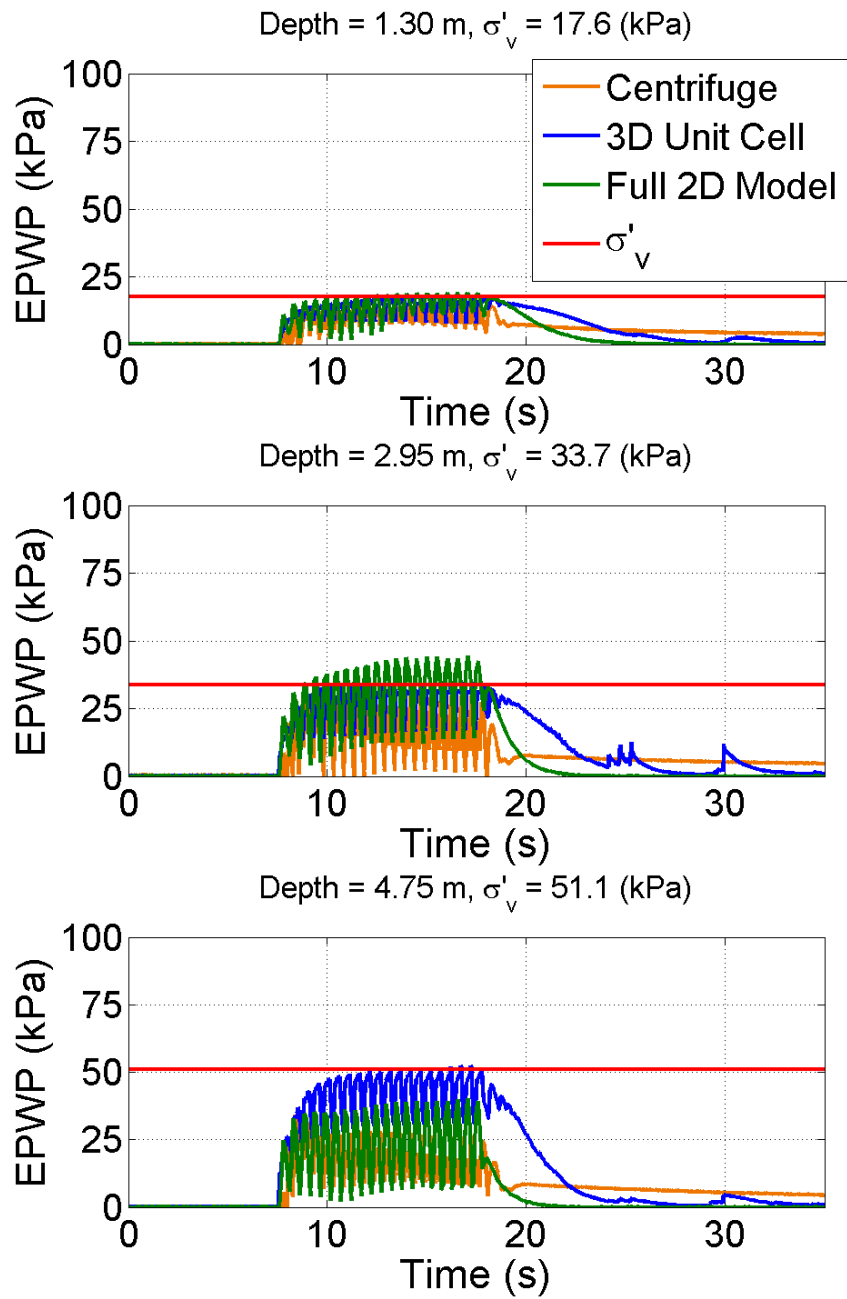


Figure 5.16: Excess pore water pressure-time histories at three different depths for the treated 3D unit cell model, the treated area of the full 2D model, and the treated area of the SSK01 centrifuge model for shaking event SSK01.12 (PGA = 0.30 g).

Figure 5.17 shows the horizontal displacement-time histories at the top of the clay layer for the treated 2D and 3D unit cell models and the treated area of the SSK01 centrifuge model for shaking events SSK01.09 (PGA = 0.11 g) through SSK01.12 (PGA = 0.30 g). The deformations in the centrifuge model for SSK01.09, SSK01.10, and SSK01.11 are minimal (less than 2 cm) due to the small levels of induced pore pressure (Figure 5.14). The numerical models also predict minimal deformations for these events, although the details in the deformation-time histories do not match with the centrifuge data. For shaking event SSK01.12, which induced significant pore pressures, the unit cell models predict significantly larger deformations than observed in the centrifuge model (50-85 cm vs. 8 cm).

The lack of horizontal deformation in the treated area of the SSK01 centrifuge model can be attributed to reinforcement of the slope. The model drains used in the SSK01 centrifuge model were constructed using a stiff nylon material. These drains were stiff enough such that their presence affected the response of the drain-treated slope, which was confirmed in the RNK01 centrifuge test (see Section 3.4.2). Given that the treated slope in the centrifuge model was reinforced by the presence of the stiff drains and the stiffness of these drains was not modeled in the numerical models, the treated 2D and 3D numerical models should undergo larger horizontal deformations than were observed in the centrifuge test. This difference was only noticeable for shaking event SSK01.12 because this was the only shaking event for which the treated numerical models reached an r_u of one over the entire depth of the model.

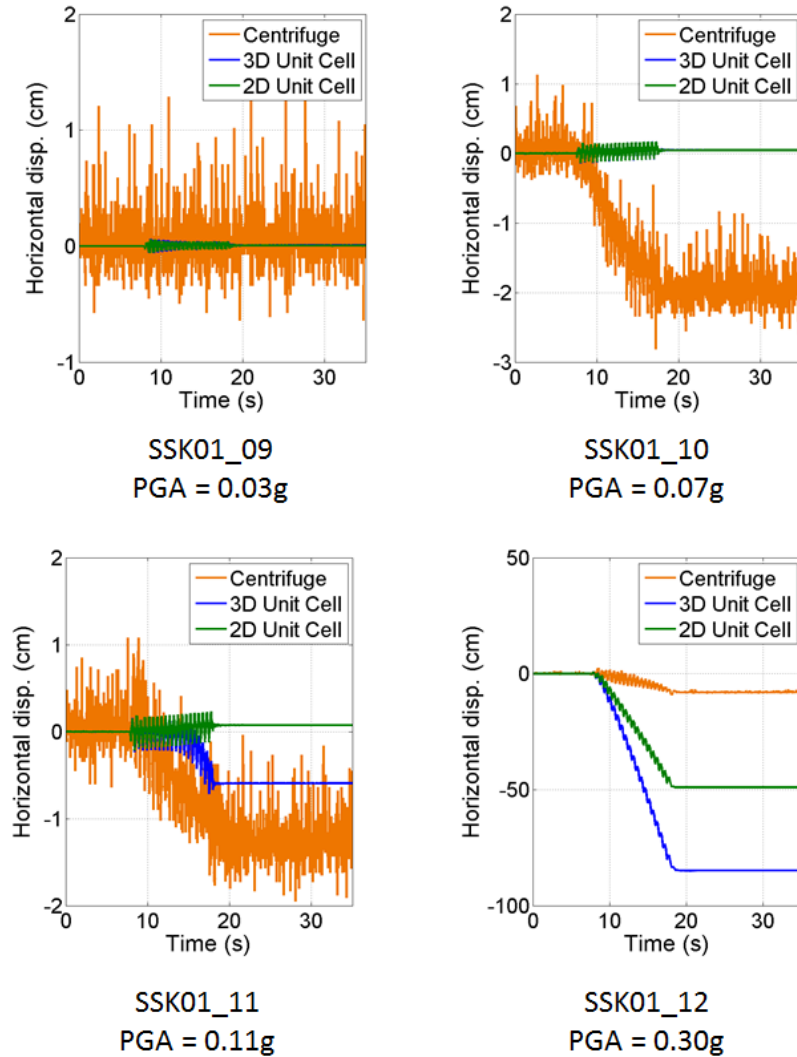


Figure 5.17: Horizontal displacement-time histories at the top of the clay layer for the treated 2D and 3D unit cell models and the treated area of the SSK01 centrifuge model for shaking events SSK01_09 (PGA = 0.11 g) through SSK01_12 (PGA = 0.3 g).

5.6 Comparison of Treated and Untreated Numerical Models

One important use of numerical modeling of soil improvement is the evaluation of improved performance. The treated and untreated unit cell models previously compared with the centrifuge data are now interpreted within the context of the predicted improvement in performance. The predicted level of improvement is compared with the observed level of improvement from the centrifuge tests.

Figure 5.18 shows the excess pore water-pressure time histories for the untreated and treated 3D unit cell models. It can be seen that for shaking events SSK01_09 through SSK01_11, the drains significantly reduce the peak excess pore water pressures. For shaking event SSK01_12, the peak excess pore water pressures are similar, but the pore pressures dissipate much more quickly in the treated unit cell model even though the untreated unit cell model is also allowed to drain through the clay crust at the end of shaking (vertical drainage only). The excess pore pressure-time histories for the SSK01_12 shaking event demonstrate that for very large shaking events, pore pressure dissipation towards a drain may not be fast enough to overcome the rate of pore pressure generation. Of course, this result depends on the drainage characteristics (i.e., c_v) of the sand. Nonetheless, even in these cases the shortened drainage paths and the horizontal drainage due to the presence of the drain facilitate the dissipation of excess pore water pressures.

Figure 5.19 shows the $\bar{r}_{u,\max}$ values as a function of PGA for the untreated and treated unit cell models and the untreated and treated areas of the SSK01 centrifuge model. As expected, the untreated condition experienced higher $\bar{r}_{u,\max}$

values than did the treated condition, for both the centrifuge data (Figure 5.19a) and the unit cell models (Figure 5.19b). This reduction holds true even for shaking event SSK01_12 (PGA = 0.30 g), in which the untreated and treated peak excess pore pressure values shown in Figure 5.18 for the unit cell models are similar. The reason for the difference between the untreated and treated $\bar{r}_{u,\max}$ values is illustrated in Figure 5.20. While the untreated and treated unit cell models have similar peak excess pore pressures, the \bar{r}_u values for the untreated unit cell model are higher than those for the treated unit cell model (Figure 5.20a and b). The smaller \bar{r}_u values in the treated unit cell model is a result of the timing of the peaks in the r_u -time histories. In the untreated unit cell model there are times when all of the r_u -time histories are at 1.0 (e.g., 15.0 to 15.1 s and 15.5 to 15.6 s in Figure 5.20c) and thus, \bar{r}_u is equal to 1.0. In the treated unit cell model (Figure 5.20d), each node spends less time at an $r_u = 1.0$ and the $r_u = 1.0$ peak is offset in time for each node, which lowers the overall average peak in the \bar{r}_u -time history.

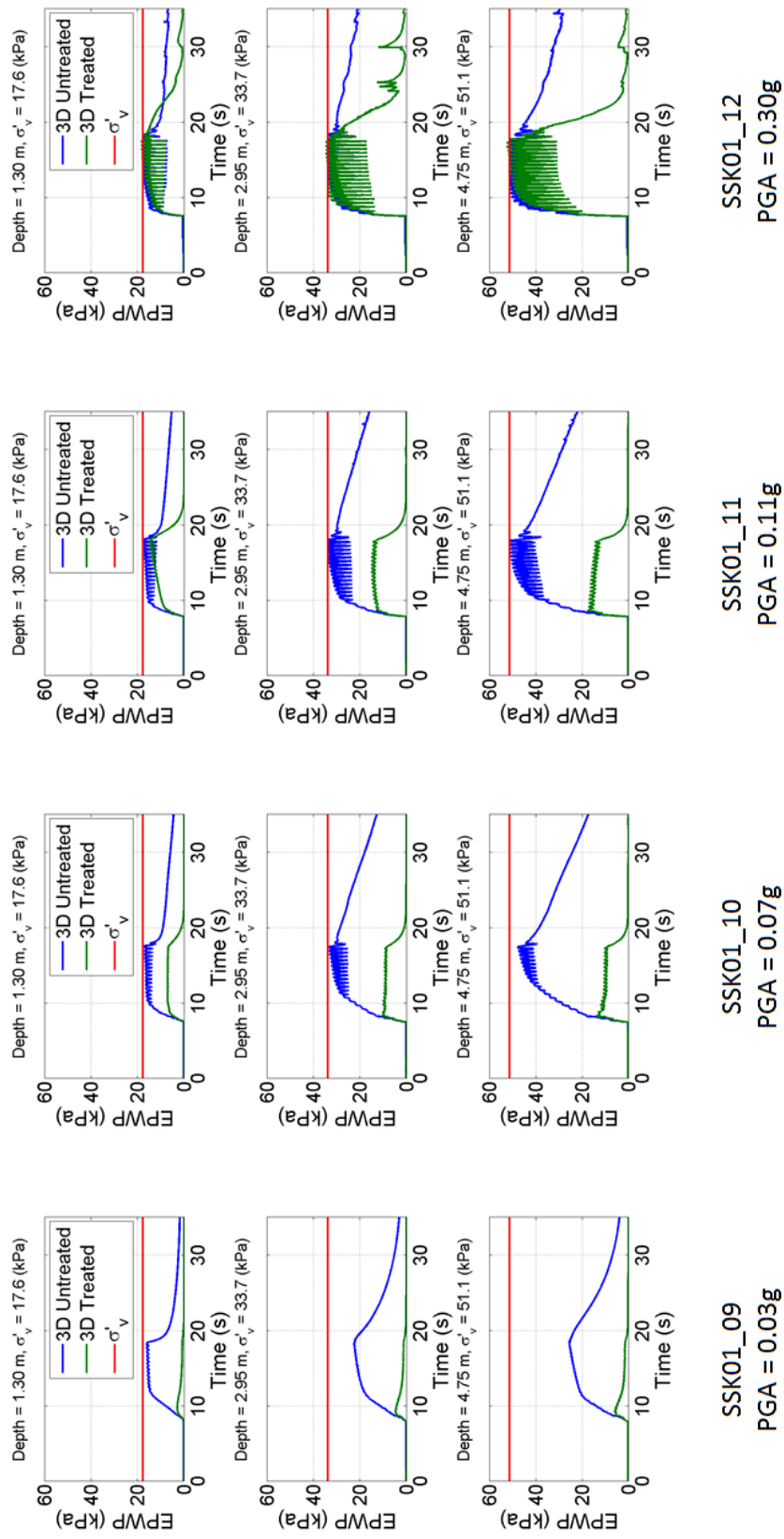
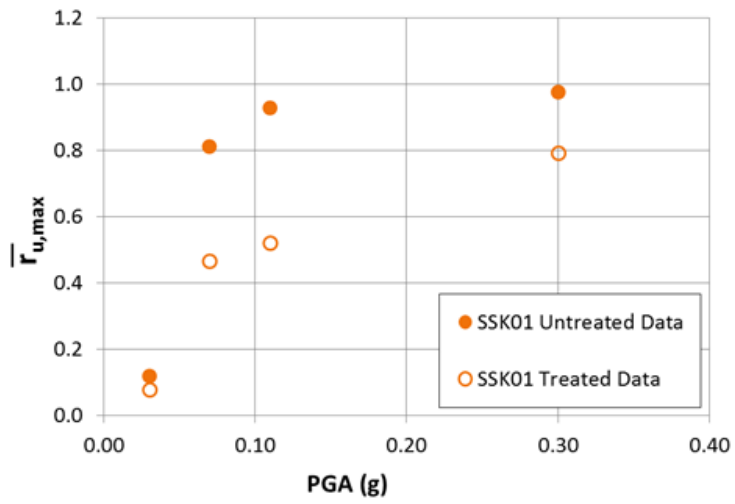
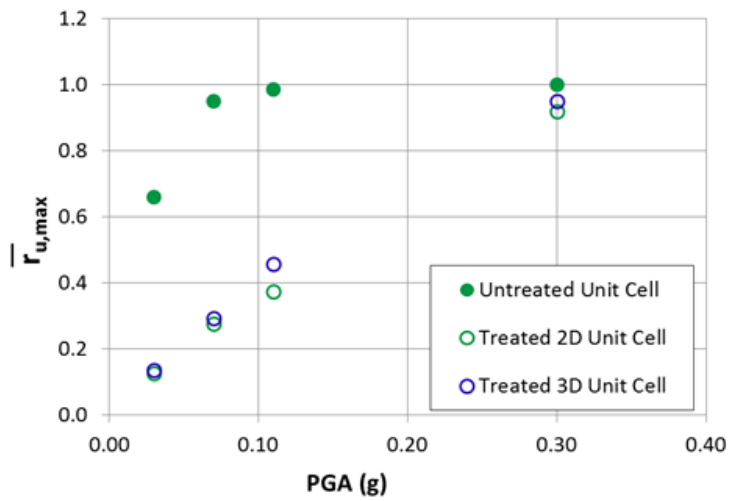


Figure 5.18: Excess pore water pressure-time histories for the untreated and treated 3D unit cell models at three different depths within the model for shaking events SSK01_09 (PGA = 0.11 g) through SSK01_12 (PGA = 0.3 g).



(a)



(b)

Figure 5.19: Peak average excess pore water pressure ($\bar{r}_{u,max}$) vs. PGA for (a) the untreated and treated unit cell models and (b) the untreated and treated areas of the SSK01 centrifuge model.

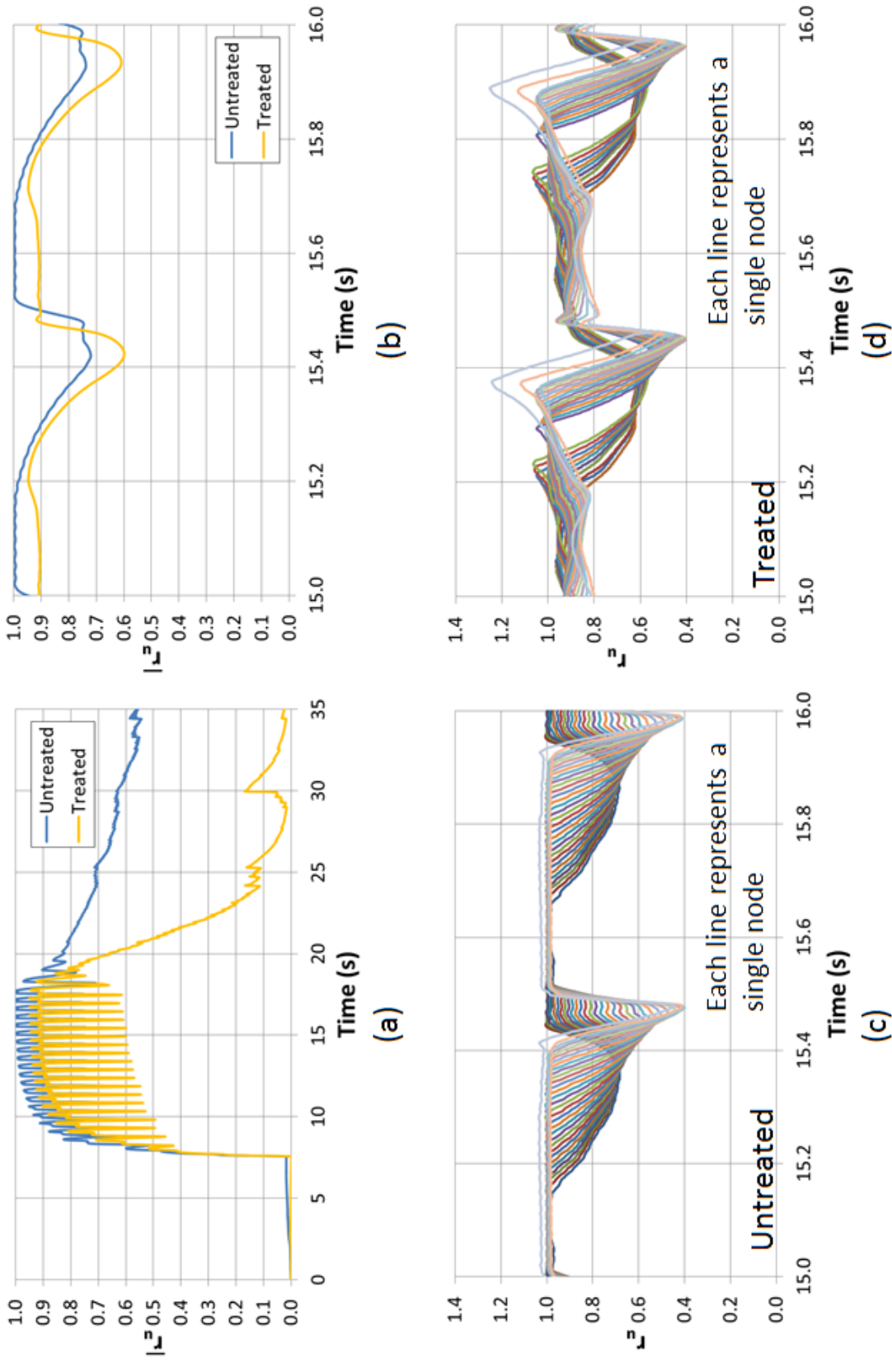


Figure 5.20: (a) \bar{r}_u vs. time for the untreated and treated unit cell models for SSK01_12, (b) Treated and untreated \bar{r}_u data for time = 15 to 16 s, (c) r_u data at every node along the vertical centerline of the untreated unit cell model for time = 15 to 16 s, (d) r_u data at every node along the upslope boundary of the treated unit cell model for time = 15 to 16 s.

Figure 5.21 shows the horizontal displacement-time histories at the top of the clay layer and the horizontal displacement vs. depth profiles at the end of shaking for the untreated and treated 3D unit cell models for shaking events SSK01.09 through SSK01.12. It can be seen that for all shaking events, the untreated horizontal displacements are significantly larger than the treated horizontal displacements. For SSK01.09 through SSK01.11, the treated deformations are essentially reduced to zero. For SSK01.12, the treated deformations are about 35% smaller than the untreated deformations, even though the untreated and treated $\bar{r}_{u,\max}$ values were similar. It should be noted that the horizontal deformations in both the untreated and treated unit cell models for shaking event SSK01.12 stop at the end of shaking ($t \sim 19$ seconds), so the difference in the horizontal deformations cannot be ascribed to the faster post-shaking pore pressure dissipation in the treated model. While the treated and untreated $\bar{r}_{u,\max}$ values were similar for SSK01.12, the treated values were computed at the edge of the area of influence for the drain. However, the the average r_u across the area of influence in the treated model would be smaller because the pore pressures are smaller near the drain (Figure 5.13). Because deformations are affected by the excess pore pressures across the entire area of influence, the deformations for the treated model are smaller.

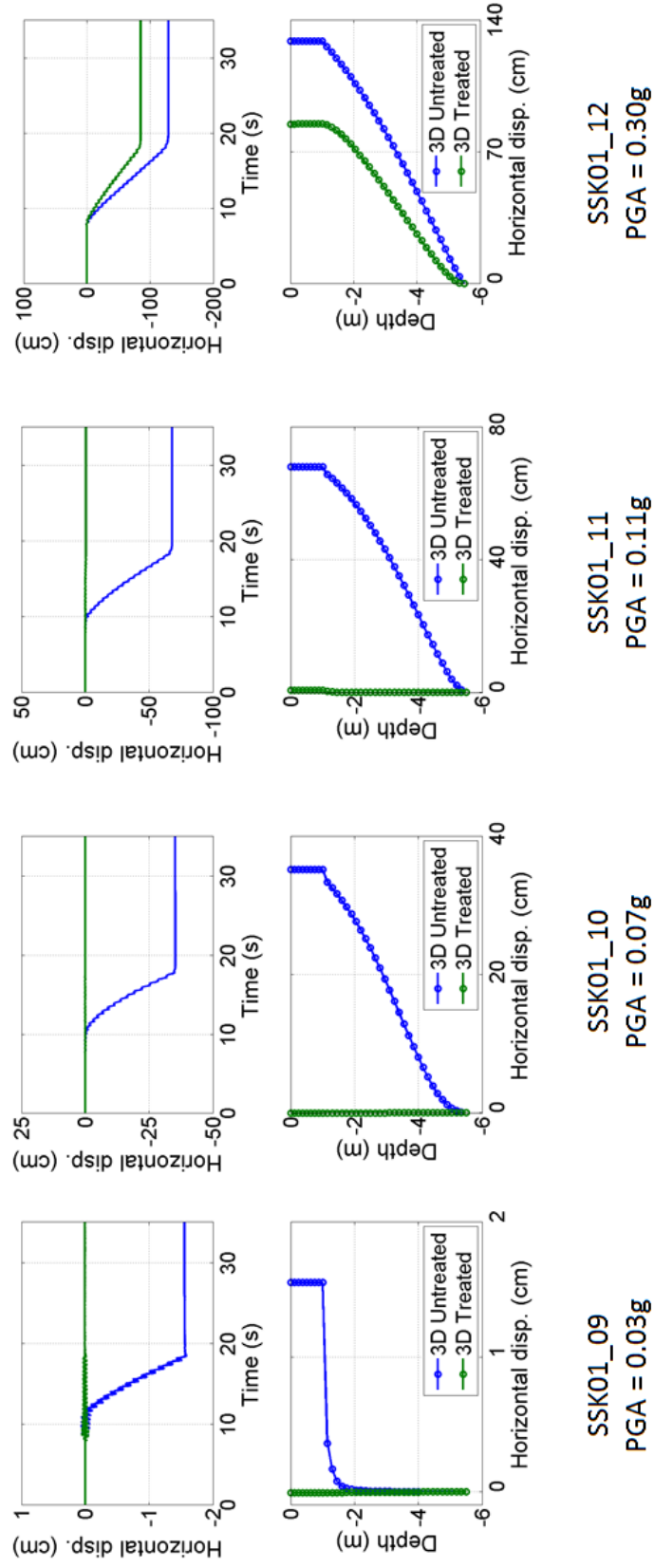


Figure 5.21: Horizontal displacement-time histories at the top of the clay layer and horizontal displacement vs. depth for the untreated and treated 3D unit cell models for shaking events SSK01_09 (PGA = 0.11 g) through SSK01_12 (PGA = 0.3 g).

Table 5.1 shows the percent improvement for each individual shaking event from the SSK01 centrifuge test. There were no deformations in either the treated or untreated slopes for shaking event SSK01_09 (PGA = 0.03 g). There were 86% and 96% reductions in the horizontal deformations for shaking events SSK01_10 (PGA = 0.07 g) and SSK01_11 (PGA = 0.11 g), respectively. There was only a 40% reduction in the horizontal deformations for shaking event SSK01_12 (PGA = 0.30 g), but the horizontal deformations for the untreated slope for this shaking event were not as large as would have been expected as a result of the deformations and flattening of the slope that occurred for the previous shaking events. Also note that the untreated deformations for SSK01_11 were larger than for SSK01_12, further bringing into question the untreated deformations for SSK01_12. Negating the SSK01_12 data, the average percent reduction in the horizontal deformations for the SSK01 model is $\sim 90\%$. However, these levels of improvement were influenced by the presence of the stiff drains.

Table 5.1 also shows the percent improvement in the horizontal deformations for 2D and 3D unit cell models for shaking events SSK01_09 (PGA = 0.03 g) through SSK01_12 (PGA = 0.30 g). The treated 2D and 3D unit cell models did not show any significant deformations for shaking events SSK01_09 through SSK01_11, and thus experienced 100% improvement. For shaking event SSK01_12, the percent reduction in the horizontal deformations is 62% for the 2D unit cell model and 34% for the 3D unit cell model. The larger percent improvement for the 2D unit cell model is due to the plane strain condition in which the drain acts as a wall drain and effectively reduces pore pressures over a larger volume than does the drain in the 3D model. While the improvements indicated for the unit cell models of SSK01_12 are similar to those from the centrifuge (particularly for the 3D unit

cell model), this agreement may simply be due to the fact that the SSK01.12 centrifuge deformations in the untreated area were influenced by flattening of the slope. The deformations in the untreated area were smaller than expected because of the flattening of the slope, making the untreated deformations more similar to those in the treated area and artificially decreasing the percent improvement. For this shaking event, the centrifuge showed about 40% improvement although the absolute levels of deformations were quite different from the numerical models.

Table 5.1: Untreated and treated horizontal deformations from centrifuge test SSK01 and the 2D and 3D unit cell models

Centrifuge Test				
Event	PGA (g)	Untreated (cm)	Treated (cm)	Improvement (%)
SSK01.09	0.01	0.0	0.0	N/A
SSK01.10	0.07	14.1	2.0	86
SSK01.11	0.11	29.9	1.3	96
SSK01.12	0.30	13.3	8.0	40
2D Unit Cell Models				
Event	PGA (g)	Untreated (cm)	Treated (cm)	Improvement (%)
SSK01.09	0.01	1.6	0.0	100
SSK01.10	0.07	32.8	0.0	100
SSK01.11	0.11	66.6	0.0	100
SSK01.12	0.30	129.0	49.1	62
3D Unit Cell Models				
Event	PGA (g)	Untreated (cm)	Treated (cm)	Improvement (%)
SSK01.09	0.01	1.6	0.0	100
SSK01.10	0.07	32.8	0.0	100
SSK01.11	0.11	66.6	0.6	99
SSK01.12	0.30	129.0	84.9	34

5.7 Summary

This chapter detailed the numerical simulations of the SSK01 centrifuge test and comparisons of the SSK01 simulation and experimental data. Simulations of the SSK01 shaking events were performed using untreated and drain-treated 2D and 3D unit cell models and the numerical data was analyzed with emphasis placed on identifying the behavioral trends related to pore pressure generation and dissipation and the development of horizontal deformations and comparing these trends to those observed in the centrifuge test.

The excess pore pressures in the untreated unit cell model were comparable to the centrifuge data with the exception of the data for SSK01_09. Through simulations performed using the full 2D model, it was shown that the centrifuge model produced much smaller excess pore pressures than the unit cell model for SSK01_09 as a result of the container effects. In comparison to the centrifuge data, the untreated unit cell models overpredict the horizontal deformations and underpredict the vertical settlements. This was shown to be due to differences in the unit cell and centrifuge model geometries. The untreated unit cell models do well in capturing the fundamental relationship between the intensity of shaking and the magnitudes of the pore pressure and deformation responses.

The hydraulic conductivity of the drain-treated 2D unit cell model was scaled to account for the differences between the 2D and 3D drainage conditions; however, there were minor differences in the 2D and 3D excess pore pressure data. Even with the scaling of the hydraulic conductivity, the 2D model had more drainage, and the difference between the 2D and 3D drainage conditions resulted in larger horizontal deformations in the 3D unit cell model. The pore pressure

data for the treated 3D unit cell model is comparable to the centrifuge data, particularly for the mid-range shaking events, which were used to calibrate the hydraulic conductivity of the model. Both the centrifuge model and the numerical models predict minimal horizontal deformations for shaking events SSK01_09 through 11. For SSK01_12, the treated 3D unit cell model predicts horizontal deformations that are significantly larger than those observed in the centrifuge test as a result of the infinite slope geometry, which lacks the passive resistance at the toe of the slope that was present in the centrifuge model.

In comparing the untreated and treated simulation data, the untreated models were shown to develop higher excess pore pressures and larger horizontal deformations than the treated models. SSK01_12 is the only shaking event in which the treated model underwent significant deformations. For this event, the percent reduction observed in the horizontal deformations for the centrifuge and numerical models was similar even though the experimental and simulation deformation data differed greatly in magnitude.

Chapter 6

Comparison of Numerical Models and Data from Centrifuge Test RNK01

6.1 Introduction

This chapter describes the results of the numerical simulations of centrifuge test RNK01. The SSK01 and RNK01 centrifuge models had the same geometry; thus, the unit cell models used to simulate RNK01 are identical to the models that were used to simulate SSK01. The primary differences between the RNK01 and SSK01 centrifuge tests were the non-draining tubes in the untreated area of the RNK01 model and the input motions. While the SSK01 centrifuge test had only sine wave input motions, the RNK01 centrifuge test had two different earthquake input motions (as described in Section 3.4.1). The numerical models will not be used to simulate the presence of the non-draining tubes in the RNK01 model;

therefore, the only difference between the RNK01 and SSK01 simulations is the input motions.

Simulations of shaking events PAC01 (PGA = 0.02 g) through PAC08 (PGA = 0.88 g), PSL01 (PGA = 0.01 g) through PSL07 (PGA = 0.88 g), SIN01 (PGA = 0.26 g), and SIN02 (PGA = 0.56 g) were performed using the untreated and drain-treated 2D and 3D unit cell models. The simulated excess pore pressure and deformation data is analyzed with emphasis given to identifying the behavioral trends that were observed in the experimental data. For many of the shaking events, the excess pore pressure and deformation response was not significant; therefore, the figures and discussions in this chapter will focus on the earthquake shaking events with $\text{PGA} > 0.4 \text{ g}$ (PAC06 through PAC08 and PSL06 and PSL07) and the two sine wave shaking events (SIN01 and SIN02).

6.2 Comparison of Untreated Numerical Models and Centrifuge Data

This section compares the excess pore pressure and deformation responses of the numerical models with the centrifuge data for the untreated condition. It was shown for the SSK01 simulations that the untreated 2D and 3D unit cell models have nearly identical excess pore pressures, thus, only one data set is shown for the untreated unit cell models when comparing the simulated and experimental pore pressure data.

Figure 6.1 shows the excess pore pressure-time histories for the untreated unit cell models and the untreated area of the RNK01 centrifuge model for the PAC06, PAC07, and PAC08 shaking events. For PAC06 and PAC07, the numerical models significantly overestimate the excess pore water pressures in comparison to the centrifuge data. For PAC08, the numerical models agree well with the centrifuge data for the first peak in the excess pore pressure-time histories (time ~ 8 s), but overestimate the excess pore pressures for the second peak (time ~ 12 s) near the base of the model. For pore pressures to be lower at time = 12 s than at time = 8 s, some drainage must have occurred in the untreated area of the centrifuge model. The untreated unit cell models are completely undrained until drainage is manually triggered at the end of shaking by increasing the hydraulic conductivity of the clay layer; therefore, it is not possible for the unit cell models to match the lower second excess pore pressure peak at time = 12 seconds.

Figure 6.2 shows the excess pore pressure-time histories for the untreated unit cell models and the untreated area of the RNK01 centrifuge model for the PSL06 and PSL07 shaking events. For PSL06, the numerical models again significantly overestimate the excess pore water pressures in comparison to the centrifuge data, particularly at mid-depth and near the base of the model. For PSL07, the the peak excess pore water pressures in the numerical models are similar to the peak excess pore water pressures from the centrifuge model, but the pore pressures at mid-depth and near the base of the numerical model reach their peak value several seconds earlier than in the centrifuge model, where the pore pressures increase more gradually at the start of shaking.

Figure 6.3 shows the excess pore pressure-time histories for the untreated unit cell models and the untreated area of the RNK01 centrifuge model for the SIN01 and SIN02 shaking events. For SIN01, the excess pore pressure data from the numerical models near the sand/clay interface and at mid-depth compares well with the centrifuge data, while the numerical model overestimates the excess pore pressures near the base of the model. For SIN02, the simulated data and the experimental data matches well at all depths. In general, the simulated and experimental data agree better for the sine wave motions than the earthquake motions.

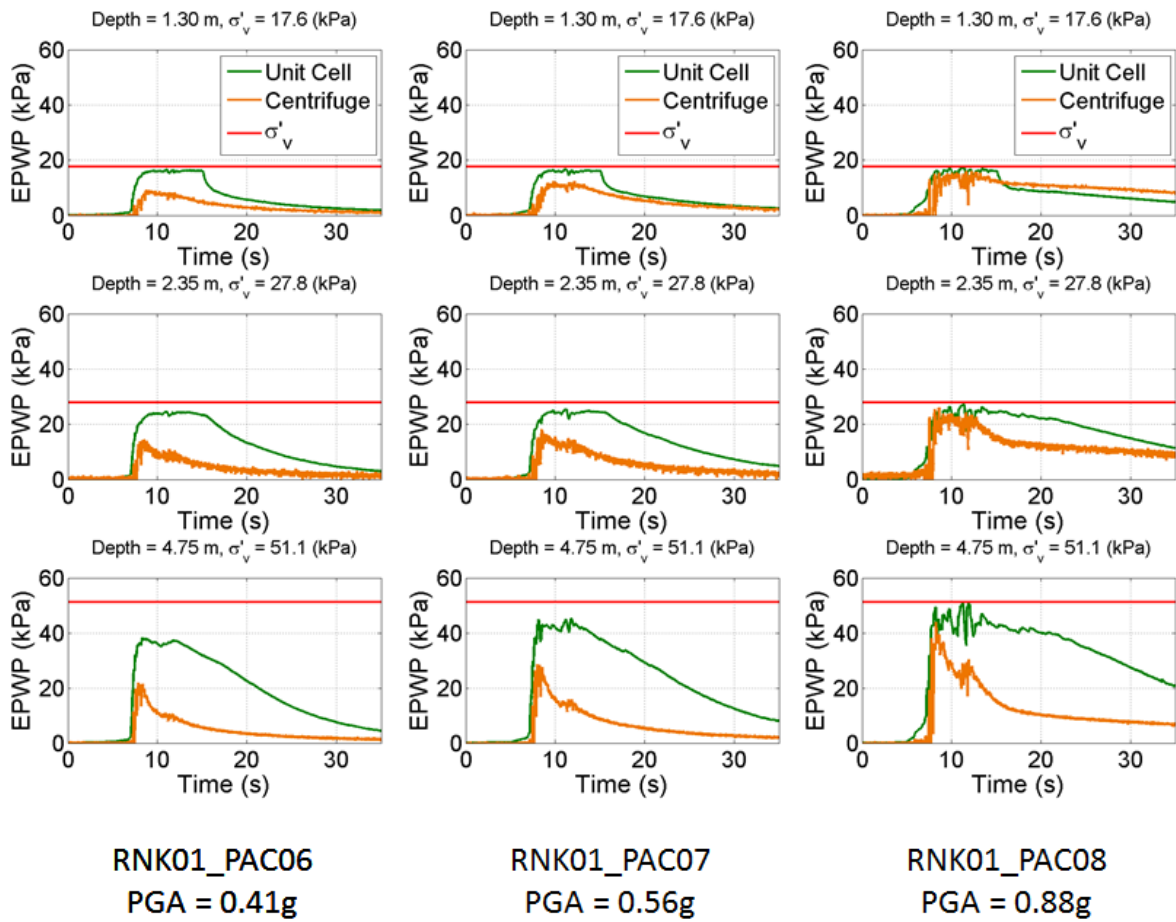


Figure 6.1: Excess pore water pressure-time histories for the untreated unit cell models and the untreated area of the RNK01 centrifuge model for shaking events RNK01_PAC06 (PGA = 0.41 g) through RNK01_PAC08 (PGA = 0.88 g).

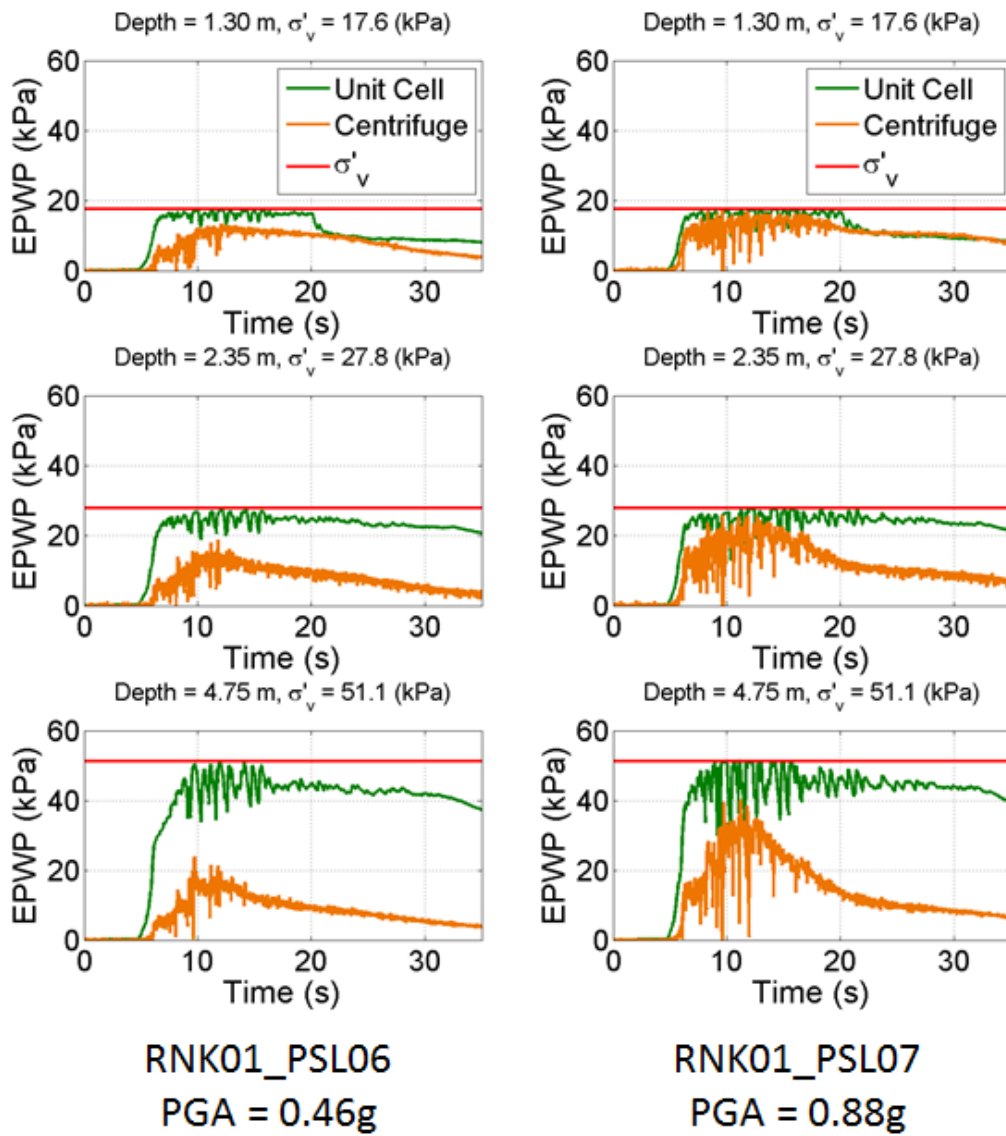


Figure 6.2: Excess pore water pressure-time histories for the untreated unit cell models and the RNK01 centrifuge model for shaking events RNK01_PSL06 (PGA = 0.46 g) and RNK01_PSL07 (PGA = 0.88 g).

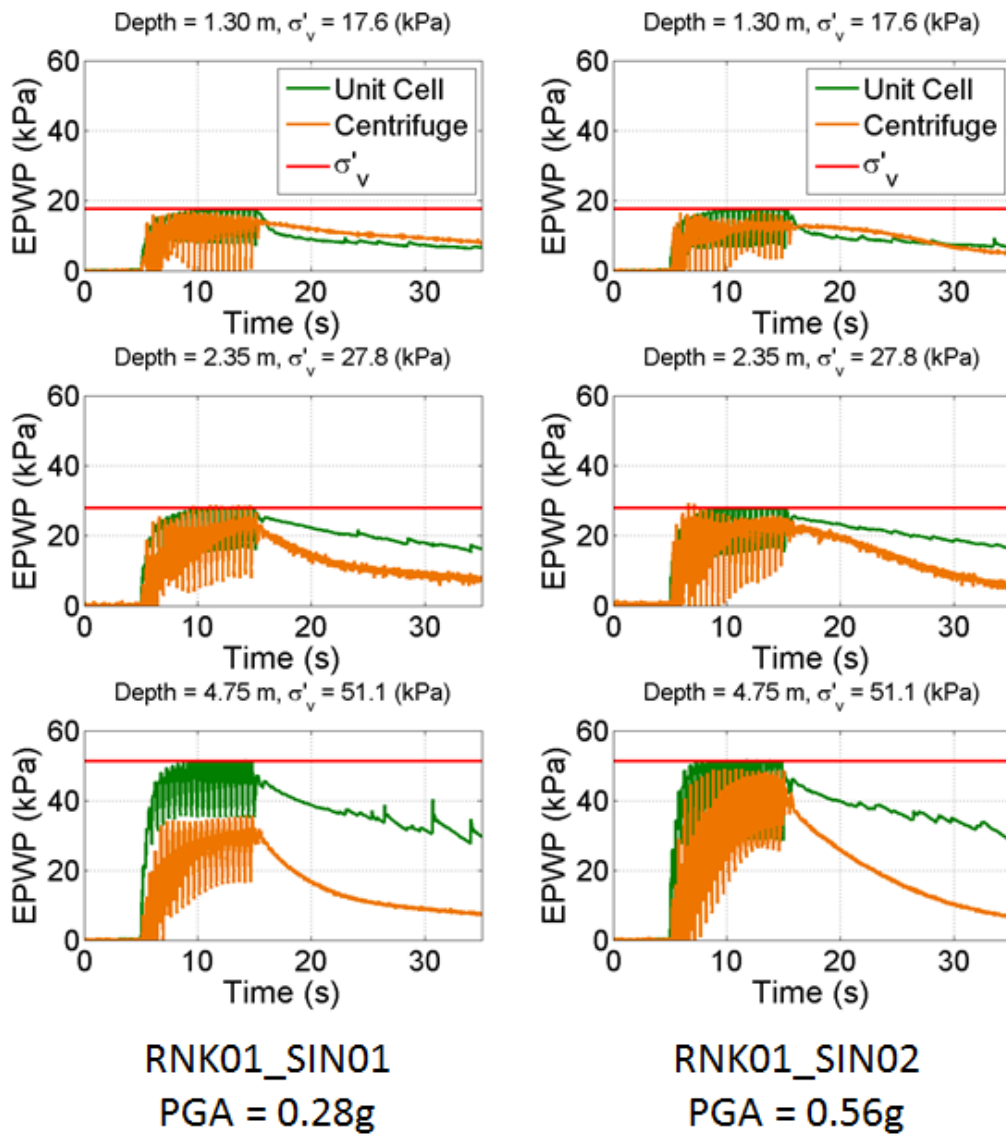


Figure 6.3: Excess pore water pressure-time histories for the untreated unit cell models and the RNK01 centrifuge model for shaking events RNK01_SIN01 (PGA = 0.28 g) and RNK01_SIN02 (PGA = 0.56 g).

There are two possible reasons for the differences between the simulated and experimental pore pressure data shown in Figures 6.1 through 6.3. First, the relative density of the lower half of the "loose" sand layer in the RNK01 centrifuge model was actually about 68% due to a problem with the box pluviator (Kamai et al., 2008). Second, excess pore pressures in the centrifuge model are affected by the presence of the centrifuge container, which reduces pore pressure generation resulting from low-intensity accelerations (see Section 5.3) and peak pore pressures near the base of the model (see Section 5.5). To study the effects of the centrifuge container and the relative density on the numerical data, the unit cell models and full 2D model were used to simulate the PAC06 shaking events using PDMY02 model parameters representative of sands at relative densities of 40%, 60%, and 75%. $D_R = 40\%$ corresponds to the parameters already being used for the simulated sand. For the $D_R = 60\%$ and 75% simulations, the recommended parameters provided by Yang et al. (2008) were used. All three parameter sets, as well as the resulting cyclic resistances from simulated cyclic simple shear tests, are summarized in Table 6.1. Increasing the relative density, results in increases in the shear wave velocity and the soil's resistance to liquefaction. The $D_R = 40\%$ sand has a shear wave velocity of 139 m/s and will liquefy in 10 cycles of motion at a CSR of 0.158. The $D_R = 75\%$ sand has a much higher shear wave velocity at 178 m/s and at 10 cycles of motion a CSR of 1.08 is required to trigger liquefaction.

Table 6.1: PDMY02 model parameters for sands at relative densities of 40%, 60%, and 75%.

Parameter	$D_R = 40\%$	$D_R = 60\%$	$D_R = 75\%$
ρ (ton/m ³)	1.99	2.00	2.10
G_r (kPa)	7.5e4	11.0e4	13.0e4
B_r (kPa)	20.e4	24.e4	26.e4
ϕ (deg)	32.0	35.0	36.5
ϕ_{PT} (deg)	26	26	26
α_1	0.057	0.028	0.013
α_3	0.23	0.05	0.00
β_1	0.06	0.10	0.30
β_3	0.27	0.05	0.00
e	0.80	0.65	0.55
$V_{s,1}$ (m/s)	139	166	178
CRR at 10 cycles	0.158	0.26	1.08
CRR at 20 cycles	0.099	0.13	0.44

Figure 6.4 compares the pore pressure results from the full 2D model with the results from the unit cell and centrifuge models for PAC06. Results are shown for simulations with $D_R = 40\%$, 60% , and 75% . It can be seen in Figure 6.4 that the peak excess pore pressures near the base of the full 2D model compare well with the centrifuge data; however, the peak excess pore pressures at mid-depth and near the sand/clay interface are still slightly higher than in the centrifuge model. When the relative density of the simulated sand in the unit cell models and the full 2D model is increased to 60% , the peak excess pore pressures decrease slightly for both the unit cell models and the full 2D model and the match between the centrifuge data and the full 2D model data improves slightly. When the relative

density is increased to 75%, the peak pore pressures for both the unit cell models and the full 2D model agree well with the centrifuge data at all three depths.

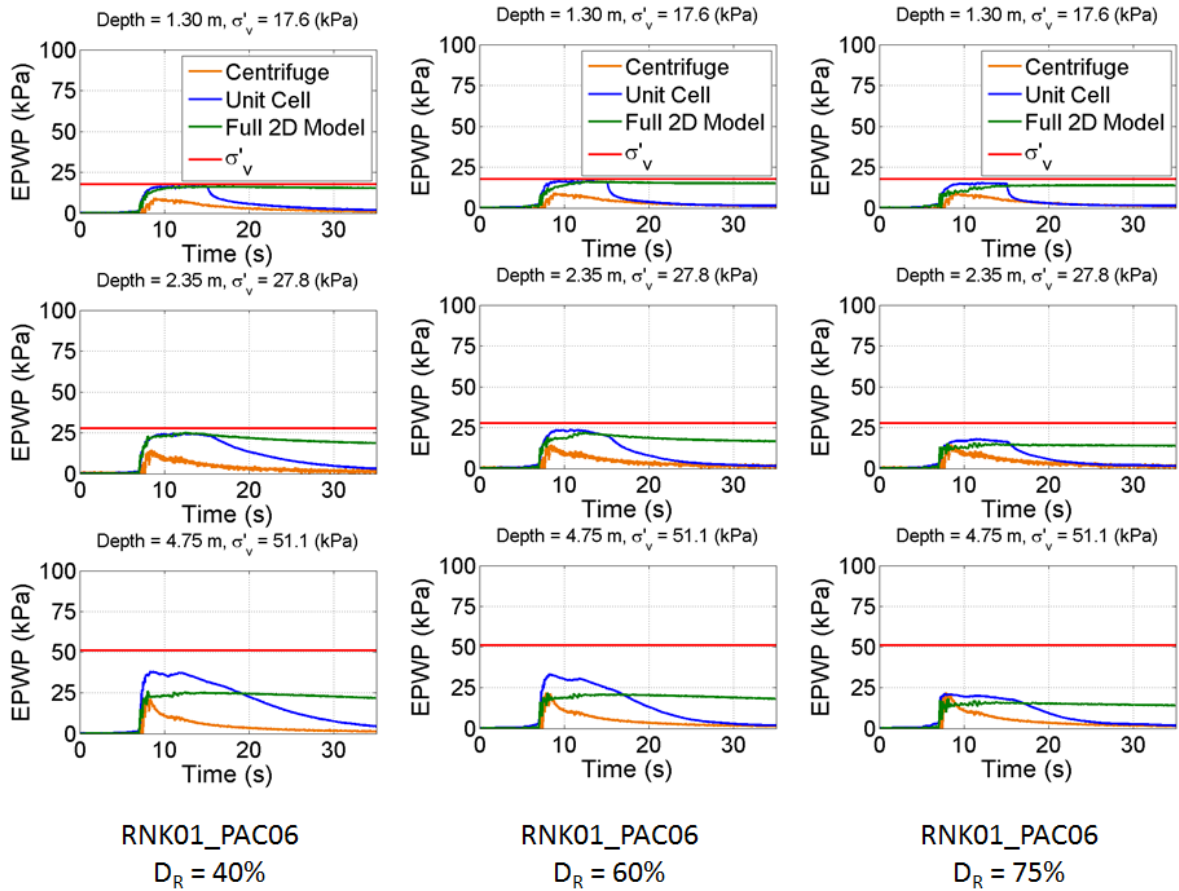
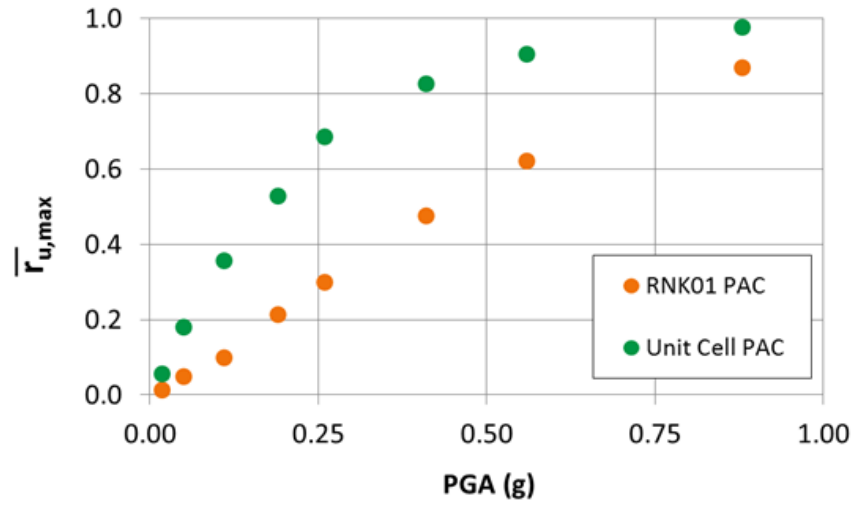


Figure 6.4: Excess pore water pressure-time histories for the untreated unit cell models, the full 2D model, and the RNK01 centrifuge model for shaking event RNK01_PAC06 ($PGA = 0.41 g$) for $D_R = 40\%$, 60% , and 75% .

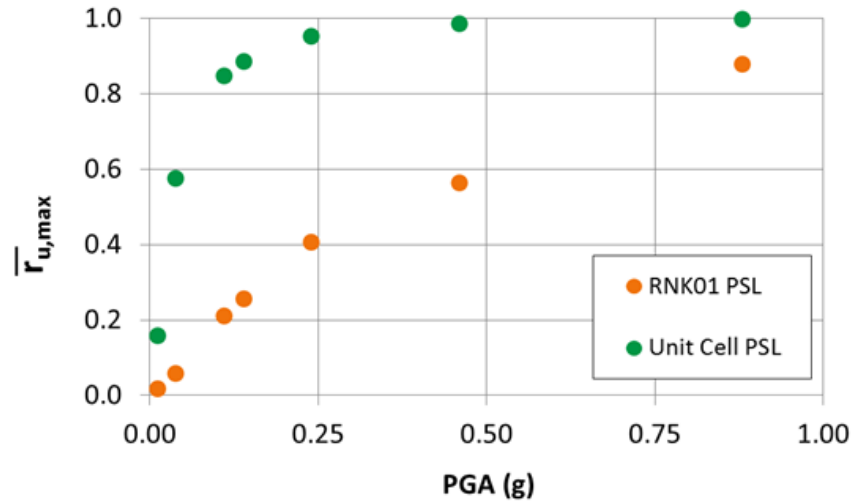
It should be noted in Figure 6.4 that the excess pore pressures at shallow depths reach an r_u of nearly 1.0 for all three relative densities. This behavior is not consistent with the results expected based on the CRR data for these simulated sands. The PAC06 motion with $PGA = 0.41g$ is estimated to induce a CSR between 0.2 and 0.3 ($CSR = 0.65 * \frac{\sigma_v}{\sigma'_v} * PGA * rd$, where $rd = 0.9$). For CSRs of 0.2 to 0.3 and a σ'_v of 18 kPa (i.e., the vertical effective stress at 1.30 m depth), the cyclic simple shear simulation for $D_R = 75\%$ predicts that 28 to 32 cycles of motion would be needed to reach an r_u of 0.95. Even at a larger CSR of 0.4, the simulations predict 23 cycles of motion to trigger liquefaction in the $D_R = 75\%$ sand. In Figure 6.4, the $D_R = 75\%$ model reaches an r_u of nearly 1 within 2-3 cycles. This result is caused by the vertical migration of pore water from the base of the model to the sand/clay interface. When vertical drainage is stopped by assigning $k = 1.e-10$ m/s to the sand, an r_u of 0.4 to 0.5 is reached in the first 2 to 3 cycles and the peak r_u is reduced to about 0.7. This agrees well with the simple cyclic shear data for the $D_R = 75\%$ sand, which predicts an r_u of 0.5 in 2 to 3 cycles and an r_u of 0.7 in 6 to 7 cycles of loading.

In addition to being overly dense, the sand layer in the RNK01 centrifuge model was also reinforced by the stiff drains/tubes, which were found in both the treated and untreated areas. The horizontal displacements in the untreated area of the RNK01 centrifuge model were less than 1 cm for all but the highest intensity PAC and PSL motions ($PGA = 0.88$ g) and the two sine wave motions. Due to the lack of horizontal deformations in the RNK01 centrifuge model, a comparison of the simulated and experimental untreated deformations will not be included in this discussion.

Figure 6.5 shows the peak average excess pore water pressures ($\bar{r}_{u,\max}$) as a function of PGA for the untreated unit cell models for the PAC and PSL shaking events. It can be seen in Figure 6.5 that the $\bar{r}_{u,\max}$ values for both the untreated unit cell models and the RNK01 centrifuge model increase with increasing PGA up to a maximum $\bar{r}_{u,\max}$ of 1.0. However, for both PAC and PSL, the numerical models reach $\bar{r}_{u,\max} = 1.0$ at smaller intensity motions than the centrifuge data. Additionally, the relationship is different for different input motions. For example, the 0.26 g PAC event results in smaller $\bar{r}_{u,\max}$ values than the 0.04 g PSL event. This result demonstrates the importance of the ground motion characteristics on the pore pressure response.



(a)



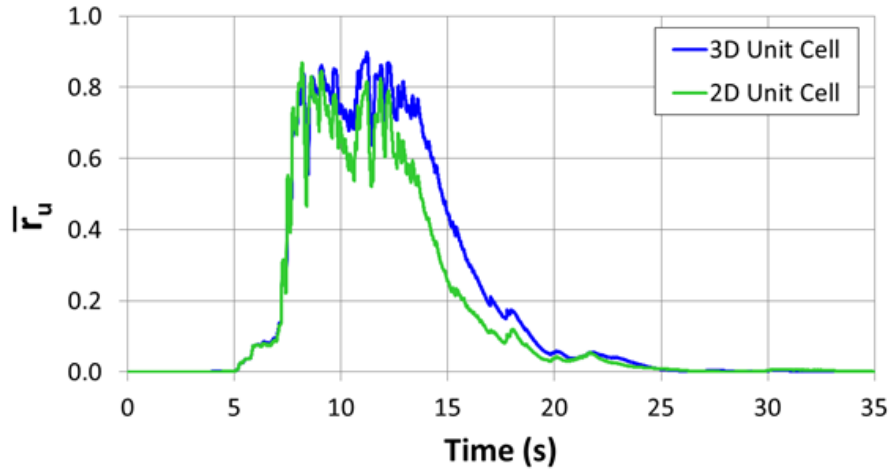
(b)

Figure 6.5: Peak average excess pore water pressures ($\bar{r}_{u,max}$) vs. PGA for the untreated unit cell models and the untreated area of the RNK01 centrifuge model for (a) the PAC and (b) the PSL motions.

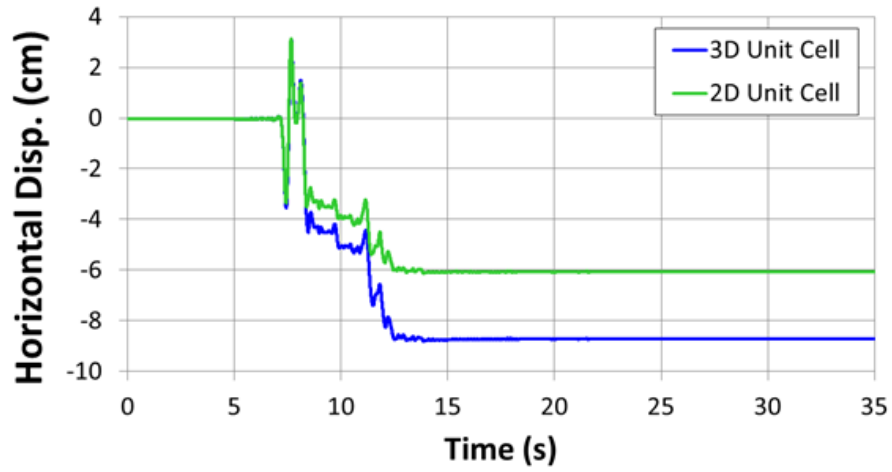
6.3 Comparison of the Treated 2D and 3D Unit Cell Models

It was shown for the SSK01 simulations that the 2D unit cell models drain more effectively than the 3D unit cell models, which results in smaller horizontal deformations. This is illustrated again in Figure 6.6 for the RNK01_PAC08 shaking event. The average excess pore pressure (\bar{r}_u) - time histories for the treated 2D and 3D unit cell models are shown in Figure 6.6a. It can be seen that the 2D and 3D data are similar up until about time = 8 seconds, at which point the difference in the 2D and 3D pore pressure dissipation becomes evident. For the remainder of significant shaking, the pore pressures in the 2D model are lower than the pore pressures in the 3D model. The smaller pore pressures for the 2D model at times greater than 8 seconds, leads to a smaller rate of deformation accumulation for the 2D model over this time interval (Figure 6.6b).

Table 6.2 summarizes the horizontal deformations for the treated 2D and 3D unit cell models for the RNK01 simulations. For PAC06 and PAC07, the differences between the 2D and 3D horizontal deformations are minor (less than 5%) because the induced pore pressures are relatively small ($\bar{r}_{u,\max} < 0.7$). For PAC08 and the PSL and SIN motions, the 3D horizontal deformations are 30 to 55% larger. These motions induced larger pore pressures ($\bar{r}_{u,\max} > 0.9$), such that the slower drainage in the 3D models lead to more deformation.



(a)



(b)

Figure 6.6: (a) Average excess pore pressure (\bar{r}_u)-time histories and (b) Horizontal deformation time histories for the treated 2D and 3D unit cell models for shaking event RNK01_PAC08 (PGA = 0.88 g).

Table 6.2: Treated 2D and 3D horizontal deformations from centrifuge test RNK01 for shaking events with a PGA greater than 0.4 g.

Motion	PGA (g)	$\bar{r}_{u,\max}$	2D Model (cm)	3D Model (cm)	2D/3D
PAC06	0.41	0.60	0.7	0.7	0.97
PAC07	0.56	0.69	1.2	1.3	0.96
PAC08	0.88	0.90	6.1	8.7	0.70
PSL06	0.46	0.92	8.7	18.9	0.46
PSL07	0.88	0.98	32.3	53.6	0.60
SIN01	0.28	0.95	46.1	77.5	0.59
SIN02	0.56	0.96	85.2	122.9	0.69

Because the drainage conditions in the treated 3D unit cell model more accurately reflect the drainage conditions that existed in the centrifuge tests and the drainage conditions that would exist in the field, the 3D unit cell pore pressure and deformation responses will be used for the remaining discussions in this section. No further comparisons involving the treated 2D unit cell data will be shown.

6.4 Comparison of Treated Numerical Models and Centrifuge Data

Figures 6.7 through 6.9 show the excess pore water pressure-time histories for the treated 3D unit cell model and the treated area of the RNK01 centrifuge model at three different depths for the shaking events with $PGA > 0.4$ g. For the PAC shaking events (Figure 6.7), the 3D unit cell model has peak excess pore pressures that are similar to the centrifuge data for the initial cycle of loading, but they are larger than the centrifuge data thereafter. For the PSL and SIN shaking events (Figures 6.8 and 6.9, respectively), the 3D unit cell model overestimates the peak excess pore pressures, particularly at mid-depth and near the base of the model.

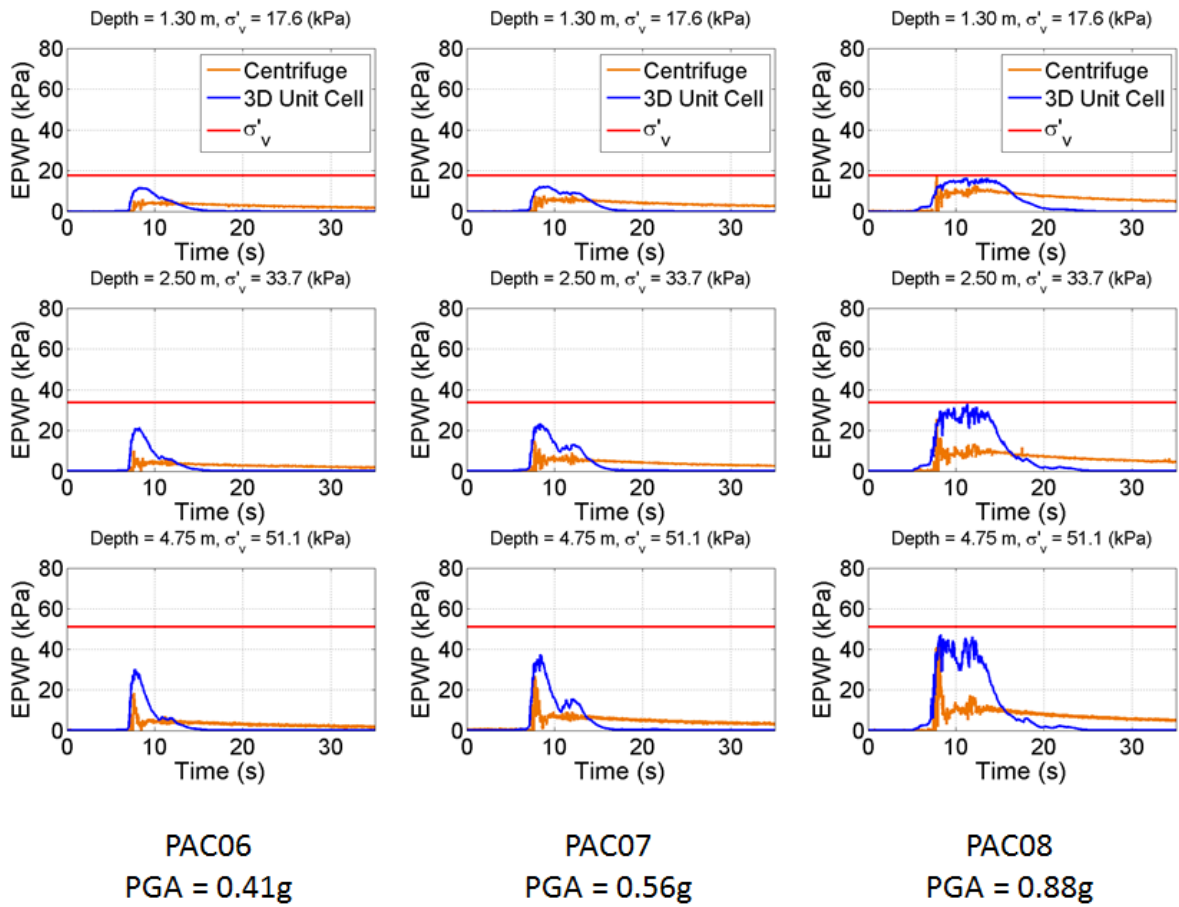


Figure 6.7: Excess pore water pressure-time histories for the treated 3D unit cell model and the treated area of the RNK01 centrifuge model at three different depths for shaking events PAC06 (PGA = 0.41 g) through PAC08 (PGA = 0.88 g).

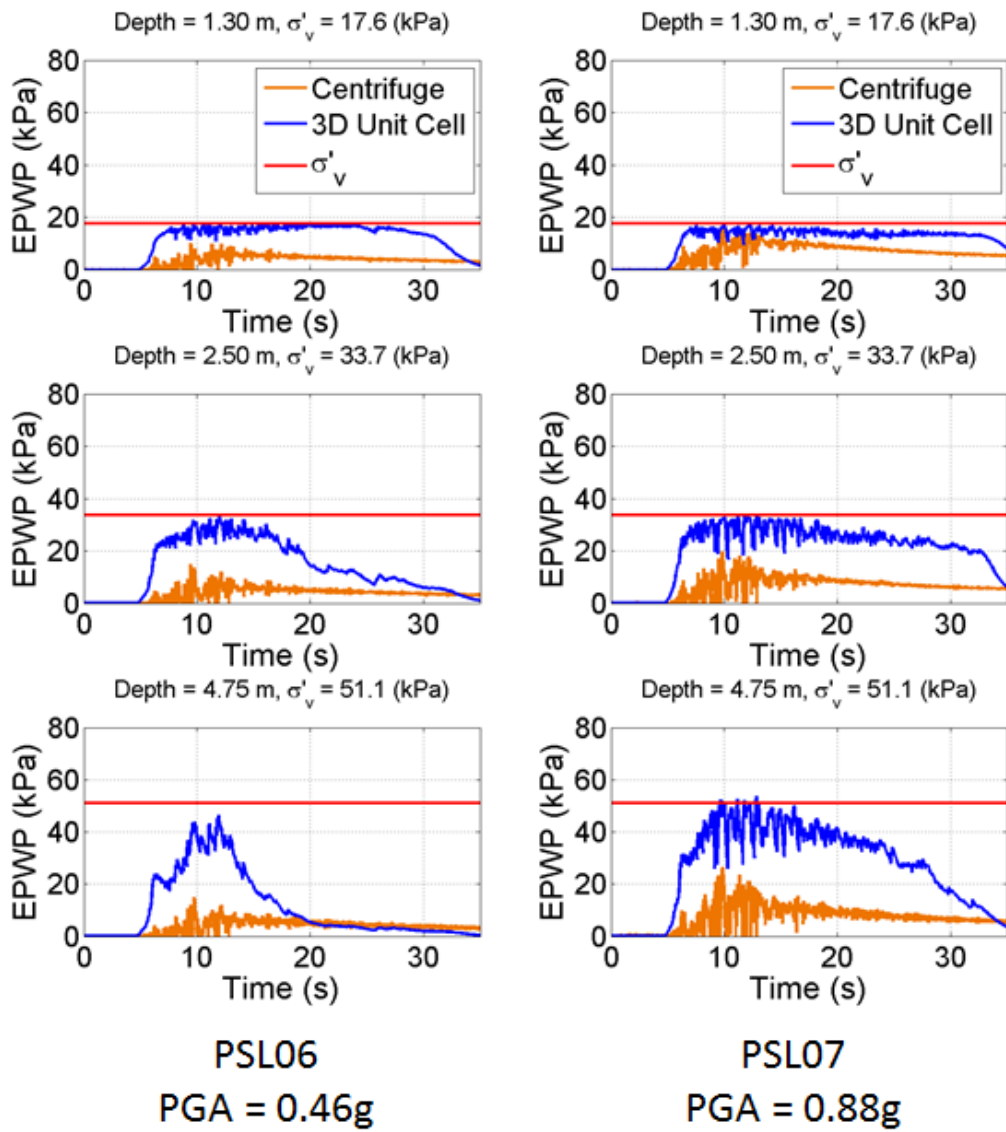


Figure 6.8: Excess pore water pressure-time histories for the treated 3D unit cell model and the treated area of the RNK01 centrifuge model at three different depths for shaking events PSL06 (PGA = 0.46 g) and PSL07 (PGA = 0.88 g).

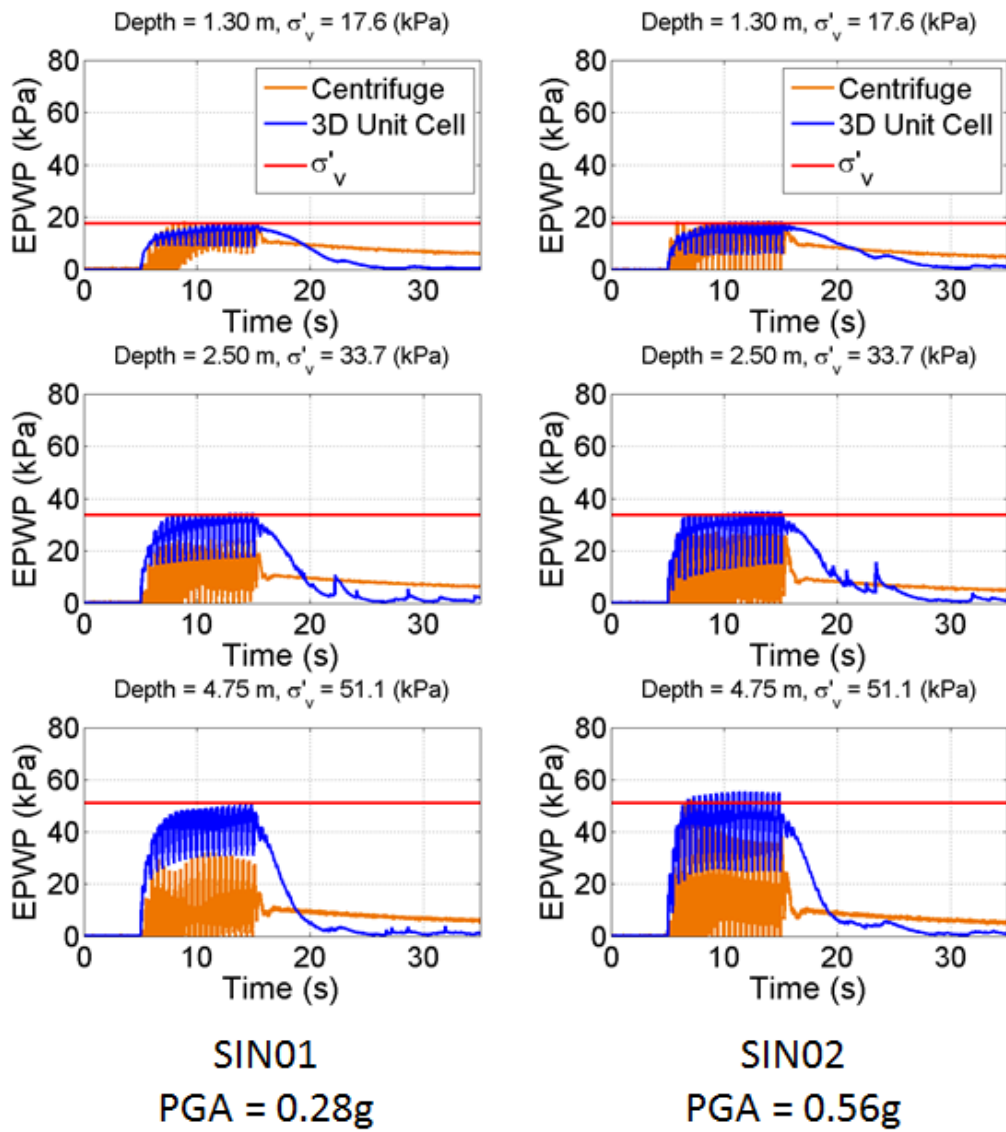


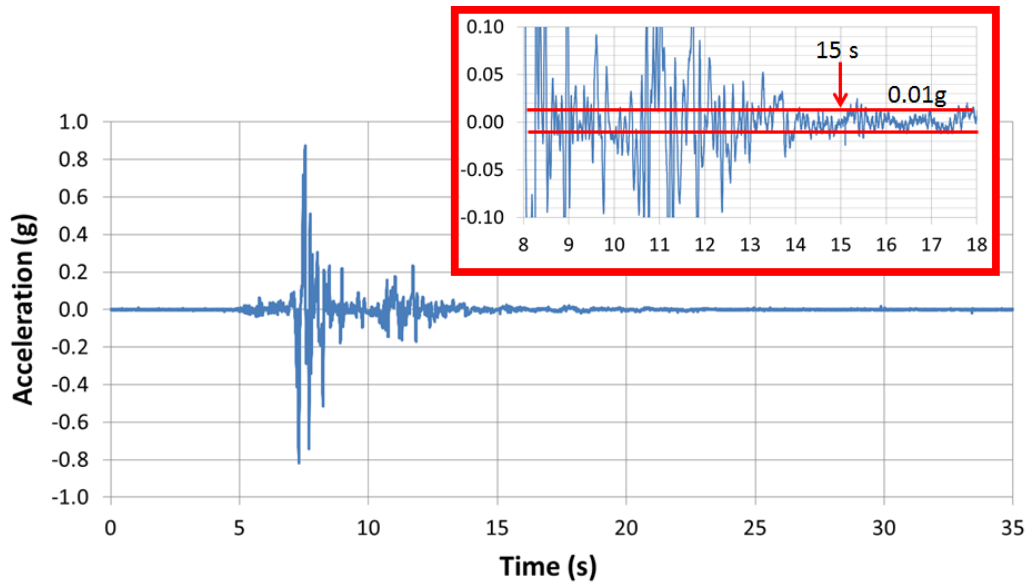
Figure 6.9: Excess pore water pressure-time histories for the treated 3D unit cell model and the treated area of the RNK01 centrifuge model at three different depths for shaking events SIN01 (PGA = 0.28 g) and SIN02 (PGA = 0.56 g).

An interesting feature for the PAC08 and two PSL shaking events (Figures 6.7 and 6.8) is that the excess pore pressures near the sand/clay interface remain elevated well beyond the end of significant shaking. For PAC, significant shaking ends at about 8 seconds, but pore pressures remain elevated until 15 seconds. For PSL, significant shaking ends at about 13 seconds but pore pressures remain elevated until about 30 to 35 seconds. The levels of shaking immediately before drainage initiates (i.e., 8-15 s for PAC, 13-30 s for PSL) in the numerical models are very small (< 0.05 g, Figure 6.10) and the rate of pore pressure generation should be small enough for the rate of pore pressure dissipation to take over and significant drainage to occur. However, dissipation does not fully develop until the input accelerations fall below ~ 0.01 g for these events (Figure 6.10). This effect was not observed in the SIN motions because the SIN motions end abruptly rather than tapering off gradually, and the acceleration levels immediately drop to < 0.005 g when shaking ends.

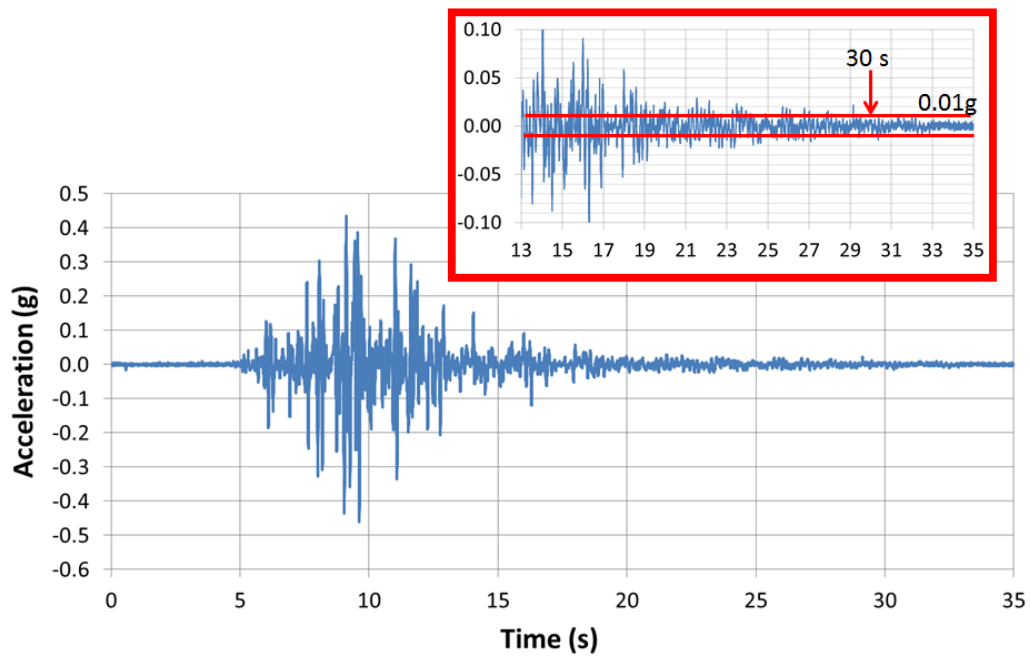
To investigate the effects of the low-level accelerations, the 2D unit cell model was analyzed for the PSL06 input motion with the low-level accelerations removed from the input acceleration-time history starting at time = 21 seconds. Under these conditions, the excess pore pressures in the treated unit cell models start to dissipate quickly at $t = 21$ seconds (Figure 6.11a). These results indicate that pore pressure generation in the PDMY02 model is sensitive to low levels of shaking the stress path is near the failure surface. This issue with PDMY02 is magnified when using a unit cell model because the centrifuge container and the influence of its inertia are not included such that low levels of acceleration are fully transmitted to the soil elements. When the PSL06 input motion is simulated using the full 2D model, drainage begins much earlier at around time =

18 seconds (Figure 6.11b) because the container effectively damps out the low-level accelerations.

Figure 6.12 shows the stress paths near the sand/clay interface for the PAC08 and PSL06 shaking events. For each event, the 2 to 3 seconds before the start of significant pore pressure dissipation have been highlighted in red, and the first 2 to 3 seconds of significant pore pressure dissipation have been highlighted in blue. For both events, in the seconds before the start of significant pore pressure dissipation the stress paths stay near the origin and do not show the effects of drainage, indicating that the rate of pore pressure generation is similar to the rate of drainage. This rate of pore pressure generation is not generally expected for such small levels of excitation. If the hydraulic conductivity of the sand is increased, this issue is minimized because the drainage rate starts to exceed the rate of pore pressure generation.



(a)



(b)

Figure 6.10: Input acceleration-time history for (a) the RNK01_PAC08 shaking event and (b) the RNK01_PSL06 shaking event.

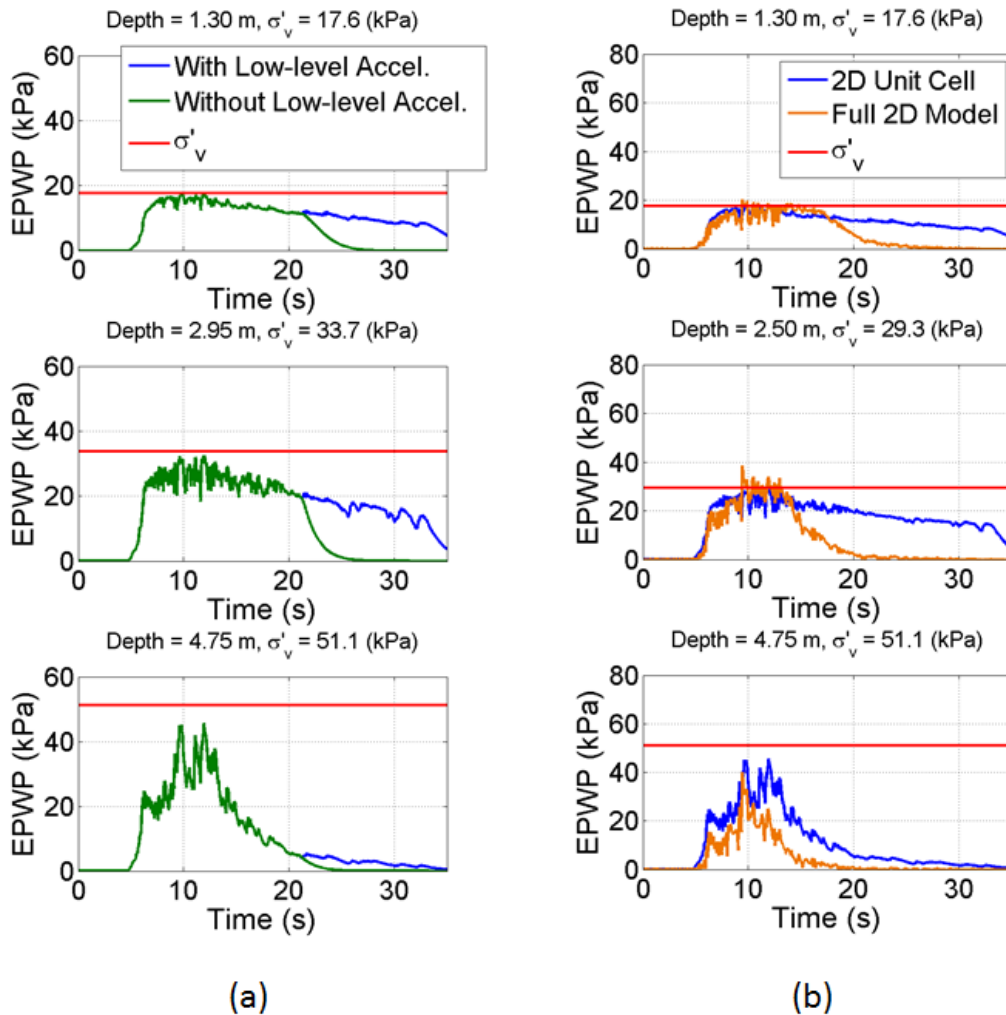


Figure 6.11: Excess pore pressure-time histories at three different depths for (a) the treated 2D unit cell model for the PSL06 shaking event with and without low-level accelerations in the input motion, and (b) the treated 2D unit cell model and the full 2D model for the PSL06 shaking event.

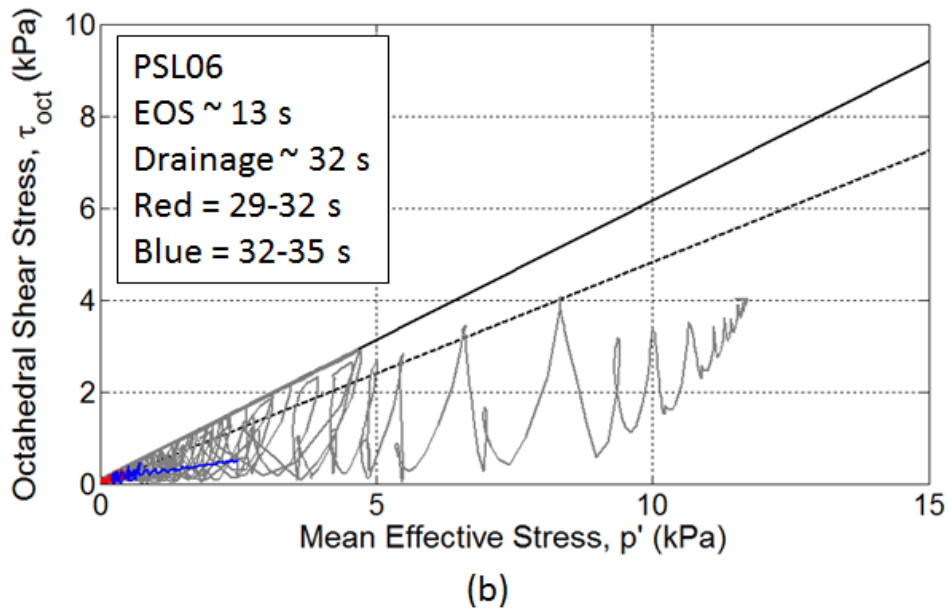
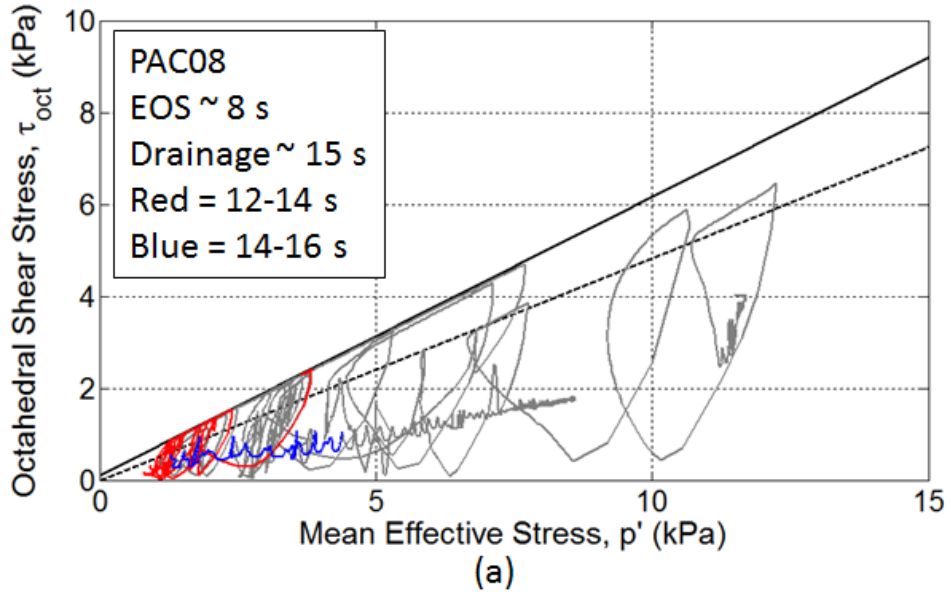


Figure 6.12: Octahedral shear stress (τ_{oct}) vs. mean effective stress (p') for (a) PAC08 and (b) PSL06.

As was discussed in Section 6.2 for the untreated condition, the pore pressures in the RNK01 centrifuge model were affected by the presence of the centrifuge container and the increased relative density of the liquefiable sand layer. The influence of these factors on the treated condition are evaluated through 3D unit cell and 2D full model analyses with PDMY02 parameters for $D_R = 40$ and 75%. Again, the parameters suggested by Yang et al. (2008) for a $D_R = 75\%$ sand were used for the simulations (Table 6.1). Figure 6.13 shows the excess pore water pressure-time histories for these analyses for shaking events PAC06 (PGA = 0.41 g) and PSL06 (PGA = 0.46 g). It can be seen in Figure 6.13 that for PAC06, the presence of the container reduces the peak excess pore pressures near the base of the model for the $D_R = 40\%$ simulations. At mid-depth and near the sand/clay interface, there are some minor differences in how quickly the models drain, but the peak excess pore pressures are the same for both the 3D unit cell model and the full 2D model. Both models overestimate the peak excess pore pressures in comparison to the centrifuge data. When the relative density is increased to 75%, the peak excess pore pressures at all three depths for both the 3D unit cell model and the full 2D model agree well with the centrifuge data. For the PAC06 shaking event, the effects of the relative density are more critical than the effects of the container.

For the PSL06 shaking event, the presence of the container has a significant effect on the excess pore pressure-time histories at all three depths for the $D_R = 40\%$ simulations. In the 3D unit cell model, the excess pore pressures at mid-depth and near the sand/clay interface remain elevated well after significant shaking has ended at time = 19 seconds. Again, this effect is due to the model's sensitivity to low acceleration levels when the stress path is near the failure surface. In the

full 2D model, the mass of the centrifuge container and its associated inertia dampen out the low-intensity accelerations, which in turn reduces the pore pressure generation. Thus, the pore pressures in the full 2D model are able to fully dissipate at the end of shaking. However, these drainage differences do not affect the peak excess pore pressures that develop during shaking; both the 3D unit cell model and the full 2D model overestimate the peak excess pore pressures at all three depths shown when model parameters for $D_R = 40\%$ are used. When the relative density is increased to 75%, the peak excess pore pressures at all three depths for both the 3D unit cell model and full 2D model compare better with the centrifuge data. Additionally, the effects of the container are still evident near the sand/clay interface as the pore pressures in the full 2D model dissipate more quickly than in the 3D unit cell model. For the PSL06 shaking event, the effects of the container are significant, but in terms of matching the centrifuge data, the relative density is again the most critical factor.

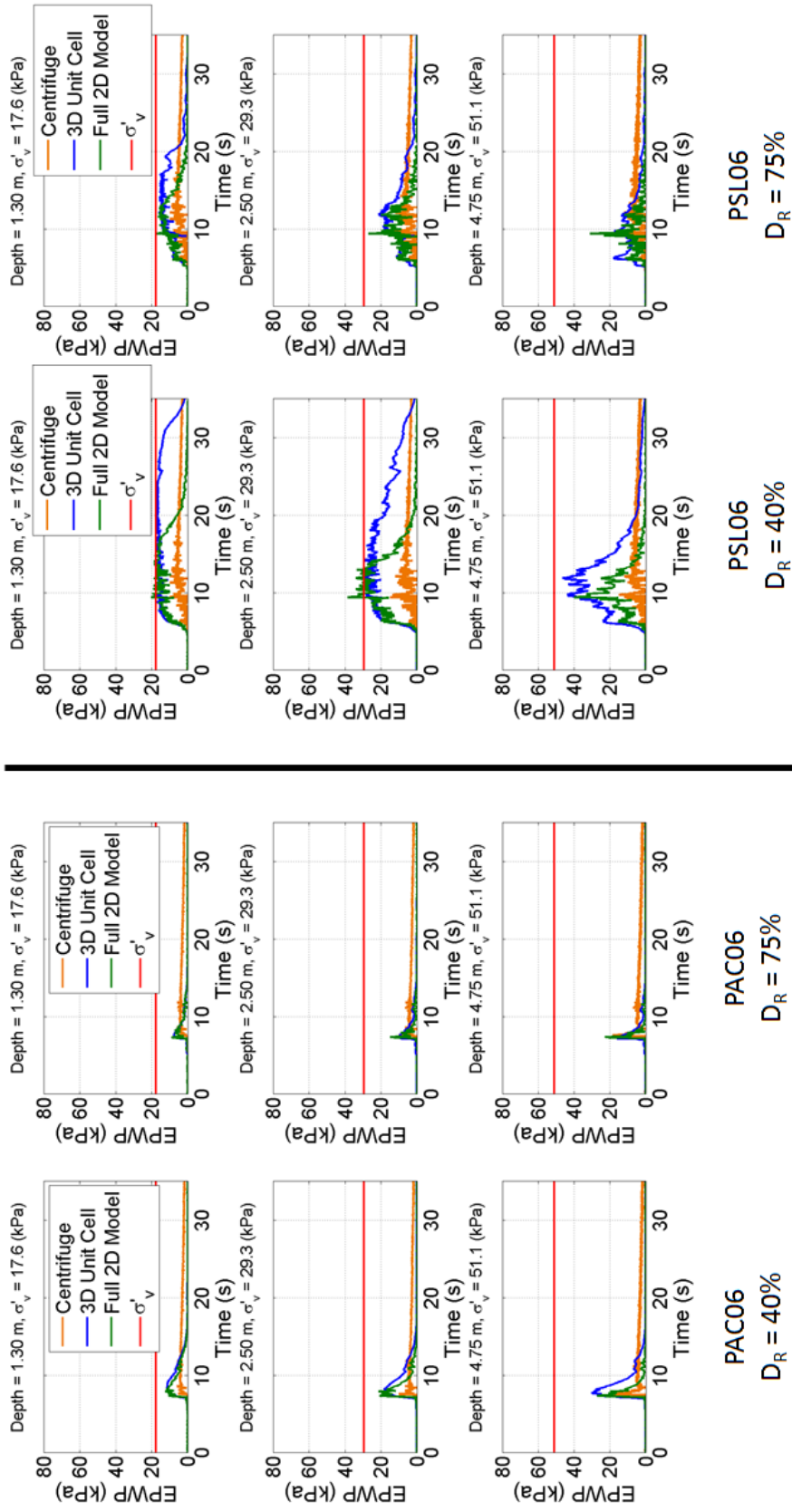


Figure 6.13: Excess pore water pressure-time histories for the treated 3D unit cell model, the treated area of the full 2D model, and the treated area of the RNK01 centrifuge model at relative densities of 40% and 75% for shaking events PAC06 (PGA = 0.41 g) and PSL06 (PGA = 0.46 g).

The treated area of the RNK01 centrifuge model, like the untreated area was reinforced by the presence of the stiff model drains. Horizontal deformations in the treated area of the RNK01 centrifuge model were less than 1 cm for all but the three highest intensity shaking events (PSL07, SIN01, and SIN02). Due to the reinforcement of the slope and the lack of horizontal deformations in the centrifuge model, a comparison of the simulated and experimental deformation data will not be shown for the treated condition.

6.5 Comparison of Treated and Untreated Numerical Models

Even though both areas of the RNK01 centrifuge model were reinforced by the tubes/drains, it may still be possible to compare the improved performance for the largest shaking events to the improved performance seen in the simulations. The only difference between the untreated and treated areas of the RNK01 centrifuge model was drainage. Therefore, the improved performance for those shaking events in which there were deformations can be compared to the improvements predicted by the numerical models. In this section the treated and untreated unit cell models are interpreted within the context of the predicted improvement in performance, and then the predicted level of improvement is compared with the observed level of improvement from the centrifuge tests.

Figures 6.14 through 6.16 show the excess pore water pressure-time histories for the untreated and treated 3D unit cell models for the RNK01 shaking events with $PGA < 0.40$ g. It can be seen in Figure 6.14 that for PAC06 and PAC07, the

drains reduce the peak excess water pressures and significantly increase the rate of pore pressure dissipation. For PAC08, the treated and untreated peak excess pore pressures are similar, but again the pore pressures dissipate more quickly in the treated model. For PSL06 and PSL07 (Figure 6.15), the peak excess pore pressures for the treated and untreated models are again similar, and again the treated unit cell model drains more quickly at mid-depth and near the base of the model. Near the sand/clay interface, the excess pore pressures for time = 20 to 35 seconds are actually higher in the treated model than in the untreated model. This is related to the model's sensitivity to low-intensity accelerations (see Section 6.4) and the manual drainage imposed in the untreated model time = 20 seconds. For SIN01 and SIN02 (Figure 6.16), the treated and untreated unit cell models again have similar peak excess pore water pressures at all three depths shown with the treated unit cell models draining faster after significant shaking ends.

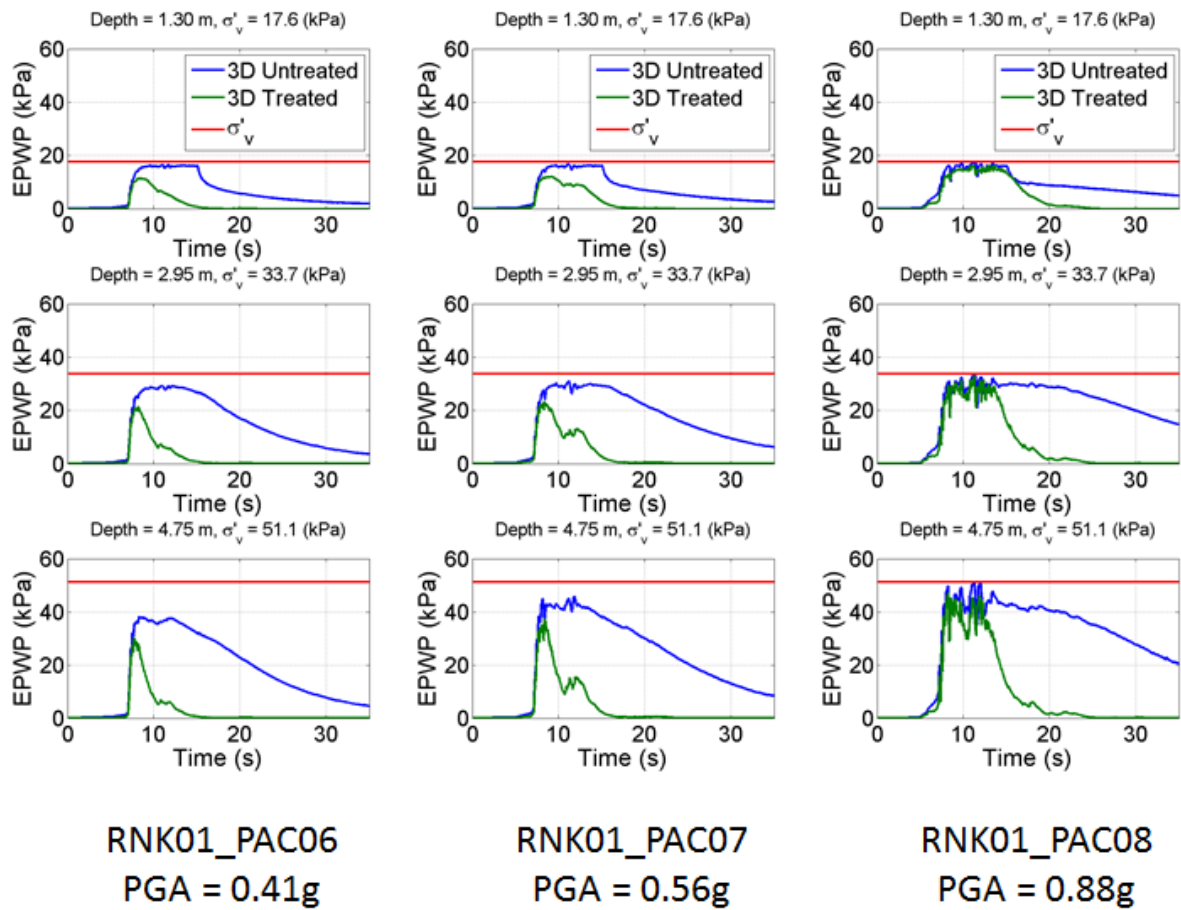


Figure 6.14: Excess pore water pressure-time histories for the untreated and treated 3D unit cell models at three different depths for shaking events PAC06 (PGA = 0.41 g) through PAC08 (PGA = 0.88 g).

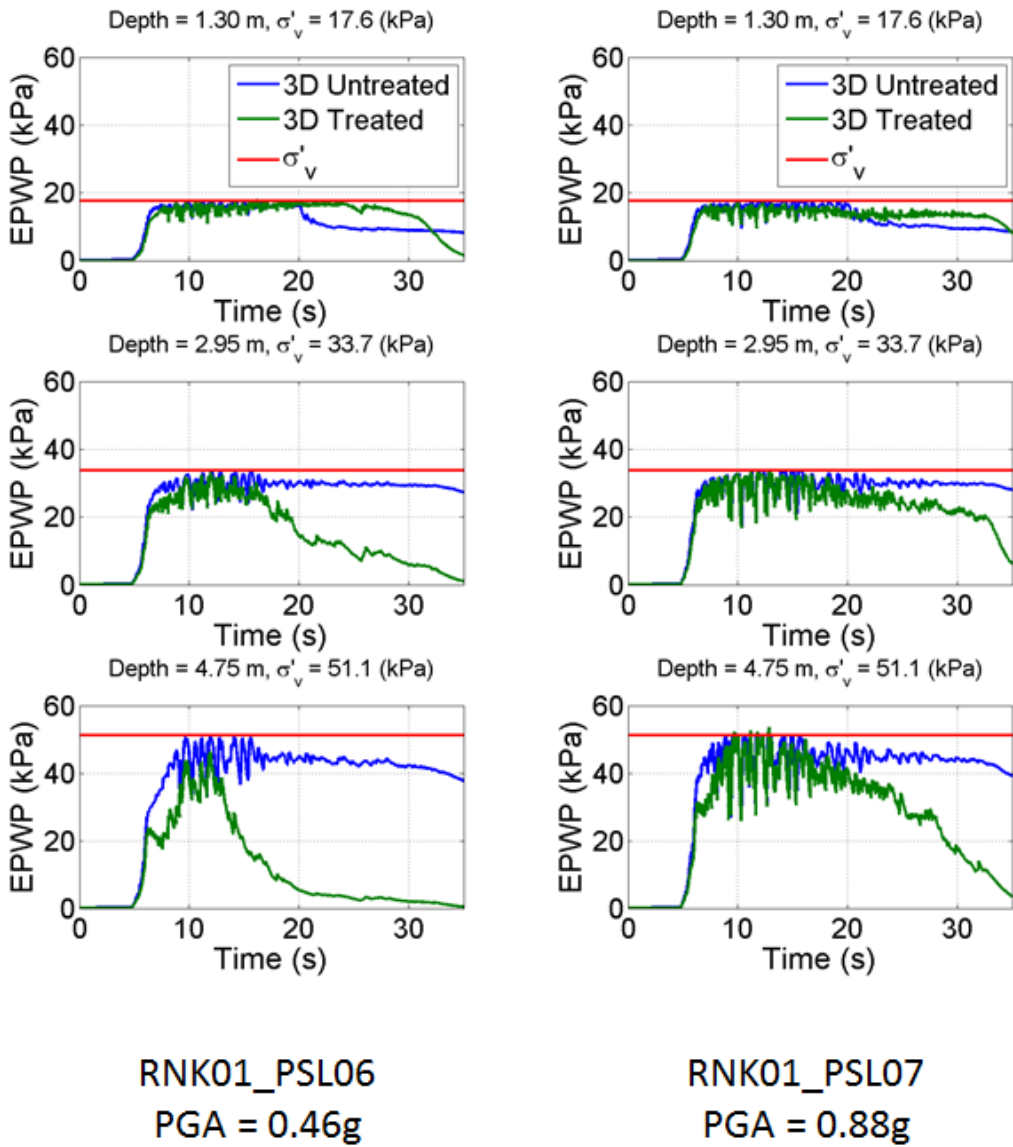


Figure 6.15: Excess pore water pressure-time histories for the untreated and treated 3D unit cell models at three different depths for shaking events PSL06 (PGA = 0.46 g) and PSL07 (PGA = 0.88 g).

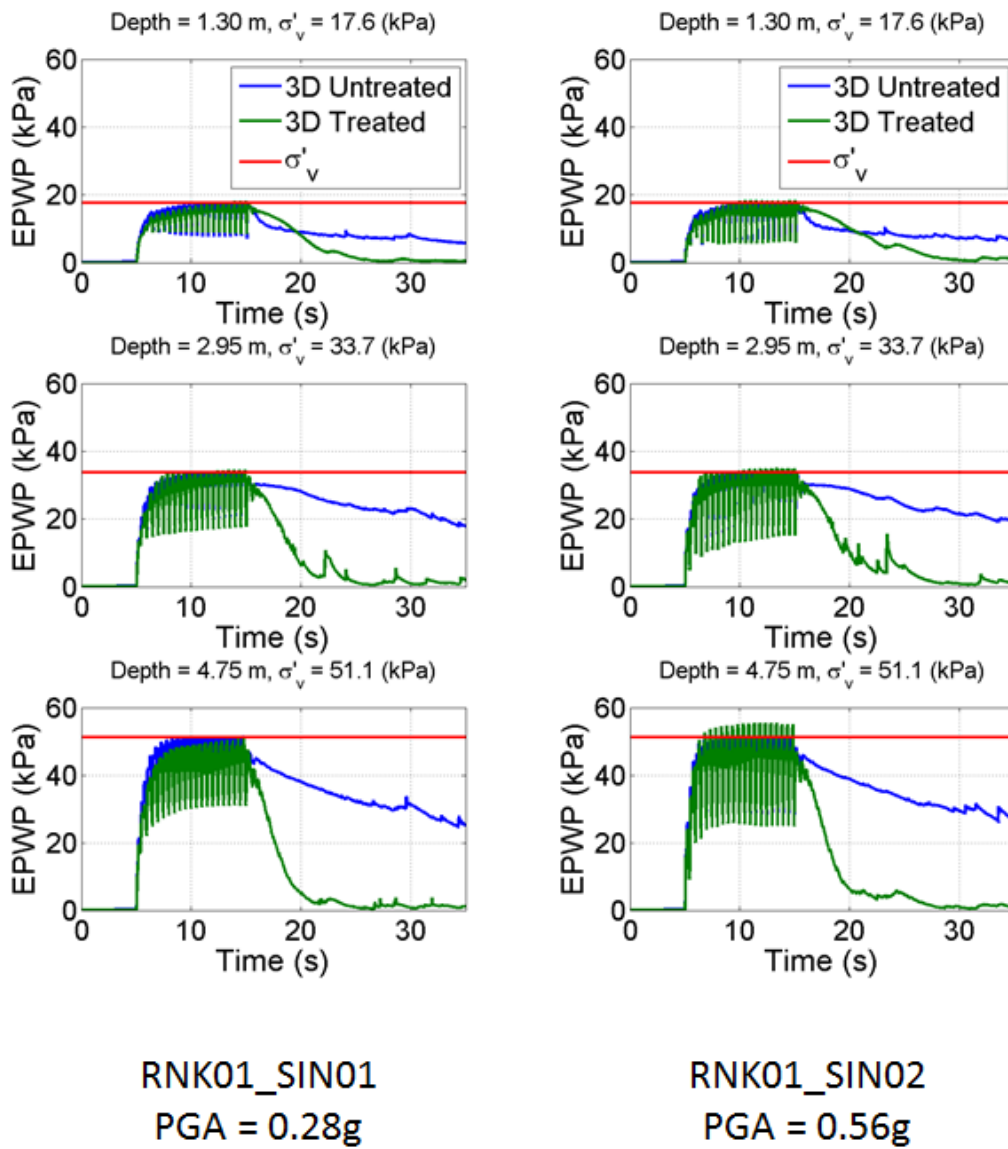


Figure 6.16: Excess pore water pressure-time histories for the untreated and treated 3D unit cell models at three different depths for shaking events SIN01 (PGA = 0.28 g) and SIN02 (PGA = 0.56 g).

Figure 6.17 shows the peak average excess pore water pressures ($\bar{r}_{u,max}$) as a function of PGA for the untreated and treated unit cell models for the PAC and PSL events. In general, for both motions $\bar{r}_{u,max}$ is lower in the treated model than in the untreated model, although the difference is less significant as $\bar{r}_{u,max}$ approaches 1.0.

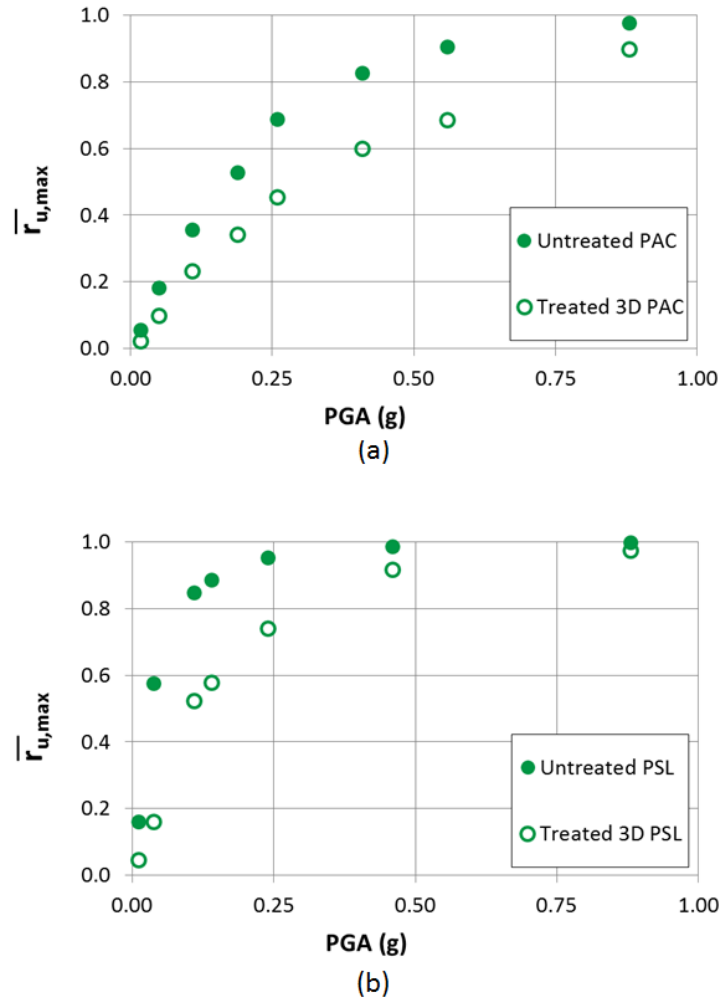


Figure 6.17: Peak average excess pore water pressures ($\bar{r}_{u,max}$) vs. PGA for the untreated and treated unit cell models for (a) the PAC shaking events and (b) the PSL shaking events.

Figure 6.18 shows the horizontal displacement-time histories at the top of the clay layer for the untreated and treated 3D unit cell models for the RNK01 shaking events with $\text{PGA} > 0.4 \text{ g}$. It can be seen that for all shaking events, the untreated horizontal deformations are larger than the treated horizontal deformations. This holds true even for the shaking events in which the untreated and treated $\bar{r}_{u,\max}$ values are similar (i.e., PSL07, SIN01, and SIN02) because the horizontal deformations are influenced by the time the model spends at those pore water pressures. For the PAC events, the deformations stop at a much earlier time for the treated model than the untreated model. For the PSL and SIN events, the deformations occur over approximately the same time interval for the treated and untreated conditions, but they accumulate less rapidly for the treated model due to the fact that the center of the treated model has smaller pore pressures than the untreated model.

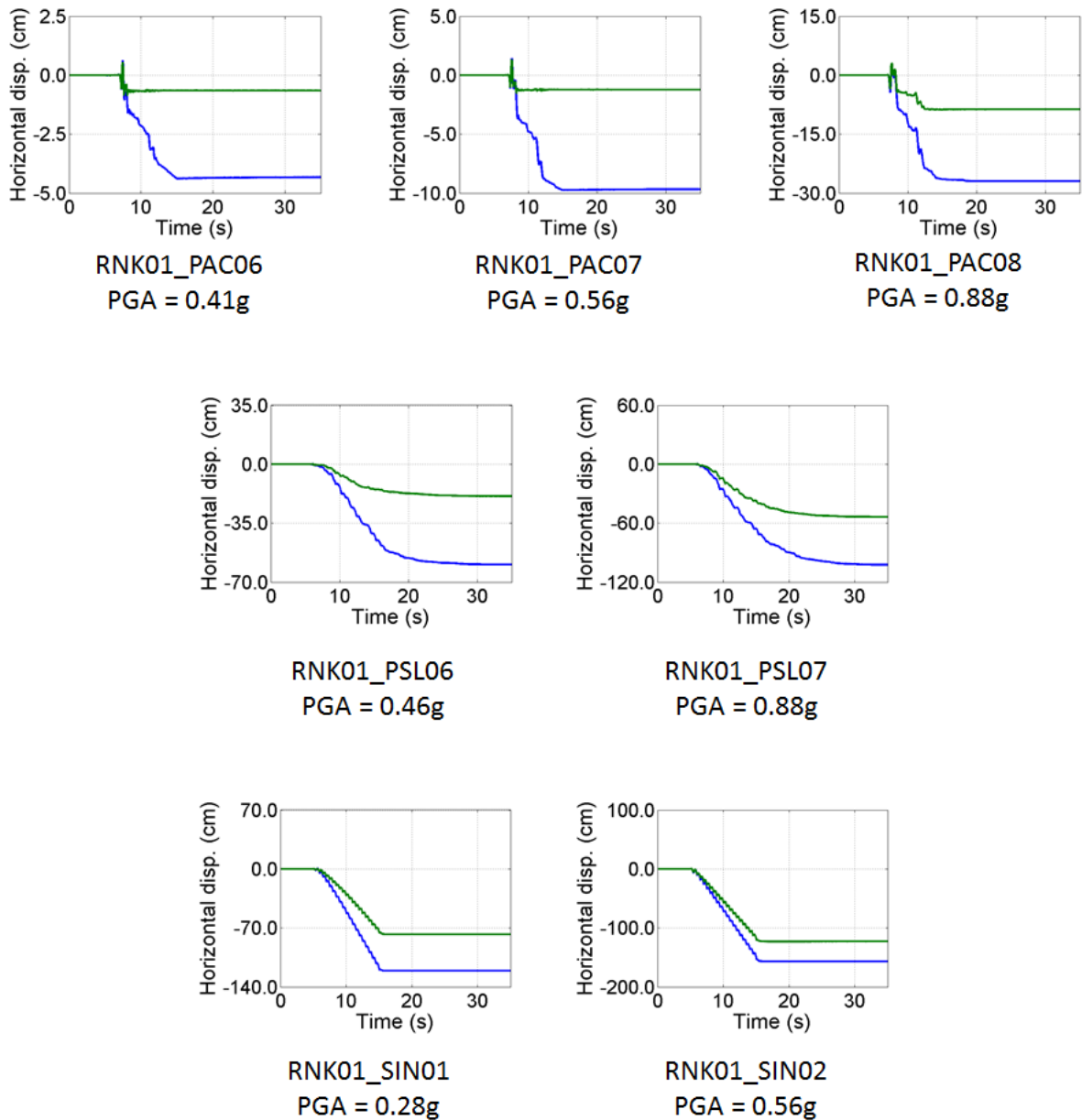


Figure 6.18: Horizontal displacement-time histories at the top of the clay layer for the untreated and treated 3D unit cell models for RNK01 shaking events with $PGA > 0.4$ g.

In centrifuge test RNK01, both the untreated and treated areas of the centrifuge model were reinforced such that the only difference between the two areas was drainage. The untreated and treated horizontal deformations for the RNK01 centrifuge model are detailed in Table 6.3. The percent improvement varies considerably from event to event, although generally the treated deformations are smaller than the untreated. Neglecting events with less than 1 cm of deformation, the improvement was 50 to 80% for the earthquake events and only 2-25% for the SIN events. Table 6.3 also details the untreated and treated horizontal deformations for the 3D unit cell models for the RNK01 simulations. The deformations for the 3D unit cell models are more than an order of magnitude greater than the centrifuge results due to both the stiff tubes in the centrifuge model and the larger pore pressure response in the numerical models. In terms of percent improvement for the numerical models, the PAC events showed about 70 to 80% improvement while the PSL events showed about 50 to 70% improvement, and the SIN events showed only about 20 to 35% improvement. The average percent improvement for the 3D unit cell simulations of the earthquake shaking events shown in Table 6.3 is a little over 60%, which is slightly lower than the average percent improvement for the earthquake events in the centrifuge model. However the average percent improvement for the SIN events in the 3D unit cell models is around 30%, which is higher than the percent improvement observed for the SIN events in the centrifuge model.

Table 6.3: Untreated and treated horizontal deformations from centrifuge test RNK01 and the 3D unit cell models for shaking events with a PGA greater than 0.4 g.

Centrifuge Test				
Motion	PGA (g)	Untreated (cm)	Treated (cm)	Improvement (%)
PAC06	0.41	0.3	0.2	33
PAC07	0.56	0.5	0.5	0
PAC08	0.88	3.3	1.5	54
PSL06	0.46	0.7	0.4	43
PSL07	0.88	5.4	1.2	78
SIN01	0.28	12.2	11.9	2
SIN02	0.56	16.2	12.2	25

3D Unit Cell Models				
Motion	PGA (g)	Untreated (cm)	Treated (cm)	Improvement (%)
PAC06	0.41	4.2	0.7	83
PAC07	0.56	9.3	1.3	86
PAC08	0.88	26.0	8.7	67
PSL06	0.46	56.0	18.9	66
PSL07	0.88	101.0	53.6	47
SIN01	0.28	121.2	77.5	36
SIN02	0.56	157.7	122.9	22

6.6 Summary

This chapter detailed the numerical simulations of the RNK01 centrifuge test and comparisons of the RNK01 simulation and experimental data. Simulations of shaking events PAC01 through PAC08, PSL01 through PSL07, and SIN01 and SIN02 were performed using untreated and drain-treated 2D and 3D unit cell models. These analyses focused only on those events in which significant pore pressures were generated - PAC06 through PAC08, PSL06 and PSL07, and SIN01 and SIN02. The data from these events was analyzed with emphasis placed on identifying the pore pressure and deformation-related behavioral trends that were observed in the centrifuge test.

A good portion of the loose sand layer in the RNK01 centrifuge model had a relative density of about 70%, which is much denser than the target relative density of 40%. Additionally, both the untreated and treated areas of the RNK01 centrifuge model were reinforced by the model drains/tubes. The untreated unit cell models over predicted the peak excess pore pressures for all but the SIN shaking events. However, when the simulated sand was replaced by the $D_R = 75\%$ sand from Yang et al. (2008), the peak excess pore pressures in the unit cell models were comparable to those observed in the centrifuge test. Because the untreated area of the RNK01 centrifuge model was reinforced, and the geometry of the unit cell models does not match that of the centrifuge models, no comparison of the simulated and experimental horizontal deformation data was performed. For the numerical data, it was shown that the horizontal deformations increase with increasing input intensity and begin to exceed 1 cm when the peak $\bar{r}_{u,\max}$ exceeds 0.6.

The simulation data and the experimental data for the treated condition were compared, and it was shown that the unit cell model overestimates the peak excess pore pressures, but predicts peak excess pore pressures that are more comparable to those observed in the centrifuge model when the relative density of the simulated sand is increased to 75%. It was also shown that the unit cell models are particularly sensitive to low-level accelerations when the stress path is near the failure surface. This sensitivity resulted in excess pore pressure elevation well beyond the end of shaking for the PSL shaking events.

The treated and untreated pore pressure and deformation data from the numerical models was compared and it was shown that, as expected, the untreated model had higher peak excess pore pressures and larger horizontal deformations. The percent improvement observed in the 3D unit cell simulations was around 60%, which agrees well with the percent improvement from the centrifuge test for the earthquake shaking events in which there was more than 1 cm of deformation.

Chapter 7

Comparison of Numerical Models and Data from Centrifuge test

RLH01

7.1 Introduction

This chapter describes the results of the numerical simulations of centrifuge test RLH01. The RLH01 centrifuge test differed from the SSK01 and RNK01 centrifuge tests in that it contained three test areas and the geometry of the model was rotated such that shaking took place orthogonal to the slope in each test area. Additionally, at the mid-slope locations the liquefiable sand layer of the RLH01 model was 5.5 m thick (versus 4.5 m in the SSK01 and RNK01 models), the clay layer was 1.5 m thick (versus 1 m in the SSK01 and RNK01 models), and the slope angle for each treatment area was 10° (versus 3° in the SSK01 and RNK01 models). The RLH01 unit cell models differ from the SSK01 and RNK01 unit

cell models in terms of the slope angle and layer thicknesses, but the boundary conditions applied to the RLH01 models are the same as those applied to the SSK01 and RNK01 models.

Simulations of shaking events PAC01 (PGA = 0.11 g) through PAC04 (PGA = 0.95 g), PSL01 (PGA = 0.10 g) through PSL04 (PGA = 0.90 g), and SIN01 (PGA = 0.60 g) were performed using the untreated and drain-treated 3D unit cell models. The 2D unit cell model was not considered because shaking for RLH01 was applied orthogonal to the slope and this direction of shaking cannot be modeled in the 2D analyses. For the numerical simulations performed using the 3D unit cell models, shaking was applied either parallel or orthogonal to the slope to investigate the influence of the direction of shaking. The simulated excess pore pressure and deformation data for the 3D unit cell models were analyzed with emphasis given to identifying the behavioral trends that were observed in the experimental data.

7.2 Influence of Shaking Direction on the Untreated 3D Unit Cell Models

The RLH01 3D unit cell simulations were performed with shaking applied either parallel or orthogonal to the slope. The 3D unit cell model with shaking orthogonal to the slope has different boundary conditions in that the out-of-plane deformations are not fixed, but rather the out-of-plane deformations at each depth are constrained to be equal for all nodes along the outer boundary of the model (see Figure 4.12).

Figures 7.1 through 7.3 show the excess pore water pressure-time histories for the untreated 3D parallel and orthogonal unit cell models at three different depths for the PAC events (Figure 7.1), PSL events (Figure 7.2), and SIN event (Figure 7.3). Generally, excess pore pressure generation is not sensitive to the direction of shaking, and it can be seen in Figures 7.1 and 7.2 that for the lower-intensity PAC and PSL events ($PGA < 0.4 g$) there are only minor differences in the data from the parallel and orthogonal models. For the higher-intensity PAC and PSL events, there are differences evident in the hydrodynamic features of the pore pressure time-histories. When shaking is performed parallel to the slope, the downslope inertial forces and larger shear strains result in significant dilation that is not present in the orthogonal model. There are more differences evident in the pore pressure time-histories for the SIN01 shaking event (Figure 7.3). During shaking, the excess pore pressures for the orthogonal model are lower than the excess pore pressures for the parallel model. At the end of shaking, the excess pore pressures for the orthogonal model jump up such that they are equal in magnitude to the pore pressures for the parallel model.

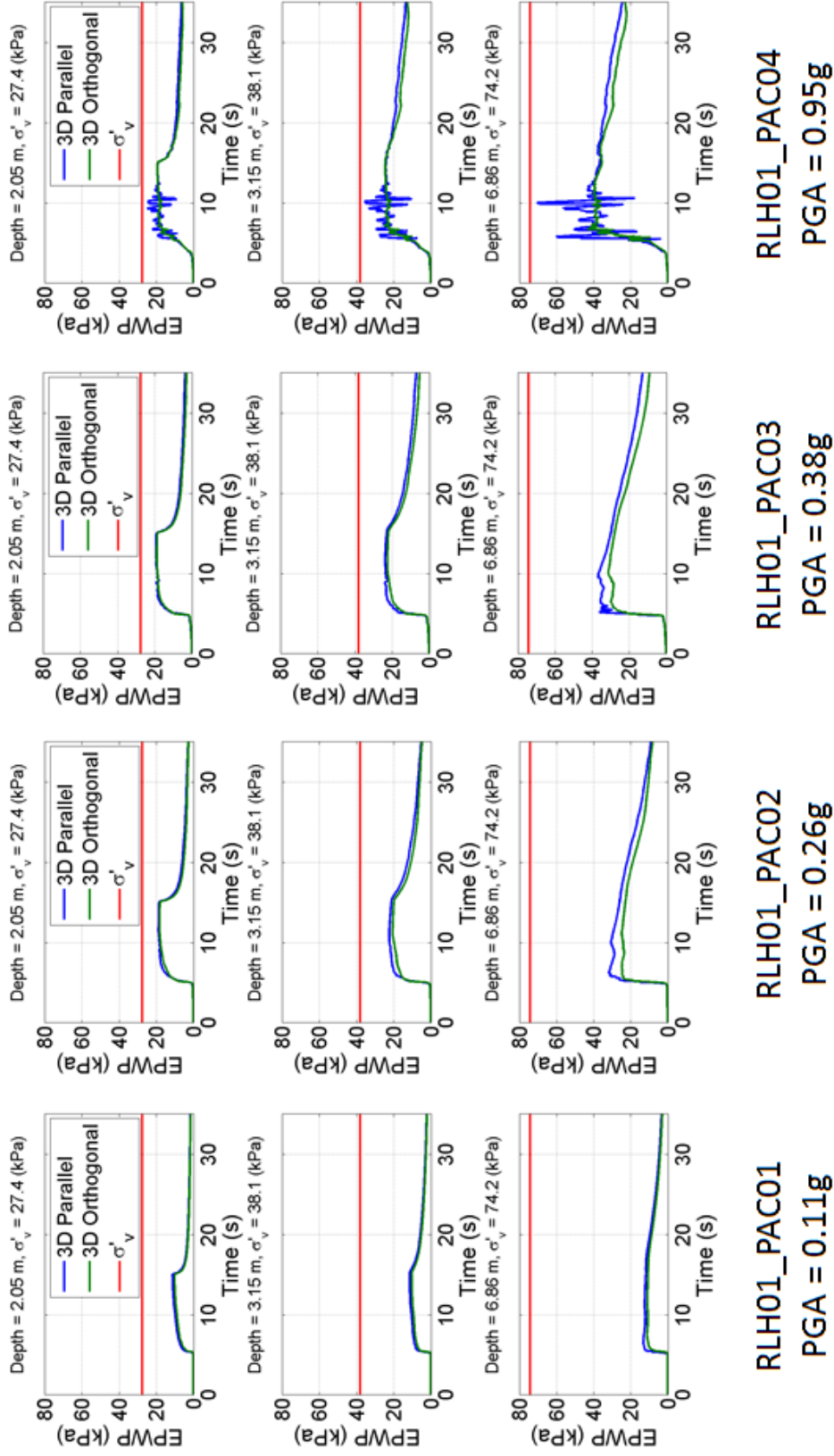


Figure 7.1: Excess pore water pressure-time histories for the untreated 3D unit cell models at three different depths for shaking events RLH01_PAC01 (PGA = 0.11 g) through RLH01_PAC04 (PGA = 0.95 g).

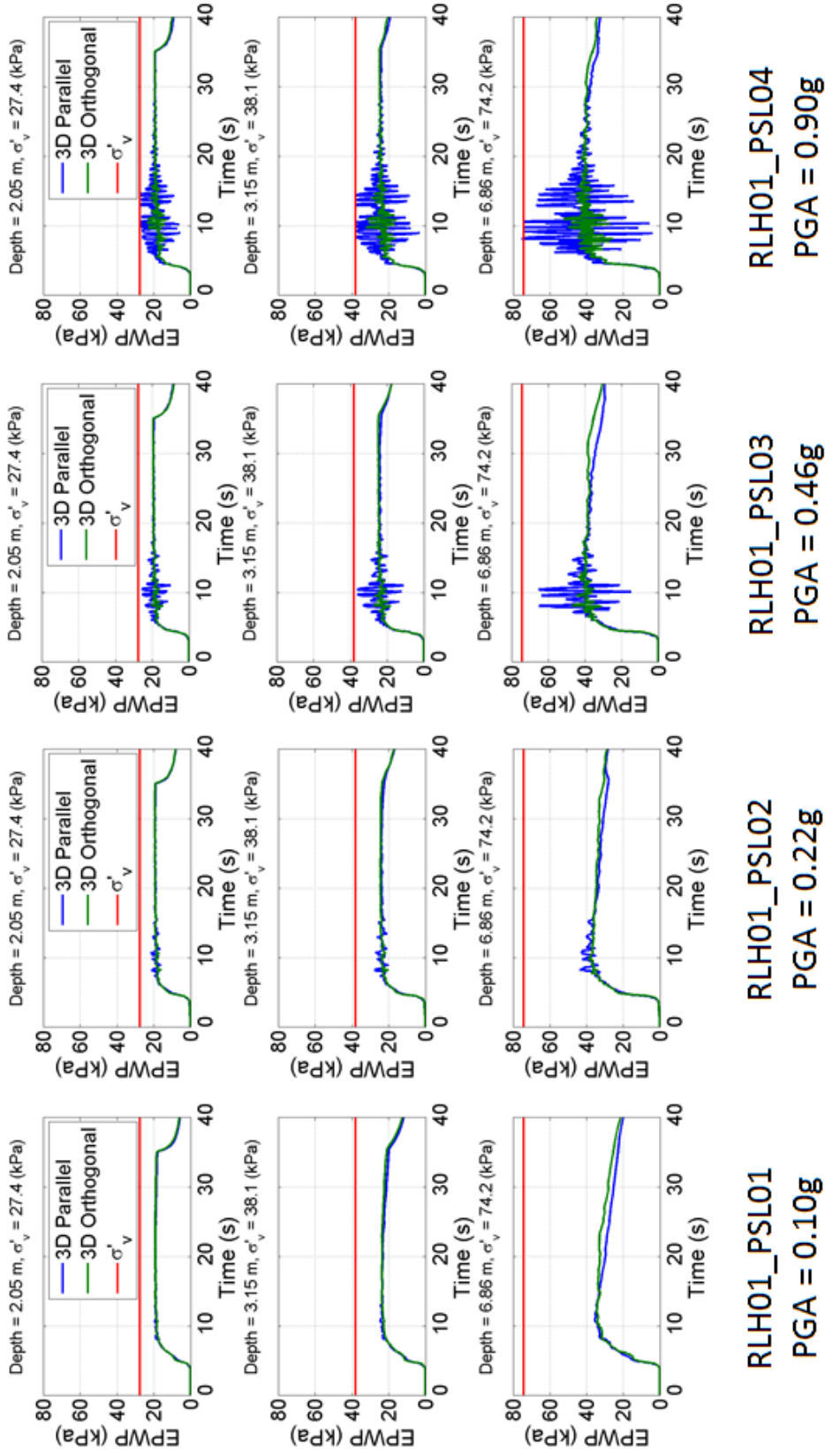
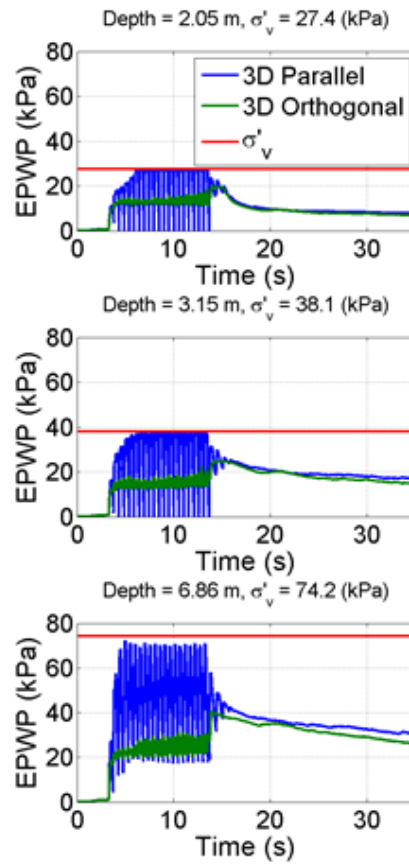


Figure 7.2: Excess pore water pressure-time histories for the untreated 3D unit cell models at three different depths for shaking events RLH01_PSL01 (PGA = 0.10 g) through RLH01_PSL04 (PGA = 0.90 g).



RLH01_SIN01
PGA = 0.60g

Figure 7.3: Excess pore water pressure-time histories for the untreated 3D unit cell models at three different depths for the RLH01_SIN01 shaking event (PGA = 0.60 g).

The pore pressure jump observed in the orthogonal model for the SIN01 shaking event was not expected and is related to the direction and constant amplitude of the cyclic shear stresses. Figure 7.4 shows the octahedral shear stress (τ_{oct}) vs. the mean effective stress (p') for an element at a depth of 2.05 m for the untreated RLH01 3D unit cell model for shaking orthogonal and parallel to the slope. It can be seen that the range of τ_{oct} for orthogonal shaking is much smaller than for parallel shaking because the dynamic shear stresses are acting perpendicular to the static shear stresses. In this case, the smaller range of τ_{oct} generates less pore water pressure than the larger range of τ_{oct} . After shaking ends, both models approach the same values of τ_{oct} and p' , with the orthogonal model decreasing its effective stress and the parallel model increasing its effective stress. Note that this behavior was not observed for the earthquake shaking events because the small loading cycles that are interspersed between the large loading cycles allow the stress path to move towards smaller effective stresses.

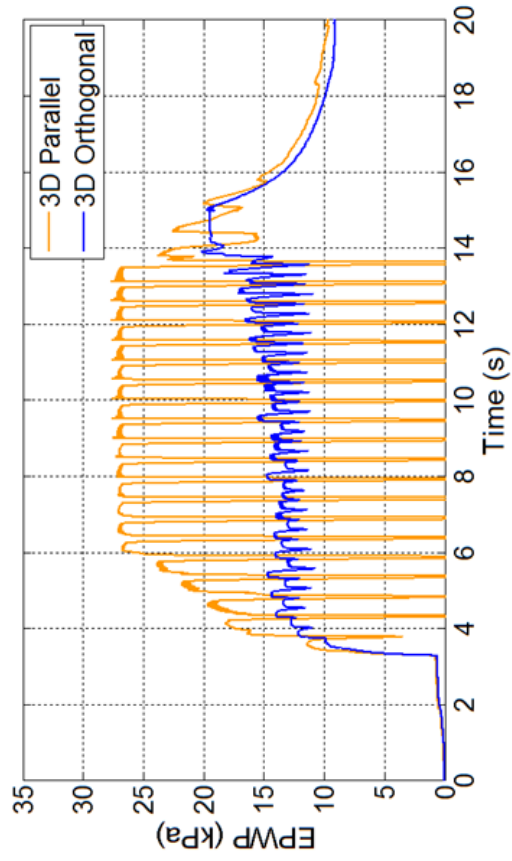
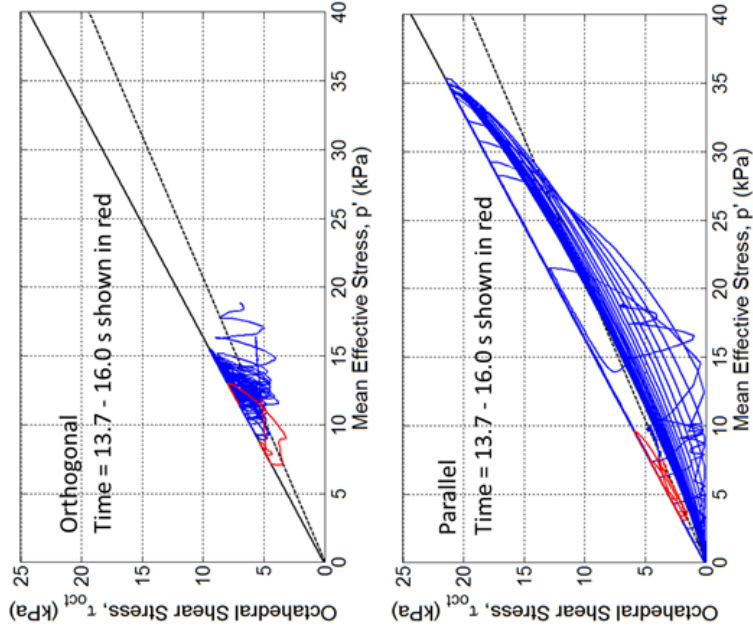


Figure 7.4: Excess pore pressure-time history and octahedral shear stress vs. mean effective stress for an element at a depth of 2.05 m in the untreated 3D unit cell models for shaking orthogonal and parallel to the slope for the SIN01 shaking event.

It should also be noted in Figures 7.1 and 7.2 that the excess pore pressures reach a maximum value at an r_u less than 1.0. This cap is related to the static shear stresses present in the slope, which limit the maximum excess pore water pressures that can be generated and sustained. Figure 7.5 shows the stress paths on the horizontal plane at a depth of 6.45 m for simulations of the PSL03 shaking event for two untreated 3D orthogonal unit cell models, one with a 10° slope and one representing flat ground. For the model with a 10° slope, the initial static shear stresses on the horizontal plane (τ_{xz}) are about 20 kPa. As shaking progresses, the vertical effective stresses decrease, but there are no stress reversals (i.e., transitions from positive to negative shear stress) and the stress path cannot reach the origin (i.e., zero effective stress and $r_u = 1.0$). At this depth, the lowest effective stress that the model with the 10° slope can reach is about 23 kPa, which corresponds to an r_u of about 0.67. For the flat model, there are no static shear stresses such that shaking induces stress reversals and the stress path can reach the origin (i.e., $r_u = 1.0$). Thus, when the slope angle is 10° , as it is in the RLH01 unit cell models, $r_u = 1.0$ is harder to achieve and the excess pore pressures will reach a maximum value at an r_u less than 1.0.

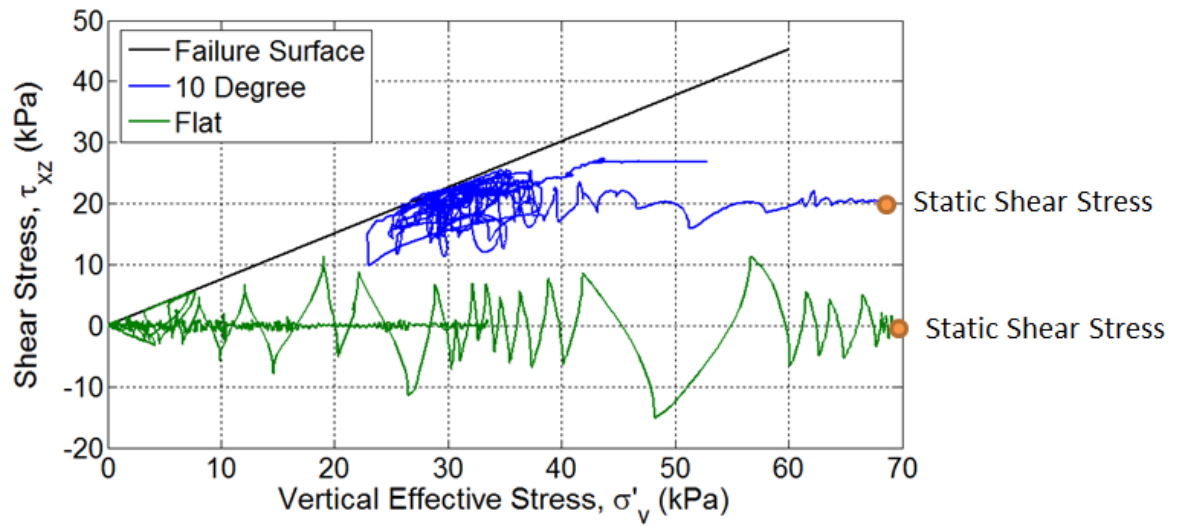


Figure 7.5: Stress paths at a depth of 6.45 m for simulations of the PSL03 shaking event for a 10° slope and flat ground.

Horizontal deformations, unlike excess pore pressures, are significantly affected by the direction of shaking. Figures 7.6 through 7.8 show the horizontal (downslope) displacement-time histories at the top of the clay layer and the horizontal displacement vs. depth profiles for the untreated 3D parallel and orthogonal unit cell models for the PAC events (Figure 7.6), PSL events (Figure 7.7), and SIN event (Figure 7.8). It can be seen that for all but the lowest intensity PAC and PSL events (PAC01 and PSL01), the horizontal (downslope) deformations are smaller for the orthogonal model than for the parallel model. For the lowest intensity shaking events, it may be that the intensity of shaking is low enough such that the upslope movement in the parallel model actually helps keep reduce the horizontal deformations. It can also be seen in Figures 7.6 through 7.8 that the difference between in the horizontal deformations for the parallel and orthogonal models increases as the intensity of shaking increases. For example, the horizontal deformations for the parallel model are 40% larger than those of the orthogonal model for PAC02, 52% larger for PAC03, and 68% larger for PAC04. For the SIN01 shaking event, which has the highest Arias intensity of all the RLH01 shaking events, the horizontal deformations for the parallel model are 78% larger than the horizontal deformations for the orthogonal model. In general, the parallel models experience 40 to 80% more deformation than the orthogonal models.

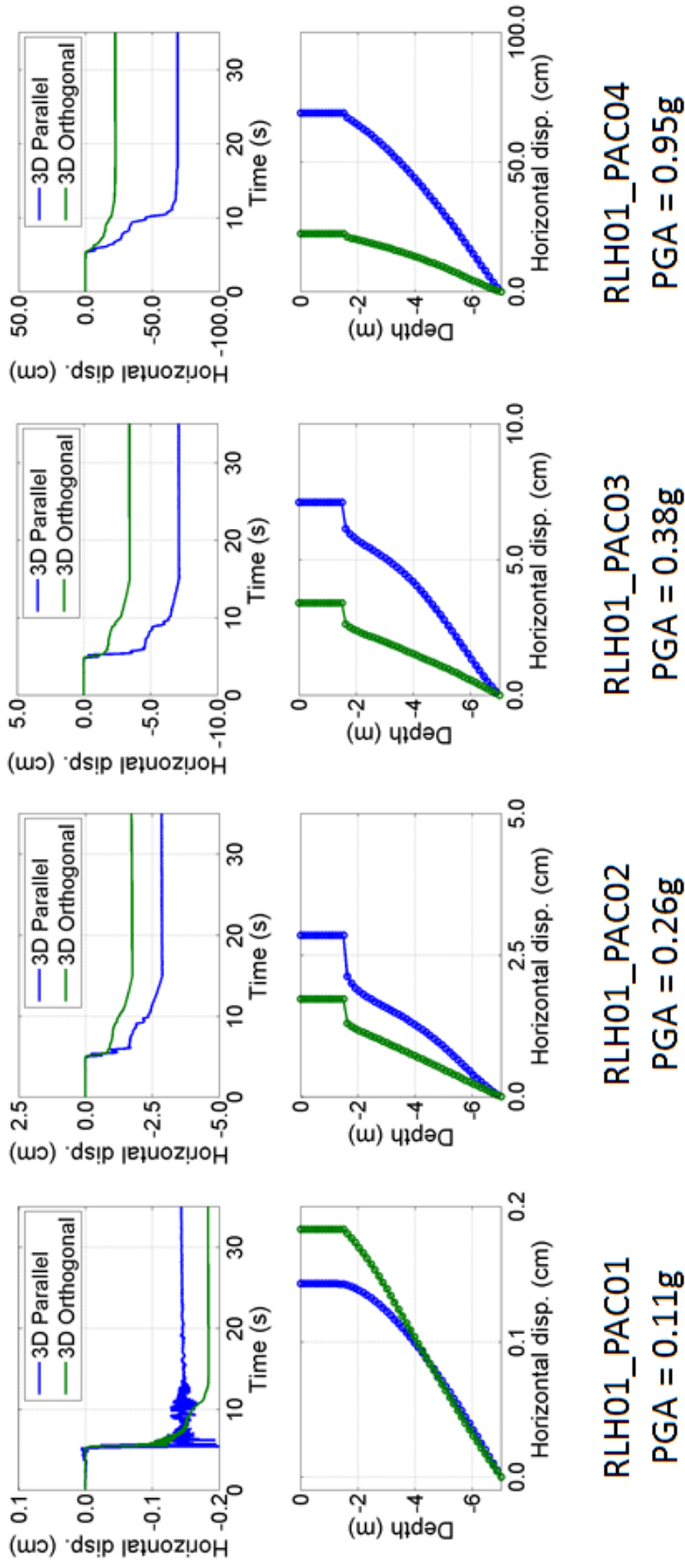


Figure 7.6: Horizontal displacement-time histories at the top of the clay layer and horizontal displacement vs. depth profiles for the untreated 3D unit cell models for shaking events RLH01_PAC01 (PGA = 0.11 g) through RLH01_PAC04 (PGA = 0.95 g).

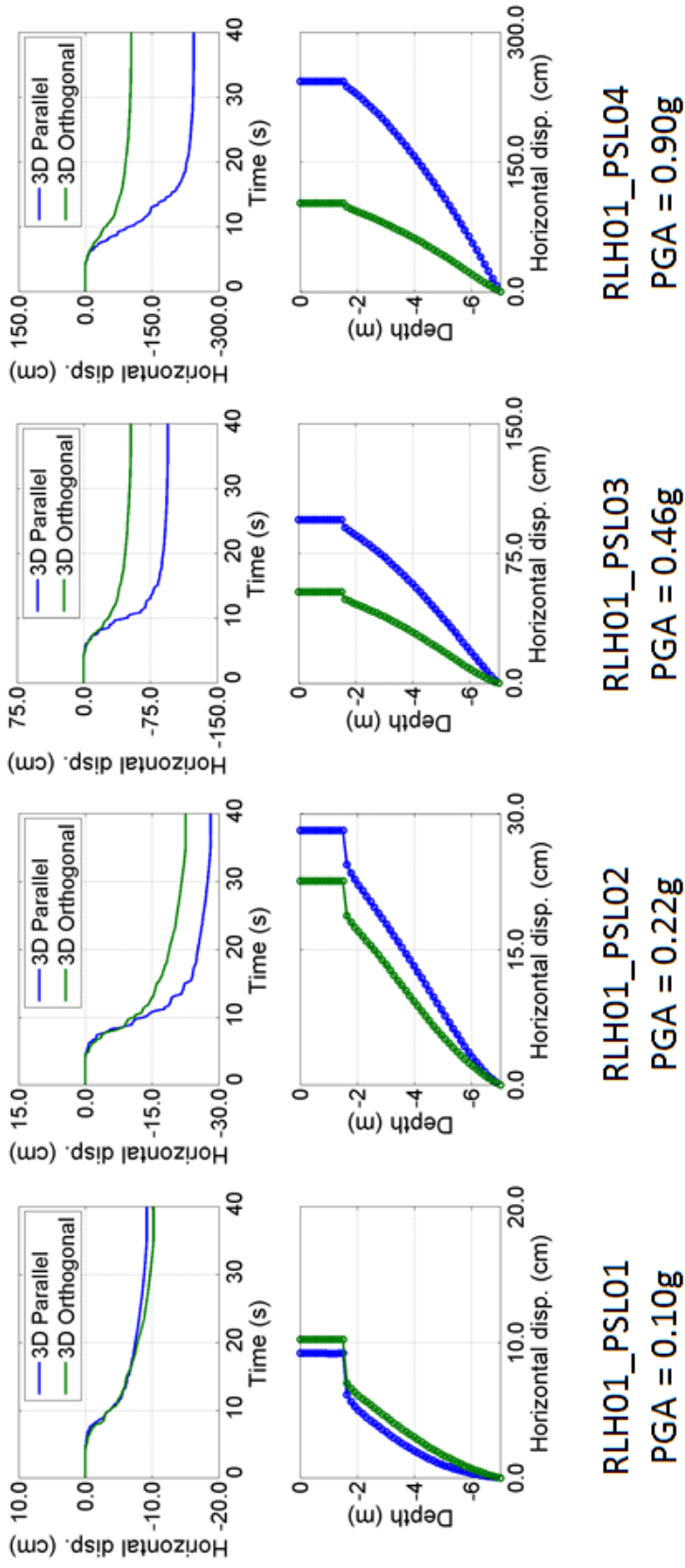
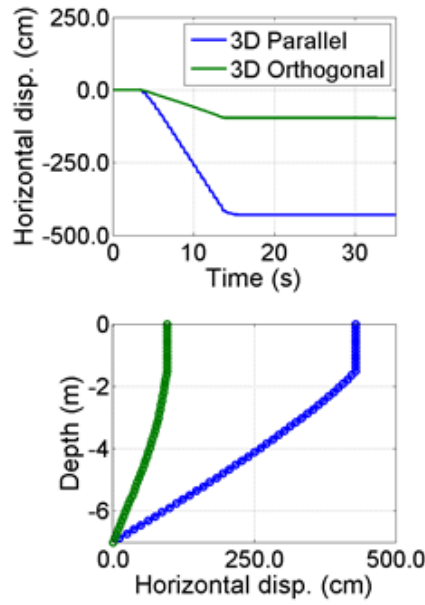


Figure 7.7: Horizontal displacement-time histories at the top of the clay layer and horizontal displacement vs. depth profiles for the untreated 3D unit cell models for shaking events RLH01_PSL01 (PGA = 0.10 g) through RLH01_PSL04 (PGA = 0.90 g).



RLH01_SIN01
PGA = 0.60g

Figure 7.8: Horizontal displacement-time histories at the top of the clay layer and horizontal displacement vs. depth profiles for the untreated 3D unit cell models for the RLH01_SIN01 shaking event (PGA = 0.60 g).

7.3 Comparison of Untreated Numerical Model and Centrifuge Data

Shaking in the RLH01 model was applied orthogonal to the slope; therefore, for the comparisons of the simulated and experimental data, only the data from the 3D unit cell model in which shaking took place orthogonal to the slope will be shown. Figures 7.9 through 7.11 show the excess pore water pressure-time histories for the untreated orthogonal 3D unit cell model and the untreated area of the RLH01 centrifuge model for the PAC events (Figure 7.9), PSL events (Figure 7.10), and SIN event (Figure 7.11).

For PAC01 (Figure 7.9), the numerical model slightly overestimates the peak excess pore pressures. However, for PAC02 through PAC04 the simulated pore pressure data show general agreement with the centrifuge data at all three depths. Near the sand/clay interface, the numerical model still slightly overestimates the peak excess pore pressures, and near the base of the model the numerical model slightly underestimates the peak excess pore pressures. While the peak pore pressures match relatively well, the simulations do not accurately model the decrease in pore pressure after the initial shaking. This result is because the unit cell model does not allow for any lateral flow out of the unit cell.

For the PSL shaking events (Figure 7.10), the match between the simulated and experimental data is not as good. The numerical model significantly overestimates the peak excess pore pressures for PSL01 and PSL02. The match between the simulated data and the centrifuge data is somewhat better for PSL03 and PSL04, but this is due to the fact that the pore pressures in both models are approaching their maximum limit based on the intersection of the static shear stresses and the failure envelope (see Section 7.2).

For SIN01, the numerical model underpredicts the pore pressures at depth and matches the pore pressures near the sand/clay interface where the pore pressures reach the pore pressure limit. Interestingly, the pore pressures from parallel shaking (Figure 7.3) match better with the centrifuge data in this case.

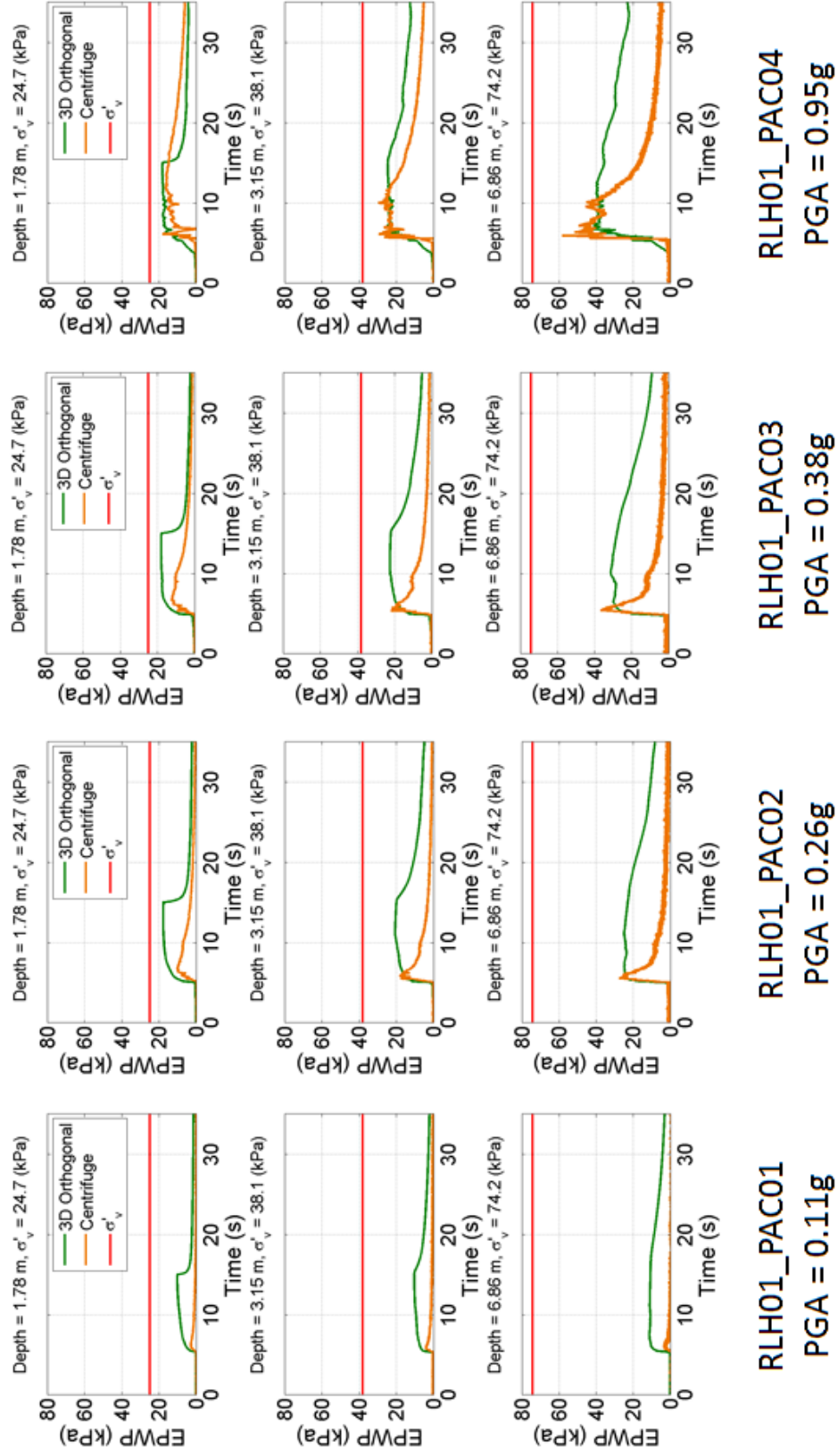


Figure 7.9: Excess pore water pressure-time histories for the untreated 3D unit cell model with shaking orthogonal to the slope and the untreated area of the RLH01 centrifuge model for shaking events RLH01_PAC01 (PGA = 0.11 g) through RLH01_PAC04 (PGA = 0.95 g).

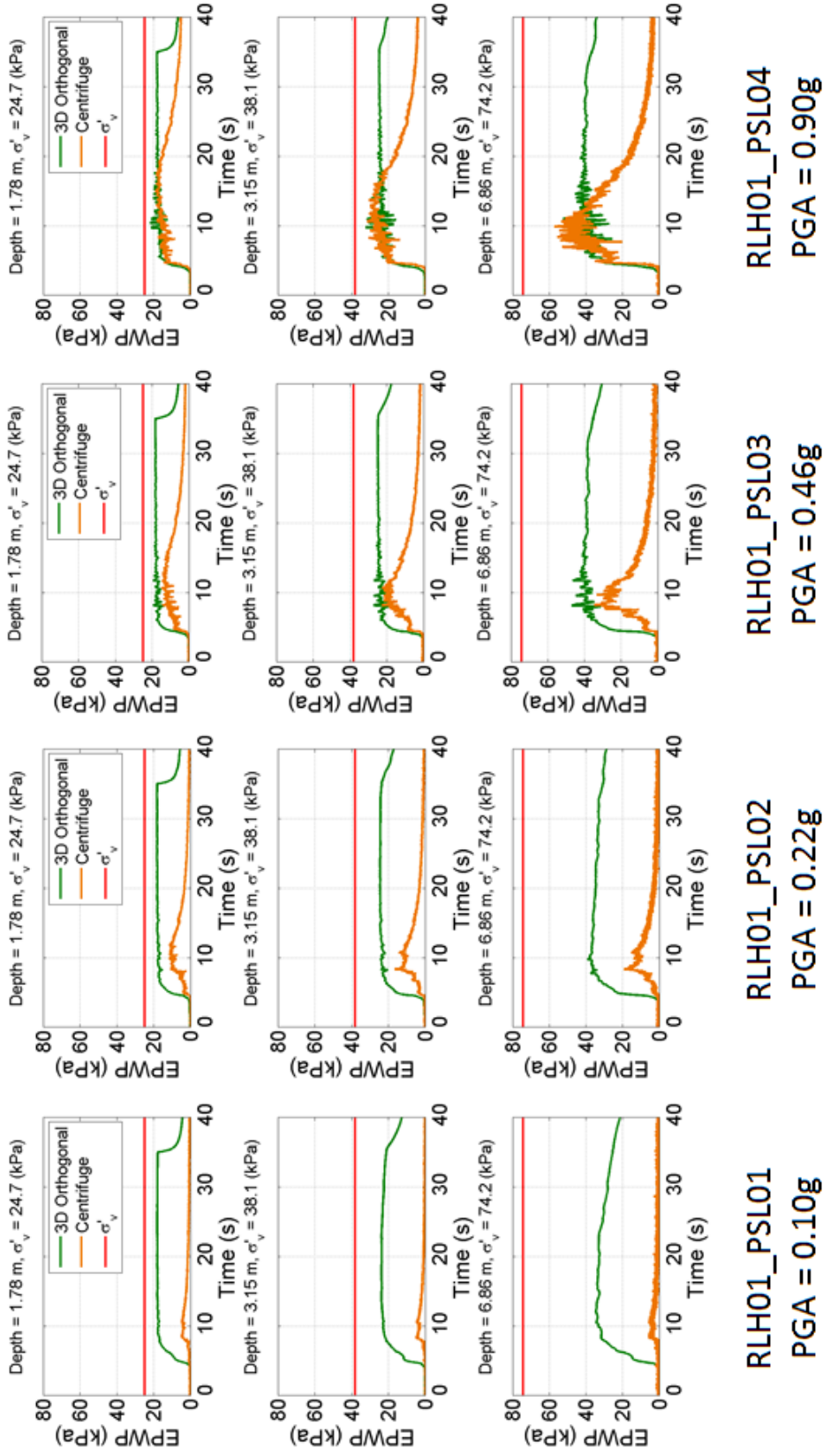
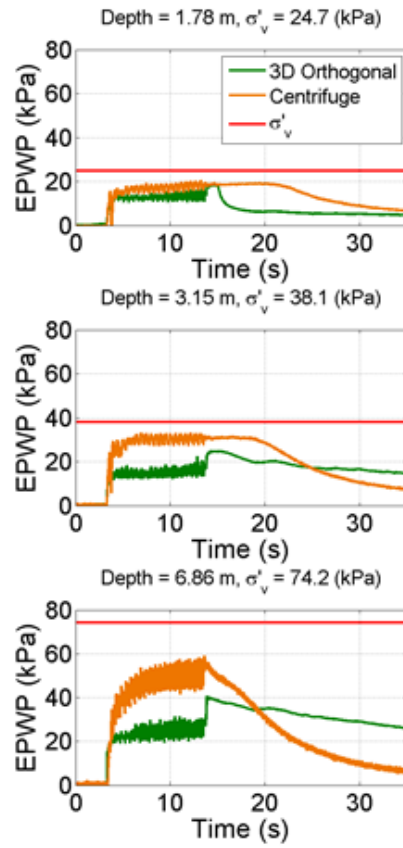


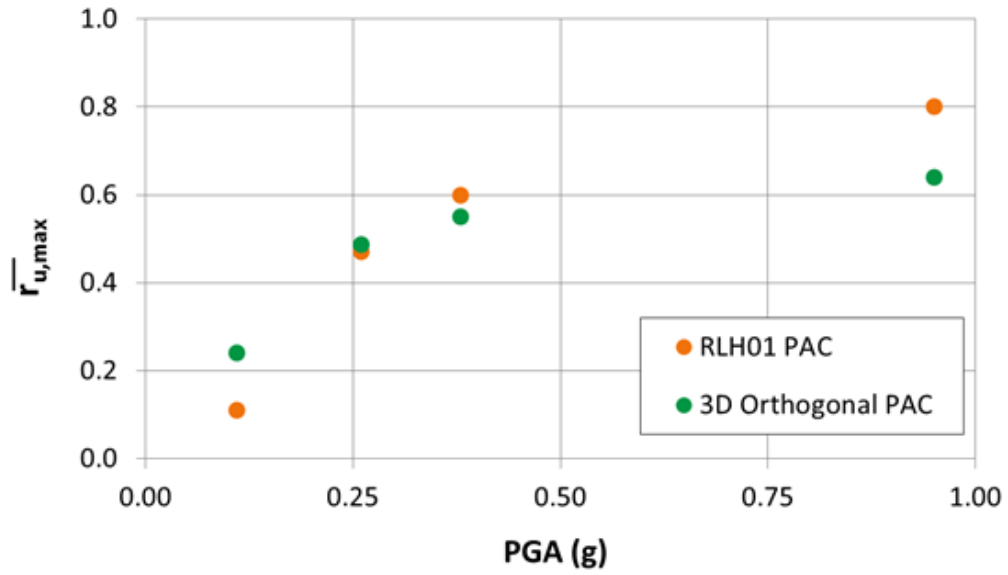
Figure 7.10: Excess pore water pressure-time histories for the untreated 3D unit cell model with shaking orthogonal to the slope and the untreated area of the RLH01 centrifuge model for shaking events RLH01_PSL01 (PGA = 0.10 g) through RLH01_PSL04 (PGA = 0.90 g).



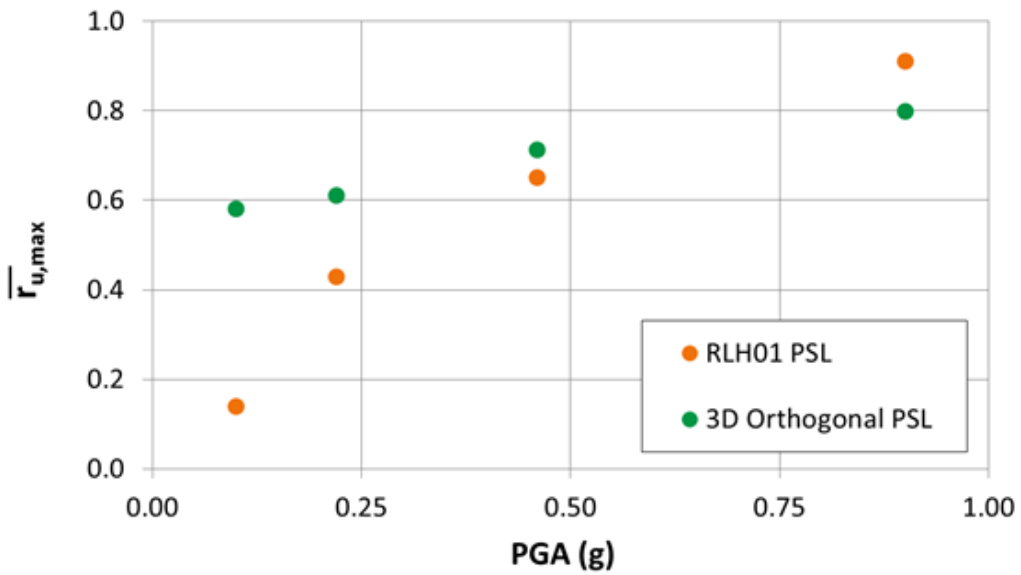
RLH01_SIN01
PGA = 0.60g

Figure 7.11: Excess pore water pressure-time histories for the untreated 3D unit cell model with shaking orthogonal to the slope and the untreated area of the RLH01 centrifuge model for the RLH01_SIN01 shaking event (PGA = 0.60 g).

Figure 7.12 shows the peak average excess pore water pressures ($\bar{r}_{u,\max}$) for the untreated orthogonal 3D unit cell model and the untreated area of the RLH01 centrifuge model for the PAC and PSL shaking events. For the PAC shaking events (Figure 7.12a), the $\bar{r}_{u,\max}$ values predicted by the numerical model are slightly high for the lowest PGA shaking event and low for the highest PGA shaking event. The match between the simulated and experimental data is good for the mid-range (0.26 g and 0.38 g) shaking events. For the PSL shaking events (Figure 7.12b), the numerical model overestimates $\bar{r}_{u,\max}$ for the two lowest PGA events. The match between the simulation data and the centrifuge for the 0.46 g shaking event is good, and the numerical model slightly underestimates $\bar{r}_{u,\max}$ for the highest intensity (0.90 g) shaking event. In general, the simulations show decent agreement with the centrifuge except for the smallest shaking events.



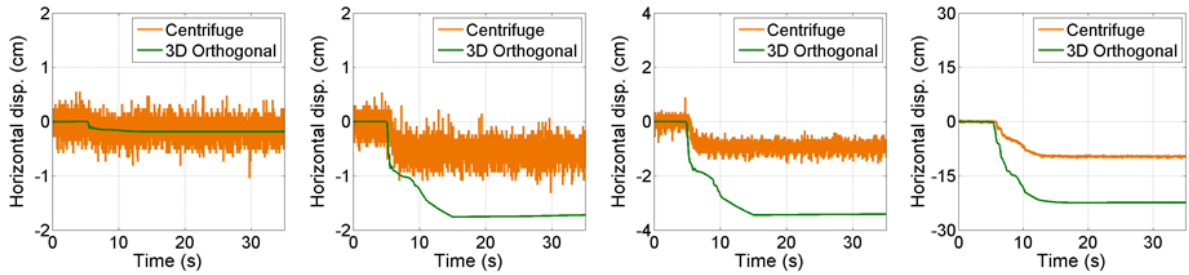
(a)



(b)

Figure 7.12: Peak average excess pore water pressures ($\bar{r}_{u,max}$) for the untreated 3D unit cell model with shaking orthogonal to the slope and the untreated area of the RLH01 centrifuge model for (a) the PAC shaking events and (b) the PSL shaking events.

Figure 7.13 shows the horizontal (downslope) displacement-time histories at the top of the clay layer for the untreated orthogonal 3D unit cell model and the untreated area of the RLH01 centrifuge model for all shaking events for which centrifuge displacement data was available. Due to sensor malfunctions, no centrifuge displacement data was available for shaking events PSL04 and SIN01 (Howell et al., 2009a). It can be seen in Figure 7.13 that the numerical model overestimates the horizontal (downslope) displacements for all shaking events. For PAC01 through PAC03, the simulated data does not consistently match the experimental data, but both the numerical model and the centrifuge model predict minimal deformations (i.e., less than a few cm) for these events. For PAC04, the numerical model predicts horizontal deformations that are more than twice those observed in the centrifuge model. For the PSL shaking events, the horizontal deformations predicted by the numerical model are 93 to 99% larger than those observed in the centrifuge model. The differences in displacements between the simulations and the centrifuge are caused by various factors. First, the pore pressures remain elevated in the unit cell models for a much longer time period than in the centrifuge model. Second, the unit cell models are infinite slope models that only model translational movement. These models have no passive resistance at the toe and thus, may overpredict displacements relative to the centrifuge model.

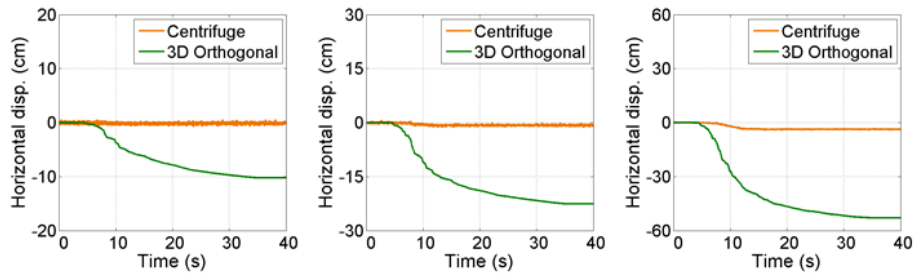


RLH01_PAC01
PGA = 0.11g

RLH01_PAC02
PGA = 0.26g

RLH01_PAC03
PGA = 0.38g

RLH01_PAC04
PGA = 0.95g



RLH01_PSL01
PGA = 0.10g

RLH01_PSL02
PGA = 0.22g

RLH01_PSL03
PGA = 0.46g

Centrifuge data is not available for shaking events RLH01_PSL04 and RLH01_SIN01 due to sensor malfunction.

Figure 7.13: Horizontal displacement-time histories for the untreated 3D unit cell model with shaking orthogonal to the slope and the untreated area of the RLH01 centrifuge model for shaking events RLH01_PAC01 (PGA = 0.11 g) through RLH01_PAC04 (PGA = 0.95 g) and RLH01_PSL01 (PGA = 0.10 g) through RLH01_PSL03 (PGA = 0.46 g).

7.4 Influence of Shaking Direction on the Treated 3D Unit Cell Models

This section focuses on the numerical modeling of the drain-treated condition and examines how the direction of shaking affects the 3D drainage conditions. Specifically, the pore pressure and horizontal deformation data for the treated 3D unit cell models are compared for shaking parallel and orthogonal to the slope.

Figures 7.14 through 7.16 show the excess pore pressure-time histories for the treated parallel and orthogonal 3D unit cell models for the PAC events (Figure 7.14), PSL events (Figure 7.15), and SIN event (Figure 7.16). It can be seen in Figures 7.14 and 7.15 that for the PAC and PSL events, the most significant difference is again in the hydrodynamic effects due to the downslope inertial forces and large shear strains that develop in the parallel model and do not develop in the orthogonal model. For SIN01 (Figure 7.3), the pore pressures in the orthogonal model are again lower during shaking and then jump up after immediately at the end of shaking, although the pore pressure jump for the treated model is not as significant as it was for the untreated model.

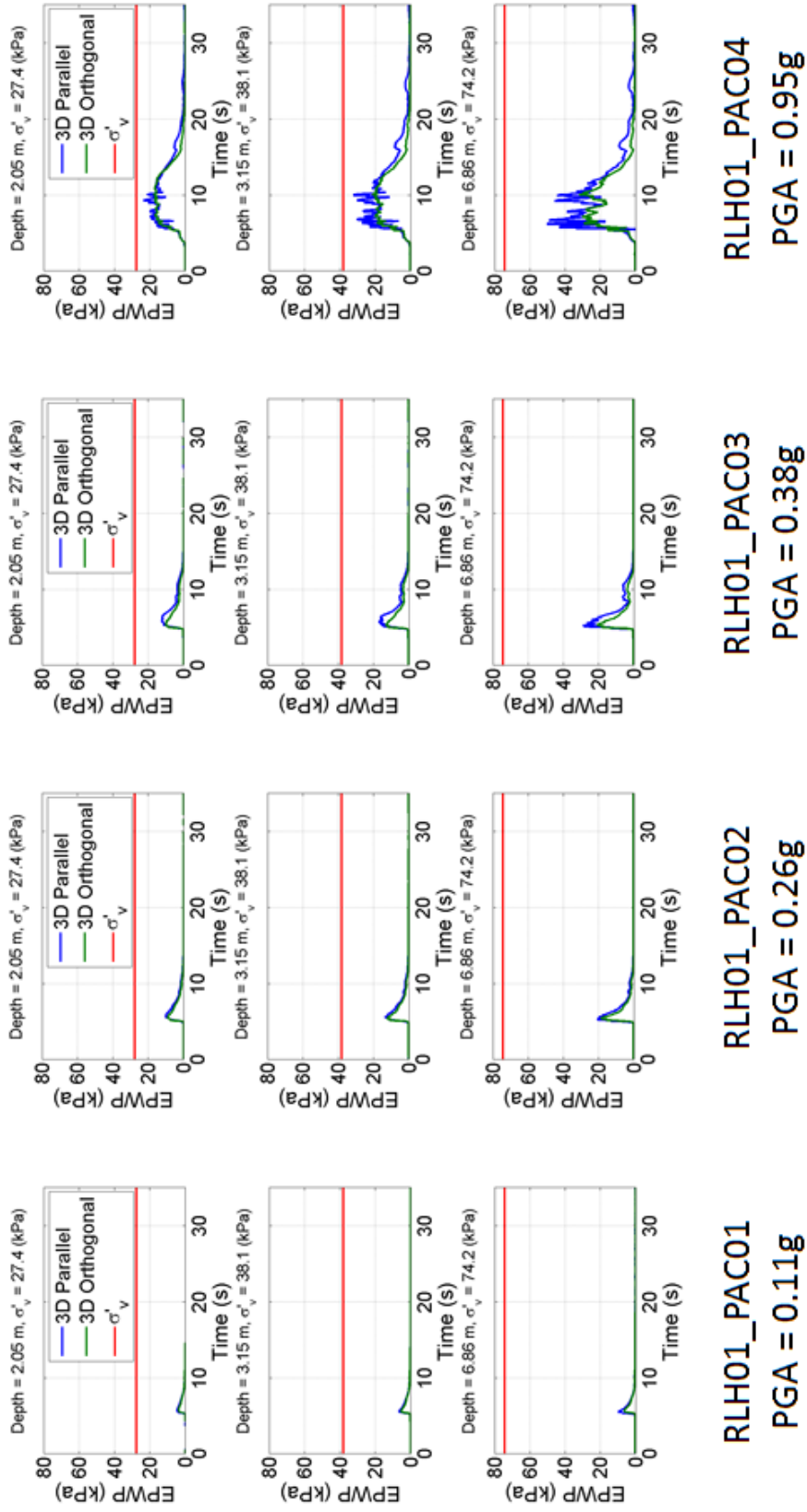


Figure 7.14: Excess pore water pressure-time histories for the treated 3D unit cell models at three different depths for shaking events RLH01_PAC01 (PGA = 0.11 g) through RLH01_PAC04 (PGA = 0.95 g).

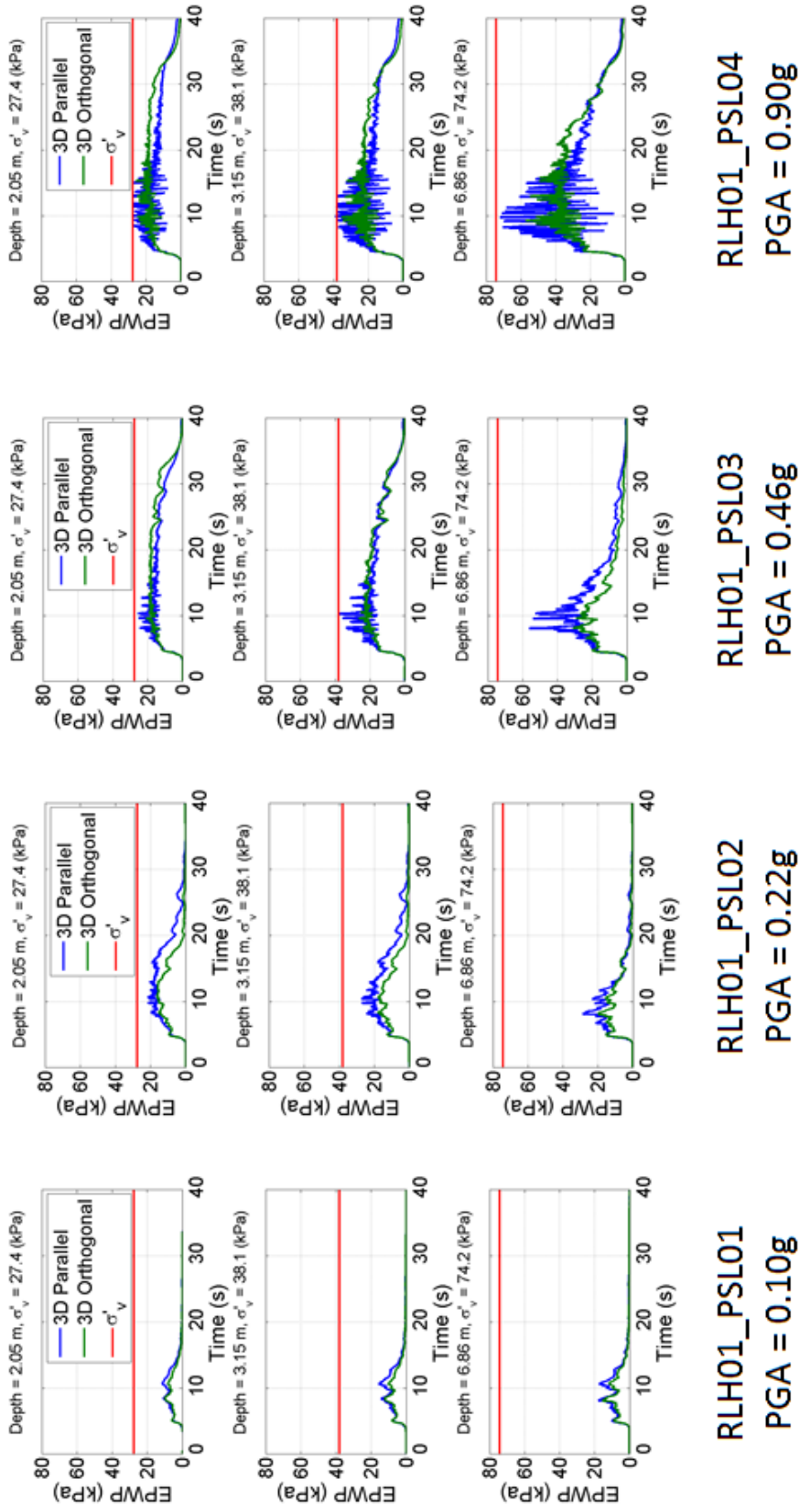
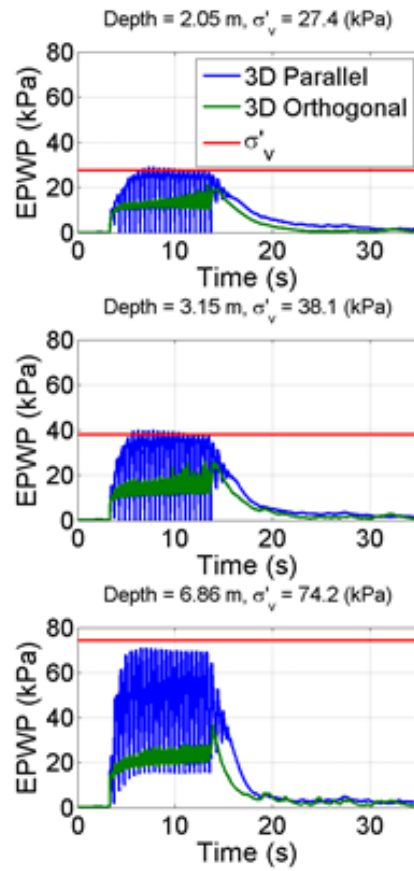


Figure 7.15: Excess pore water pressure-time histories for the treated 3D unit cell models at three different depths for shaking events RLH01_PSL01 (PGA = 0.10 g) through RLH01_PSL04 (PGA = 0.90 g).



RLH01_SIN01
 PGA = 0.60g

Figure 7.16: Excess pore water pressure-time histories for the treated 3D unit cell models at three different depths for the RLH01_SIN01 shaking event (PGA = 0.60 g).

Figures 7.17 through 7.19 show the horizontal (downslope) displacement-time histories at the top of the clay layer and horizontal displacement vs. depth profiles for the treated parallel and orthogonal 3D unit cell models for the PAC events (Figure 7.17), PSL events (Figure 7.18), and SIN event (Figure 7.19). Similar to the untreated models, parallel shaking leads to 20 to 80% larger deformations because of the downslope inertial effects. This difference is most significant under higher levels of shaking where the inertial effects are more destabilizing. These results are similar to those for the untreated simulations (Section 7.3).

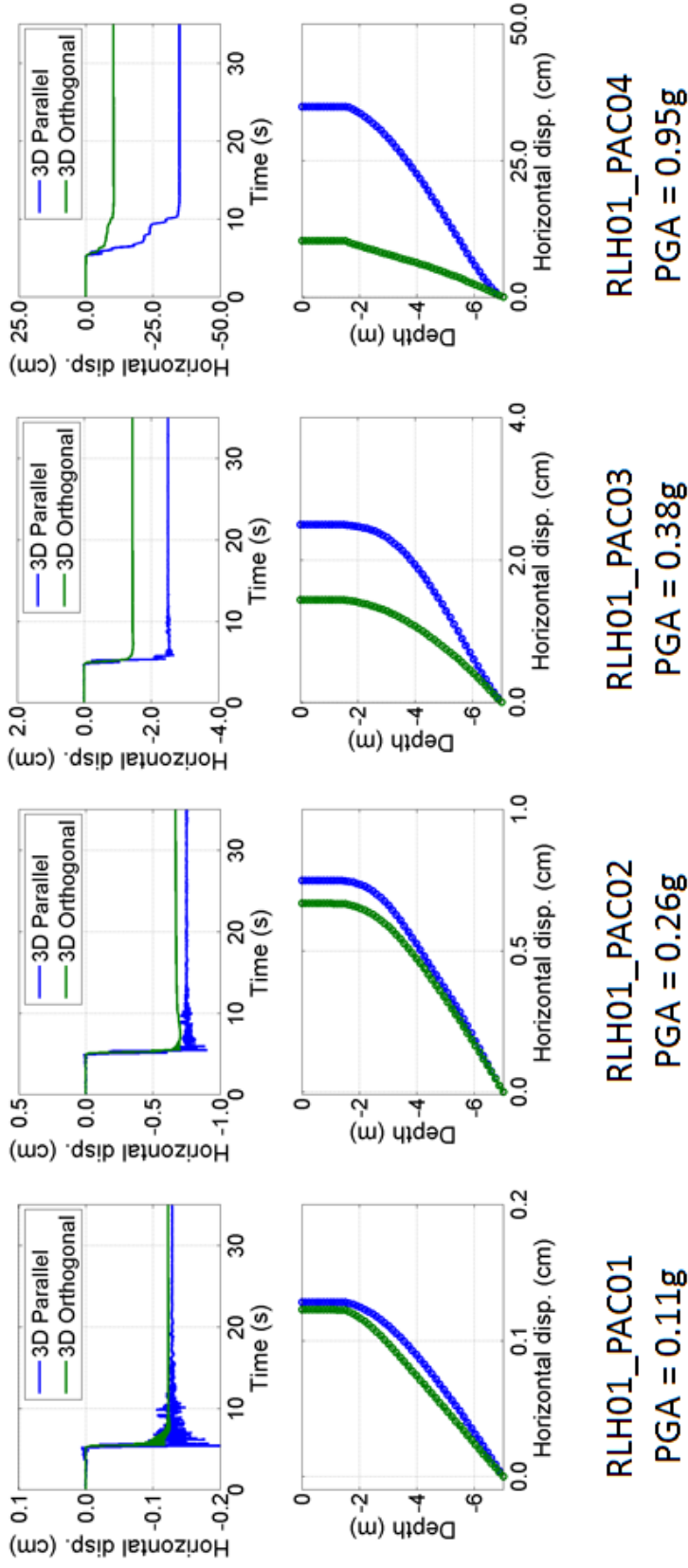


Figure 7.17: Horizontal displacement-time histories at the top of the clay layer and horizontal displacement vs. depth profiles for the treated 3D unit cell models for shaking events RLH01_PAC01 (PGA = 0.11 g) through RLH01_PAC04 (PGA = 0.95 g).

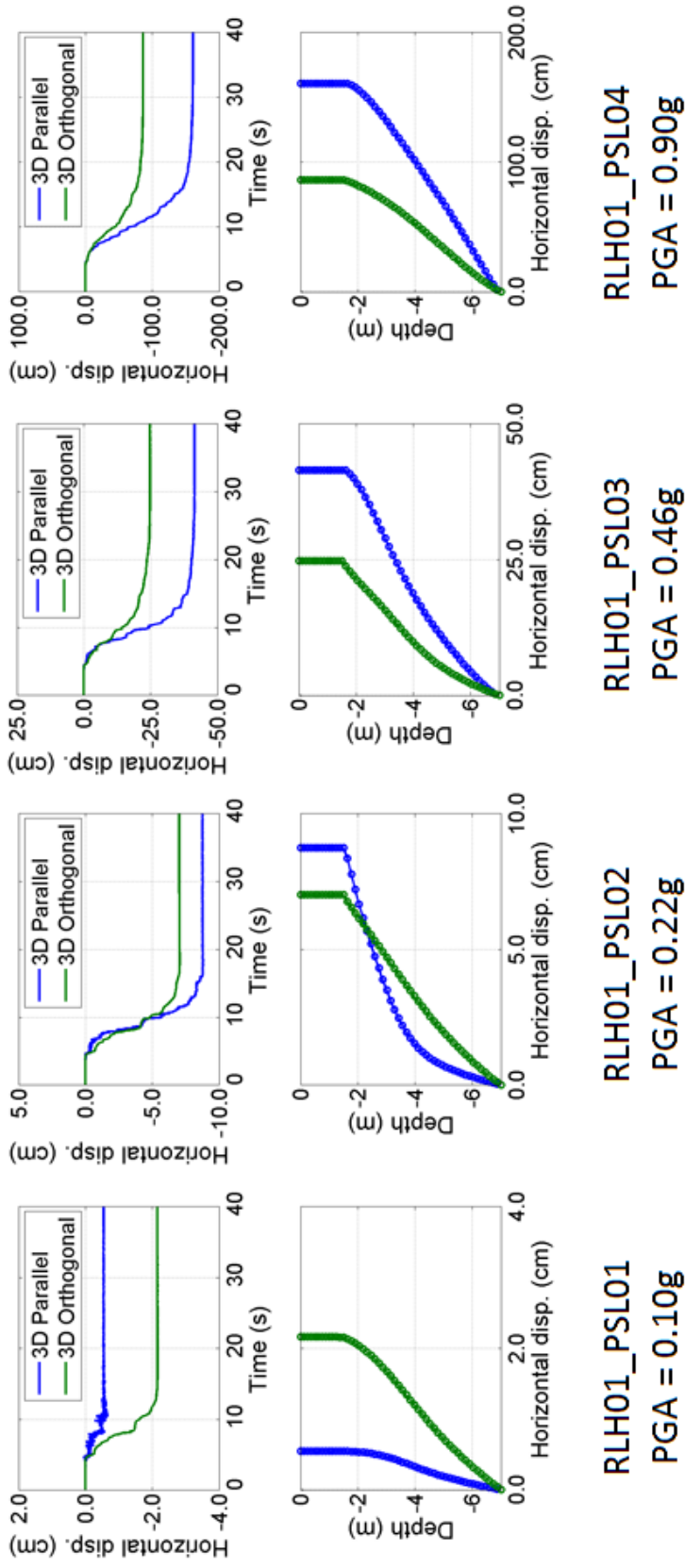
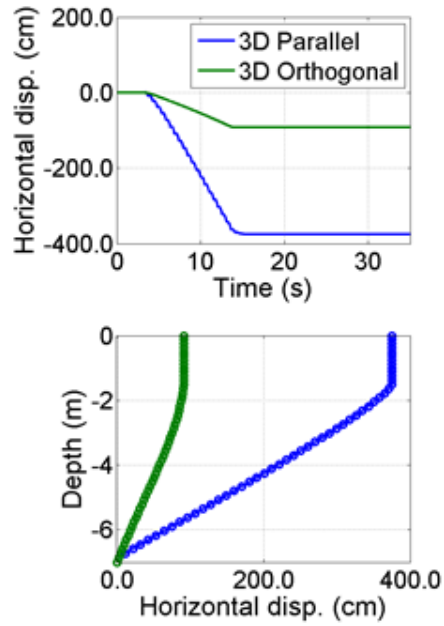


Figure 7.18: Horizontal displacement-time histories at the top of the clay layer and horizontal displacement vs. depth profiles for the treated 3D unit cell models for shaking events RLH01_PSL01 (PGA = 0.10 g) through RLH01_PSL04 (PGA = 0.90 g).



RLH01_SIN01
PGA = 0.60g

Figure 7.19: Horizontal displacement-time histories at the top of the clay layer and horizontal displacement vs. depth profiles for the treated 3D unit cell models for the RLH01_SIN01 shaking event (PGA = 0.60 g).

7.5 Comparison of Treated Numerical Model and Centrifuge Data

This section details the comparison between the pore pressure and deformation data for the 3D unit cell model with shaking orthogonal to the slope (i.e. orthogonal 3D unit cell model) and the RLH01 centrifuge model for the treated condition. Figures 7.20 through 7.22 show the excess pore pressure-time histories for the treated orthogonal 3D unit cell model and the treated area of the RLH01 centrifuge model. It can be seen in Figure 7.20 that there is a fairly good match between the simulated and experimental pore pressure data for the PAC shaking events. For all four of the PAC shaking events, the peak pore pressures and the rate of pore pressure dissipation predicted by the numerical model are similar to the centrifuge data. The match between the simulated and experimental pore pressure data is not as good for the PSL events (Figure 7.21). For PSL01 and PSL02, the numerical model slightly overestimates the peak excess pore pressures. Additionally, pore pressures in the numerical model are generated earlier, which is likely a result of the low-level accelerations at the start of shaking to which the centrifuge model is less sensitive as a result of the inertia of the container. For PSL03 and PSL04, the excess pore pressures in the numerical model remain elevated well after significant shaking ends, particularly at mid-depth and near the sand/clay interface. This behavior was also observed in the RNK01 simulations (see Section 6.4) and is related to the numerical model's response to low-level accelerations when the stress path is near the failure surface. For SIN01 (Figure 7.22), the numerical model does well in predicting the excess pore pressures and even with the pore pressure jump, the simulated data compares well to the centrifuge data.

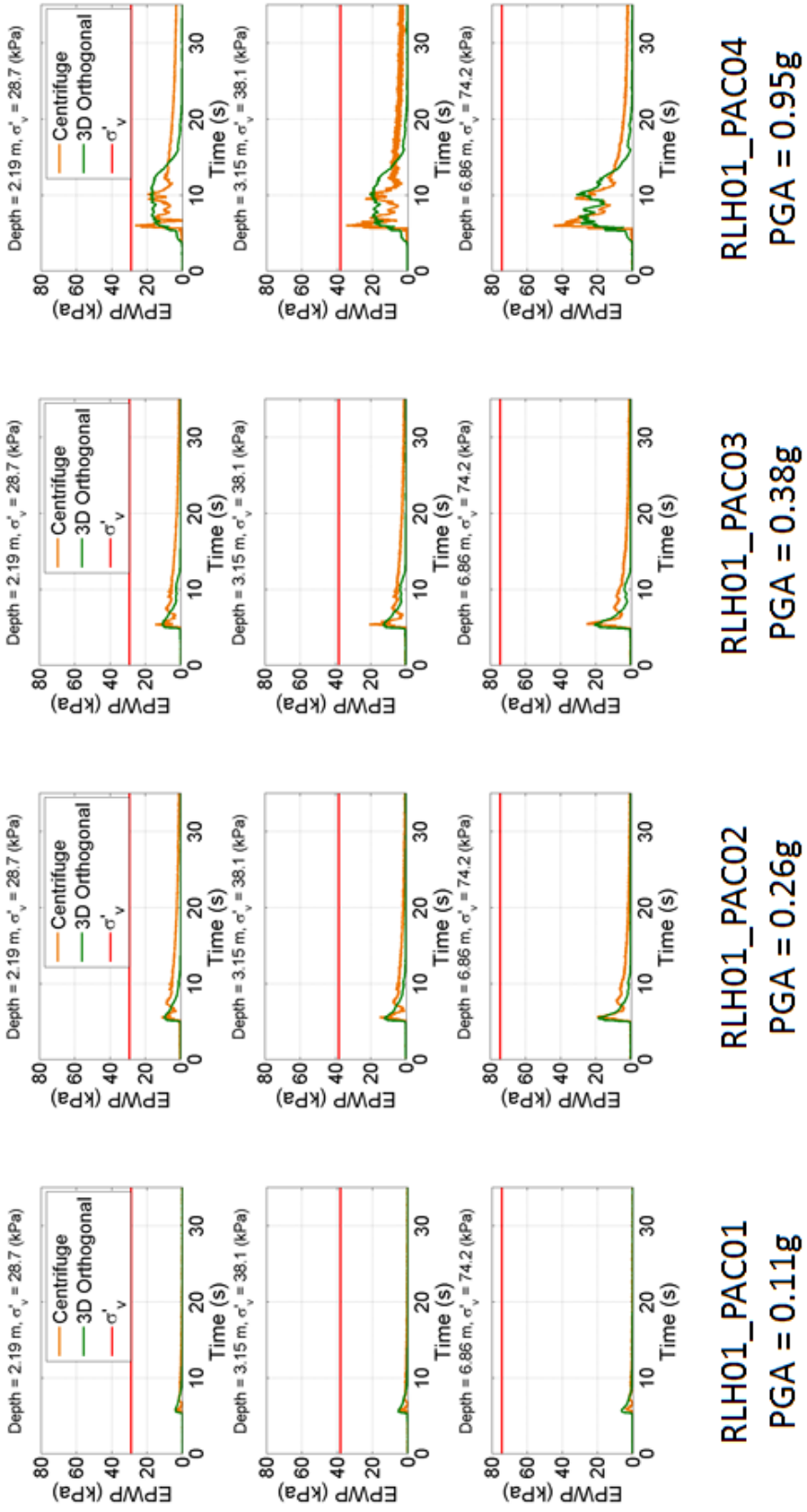


Figure 7.20: Excess pore water pressure-time histories for the treated 3D unit cell model with shaking orthogonal to the slope and the treated area of the RLH01 centrifuge model for shaking events RLH01_PAC01 (PGA = 0.11 g) through RLH01_PAC04 (PGA = 0.95 g).

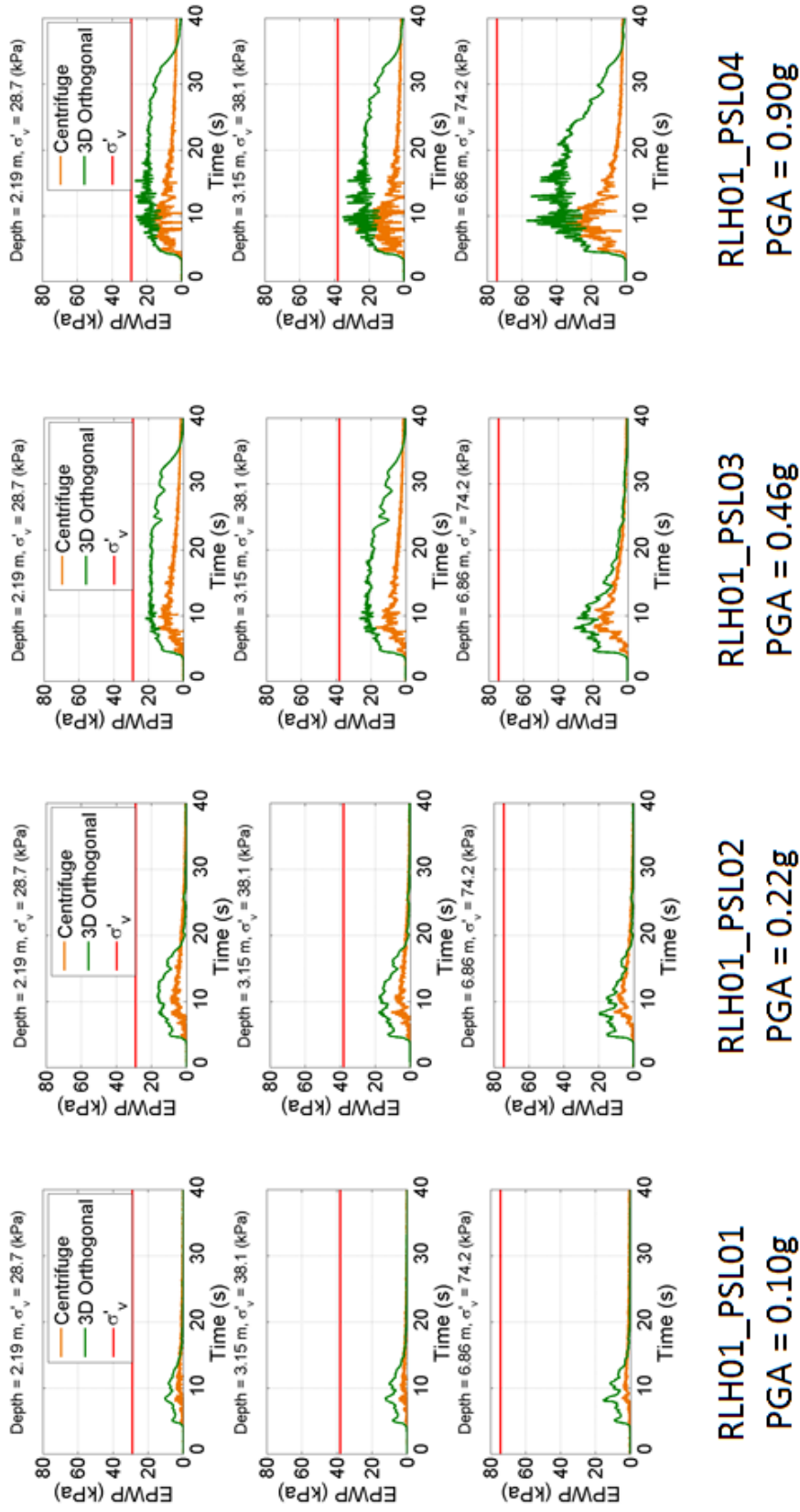
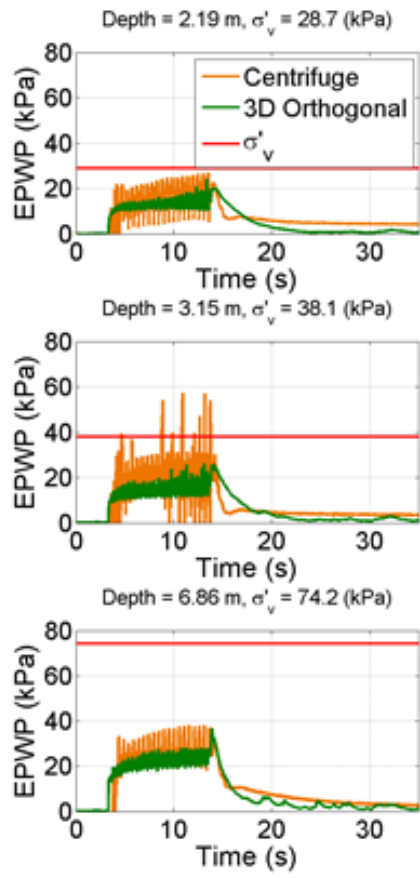


Figure 7.21: Excess pore water pressure-time histories for the treated 3D unit cell model with shaking orthogonal to the slope and the treated area of the RLH01 centrifuge model for shaking events RLH01_PSL01 (PGA = 0.10 g) through RLH01_PSL04 (PGA = 0.90 g).



SIN01
PGA = 0.60g

Figure 7.22: Excess pore water pressure-time histories for the treated 3D unit cell model with shaking orthogonal to the slope and the treated area of the RLH01 centrifuge model for the RLH01_SIN01 shaking event (PGA = 0.60 g).

Figure 7.23 shows the horizontal (downslope) displacement-time histories at the top of the clay layer for the treated orthogonal 3D unit cell model and the treated area of the RLH01 centrifuge model. It can be seen that the simulated and experimental data are comparable for the PAC shaking events, and even though the data differs both models predict relatively small deformations (i.e., less than about 10 cm) for all four events. For the PSL and SIN shaking events, the simulated and experimental data are not as comparable; the numerical model overpredicts the horizontal deformations by 80 to 95%. Again this overprediction is a result of the infinite slope geometry and the lack of passive resistance at the toe of the slope in the numerical model. Additionally, for the PSL shaking events, the peak pore pressures in the numerical model are larger than in the centrifuge and these large pore pressures are maintained for a longer time (Figure 7.21). As a result, the deformations occur over a longer time period for the numerical model. For example, significant shaking ends at around 19 seconds, but the horizontal deformations for the simulations of PSL03 and PSL04 continue on for several seconds after shaking ends, while the centrifuge model stopped at around 11 seconds.

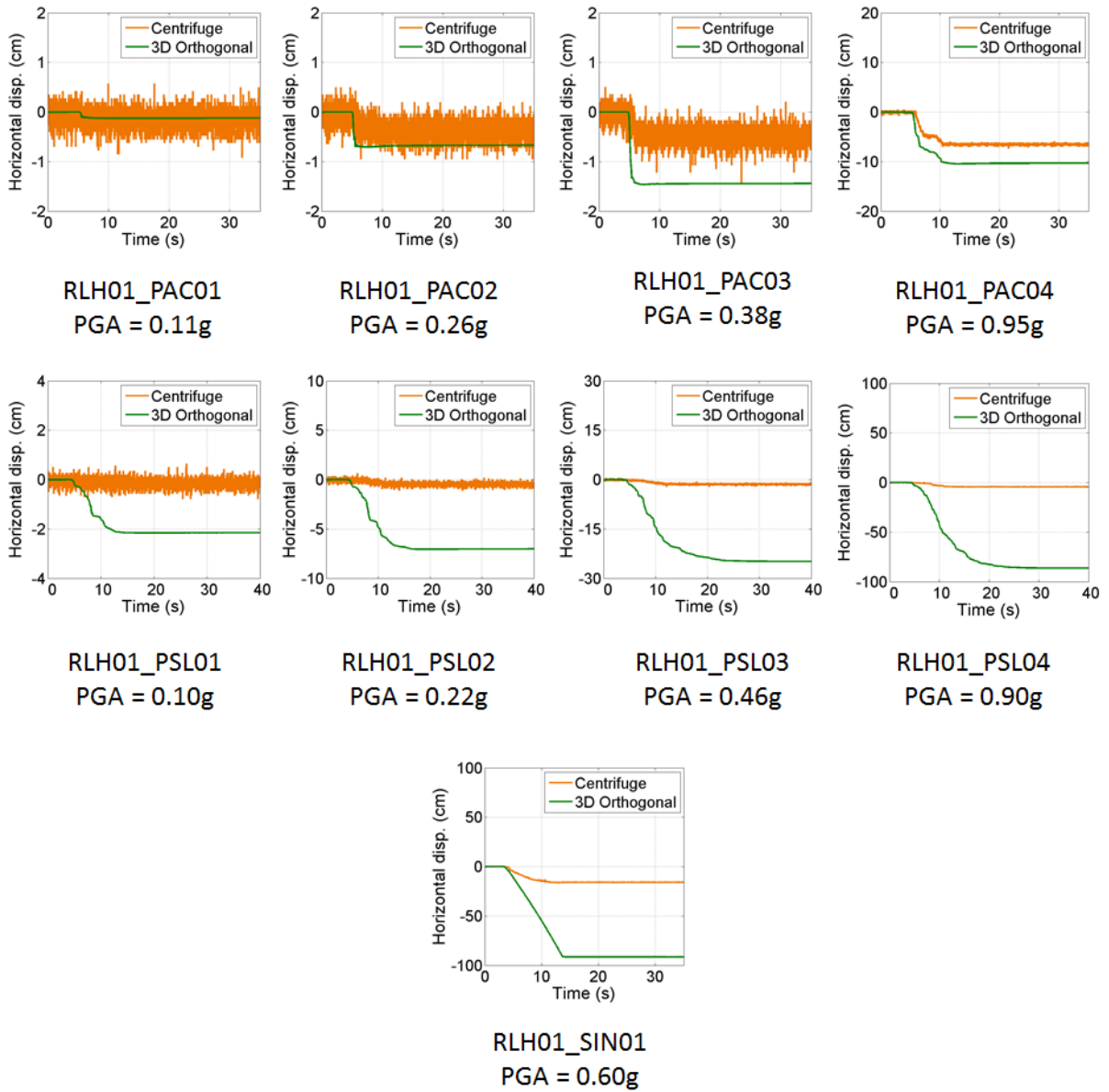


Figure 7.23: Horizontal displacement-time histories for the treated 3D unit cell model with shaking orthogonal to the slope and the treated area of the RLH01 centrifuge model for shaking events RLH01_PAC01 (PGA = 0.11 g) through RLH01_PAC04 (PGA = 0.95 g), RLH01_PSL01 (PGA = 0.10 g) through RLH01_PSL04 (PGA = 0.90 g), and RLH01_SIN01 (PGA = 0.60 g).

7.6 Comparison of Treated and Untreated Numerical Models

RLH01 is the only one of the three centrifuge tests in which reinforcement due to the stiffness of the model drains was not an issue; thus, the improvement observed in the RLH01 centrifuge test can be ascribed solely to the effects of drainage. This section compares the pore pressure and deformation data for the treated and untreated orthogonal 3D unit cell models, and compares the improvement observed in the numerical models to that observed in the centrifuge test.

Figures 7.24 through 7.26 show the excess pore pressure-time histories for the untreated and treated orthogonal 3D unit cell models. For the PAC shaking events (Figure 7.24), it can be seen that the drain-treated model has lower peak excess pore pressures and faster pore pressure dissipation than the untreated model (note the untreated model is manually drained via vertical drainage through the clay layer at the end of significant shaking). For PSL01 and PSL02 (Figure 7.25), the treated model again has lower peak excess pore pressures and faster pore pressure dissipation. For PSL03 and PSL04 (Figure 7.25), the excess pore pressures are approaching their maximum based on the inclination of the slope and the treated and untreated peak excess pore pressures are similar, particularly near the sand/clay interface and at mid-depth. For SIN01 (Figure 7.26), the treated and untreated excess pore pressures are nearly identical and both models exhibit the post-shaking pore pressure jump; however, the pore pressures in the treated model dissipate while the excess pore pressures in the untreated model decrease some but are dissipating at a much slower rate.

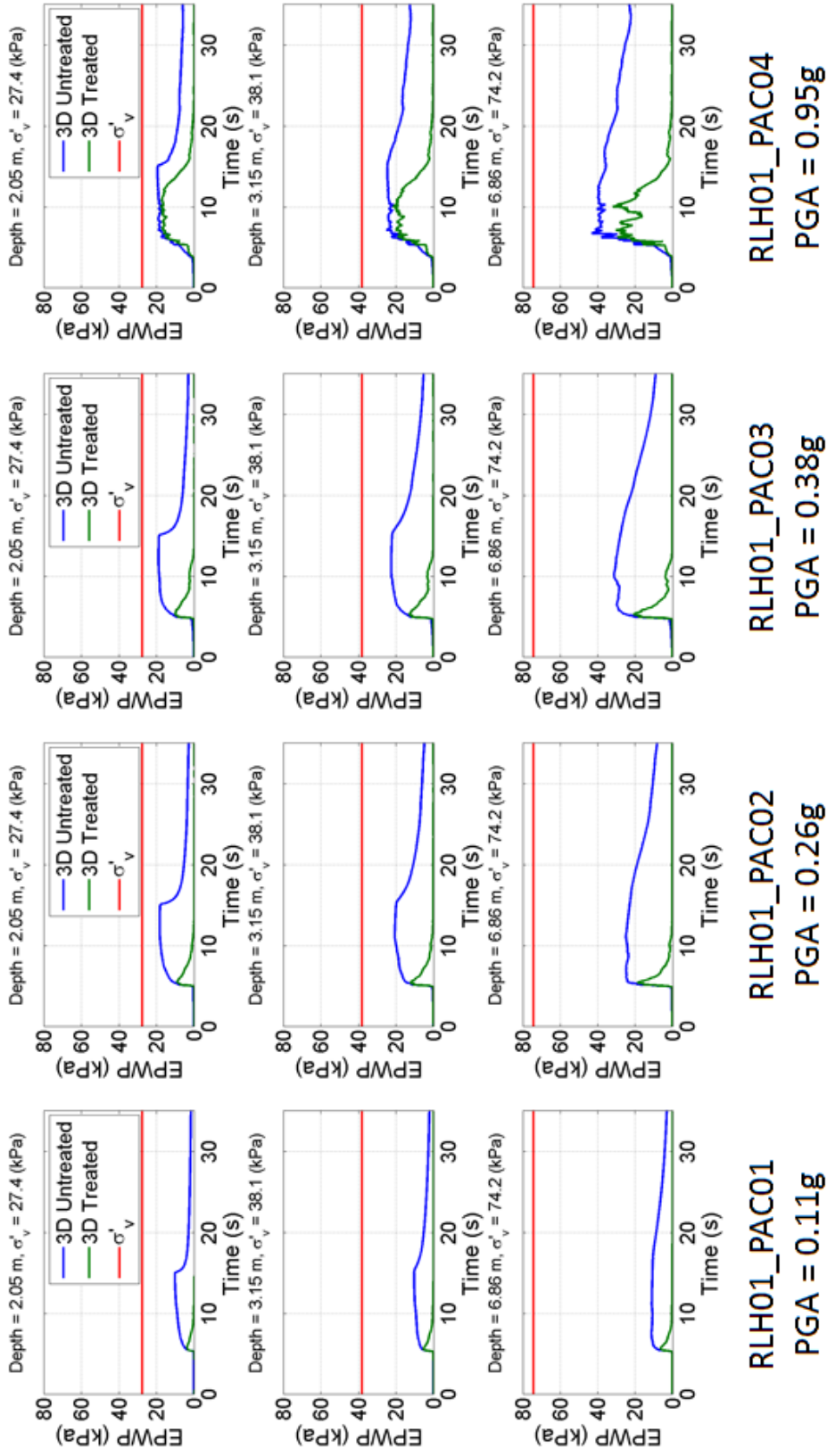


Figure 7.24: Excess pore water pressure-time histories for the untreated and treated 3D unit cell models with shaking orthogonal to the slope for shaking events RLH01_PAC01 (PGA = 0.11 g) through RLH01_PAC04 (PGA = 0.95 g).

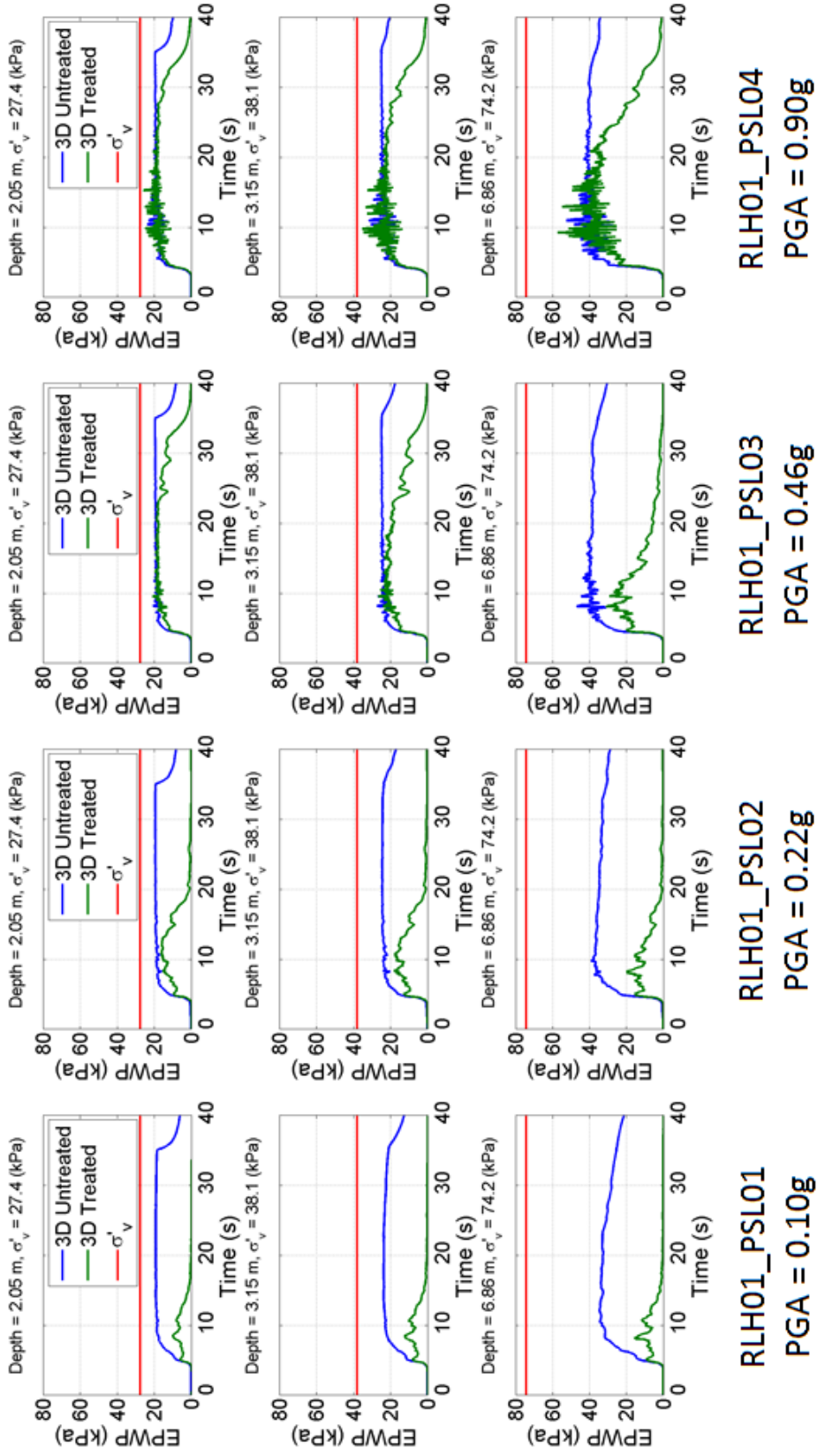


Figure 7.25: Excess pore water pressure-time histories for the untreated and treated 3D unit cell models with shaking orthogonal to the slope for shaking events RLH01_PSL01 (PGA = 0.10 g) through RLH01_PSL04 (PGA = 0.90 g).

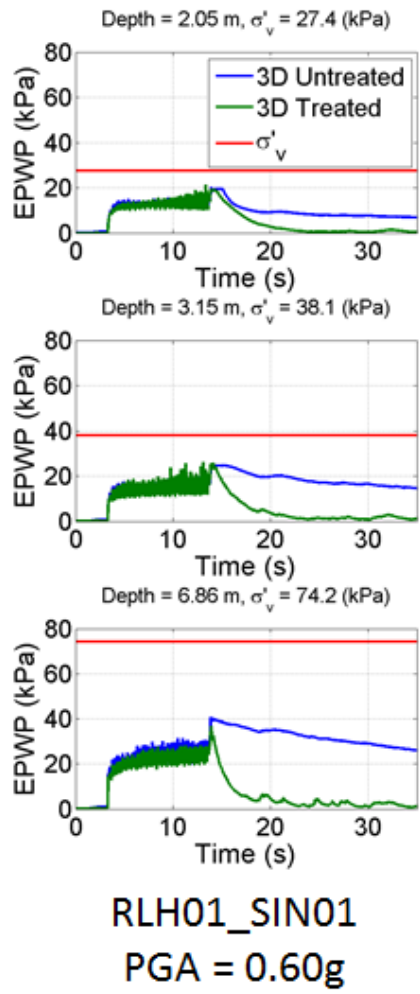


Figure 7.26: Excess pore water pressure-time histories for the untreated and treated 3D unit cell models with shaking orthogonal to the slope for the RLH01_SIN01 shaking event (PGA = 0.60 g).

Figure 7.27 shows the displacement vs. depth profiles at selected times for the three highest intensity RLH01 shaking events - PAC04, PSL04, and SIN01. In comparison to the displacement vs. depth profiles for the centrifuge data (Figure ??), the maximum r_u achieved and sustained by the numerical models is lower due to the static shear stresses in the slope. In the centrifuge test, flattening of the slopes over the course of the test decreased the static shear stresses, which allowed the slopes to develop higher excess pore pressures in the later shaking events. For the PAC04 events (Figures 7.27a and b), the excess pore pressures in the untreated and treated areas are similar at time = 6 seconds. The pore pressures increase at time = 8 and 10 seconds, and that increase is larger in the untreated area than in the treated area. The pore pressures in the treated area dissipate by time = 14 seconds while the pore pressures in the untreated area remain elevated because the drainage phase is not triggered until 15 seconds in the untreated simulations. For the PSL04 shaking events (Figures 7.27c and d), the excess pore pressures in the untreated and treated areas are similar throughout the time of significant shaking and even up to time = 20 seconds as a result of the treated numerical model's sensitivity to low level accelerations, which keeps the excess pore pressures elevated. For the SIN01 events (Figures 7.27e and f), the treated and untreated excess pore pressures are similar at times = 8 and 12 seconds. The pore pressure jump occurs at time = 13 to 15 seconds (Figure 7.26). After the pore pressure jump, the excess pore pressures in the untreated area remain elevated even though the drainage phase has been triggered and the model is able to drain vertically through the clay layer, while the excess pore pressures in the treated model dissipate.

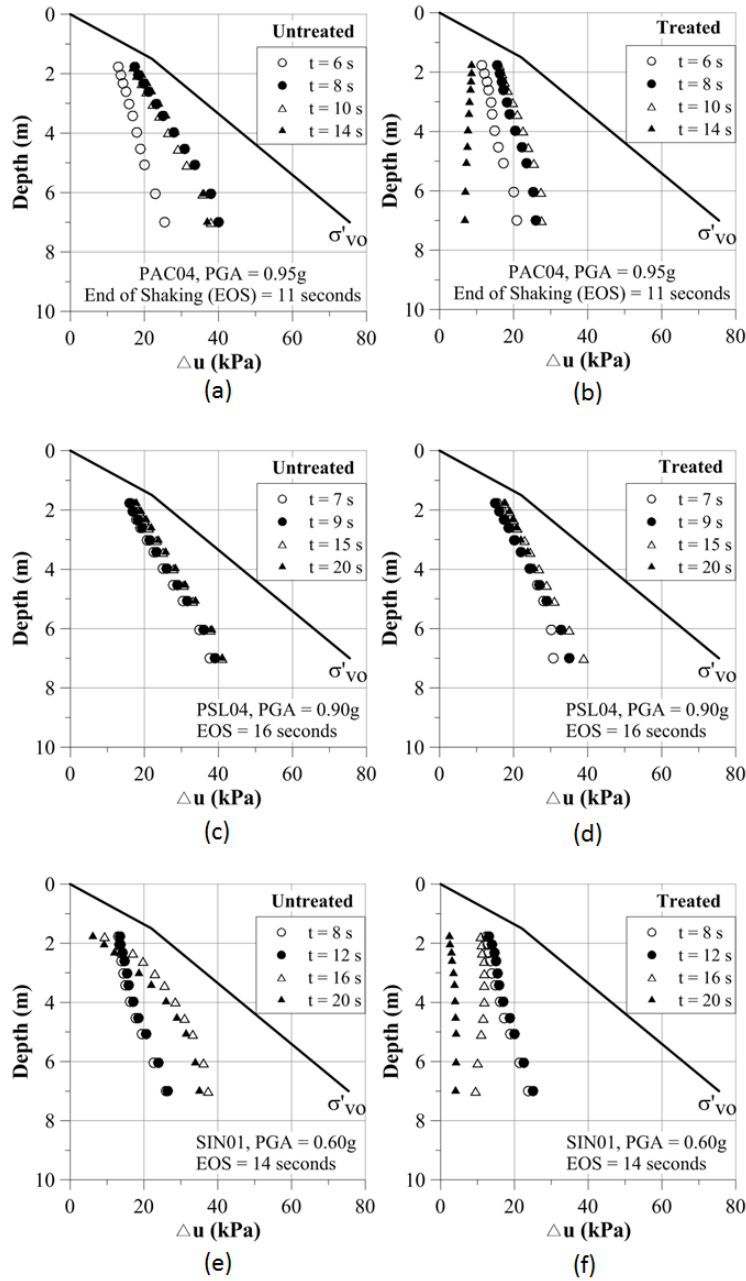


Figure 7.27: Excess pore water pressure vs. depth profiles at selected times for the untreated and treated 3D unit cell models with shaking orthogonal to the slope for the RLH01 PAC04, PSL04, and SIN01 shaking events.

Figure 7.28 shows the peak average excess pore water pressures ($\bar{r}_{u,\max}$) as a function of PGA for the treated and untreated orthogonal 3D unit cell models for the PAC and PSL shaking events. It can be seen that for all but the PSL04 shaking event, the $\bar{r}_{u,\max}$ values in the treated model are lower than in the untreated model. For the PSL04 shaking event, the treated model actually had a slightly higher $\bar{r}_{u,\max}$ than the untreated model. For this shake, both the untreated and treated pore pressures reach the maximum pore pressure cap that results from the presence of the static shear stresses in the slope, but hydrodynamic effects for the treated model result in slightly higher peaks in the pore pressure fluctuations, likely due to the effects of drainage, which increases the soil's strength and results in a stronger dilative response.

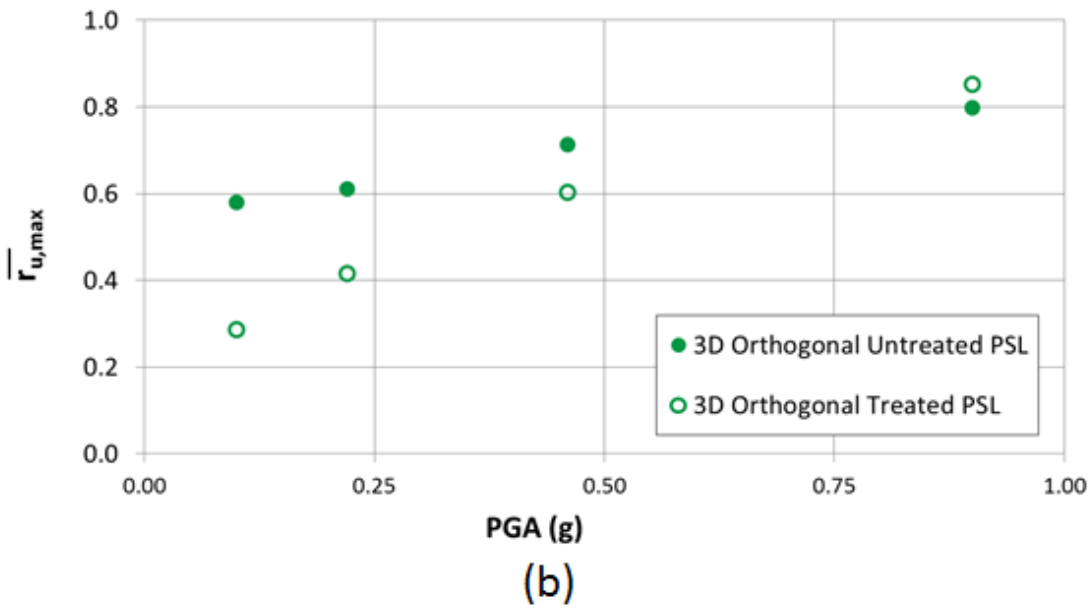
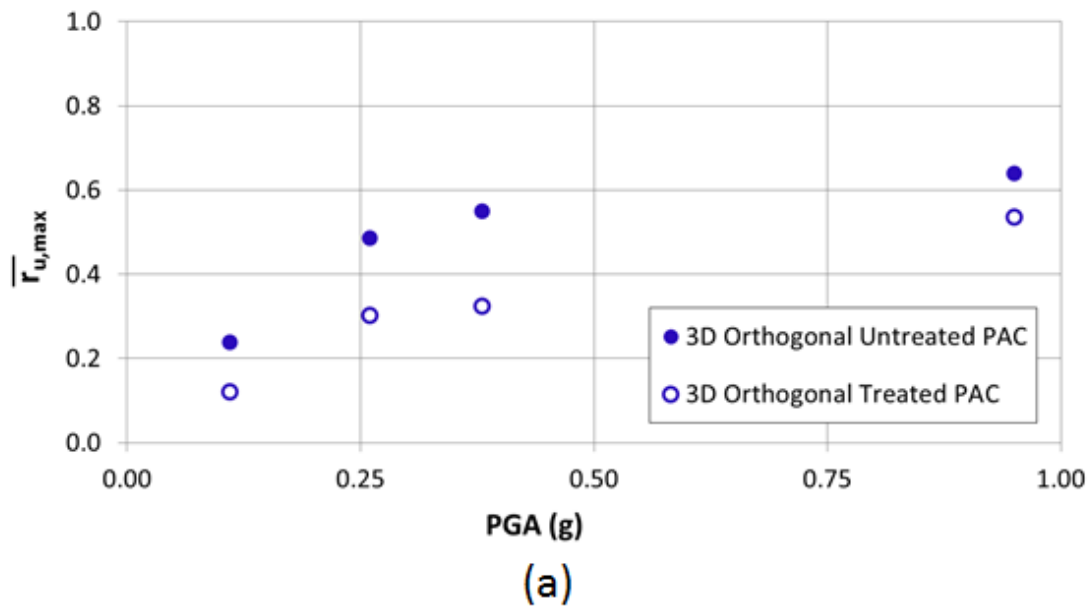


Figure 7.28: Peak average excess pore water pressures ($\bar{r}_{u,max}$) vs. PGA for the untreated and treated 3D unit cell models with shaking orthogonal to the slope for (a) the PAC shaking events and (b) the PSL shaking events.

Figures 7.29 through 7.31 show the horizontal (downslope) displacement-time histories at the top of the clay layer and the horizontal displacement vs. depth profiles for the untreated and treated orthogonal 3D unit cell models. It can be seen that for the PAC and PSL01 through PSL03 shaking events (Figures 7.29 and 7.30, respectively), the untreated model produced significantly larger horizontal deformations (i.e., about 30 to 80% reduction). For shaking events PSL04 and SIN01 (Figures 7.30 and 7.31, respectively), the untreated and treated horizontal deformations are very similar. In both cases the treated and untreated pore pressures were very similar because they hit the threshold associated with the slope angle.

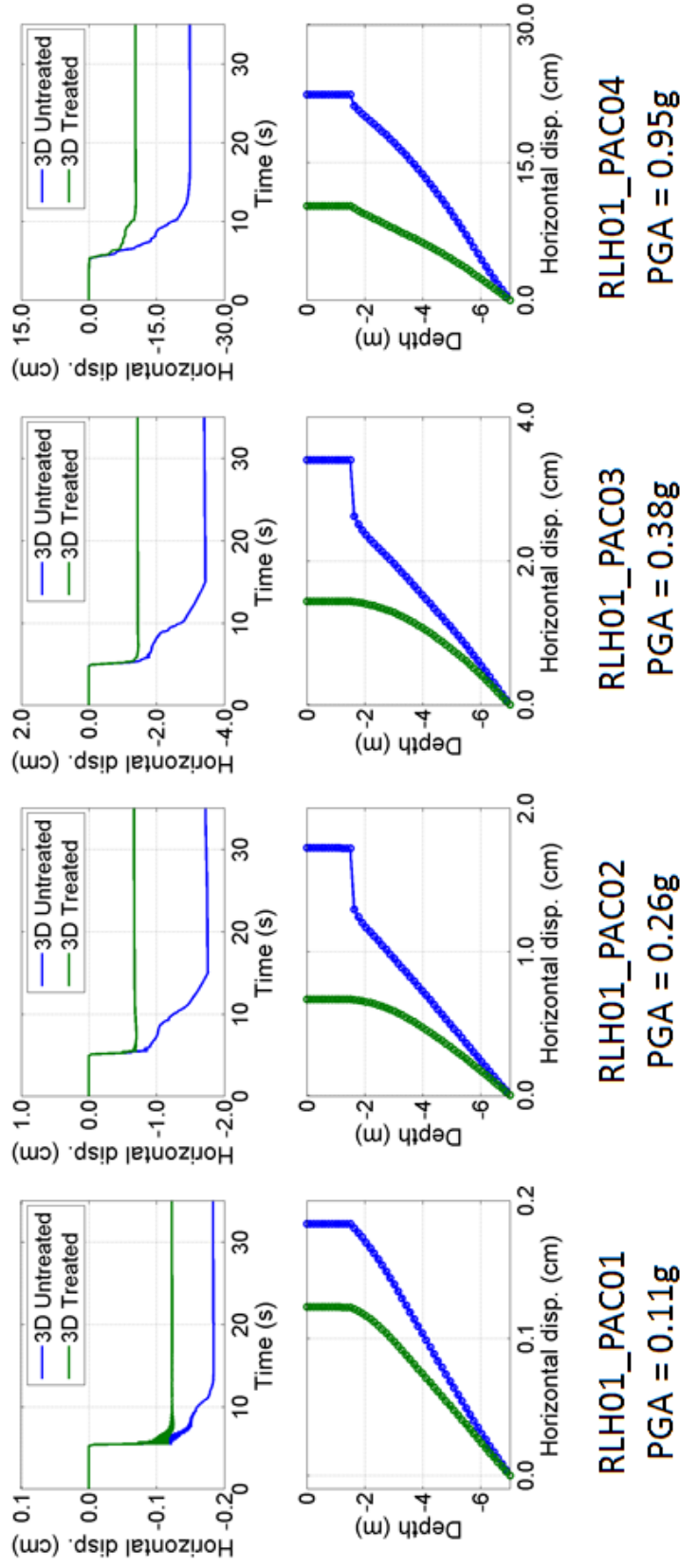


Figure 7.29: Horizontal displacement-time histories at the top of the clay layer and horizontal displacement vs. depth profiles for the untreated and treated 3D unit cell models with shaking orthogonal to the slope for shaking events RLH01_PAC01 (PGA = 0.11 g) through RLH01_PAC04 (PGA = 0.95 g).

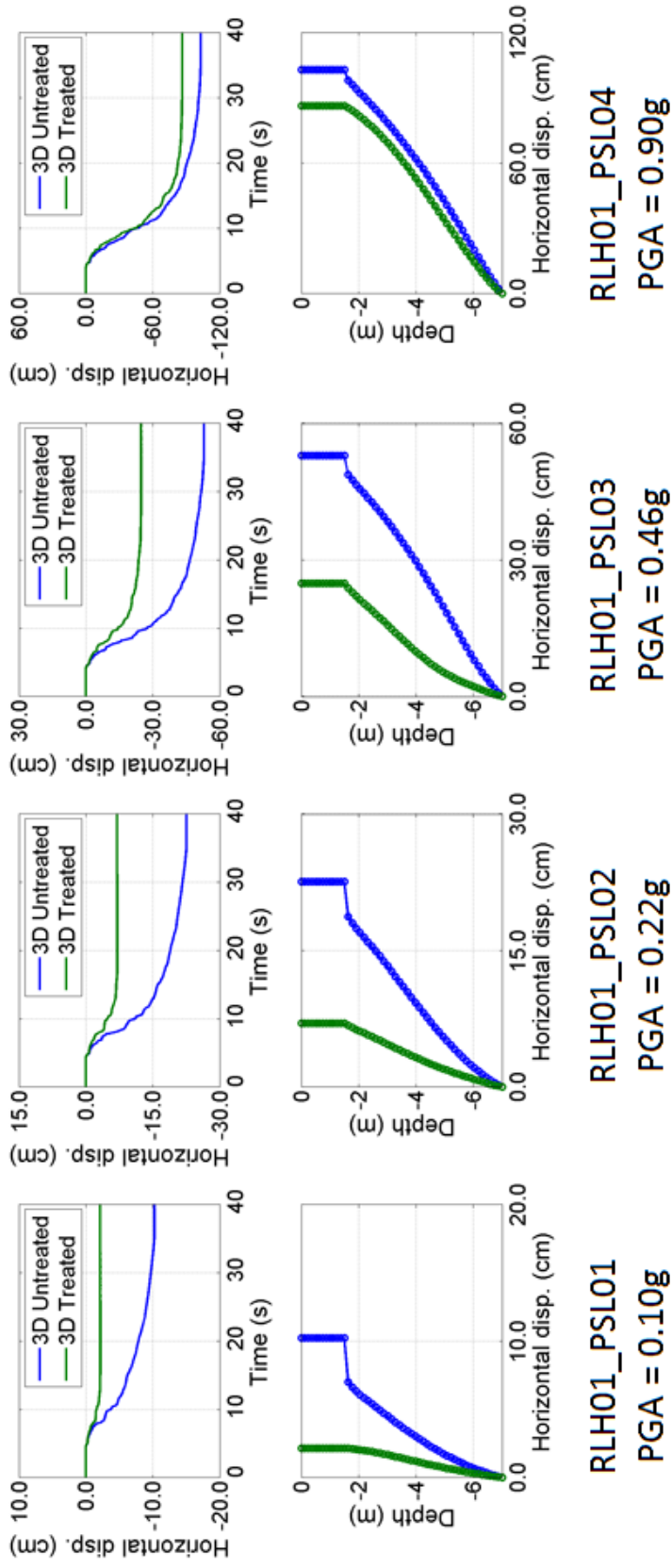


Figure 7.30: Horizontal displacement-time histories at the top of the clay layer and horizontal displacement vs. depth profiles for the untreated and treated 3D unit cell models with shaking orthogonal to the slope for shaking events RLH01_PSL01 (PGA = 0.10 g) through RLH01PSL04 (PGA = 0.90 g).

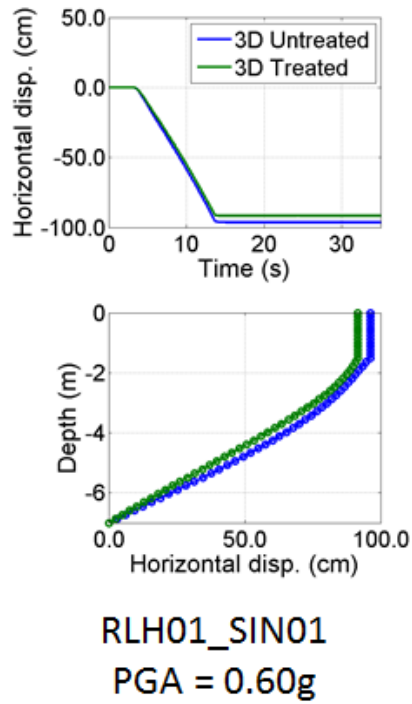


Figure 7.31: Horizontal displacement-time histories at the top of the clay layer and horizontal displacement vs. depth profiles for the untreated and treated 3D unit cell models with shaking orthogonal to the slope for the RLH01_SIN01 shaking event (PGA = 0.60 g).

Table 7.1 details the untreated and treated horizontal (downslope) deformations for the RLH01 centrifuge model and the orthogonal 3D unit cell models. In the centrifuge model, the horizontal deformations in the treated model are generally 20 to 60% smaller than the horizontal deformations in the untreated model. Considering only the larger shakes where deformations were significant (PAC03, PSL04, and PAC04), the improvement in the horizontal deformation ranged from about 40 to 70%. Unfortunately, the percent improvement for PSL04 and SIN01 could not be evaluated in the centrifuge because of sensor malfunctions. In the 3D unit cell models, there was a 30 to 60% improvement in the horizontal deformations for the PAC motions, a 20 to 80% improvement in the horizontal deformations for the PSL motions, and only a 5% improvement for the SIN01 motion. Considering the same three vents with significant deformation in the centrifuge test (PAC03, PSL03, and PAC04), the numerical models predicted percent improvement is about 50 to 60%. These values are consistent with those from the centrifuge. The numerical models show little to no improvement in the deformations for PSL04 and SIN01. However, the PSL pore pressure data is affected by the low-level accelerations and the SIN01 pore pressures are limited by the intersection of the octahedral shear stress with the failure plane.

Table 7.1: Untreated and treated horizontal deformations from centrifuge test RLH01 for all shaking events.

Centrifuge Test				
Motion	PGA (g)	Untreated (cm)	Treated (cm)	Improvement (%)
PAC01	0.11	0.13	0.10	22
PSL01	0.10	0.07	0.09	-32
PAC02	0.26	0.51	0.34	33
PSL02	0.22	0.70	0.44	37
PAC03	0.38	0.91	0.46	50
PSL03	0.46	3.64	1.34	63
PAC04	0.95	9.63	6.49	33
PSL04	0.90	–	4.30	–
SIN01	0.60	–	15.86	–

Orthogonal 3D Unit Cell Models				
Motion	PGA (g)	Untreated (cm)	Treated (cm)	Improvement (%)
PAC01	0.11	0.18	0.12	33
PSL01	0.10	10.23	2.16	79
PAC02	0.26	1.72	0.67	61
PSL02	0.22	22.56	7.02	69
PAC03	0.38	3.41	1.44	58
PSL03	0.46	51.74	24.84	52
PAC04	0.95	22.38	10.30	54
PSL04	0.90	102.98	86.38	16
SIN01	0.60	96.31	91.59	5

7.7 Summary

This chapter detailed the numerical simulations of the RLH01 centrifuge test and comparisons of the RLH01 simulation and experimental data. The RLH01 centrifuge test differs from the SSK01 and RNK01 centrifuge tests in that shaking took place orthogonal to the slope. It is not possible to shake a 2D model orthogonal to the slope; thus, the RLH01 simulation data was generated using the untreated and drain-treated 3D unit cell models. For comparison purposes, shaking was performed both parallel and orthogonal to the slope although only the orthogonal is used in the comparisons to the centrifuge data. The data was analyzed with emphasis placed on identifying the behavioral trends in the pore pressure and deformations that were observed in the centrifuge test.

The direction of shaking has a minimal effect on the induced pore water pressures for the untreated condition, although the data for the model in which shaking was applied parallel to the slope show more hydrodynamic effects, particularly for the higher-intensity events. For both the parallel and orthogonal models, the excess pore pressures peak at an r_u less than one, which is caused by the static shear stresses in the slope. The horizontal deformations for the orthogonal model were shown to be 40 to 80% smaller than those produced by the parallel model because of the lack of downslope, destabilizing inertial effects when shaking is orthogonal to the slope.

When compared with the centrifuge data, the simulated peak excess pore pressures for the untreated condition were similar for the PAC events, but they were larger for the PSL events. For the SIN event the pore pressure data for the untreated condition is affected by the intersection of the octahedral shear stresses with the failure plane, which in combination with the lack of small cycles of acceleration in the SIN motion cause excess pore pressures to remain below the r_u threshold determined by the static shear stress. Both the numerical model and the centrifuge model predict comparable deformations for the PAC events, but the numerical model overpredicts the horizontal (downslope) deformations for the PSL events by over 90%. The overprediction in deformation is due to the lack of passive resistance at the toe for the infinite slope modeled by the 3D unit cell.

For the treated condition, the simulated and experimental peak excess pore pressures for the PAC and PSL events are comparable, although the simulated excess pore pressures for the PSL events remain elevated well after shaking ends. This behavior was also observed in the RNK01 simulations and was shown to be a result of the model's sensitivity to low-level accelerations when the stress path is near the failure surface. The numerical and centrifuge models predict minimal horizontal deformations for the PAC events, and the numerical model overestimates the horizontal deformations for the PSL and SIN events by 80 to 95%. These events have the largest peak r_u values and thus are most influenced by the infinite slope condition.

The treated and untreated simulation data showed that the treated model generally produced lower peak excess pore pressures and smaller horizontal deformations. There was about a 30 to 60% improvement in the horizontal (downslope) deformations for the PAC motions, which compares well with the percent improvement observed in the centrifuge test. The percent improvement from the numerical models for the PSL and SIN events was not as comparable to the centrifuge observations, but the pore pressures for the PSL events were affected by the model's sensitivity to low-level accelerations and the pore pressures for the SIN event were affected by the intersection of the octahedral shear stress with the failure plane.

Chapter 8

Investigation of the Pore Pressure - Deformation Relationship

8.1 Introduction

The design methods currently used for drains are based almost exclusively on maintaining the seismically-induced excess pore pressures below a specified threshold. These tools do not provide estimates of expected deformations, and therefore the performance of a drain-treated site cannot be evaluated. This approach implies that acceptable performance will be achieved if the pore pressures are maintained below the selected threshold and unacceptable performance will occur if the threshold is exceeded. However, it is possible that drainage will improve the site performance even if the pore pressure threshold is exceeded.

Performance-based design of a drain-treated lateral spread site requires a better understanding of the complex interaction between pore pressure generation and dissipation and the development of deformations at a drain-treated lateral spread site. This chapter investigates the relationship between excess pore pressures and horizontal deformations using both the centrifuge and numerical modeling results. First, the critical features of the pore pressure and deformation responses will be identified. Then, these features will be used to determine the parameters that are most indicative of site performance.

8.2 Characteristics of Pore Pressure and Deformation Responses

To investigate the factors that influence deformation at a lateral spread site, the pore pressure and deformation responses are considered for centrifuge test RLH01. This test is considered because it is the only test where deformations were not influenced by the presence of stiff drains. Figures 8.1 through 8.3 show the \bar{r}_u , horizontal deformation, and input acceleration-time histories for the untreated and treated areas of the RLH01 centrifuge model for the PAC, PSL, and SIN shaking events. For the PAC events (Figure 8.1), it can be seen that the untreated and treated deformation responses for PAC01 through PAC03 are minimal. For these events, \bar{r}_u generally stays below 0.4 to 0.5. Deformations finally become significant (> 1 cm) for the PAC04 event where \bar{r}_u exceeds 0.5 to 0.6. For this event, $\bar{r}_{u,\max}$ is actually higher in the treated area, but the pore pressures in the untreated area remain elevated while the pore pressures in the treated area

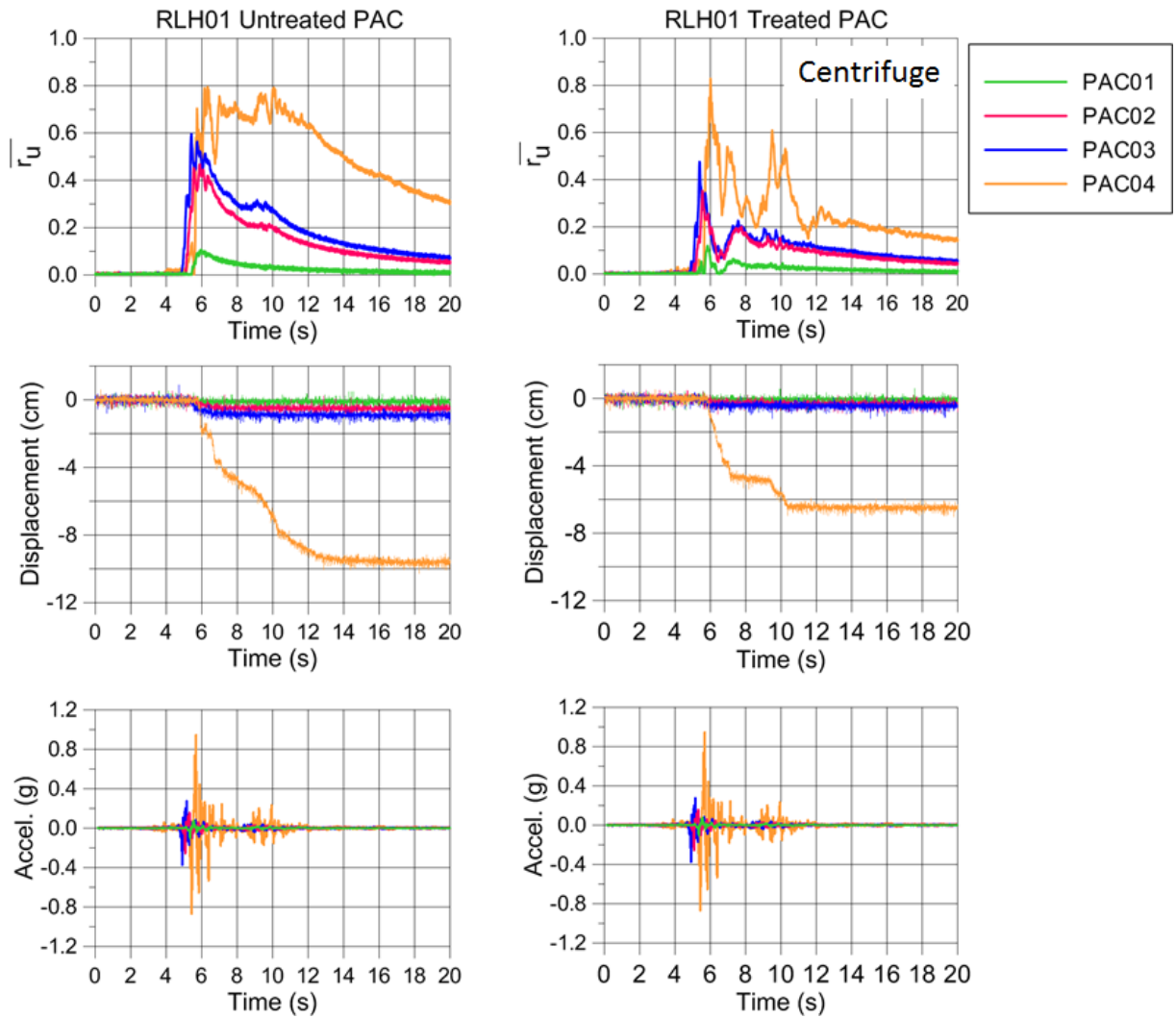


Figure 8.1: \bar{r}_u , horizontal deformation, and input acceleration-time histories for the untreated and treated areas of the RLH01 centrifuge model for the PAC shaking events.

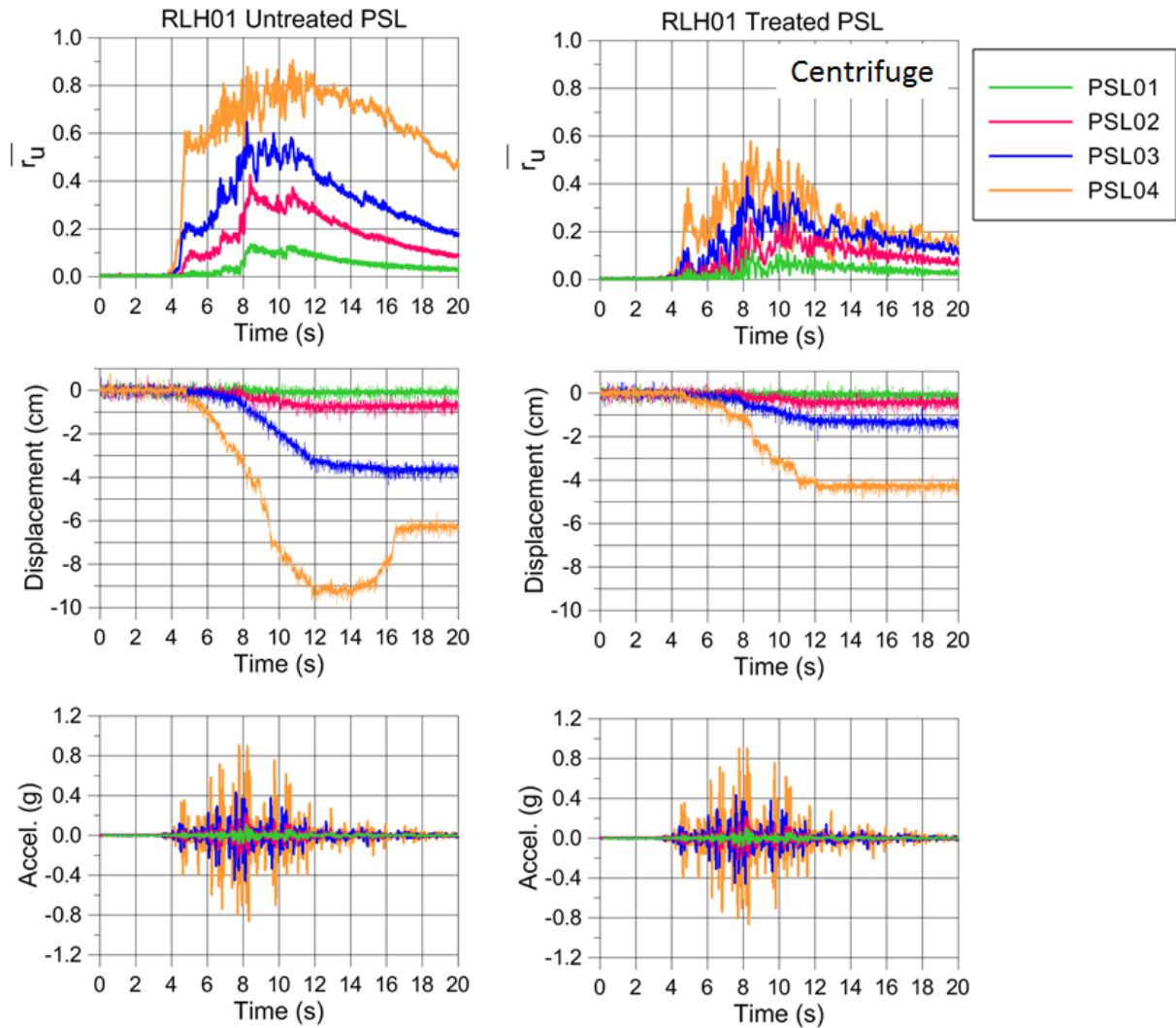


Figure 8.2: \bar{r}_u , horizontal deformation, and input acceleration-time histories for the untreated and treated areas of the RLH01 centrifuge model for the PSL shaking events.

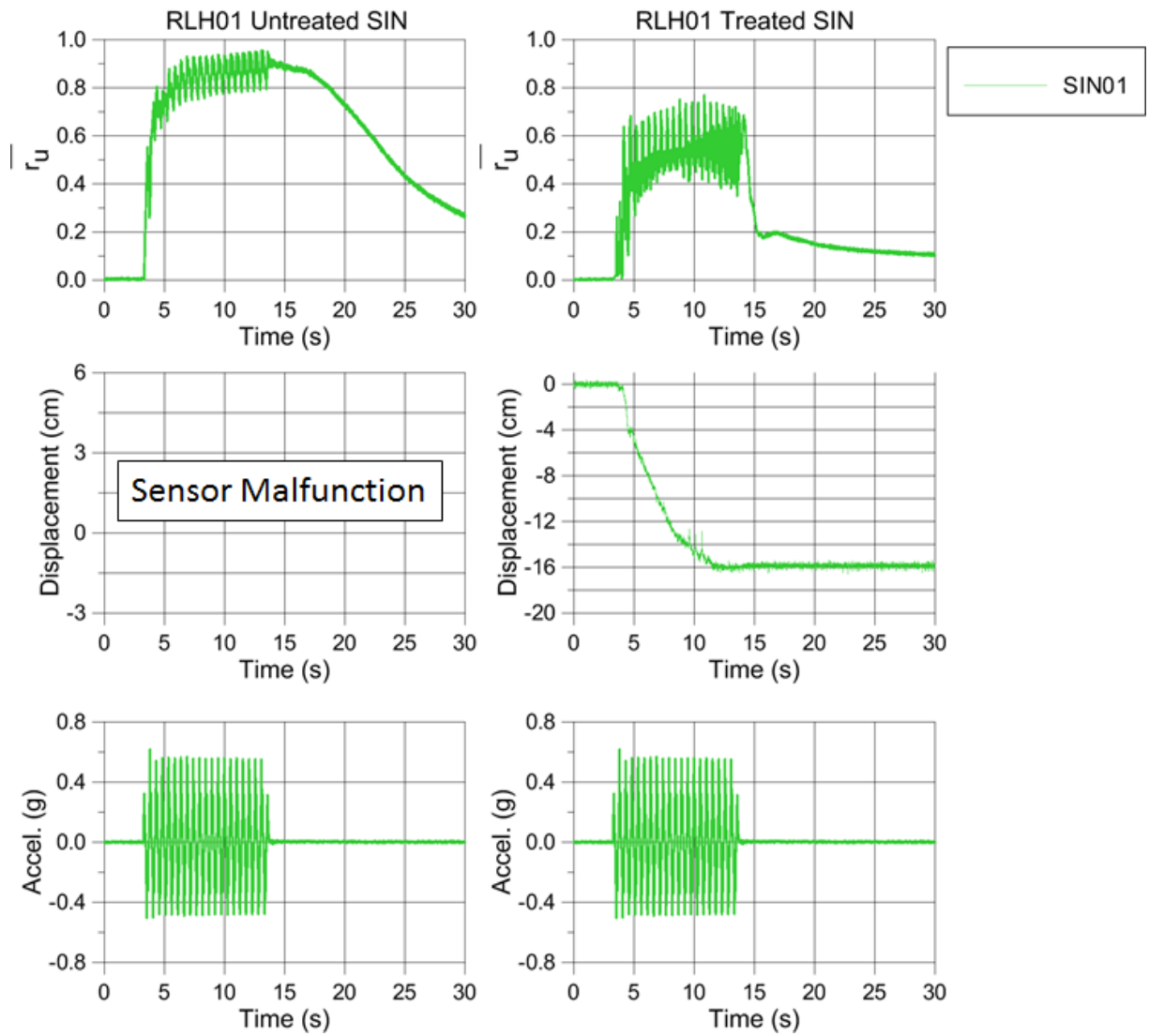


Figure 8.3: \bar{r}_u , horizontal deformation, and input acceleration-time histories for the untreated and treated areas of the RLH01 centrifuge model for the SIN01 shaking event.

dissipate quickly, which results less deformation for the treated area. During the initial cycles of acceleration (i.e., between 5 and 7 seconds), the excess pore pressures in both the untreated and treated areas spike and the rate of deformation is similar for both areas (i.e., about 4 cm of movement by time = 7 seconds). However, the excess pore pressures in the treated area begin to dissipate immediately after the initial peak and no deformation occurs between about 7 and 9 seconds. In the untreated area, \bar{r}_u stays above 0.6 and the deformations continue during this time interval even though the accelerations are relatively small. During the second set of acceleration cycles (i.e., between 9 and 11 seconds), the treated area exhibits another spike in pore pressures ($\bar{r}_u \sim 0.6$) with an associated increase in deformation between 9.5 and 10.5 seconds. However, the pore pressures dissipate quickly and the deformation stops at about 10.5 seconds when shaking becomes small. In the untreated area, \bar{r}_u maintains values between 0.6 and 0.8 from about 5 to 12 seconds because the water cannot quickly drain from the liquefiable layer through the clay cap. Deformations occur throughout the time from 5 to 12 seconds and only stop when the pore pressures drop below 0.6, which is after significant shaking ends.

For the PSL events (Figure 8.2), the deformations are significant (> 1 cm) for both the PSL03 and PSL04 shaking events. During PSL03, the pore pressure ratios are between 0.4 and 0.6 in the untreated area, and deformations occur over the time period from about 8 to 12 seconds. The end of deformation corresponds with \bar{r}_u dropping below 0.4, as well as the end of significant shaking. The peak excess pore pressures for the PSL03 event are actually similar to those for the PAC03 event (Figure 8.1), although deformations were minimal for PAC03. However, the duration of shaking is longer for PSL03 and, as a result, the pore

pressures remain elevated for a longer period of time for PSL03, which leads to more deformation. In the treated area, \bar{r}_u stays below about 0.4, but deformation still occurs. The measured displacement is smaller than in the untreated area, however the displacement occurs over a similar time period (8 to 12 seconds). The smaller displacement is a result of the rate of deformation being slower.

During the PSL04 shaking event, \bar{r}_u stays between 0.6 and 0.8 for an extended period of time (6 to 18 seconds). There was a sensor malfunction in the untreated area at 12 to 14 seconds. While the data before this point is still valid, high resolution video recorded during this event shows that the sensor malfunction occurred shortly before the deformations stopped and thus, the displacement recorded at the time of the malfunction is not the total displacement. Deformations in the untreated area begin just before 5 seconds, which corresponds to the start of shaking and a rapid increase in pore pressures. The deformations continue at a steady rate until about 8 seconds, at which point there are large acceleration cycles and the rate of deformation increases temporarily. By 10 seconds, the large acceleration cycles have ended and the deformation rate is once again similar to what it was at the start of shaking. Deformations stop shortly after 12 seconds, which corresponds to the end of strong shaking although the pore pressures remain elevated at this time. During the same shaking event, the treated area experience significantly smaller pore pressures ($\bar{r}_u \sim 0.4$ to 0.5). As a result, the deformations are smaller but deformation still occurs over a similar time period (4 to 12 seconds) as for the untreated area.

For the SIN01 event (Figure 8.3), the untreated deformations are unknown due to a sensor malfunction, but it can be assumed that the deformations would have been significant (> 1 cm) based on the magnitude of the treated deformations

(~ 16 cm). The excess pore pressures in both the untreated and treated areas increase rapidly at the start of shaking, and the untreated \bar{r}_u peaks at about 0.95 and remains elevated for some time after shaking ends while the treated \bar{r}_u peaks below 0.8 and drops sharply at the end of shaking. Deformations in the treated area start at 4 seconds, which corresponds to the start of shaking and the initial increase in the excess pore pressures. The deformations continue at a fairly steady rate up until 12 seconds, stopping before the end of shaking and while the pore pressures are still elevated. It is unlikely that deformations would have stopped during such strong shaking, and more likely that this is a sensor malfunction rather than true stoppage of the displacements. High resolution video recorded for this event confirms that the displacement sensor became disconnected from its flag near the end of shaking.

While the deformation results presented generally show an increase in displacement with increasing $\bar{r}_{u,\max}$, the time over which displacement occurs is most closely related to the characteristics of shaking. Pore pressures may remain elevated beyond the end of shaking, particularly in the untreated areas (PAC04, PSL04), but deformations almost exclusively end at the end of shaking. This result indicates that the deformations are not being controlled by the pore pressures alone; the characteristics of the input-acceleration are also important. For example, both the treated and untreated responses for PAC04 have two distinct periods of deformation that correspond well to the two periods of strong shaking (5 to 7 seconds and 9 to 11 seconds). Here, the timing of significant deformation is related to the shaking, but the rate of deformation is influenced by the level of induced pore pressure. A similar observation can be made about PSL04, where deformations generally occurred over the time of significant shaking

(5 to 12 seconds) for both the treated and untreated areas, but more deformation occurred for the untreated area where pore pressures were larger. It should be noted that shaking took place orthogonal to the slope for this centrifuge test, and that the effect of the shaking intensity would most likely be even larger if shaking had been parallel to the slope.

Figures 8.4 through 8.6 show the \bar{r}_u , horizontal deformation, and input acceleration-time histories for the RLH01 untreated and treated orthogonal 3D unit cell models for the PAC, PSL, and SIN shaking events. For the PAC events (Figure 8.4), the untreated deformations begin to exceed 1 cm during the PAC02 event (1.7 cm); they increase slightly for the PAC03 event (3.4 cm), and then increase significantly for the PAC04 event (22.4 cm). The excess pore pressures for these three events are similar and cannot explain the differences in the deformations. In this case, the intensity of shaking is influencing the magnitude of the deformations, with PGA values of 0.26 g, 0.38 g, and 0.95 g for PAC02, PAC03, and PAC04, respectively. However, pore pressures are still important, which can be seen when comparing the untreated and treated deformation responses. In the treated model, there was 50 to 60% improvement in the deformation responses for these three PAC events in comparison to the untreated deformations. The untreated and treated models are subjected to the same input motion and thus shaking intensity cannot account for the disparity in the deformations; the only difference between the two models is the excess pore pressures. Similar to the centrifuge tests, the deformations generally occur over two time periods (\sim 5 to 7 seconds and 9 to 11 seconds) and deformations generally stop when strong shaking ends.

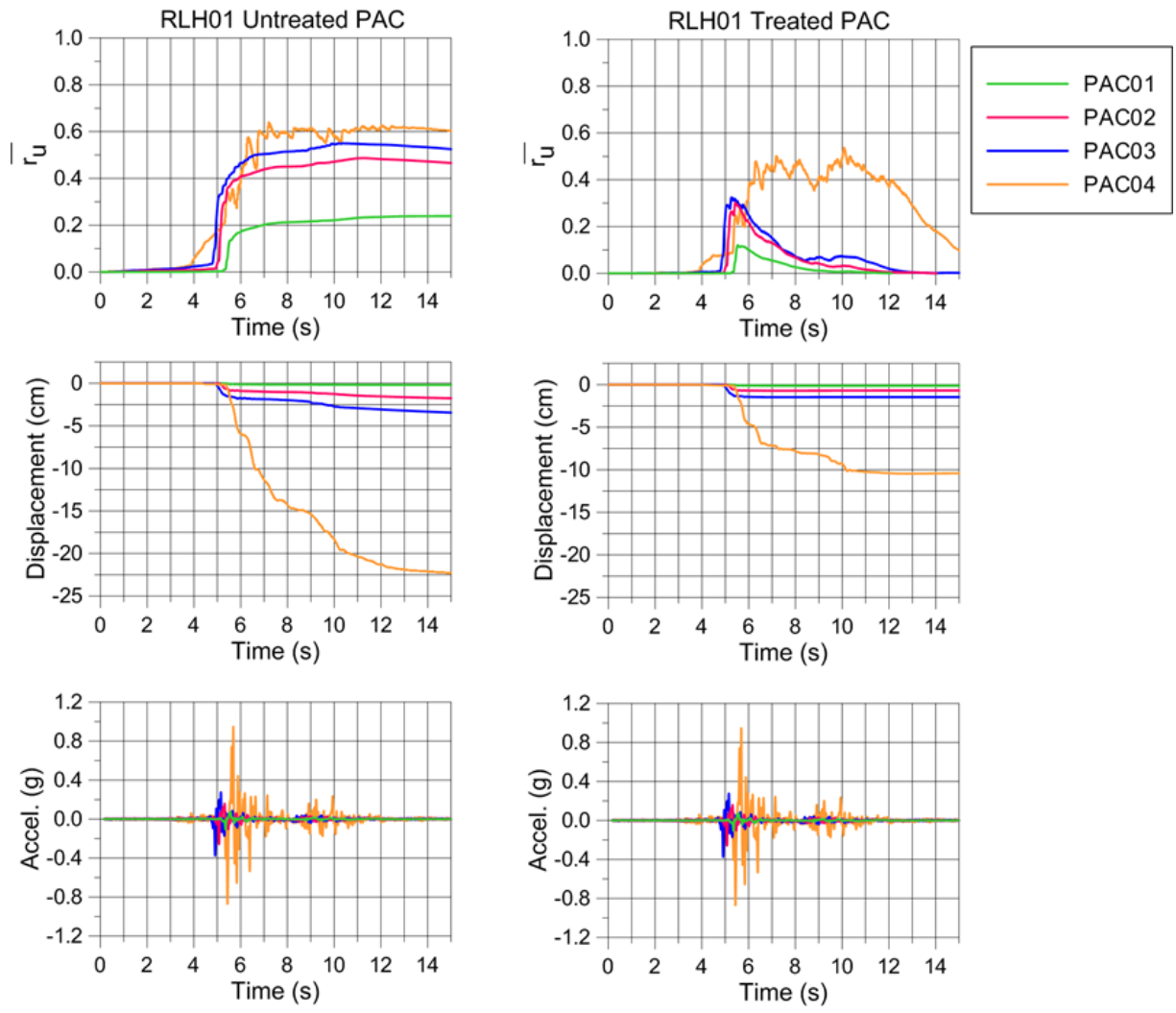


Figure 8.4: \bar{r}_u , horizontal deformation, and input acceleration-time histories for the RLH01 untreated and treated orthogonal 3D unit cell models for the PAC shaking events.

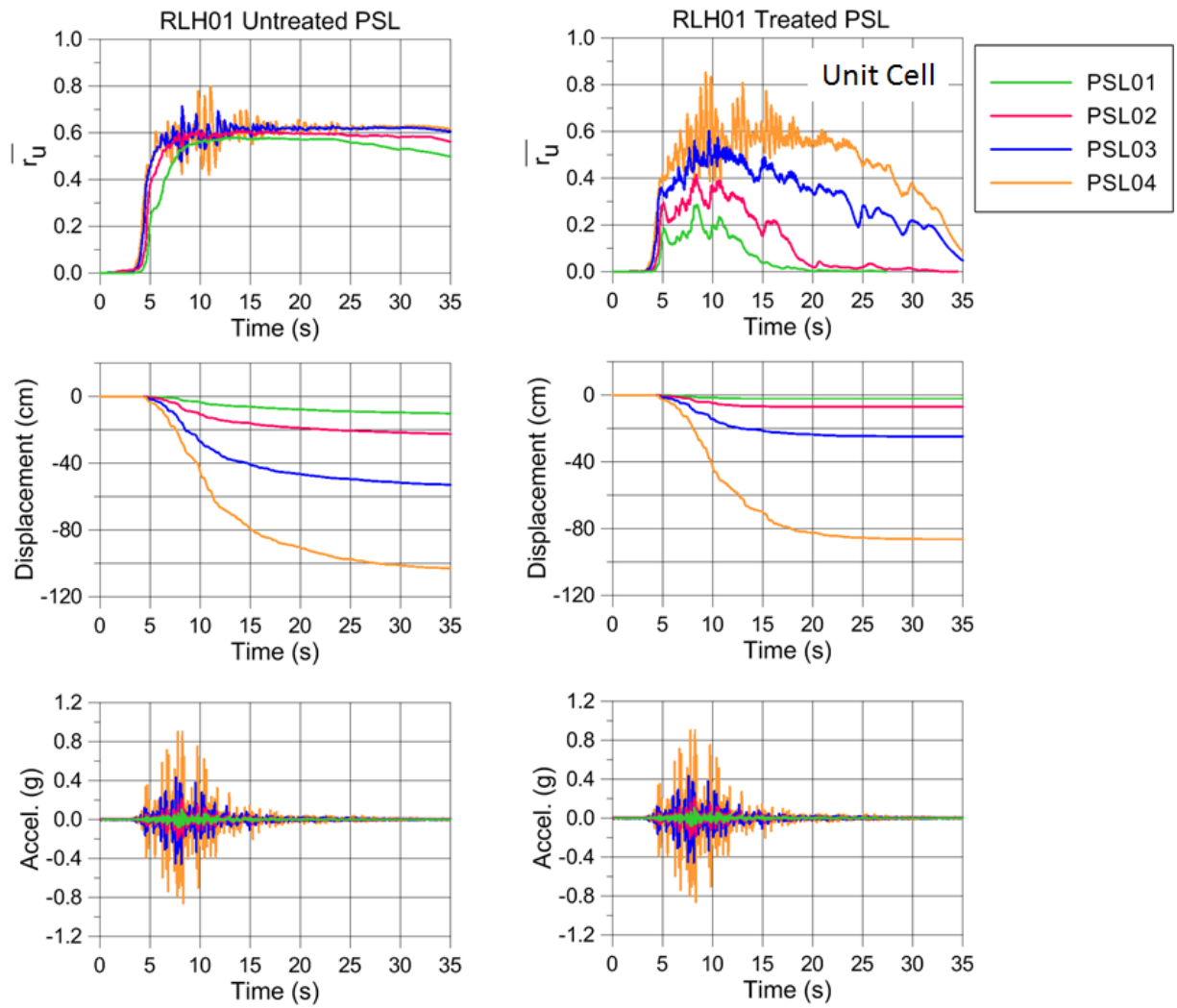


Figure 8.5: \bar{r}_u , horizontal deformation, and input acceleration-time histories for the RLH01 untreated and treated orthogonal 3D unit cell models for the PSL shaking events.

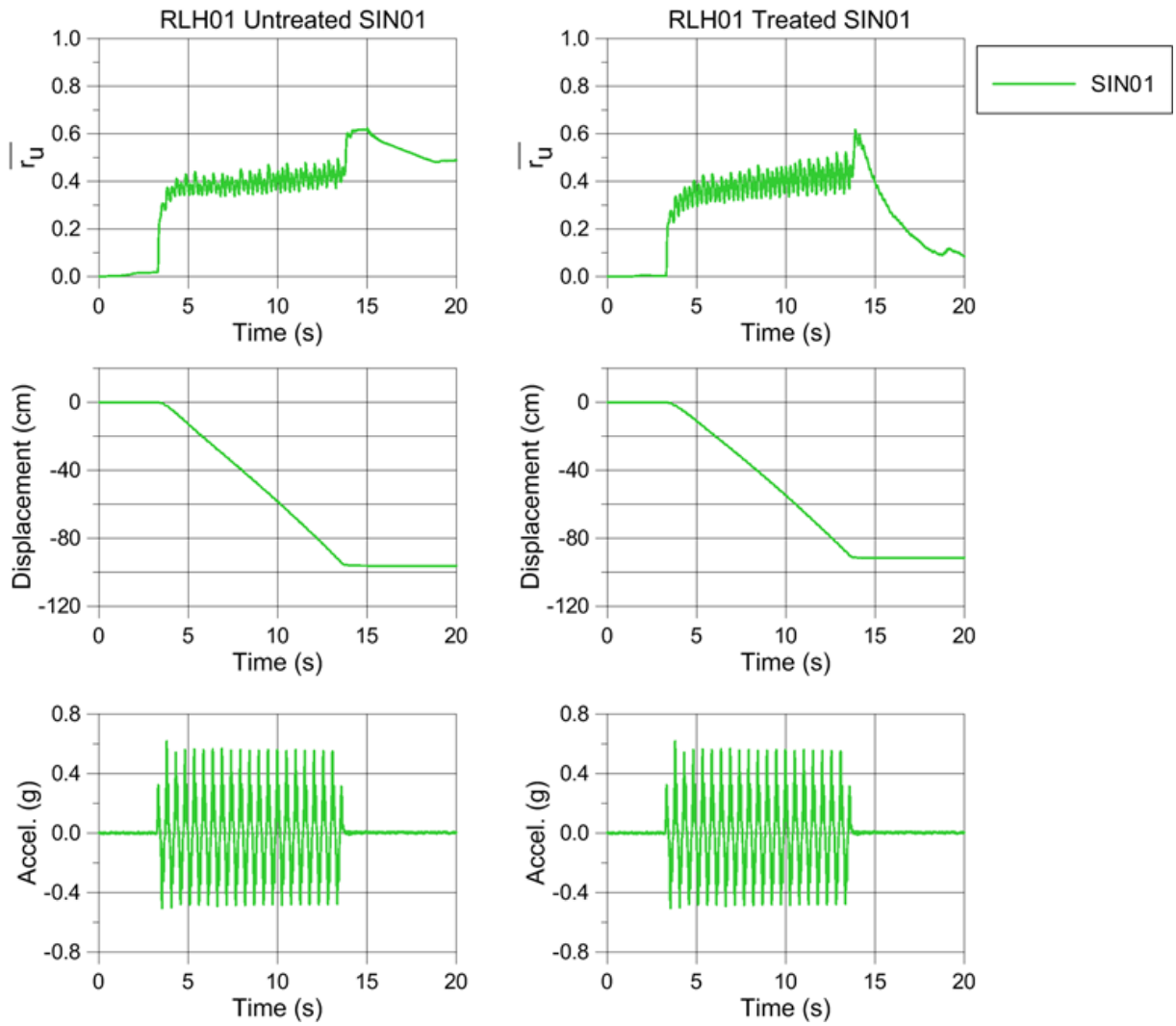


Figure 8.6: \bar{r}_u , horizontal deformation, and input acceleration-time histories for the RLH01 untreated and treated orthogonal 3D unit cell models for the SIN01 shaking event.

For the PSL events (Figure 8.5), the treated and untreated deformations exceeded 1 cm for all four events. In the untreated simulations, the magnitudes of the deformations range from 10 cm (PSL01) to 103 cm (PSL04). It can be seen in Figure 8.5 that the \bar{r}_u -time histories for these four events are nearly identical. Again, this result indicates that the intensity of shaking is controlling the magnitude of the untreated deformations. As the magnitude of the input motion increases, the rate of deformation increases and the model displaces for a slightly longer period of time. For example, most of the deformation is complete by 20 seconds for PSL02, but deformations continue up until 25 seconds for PSL04. These deformations occur over a considerably longer period of time than the deformations in the centrifuge model although this may be due to the numerical models' sensitivity to the low-level accelerations as was demonstrated in Section 6.4. For the treated simulations, deformations are 50 to 80% smaller than those predicted by the untreated models for PSL01 through PSL03 due to reduced pore pressures. For PSL04, the treated deformations are only about 20% smaller than the untreated deformations because the pore pressures are very similar in the treated and untreated analyses. Deformations in the treated model also continue for a longer period of time than in the centrifuge, which again may be due to the numerical models' sensitivity to low-level accelerations.

For the SIN01 event (Figure 8.5), the treated and untreated deformations are similar as a result of the similarities in the treated and untreated excess pore pressures during shaking. The simulations using the earthquake motions peaked an r_u of 0.6 due to the static shear stresses in the slope, however the excess pore pressures for the untreated and treated SIN01 simulations stayed well below 0.6 during shaking due to the characteristics of the input motion (see Section

7.2), with both the untreated and treated models maintaining an \bar{r}_u of about 0.4 during shaking. As soon as shaking ended, the r_u jumped up to the limiting value of 0.6. The deformations in both simulations start when shaking begins and stop when shaking ends, even though pore pressures in the untreated simulation remain elevated after shaking ends. With both the time of displacement and the peak pore pressures being the same in the untreated and treated model, it is not surprising that the magnitudes of the untreated and treated deformations are so similar.

Both the centrifuge data and the numerical simulations show that deformations at a lateral spread site are a function of both the pore pressure response and the characteristics of shaking. The strong shaking plays two roles in the deformation responses: it induces excess pore pressures that reduce a site's resistance to movement and it induces dynamic shear stresses that drive movements. Deformations in the physical and numerical models generally stopped when strong shaking stopped, even if the levels of excess pore pressure were still high, while the rate of deformation over the time period of movement was related to the levels of induced pore pressures.

8.3 Correlating Pore Pressures and Deformations

Current design practice for prefabricated vertical drains typically involves selecting a drain spacing that keeps $\bar{r}_{u,\max}$ below a selected threshold (typically 0.5 to 0.6). Figure 8.7 shows the horizontal displacements as a function of $\bar{r}_{u,\max}$ for the untreated and treated areas of the RLH01 centrifuge model and the untreated and treated orthogonal 3D unit cell models. For the centrifuge model (Figure

8.7a), the $\bar{r}_{u,\max}$ at which deformations begin to become significant is about 0.5, although deformations begin to exceed 1 cm around an $\bar{r}_{u,\max}$ of about 0.4. This threshold holds for both the untreated and treated areas, and agrees well with the threshold generally used in practice. In the numerical models (Figure 8.7b), the threshold appears to be about 0.5, although a closer inspection (Figure 8.7c) shows that the threshold is actually around 0.25 if one considers deformations greater than 1 cm to be significant. This threshold is significantly lower than the threshold in the centrifuge model and can be attributed to the infinite slope geometry, which produces larger deformations than the centrifuge model geometry because it lacks the passive resistance at the toe of the slope. Thus, in the numerical models, lower-intensity shaking events with smaller pore pressures can still produce significant deformations, and the $\bar{r}_{u,\max}$ threshold is lower.

Performance-based design typically evaluates a design based on the induced deformations, and it can be seen in Figure 8.7 that while $\bar{r}_{u,\max}$ is a good indicator of when deformations will begin to become significant, it is not a good indicator of the actual magnitude of the deformations. For example, for the centrifuge data (Figure 8.7a) an $\bar{r}_{u,\max}$ of 0.75 to 0.80 is associated with deformations ranging from 6 to 16 cm, and for the numerical data (Figure 8.7b) an $\bar{r}_{u,\max}$ of about 0.6 is associated with deformations ranging from 20 to 100 cm. To relate the excess pore pressures to the magnitude of the deformations, a different parameter is needed. In analyzing the centrifuge data, the deformations were related to the time between the first and last exceedance of an \bar{r}_u threshold of 0.5. However, this approach does not take into account the characteristics of the \bar{r}_u time history during the times above the threshold. A parameter that can take these characteristics into account is the \bar{r}_u is to use the integral of the \bar{r}_u - time history above the \bar{r}_u threshold.

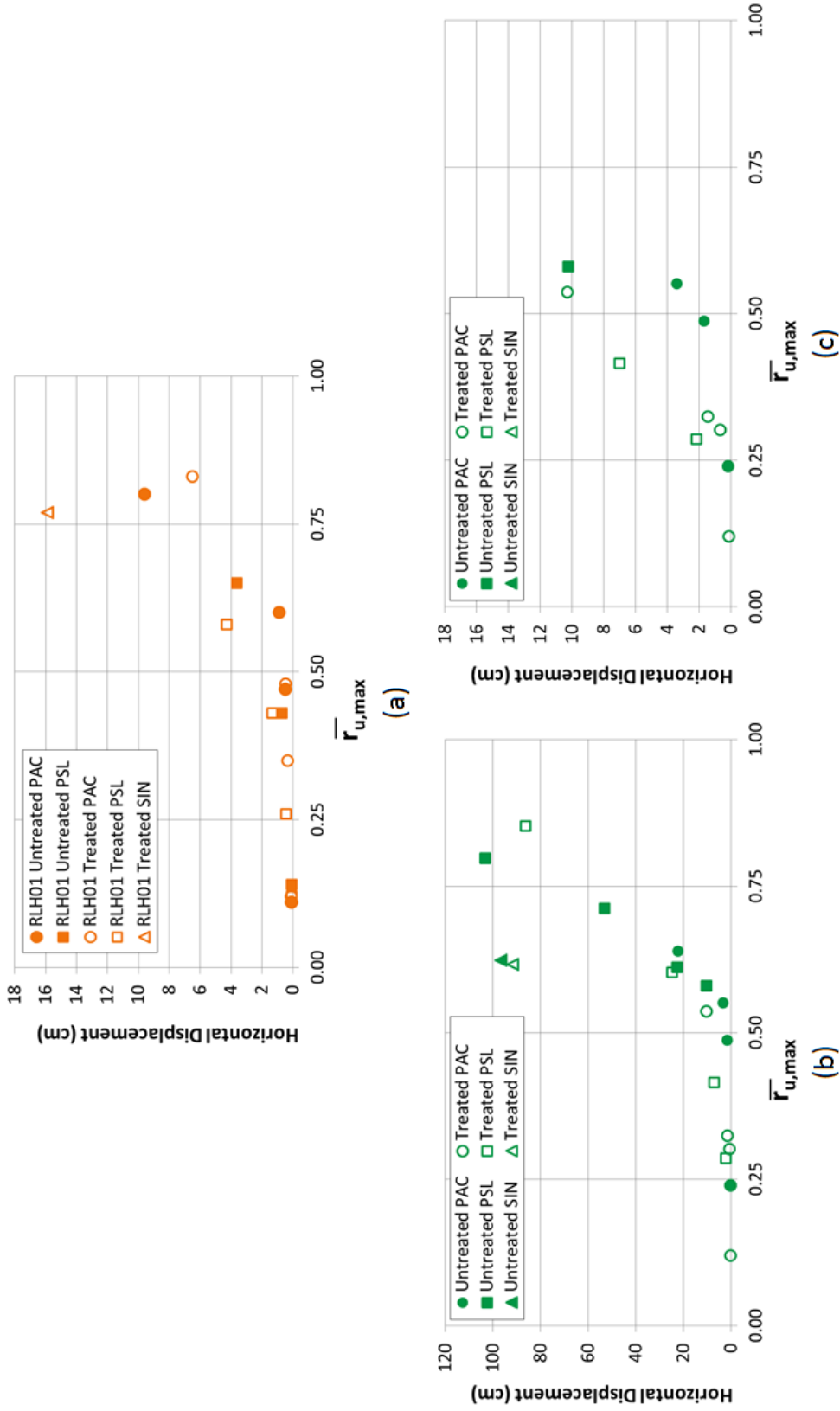


Figure 8.7: Horizontal displacement vs. peak average excess pore water pressures ($\bar{r}_{u,max}$) for (a) the RLH01 centrifuge model for all shaking events, (b) the untreated and treated orthogonal 3D unit cell models for all shaking events, and (c) the untreated and treated orthogonal 3D unit cell models in which there was less than 18 cm of deformation.

Figure 8.8 shows the horizontal deformations plotted as a function of the integral of \bar{r}_u above a threshold of 0.4 for the RLH01 centrifuge data. This integral is called $\bar{r}_u\text{Int}0.4$, and it is calculated up to time = 30 seconds for all shaking events. A threshold of 0.4 was selected based on the threshold at which deformations in the centrifuge test began to exceed 1 cm (Figure 8.7). It can be seen in Figure 8.8 that the untreated and treated deformations from the centrifuge test correlate well to $\bar{r}_u\text{Int}0.4$ with larger values of $\bar{r}_u\text{Int}0.4$ corresponding with larger values of displacement. However, the treated data plot above the untreated data and predict larger deformations for a given $\bar{r}_u\text{Int}0.4$ than the untreated data. For example, the untreated PAC03 and treated PSL04 data points both have $\bar{r}_u\text{Int}0.4 \sim 0.7$ seconds, but there was only 1 cm of displacement in the untreated area for PAC03 while there was over 4 cm of displacement in the treated area of PSL04. The reason the treated data show more deformation for the same $\bar{r}_u\text{Int}0.4$ is that the shaking required to achieve this level of $\bar{r}_u\text{Int}0.4$ was larger and the shaking characteristics are not taken into account by $\bar{r}_u\text{Int}0.4$.

Various ground motion parameters could be used to characterize the different input motions. Peak ground acceleration (PGA) works well when considering a single input motion, but this measure represents a single point on the time series and does not work well when comparing different input motions. Arias intensity ($I_a = \frac{\pi}{2g} \int_0^{T_{\max}} [a(t)]^2 dt$) and cumulative absolute velocity ($CAV_5 = \int_0^{T_{\max}} |a(t)| dt$ for accelerations greater than 5 cm/s²) have been used to predict the deformations of non-liquefiable slopes (e.g., Saygili and Rathje, 2009) and pore pressure generation in liquefiable deposits (Kramer and Mitchell, 2006). These parameters are good candidates for characterizing the input motion intensity because they represent an integral measure of the time series rather than a single point on the

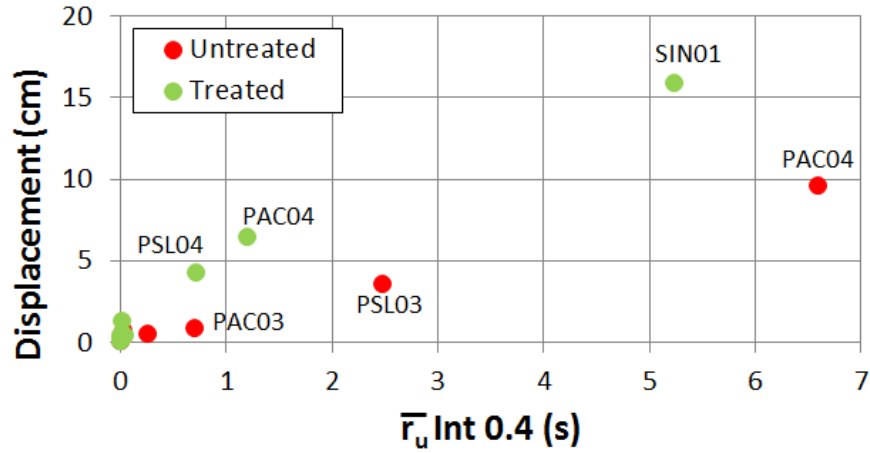
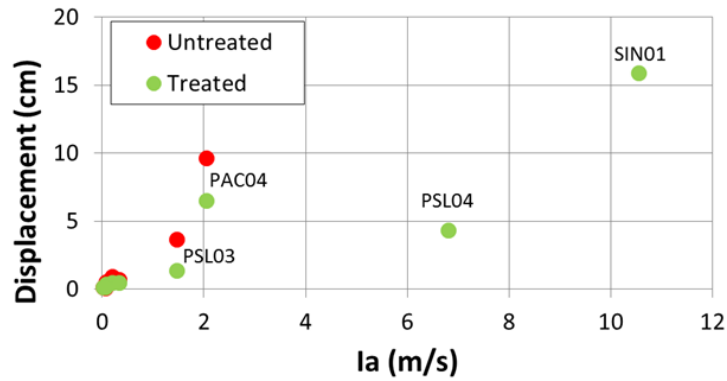


Figure 8.8: Horizontal deformation vs. $\bar{r}_u \text{Int}0.4$ for the untreated and treated areas of the RLH01 centrifuge model.

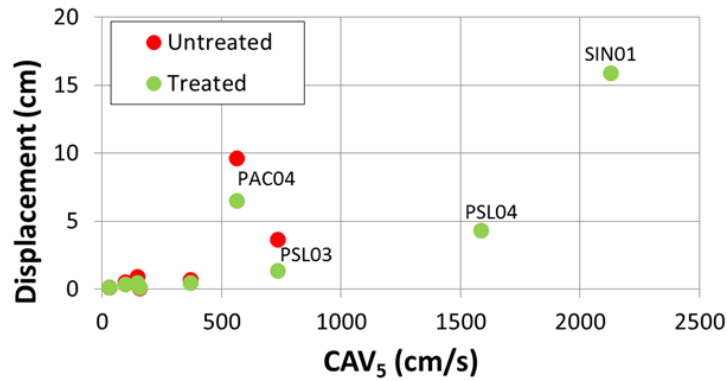
time series. Consider again the untreated PAC03 and treated PSL04 data points shown in Figure 8.8. These two motions produced similar $\bar{r}_u \text{Int}0.4$ values, but the PSL04 input motion produced larger deformations because it has a higher intensity than the PAC03 motion. PAC03 and PSL04 have I_a of 0.2 m/s and 6.8 m/s, respectively, and CAV_5 of 149 cm/s and 1587 cm/s respectively.

The horizontal deformations for the untreated and treated areas of the RLH01 centrifuge model are plotted as a function of I_a and CAV_5 in Figure 8.9. I_a and CAV_5 for the centrifuge shaking events were calculated using the acceleration-time histories recorded by an accelerometer located at the base (outside) of the container. In both cases, the data generally show that larger I_a or CAV_5 result in larger deformations. The one motion that deviates the most from the trend is PAC04. This motion generates larger deformations than expected based on either its I_a or CAV_5 . This may be due to the short duration of the PAC motion, which also includes some directivity effects. The short duration and relatively large

CAV₅ and I_a means that the intensity develops over a short period of time, which can lead to a more damaging response. Finally, the data in Figure 8.9 show that, generally, the treated deformations are smaller than the untreated deformations due to the reductions in $\bar{r}_u \text{Int} 0.4$.



(a)



(b)

Figure 8.9: Horizontal deformation vs. (a) Arias intensity (I_a) and (b) cumulative absolute velocity (CAV₅) for the untreated and treated areas of the RLH01 centrifuge model.

For the numerical models, the deformations begin to exceed 1 cm when $\bar{r}_{u,\max}$ exceeded 0.25 (Figure 8.7). The \bar{r}_u integral for the numerical models is calculated up to time = 30 seconds with a threshold of 0.25 for all shaking events; this integral is called $\bar{r}_u\text{Int}0.25$. The horizontal deformations from the untreated and treated 3D orthogonal unit cell models are shown as a function of $\bar{r}_u\text{Int}0.25$ in Figure 8.10. For the untreated models (Figure 8.10a), the PAC events span $\bar{r}_u\text{Int}0.25 = 0$ to 12 seconds with increasing $\bar{r}_u\text{Int}0.25$ corresponding to increasing deformations. The PSL events all have similar $\bar{r}_u\text{Int}0.25$ values of 13 to 16 seconds although the deformations range from 10 to 100 cm. This is because the untreated model is completely undrained, and the \bar{r}_u -time histories for the four PSL events are nearly identical (Figure 8.5) and the differences in the deformations are controlled by the intensity of the input motion more than the pore pressures. The SIN01 event has a slightly lower $\bar{r}_u\text{Int}0.25$ of 12 seconds because pore pressures were not able to reach their maximum limit during shaking for this event (see Section 7.2). For the treated models (Figure 8.10b), there is a good correlation between $\bar{r}_u\text{Int}0.25$ and the magnitude of the horizontal deformations. The SIN01 event again has a lower than anticipated $\bar{r}_u\text{Int}0.25$ value because the pore pressures were not able to reach their maximum limit during shaking. As was the case with the centrifuge model, the treated model generally exhibits larger deformations for a given value of $\bar{r}_u\text{Int}0.25$. Comparing the data points at $\bar{r}_u\text{Int}0.25 = 8$ seconds, it can be seen that this $\bar{r}_u\text{Int}0.25$ corresponds to 25 cm of deformation in the treated model and 3 cm of deformation in the untreated model. This result again is due to the fact that larger shaking intensities are required to achieve a given level of $\bar{r}_u\text{Int}0.25$ in the treated models, which leads to more deformation.

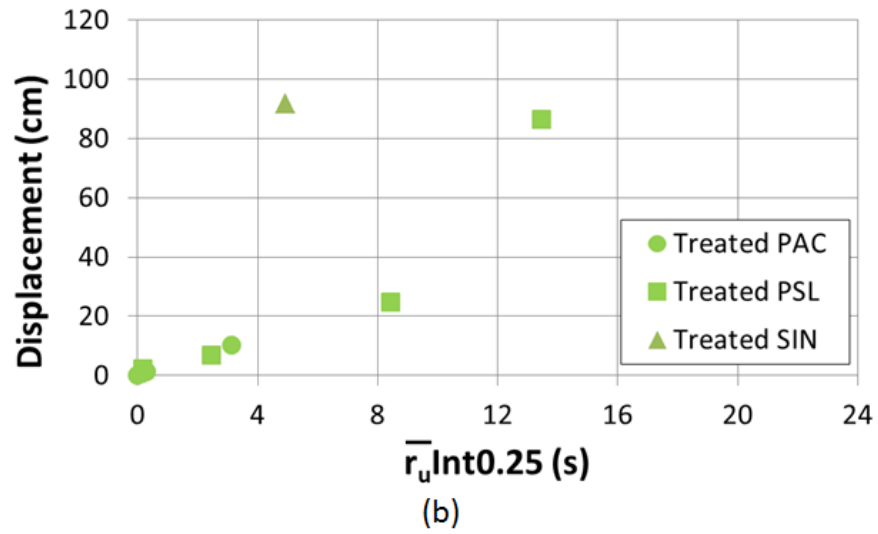
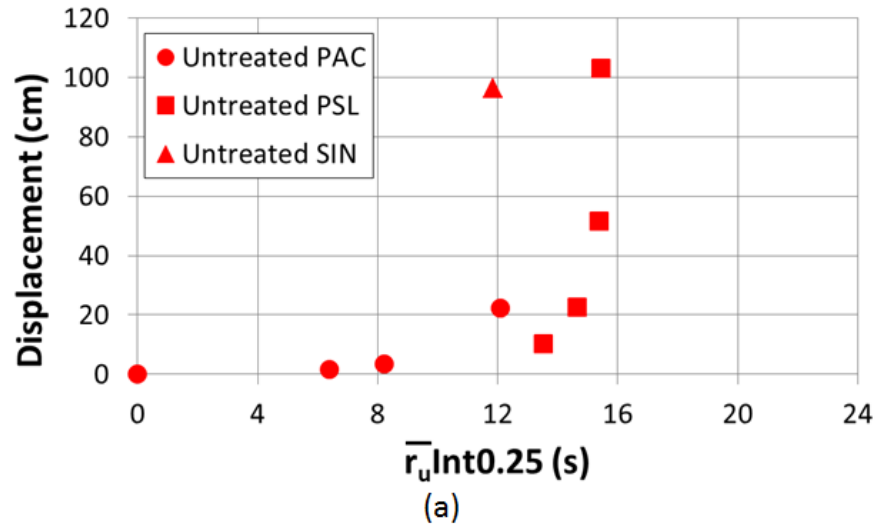


Figure 8.10: Horizontal deformation vs. $\bar{r}_u \text{Int}0.25$ for the RLH01 (a) untreated and (b) treated 3D orthogonal unit cell models.

The untreated data shown in Figure 8.10, particularly the PSL data, illustrate again the importance of shaking intensity. All four untreated PSL simulations produce very similar pore pressures and yet the deformations range from 10 to 100 cm. The horizontal deformations from the RLH01 untreated and treated 3D orthogonal unit cell models are plotted as a function of the intensity measures I_a and CAV_5 in Figure 8.11. I_a and CAV_5 for the simulations were calculated using the input acceleration-time histories, which are the acceleration-time histories recorded during the RLH01 centrifuge test by the accelerometer located at the base (outside) of the centrifuge container. For the centrifuge data, I_a and CAV_5 were similarly successful in predicting deformations, although the data from PAC04 did not follow the trends from the other motions. In the numerical models, the deformations are better correlated to CAV_5 . In particular, CAV_5 does a better job of distinguishing PSL03 and PAC04. Additionally, the I_a calculation uses the square of the acceleration-time history, which decreases the contribution of accelerations less than 1 m/s^2 . Thus, all of the lower-intensity events, have very small I_a leading to a cluster of data points at $I_a \sim 0$ corresponding to deformations that range from 0 to 23 cm. CAV_5 , which uses the absolute value of the acceleration-time history, is more sensitive to low-intensity accelerations and as a result, the data points clustered at $I_a \sim 0$ are spread out over a CAV_5 range of 0 to 400 cm/s and better show the transition from 0 to 23 cm.

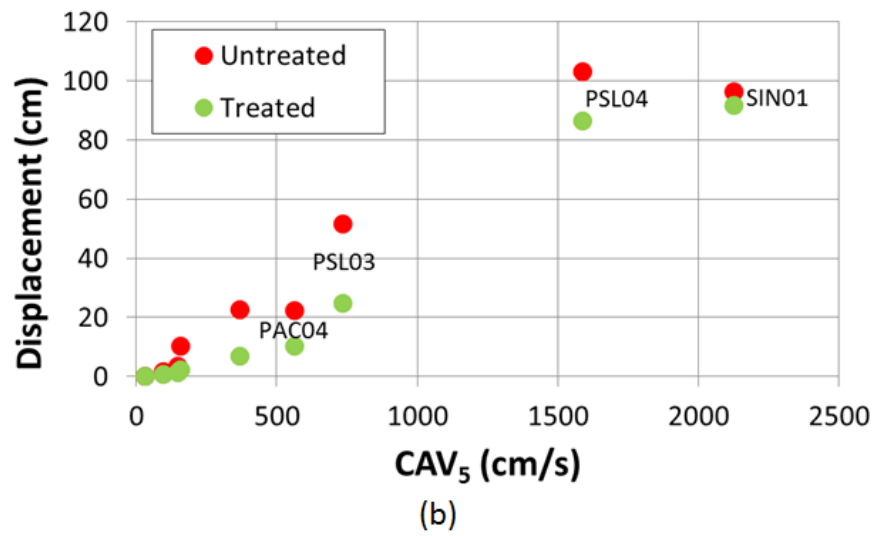
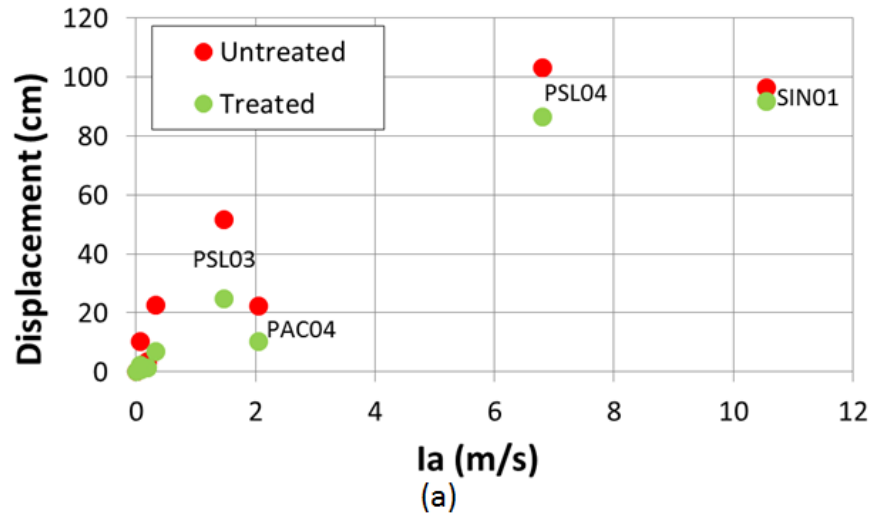


Figure 8.11: Horizontal deformation vs. (a) Arias intensity (I_a) and (b) cumulative absolute velocity (CAV_5) for the RLH01 untreated and treated 3D orthogonal unit cell models.

8.4 Summary

This chapter investigated the relationship between the excess pore pressure and deformation responses. First, the \bar{r}_u and displacement-time histories for the untreated and treated PAC, PSL, and SIN events were compared and it was shown that the magnitude of the deformations were affected by not only the excess pore pressures but also the intensity of the input motion. A threshold $\bar{r}_{u,\max}$ at which deformations begin to become significant was identified. For the centrifuge data, this threshold was about 0.4 to 0.5 and for the numerical models this threshold was 0.25. The threshold in the numerical models is lower as a result of the infinite slope geometry.

In analyzing the centrifuge data, the horizontal deformations were related to the integral of the \bar{r}_u -time history for \bar{r}_u above 0.4, called $\bar{r}_u\text{Int}0.4$. This integral characterizes the details of the \bar{r}_u -time history during the times above \bar{r}_u equal to 0.4. Deformations generally increase with increasing $\bar{r}_u\text{Int}0.4$ across the motions investigated, however the treated deformations were generally larger than the untreated deformations for a given $\bar{r}_u\text{Int}0.4$. This difference is due to the fact that it takes a larger intensity to reach a given $\bar{r}_u\text{Int}0.4$ in the treated condition, and this leads to larger deformations. Accounting for the ground motion characteristics, the deformations relate well to both I_a and CAV_5 . For each value of intensity, the treated deformations were smaller than the untreated deformations due to reductions in $\bar{r}_u\text{Int}0.4$. Similar trends were observed for the numerical simulations.

Chapter 9

Summary, Conclusions, and Recommendations

9.1 Summary

Drainage is one of the many available soil improvement methods that can be used to reduce deformations due to liquefaction-induced lateral spreading. Traditional drains (i.e., stone columns and gravel drains) were first introduced in the 1970's and relied on a combination of densification and drainage effects to mitigate liquefaction. The drainage capacity of these elements may be negatively impacted by soil mixing and soil migration into the drain over time. Prefabricated vertical drains (PVDs) are a more recently introduced drainage method. PVDs are hollow, perforated, plastic pipes wrapped in filter fabric to prevent problems experience by traditional drains. As yet, no field lateral spread site treated with PVDs has been subjected to a design-level earthquake and thus, the extent of their effectiveness remains in question.

In this research physical and numerical models were used to study the effectiveness of PVDs in reducing liquefaction-induced deformations at lateral spread sites. The main objectives of this research were to enhance our understanding of the behavioral mechanisms controlling the general response of untreated and drain-treated lateral spread sites and to evaluate the use of finite element modeling to capture the response of drain-treated sites. Data from these models were analyzed with emphasis placed on identifying the mechanisms of behavior related to pore pressure generation and dissipation and the development of horizontal deformations.

A suite of three dynamic centrifuge tests was performed at the UC Davis Center for Geotechnical Modeling. These tests modeled untreated and drain-treated sloping soil profiles subjected to scaled earthquake and sine wave shaking events. The effectiveness of the drains in mitigating liquefaction-induced deformations was evaluated through recorded pore pressure and deformation data. The first test, SSK01, showed that PVDs are effective in reducing peak excess pore pressures and increasing the rate of pore pressure dissipation. At the end of testing, the horizontal deformations in the treated slope were 80% smaller than those observed in the untreated slope, but there were concerns that the stiffness of the drains unrealistically improved the performance. The second test, RNK01, featured a drain-treated slope and an untreated slope containing non-draining tubes. The results of this test confirmed that the stiffness of the model drains affected the deformations in the drain-treated slopes such that the improved performance observed in SSK01 could not be ascribed solely to drainage. The final test, RLH01, featured a drain-treated slope, an untreated slope, and an untreated slope with non-draining tubes. New drains constructed of a more

flexible material were used in this test to minimize the effect of the drain stiffness on the deformation response. The results of this test indicated that the new drains were flexible enough such that their presence did not affect the performance of the drain-treated slope. Thus, the 30 to 60% reduction in the horizontal deformations observed in this test can be attributed solely to the effects of drainage. The data from this test also showed that the impact of the drains is sensitive to the characteristics of the input motion.

Numerical models were developed and simulations were performed using OpenSees. The numerical models consisted of 2D and 3D infinite slope unit cell models representing the area of influence around a single drain. The infinite slope geometry of these models was reflective of the geometry typical of a lateral spread site in the field while the modeled soil profiles reflected the soil profiles found in the centrifuge models. The 3D models fully captured the three-dimensional drainage towards the drain, while the 2D models used a modified hydraulic conductivity to account for the 3D drainage effects.

The PDMY02 constitutive model was chosen to represent the liquefiable sand. The model parameters were determined using lab data for Nevada sand. A range of hydraulic conductivities was identified for the simulated sand based on equilibrating the coefficient of consolidation of the simulated sand with that of Nevada sand. An additional parameter that was required and is particularly important for drainage studies was the hydraulic conductivity of the sand. The hydraulic conductivity together with the coefficient of compressibility (m_v) control pore pressure dissipation. The coefficient of compressibility is not an input parameter for the PDMY02 model but rather is modeled through the volumetric component of the flow rule.

9.2 Conclusions

When the hydraulic conductivity of the prototype sand from the centrifuge tests was used in the 3D treated unit cell models, the models drained too quickly. Further investigation showed that the equivalent m_v values modeled by the PDMY02 model are 1/3 to 1/10 of those expected for sand, resulting in an overestimation of the rate of pore pressure dissipation. As a result, the hydraulic conductivity of the sand was reduced accordingly to model an appropriate value of m_v and pore pressure dissipation.

In the absence of field data, the pore pressure and deformation data from the centrifuge tests was used to evaluate the numerical models. The 2D and 3D unit cell models were used to simulate the three dynamic centrifuge tests. For the first centrifuge test, SSK01, the simulated and experimental pore pressure data were generally similar for the treated and untreated conditions. For those events in which significant pore pressures were generated, the unit cell models predicted larger horizontal deformations than were observed in the centrifuge test. This overprediction was due to differences in the unit cell and centrifuge model geometries. Even with the scaled hydraulic conductivity, the 2D unit cell model exhibited more drainage than the 3D unit cell model and the deformations in the 3D unit cell model were significantly larger than in the 2D unit cell model.

For the second centrifuge test, RNK01, the "loose" sand layer in the centrifuge model had a relative density closer to 70%. As a result, the generated pore water pressures in the centrifuge model were smaller than those predicted by the unit cell models in which the simulated sand was calibrated to match the behavior of a loose sand with a relative density of 40%. The pore pressure data was

a better match to the centrifuge data when the relative density of the simulated sand was increased to 75%. Both the untreated and treated slopes in the centrifuge model were reinforced by the model drains/tubes, thus, no comparison of the horizontal deformation data was performed. The simulated pore pressure data for the treated condition showed that the numerical models are particularly sensitive to low-level accelerations when the stress path is near the failure surface.

For the third centrifuge test, RLH01, shaking was performed orthogonal to the slope. It is not possible to shake a 2D model orthogonal to the slope; thus, the RLH01 simulations were only performed for the 3D unit cell models. For the untreated condition, the numerical model predicted peak excess pore pressures that were comparable to or somewhat larger than the centrifuge data. The unit cell models generally predict deformations that significantly larger than were observed in the centrifuge. Again, this is a result of the infinite slope geometry, which lacks passive resistance at the toe of the slope. The model's sensitivity to low-level accelerations, which was observed in the RNK01 simulations, was observed again for the RLH01 simulations.

Finally, the relationship between the excess pore pressure and deformation responses was examined for the RLH01 centrifuge test and numerical simulations. A comparison of the \bar{r}_u and displacement time histories showed that the magnitude of the deformations were affected by both the pore pressures and the intensity of the input motion. A threshold $\bar{r}_{u,\max}$ at which deformations begin to become significant was identified. For the centrifuge data, this threshold was about 0.4 to 0.5 and for the numerical models this threshold was 0.25. The threshold in the numerical models is lower as a result of the infinite slope geometry. In analyzing the centrifuge data, the horizontal deformations were related to the integral of the

\bar{r}_u -time history for \bar{r}_u above 0.4, called \bar{r}_u Int0.4. Deformations generally increase with increasing \bar{r}_u Int0.4, and for a given \bar{r}_u Int0.4 the treated deformations are larger due to the fact that it takes a larger intensity to reach a given \bar{r}_u Int0.4 in the treated condition. To account for the ground motion characteristics, the deformations were related to both Ia and CAV_5 . In general, the deformations increase with increasing Ia and CAV_5 , and for each value of intensity, the treated deformations were smaller than the untreated deformations due to reductions in \bar{r}_u Int0.4. Similar trends were observed for the numerical simulations.

9.3 Recommendations for Future Work

The results of this research indicate that the effectiveness of prefabricated vertical drains in reducing peak excess pore pressures and liquefaction-induced deformations is sensitive to the characteristics of the input motion. Further work needs to be done to fully investigate how various input motion characteristics affect the performance of PVDs. It has been established that the rubber-blend tubing used in the RLH01 centrifuge model did not affect the performance of the slope. It is recommended that an additional centrifuge test be performed using the new drains and without the third treatment area (i.e., the untreated-tube area) that necessitated orthogonal shaking. This test should include a wider range of input motions that exemplify various loading conditions. The hydraulic conductivity of the liquefiable sand layer should be measured in situ during testing (i.e., while spinning).

Improvements should also be made to the PDMY02 constitutive model to address the issues identified during the numerical modeling phase of this research.

The first and most critical issue is that the coefficient of volumetric compressibility (m_v) modeled by the PDMY02 model is too small and does not increase with increasing pore pressures. The small m_v results in a coefficient of consolidation (c_v) that is too large, allowing the simulated soil to drain faster than in the field. Because m_v does not increase with increasing pore pressures, the PDMY02 model cannot simulate post-liquefaction reconsolidation settlements. The second issue that should be addressed is the steepness of the CRR curves produced by the PDMY02 model. The third issue that should be addressed is the PDMY02 model's sensitivity to low-level accelerations. This sensitivity results in the generation of considerable pore pressures that affect the drained condition and are not an accurate reflection of the level of pore pressures that would be generated in the field. Addressing these three issues would greatly improve the PDMY02 model's ability to capture the drained or partially-drained response of a soil deposit treated with PVDs.

Appendices

Appendix A

Scaling the hydraulic conductivity for the 2D models

This appendix details the scaling of the hydraulic conductivity from the 3D unit cell model for use in the 2D models using the Hird et al. (1992) scaling laws. The goal is to match the effects of an axisymmetric unit cell and a plane strain unit cell (Figure A.1). The Hird et al. (1992) approach is to modify the drain spacing or the soil permeability to equate the average degree of consolidation on a horizontal plane. This approach does take into account the effects of finite drain permeability and smear. The results show that the average degree of consolidation for the geometry and permeability matched models is within 10% of the average degree of consolidation of the axisymmetric model (Figure A.2). The results also showed that the pore pressure variation along a horizontal plane does not match as well as the average degree of consolidation (Figure A.3)

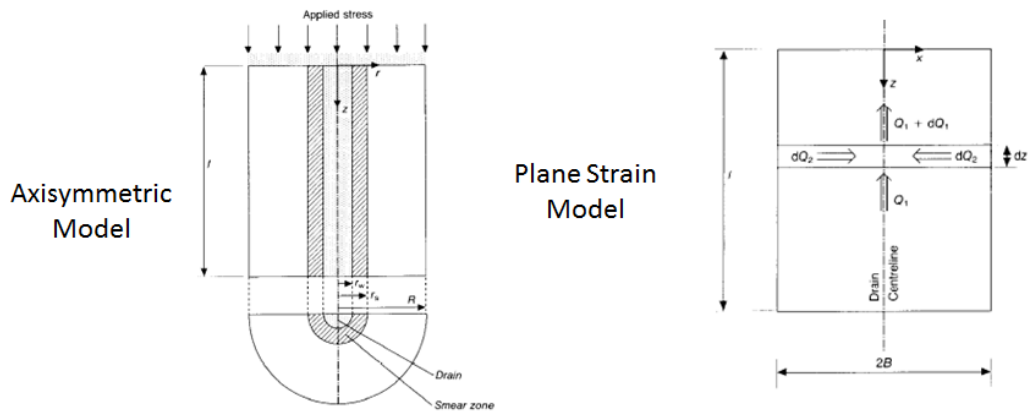


Figure A.1: Axisymmetric and plane strain models from Hird et al. (1992).

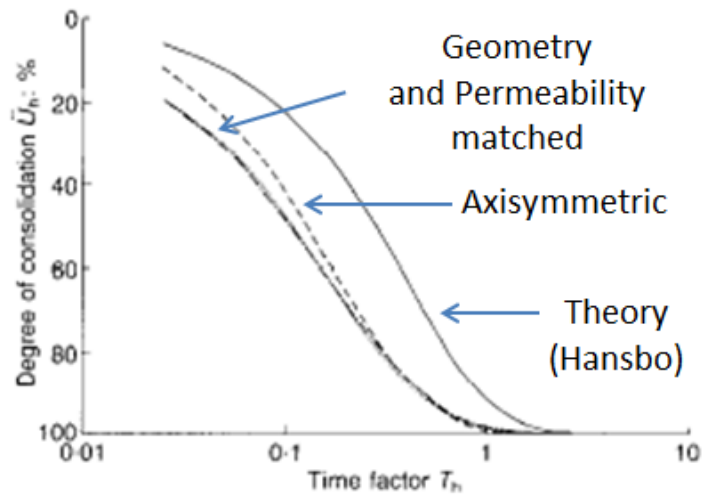


Figure A.2: Average degree of consolidation on a horizontal plane for an axisymmetric model and geometry-matched and permeability-matched plane strain models (Hird et al., 1992).

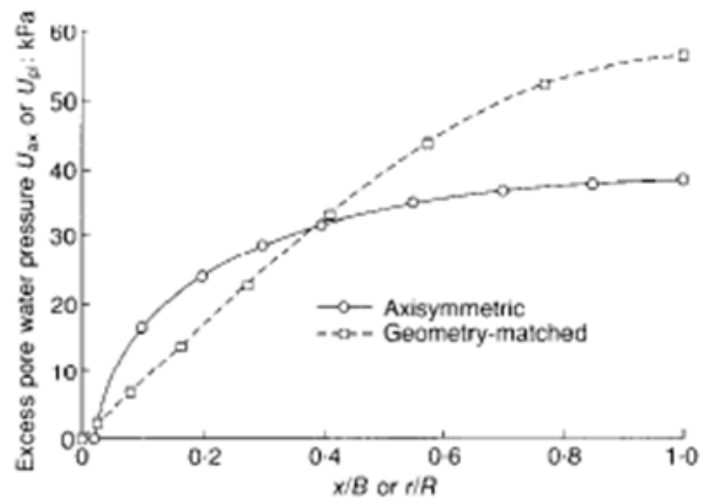


Figure A.3: Pore pressure variation along a horizontal plane for an axisymmetric model and a geometry-matched model (Hird et al., 1992).

Hird begins with Hansbo's equation for the average degree of consolidation on a horizontal plane in an axisymmetric unit cell.

$$\bar{U}_{\text{hax}} = 1 - \exp\left(\frac{-8T_{\text{h}}}{\mu_{\text{ax}}}\right) \quad (\text{A.1})$$

where

- \bar{U}_{hax} is the average degree of consolidation on a horizontal plane for an axisymmetric unit cell
- T_{h} is the time factor for radial drainage ($\frac{C_{\text{h}}t}{4R^2}$)
- $\mu_{\text{ax}} = \ln\left(\frac{n}{s} + \frac{k}{k_{\text{s}}}\ln(s) - \frac{3}{4} + z(2l - z)\frac{k}{k_{\text{w}}r_{\text{w}}^2}\right)$
 - $n = \frac{R}{r_{\text{w}}}$ where R is the radius of axisymmetric unit cell and r_{w} is the radius of the well
 - $s = \frac{r_{\text{s}}}{r_{\text{w}}}$ where r_{s} is the radius of the smear zone and r_{w} is the radius of the well
 - z is the depth
 - l is the drain length
 - k is the horizontal permeability of the soil
 - k_{s} is the horizontal permeability of the smear zone
 - k_{w} is the vertical permeability of the drain
 - neglecting the effects of the smear zone, $s = \frac{r_{\text{s}}}{r_{\text{w}}} = 1$ and $k_{\text{s}} = k$
 - neglecting well resistance, $k_{\text{w}} \rightarrow \infty$ and $\frac{k}{k_{\text{w}}r_{\text{w}}^2} \rightarrow 0$
- neglecting both smear and well resistance $\mu_{\text{ax}} = \ln(n) - \frac{3}{4}$

In a plane strain unit cell

$$\bar{U}_{\text{hpl}} = 1 - \exp\left(\frac{-8T_{\text{h}}}{\mu_{\text{pl}}}\right) \quad (\text{A.2})$$

where

- \bar{U}_{hpl} is the average degree of consolidation on a horizontal plane for an plane strain unit cell
- T_{h} is the time factor for radial drainage ($\frac{C_{\text{h}}t}{4R^2}$)
- $\mu_{\text{pl}} = \frac{2}{3} + 2z(2l - z)\frac{k}{BQ_{\text{w}}}$
 - z is the depth
 - l is the drain length
 - k is the horizontal permeability of the soil
 - B is half the width of the plane strain unit cell
 - Q_{w} is the discharge capacity of the drain
 - for perfect drainage $Q_{\text{w}} \rightarrow \infty$ and $2z(2l - z)\frac{k}{BQ_{\text{w}}} \rightarrow 0$
- for perfect drainage $\mu_{\text{pl}} = \frac{2}{3}$

To match the average degree of consolidation at every time and every depth in the unit cell

$$\bar{U}_{\text{hpl}} = \bar{U}_{\text{hax}} \quad (\text{A.3})$$

$$\frac{T_{\text{hpl}}}{\mu_{\text{pl}}} = \frac{T_{\text{hax}}}{\mu_{\text{ax}}} \quad (\text{A.4})$$

$$\frac{C_{\text{hpl}}t}{B^2\mu_{\text{pl}}} = \frac{C_{\text{hax}}t}{R^2\mu_{\text{ax}}} \quad (\text{A.5})$$

Keeping the axisymmetric and plane strain geometry the same ($B = R$) and adjusting the soil properties

$$\frac{k_{\text{pl}}}{B^2\mu_{\text{pl}}} = \frac{k_{\text{ax}}}{R^2\mu_{\text{ax}}} \quad (\text{A.6})$$

$$k_{\text{pl}} = \frac{2}{3}k_{\text{ax}}\frac{1}{\ln(n) - 3/4} \quad (\text{A.7})$$

For SSK01 and RNK01:

$$n = \frac{R}{r_w} = \frac{0.789\text{m}}{0.0525\text{m}} = 15.03, \quad k_{\text{ax}} = 0.007\text{cm/s}, \quad k_{\text{pl}} = 0.00238\text{cm/s}$$

For RLH01:

$$n = \frac{R}{r_w} = \frac{0.789\text{m}}{0.04765\text{m}} = 16.56, \quad k_{\text{ax}} = 0.007\text{cm/s}, \quad k_{\text{pl}} = 0.00227\text{cm/s}$$

Bibliography

T. Abdoun, R. Dobry, T. D. O'Rourke, and S. H. Goh. Pile response to lateral spreads: Centrifuge modeling. *Journal of Geotechnical and Geoenvironmental Engineering*, 129(10), 2003.

K. Adalier and A. Elgamal. Mitigation of liquefaction and associated ground deformations by stone columns. *Engineering Geology*, 72(3–4):275–291, 2004.

K. Andrianopoulos, A. Papadimitriou, and G. Bouckovalas. Bounding surface plasticity model for seismic liquefaction analysis of geotechnical structures. *Soil Dynamics and Earthquake Engineering*, 30:895–911, 2010.

R. J. Armstrong. *Evaluation of the Performance of Piled Bridge Abutments Affected by Liquefaction-Induced Ground Deformations Through Centrifuge Tests and Numerical Analysis Tools*. PhD thesis, University of California, Davis, 2010.

K. Arumoli, K. Muraleetharan, M. Hosain, and L. Fruth. Velacs laboratory testing program, soil data report. Report to the National Science Foundation, Washington, D.C., by the Earth Technology Corporation, Irvine, California, 1992.

- A. W. Bishop and N. Morgenstern. Stability coefficients for earth slopes. *Géotechnique*, 10(4):129–153, 1960.
- R. Boulanger, I. Idriss, D. Stewart, Y. Hashash, and B. Schmidt. Drainage capacity of stone columns or gravel drains for mitigating liquefaction. In *Geotechnical Earthquake engineering and Soil Dyanmics III*, ASCE Geotechnical Special Publication No. 75, pages 678–690, 1998.
- R. Boulanger, B. Kutter, S. Brandenberg, P. Singh, and D.Chang. Pile foundations in liquefied and laterally spreading ground during earthquakes: Centrifuge experiements and analyses. Rep. UCD/CGM–03/01, Davis, California, 2003.
- S. Brandenberg, R. Boulanger, B. Kutter, and D. Chang. Behavior of pile foundations in laterally spreading ground during centrifuge tests. *Journal of Geotechnical and Geoenvironmental Engineering*, 131(11), 2005.
- A. Brennan and S. Madabhushi. Effectiveness of vertical drains in mitigation of liquefaction. *Soil Dynamics and Earthquake Engineering*, 22:1059–1065, 2002.
- A. Brennan and S. Madabhushi. Liquefaction and drainage in stratified soil. *Journal of Geotechnical and Geoenvironmental Engineering*, 131(7):876–885, July 2005.
- A. Brennan and S. Madabhushi. Liquefaction remediation by vertical drains with varying penetration depths. *Soil Dynamics and Earthquake Engineering*, 26:469–475, 2006.
- P. Bucky. Use of models for the study of mining problems. Technical Publication No. 425, American Institute of Mining and Metallurgical Engineers, 1931.

P. M. Byrne, S. Park, M. Beaty, M. Sharp, L. Gonzalez, and T. Abdoun. Numerical modeling of liquefaction and comparison with centrifuge tests. *Canadian Geotechnical Journal*, 41:193–211, 2004.

Z. Cheng and B. Jeremić. Numerical modeling and simulation of soil lateral spreading against piles. In M. Iskander, D. Laefer, and M. Hussein, editors, *Geotechnical Special Publication No. 186: Contemporary Topics in In Situ Testing, Analysis, and Reliability of Foundations (Proceedings of the International Foundations Congress and Equipment Expo)*, pages 190–197, Orlando, Florida, 2009.

A. Chopra. *Earthquake effects on dams*. PhD thesis, University of California, Berkeley, 1996.

Civil Engineering Portal. Vertical drains can be installed in square and traingular patterns. Which pattern is better?, 2012. <http://www.engineeringcivil.com/vertical-drains-can-be-installed-in-square-and-triangular-patterns-which-pattern-is-better.html>.

M. Cubrinovski, D. Henderson, and B. Bradley. Liquefaction impacts in residential areas in the 2010-2011 Christchurch earthquakes. In *Proc., International Symposium on Engineering Lessons Learned from the 2011 Great East Japan Earthquake*, Tokyo, Japan, 2012.

Y. Dafalias and M. Manzari. Simple plasticity sand model accounting for fabric change effects. *Journal of Engineering Mechanics*, 130(6):622–634, 2004.

P. Dakoulas. *Contributions to seismic analysis of earth dams*. PhD thesis, Rensselaer Polytechnic Institute, Troy, New York, 1985.

O. Doygun. Monotonic and cyclic undrained loading behavior of intermediate soils. Master's thesis, Technische Universitat Darmstadt, Germany, 2009.

J. M. Duncan and S. G. Wright. *Soil Strength and Slope Stability*. John Wiley & Sons, Inc., Hoboken, New Jersey, 2005.

A. Elgamal, Z. Yang, T. Lai, B. L. Kutter, and D. W. Wilson. Dynamic response of saturated dense sand in laminated centrifuge container. *Journal of Geotechnical and Geoenvironmental Engineering*, 131(5), 2005.

G. Fiegel and B. L. Kutter. Liquefaction-induced lateral spreading of mildly sloping ground. *Journal of Geotechnical and Geoenvironmental Engineering*, 120(12):2236–2243, 1994.

G. Gazetas. Seismic response of earth dams; some recent developments. *Soil Dynamics and Earthquake Engineering*, 6(1):3–47, 1987.

S. Haigh, S. Madabhushi, K. Soga, Y. Taji, and Y. Shamoto. Lateral spreading during centrifuge model earthquakes. In *Proc., GeoEng2000*, Melbourne, Australia, 2000.

S. K. Haigh and S. P. Madabhushi. Centrifuge modelling of lateral spreading past pile foundations. In *International Conference on Physical Modelling on Geotechnics*, St. John's, Newfoundland, Canada, 2002.

J. Hancock and J. J. Bommer. The effective number of cycles of earthquake ground motion. *Earthquake Engineering Structural Dynamics*, 34:637–664, 2005.

M. Hatanaka. 3-dimensional consideration on the vibration of earth dams. *Journal of the Japanese Society of Civil Engineers*, 37(10), 1952.

R. Hayden and J. Baez. State of practice for liquefaction mitigation in north america. In *Proc., International Workshop on Remedial Treatment of Liquefiable Soils*, Japan, 1994.

C. C. Hird, I. C. Pyrah, and D. Russell. Finite element modelling of vertical drains beneath embankments on soft ground. *Géotechnique*, 42(3):499–511, 1992.

R. Howell, R. Kamai, C. Conlee, E. Rathje, R. Boulanger, A. Marinucci, and G. Rix. Evaluation of the effectiveness of prefabricated vertical drains for liquefaction remediation: Centrifuge data report for RLH01. Data Report UCD/CGMDR-0801, Center for Geotechnical Modeling, University of California, Davis, 2009a.

R. Howell, E. Rathje, A. Marinucci, R. Kamai, R. Boulanger, C. Conlee, and S. Kano. Centrifuge modeling of liquefaction sites treated with prefabricated drains. In *IS-Tokyo 2009 International Conference on Performance Based Design in Earthquake Geotechnical Engineering*, Tsukuba, Japan, June 2009b.

R. Howell, E. Rathje, R. Kamai, and R. Boulanger. Centrifuge modeling of prefabricated vertical drains for liquefaction remediation. *Journal of Geotechnical and Geoenvironmental Engineering*, 138(3):262–271, 2012.

S. Iai, K. Koisumi, S. Noda, and H. Tsuchida. Large scale model tests and analysis of gravel drains. In *Proc., 9th World Conference on Earthquake Engineering*, volume III, Tokyo-Kyoto, Japan, 1988.

S. Iai, Y. Matsunaga, T. Morita, M. Miyata, H. Sakurai, H. Oishi, Y. Ando, Y. Tanaka, and M. Kato. Effects of remedial measures against liquefaction

at 1993 Kushiro-Oki Earthquake. In *Proc., 5th U.S. – Japan Workshop on Earthquake Resistant Design of Lifeline Facilities and Countermeasures against Soil Liquefaction*, pages 135–152, Buffalo, NY, 1994.

I. M. Idriss and R. W. Boulanger. *Soil Liquefaction During Earthquakes*. Earthquake Engineering Research Institute (EERI), Oakland, California, 2008.

B. Indraratna and I. Redana. Plane-strain modeling of smear effects associated with vertical drains. *Journal of Geotechnical and Geoenvironmental Engineering*, 123(5):474–478, 1997.

J. Garnier and C. Gaudin, coordinators. Catalogue of scaling laws and similitude questions in centrifuge modeling, 2007. <http://www.tc2.civil.uwa.edu.au/>.

Japanese Geotechnical Society, editor. *Remedial Measures Against Soil Liquefaction*. A.A. Balkema, Rotterdam, Netherlands, 1998.

R. Kamai and R. Boulanger. Simulations of centrifuge test with lateral spreading and void redistribution effects. *Journal of Geotechnical and Geoenvironmental Engineering*, 2012. Published online ahead of print; DOI:10.1061/(ASCE)GT.1943-5606.0000845.

R. Kamai, S. Kano, C. Conlee, A. Marinucci, E. Rathje, R. Boulanger, and G. Rix. Evaluation of the effectiveness of prefabricated vertical drains for liquefaction remediation: Centrifuge data report for SSK01. Data report, Center for Geotechnical Modeling, University of California, Davis, 2007.

R. Kamai, R. Howell, C. Conlee, R. Boulanger, A. Marinucci, E. Rathje, and G. Rix. Evaluation of the effectiveness of prefabricated vertical drains for

liquefaction remediation: Centrifuge data report for RNK01. Data report, Center for Geotechnical Modeling, University of California, Davis, 2008.

R. Kamai, R. Howell, C. Conlee, R. Boulanger, E. Rathje, A. Marinucci, and G. Rix. Centrifuge test RNK01 on prefabricated vertical drains for liquefaction remediation, 2013a. Network for Earthquake Engineering Simulation (database), Dataset, DOI:10.4231/D3VX0628F.

R. Kamai, S. Kano, C. Conlee, A. Marinucci, R. Boulanger, E. Rathje, and G. Rix. Centrifuge test SSK01 on prefabricated vertical drains for liquefaction remediation, 2013b. Network for Earthquake Engineering Simulation (database), Dataset, DOI:10.4231/D32J6839J.

S. Kano. Torsional hollow cylinder tests on Nevada Sand, 2008.

D. Karamitros. *Development of a numerical algorithm for the dynamic elastoplastic analysis of geotechnical structures in two (2) and three (3) dimensions*. PhD thesis, National Technical University of Athens, Greece, 2010.

A. Khosravifar. A note on calibrating pressure dependent and pressure independent multi yield surface models (PressureDependMultiYield02 and PressureIndependMultiYield). Compiled notes, University of California, Davis, 2011.

S. Kramer. *Geotechnical Earthquake Engineering*. Prentice Hall, Upper Saddle River, New Jersey, 1996.

S. Kramer and R. Mitchell. Ground motion intensity measures for liquefaction hazard evaluation. *Earthquake Spectra*, 22(2):413–438, 2006.

B. L. Kutter. Recent advances in centrifuge modeling of seismic shaking. State-of-the-art paper. In *Proceedings of the Third International Conference on Recent Advances in Geotechnical Earthquake Engineering and Soil Dynamics*, volume 2, pages 927–942, St. Louis, MO, 1995.

B. L. Kutter, I. M. Idriss, T. Kohnke, J. Lakeland, X. S. Li, W. Sluis, X. Zeng, R. C. Tauscher, Y. Goto, and I. Kubodera. Design of a large earthquake simulator at uc davis. In Leung, Lee, and Tan, editors, *Centrifuge 94*, pages 169–175, Rotterdam, Netherlands, 1994. Balkema.

K. Lee and A. Albasia. Earthquake induced settlements in saturated sands. In *Proceedings of ASCE, Journal of the Geotechnical Engineering Division*, volume 100 (GT4), pages 387–405, 1974.

D. S. Liyanathirana and H. G. Poulos. Numerical simulation of soil liquefaction due to earthquake loading. *Soil Dynamics and Earthquake Engineering*, 22: 511–523, 2002.

J. Lu, Z. Yang, and A. Elgamal. OpenSeesPL 3D lateral pile-ground interaction: Version 0.6 user’s manual, 2010. http://cyclic.ucsd.edu/openseespl/OpenSeesPL_UserManual.pdf.

J. Lysmer and R. L. Kuhlemeyer. Finite dynamic model for infinite media. *Journal of the Engineering Mechanics Division*, 95:859–877, 1969.

S. Madabhushi. Numerical modelling of semi-infinite extent of soil medium in dynamic soil-structure interaction problems. In *EURODYN 93*, Rotterdam, The Netherlands, 1993. A.A. Balkema.

S. P. Madabhushi and X. Zeng. Seismic response of gravity quay walls II: numerical modeling. *Journal of Geotechnical and Geoenvironmental Engineering*, 124(5), 1998.

S. P. Madabhushi, B. Teymur, S. K. Haigh, and A. J. Brennan. Modelling of liquefaction and lateral spreading. In *International Workshop on Earthquake Simulation in Geotechnical Engineering*, Cleveland, Ohio, 2001. Case Western Reserve University.

A. Marinucci. *Effectiveness of Prefabricated Vertical Drains on Pore Water Pressure Generation and Dissipation in Liquefiable Sand*. PhD thesis, University of Texas at Austin, 2010.

A. Marinucci, E. Rathje, S. Kano, R. Kamai, C. Conlee, R. Howell, R. Boulanger, and P. Gallagher. Centrifuge testing of prefabricated vertical drains for liquefaction remediation. In D. Zeng, M. Manzari, and D. Hiltunen, editors, *Geotechnical Earthquake engineering and Soil Dynamics IV*, ASCE Geotechnical Special Publication No. 181. 2008.

J. Mayoral, F. A. Flores, and M. Romo. A simplified numerical approach for lateral spreading evaluation. *Geofísica Internacional*, 48(4):391–405, 2009.

S. Mazzoni, F. McKenna, and G. Fenves. Getting started with OpenSees. Technical Report NEESgrid-2004-21, University of California, Berkeley, 2004.

S. Mazzoni, F. McKenna, M. Scott, and e. a. G.L. Fenves. OpenSees command language manual. Technical report, University of California, Berkeley, 2007.

C. McGann and P. Arduino. Effective stress site response analysis of a layered soil

column, 2011. http://opensees.berkeley.edu/wiki/index.php/Effective_Stress_Site_Response_Analysis_of_a_Layered_Soil_Column.

J. K. Mitchell and J. F. J. Wentz. Performance of improved ground during the Loma Prieta Earthquake. Earthquake Engineering Research Center, Report No. UBC/EERC 91/12, College of Engineering, University of California, Berkeley, 1991.

N. Mononobe, A. Takada, and M. Matsumura. Seismic stability of the earth dam. In *Proc., 2nd Congress on Large Dams*, volume 4, Washington, D.C., 1936.

National Research Council. Liquefaction of soils during earthquakes. Committee on Earthquake Engineering, Report No. CETS-EE-001, National Academy Press, Washington, D.C., 1985.

Y. Ohkita, T. Yunoki, K. Ito, Y. Nakajima, and H. Simaoka. Effect of drain permeability on nomograph of gravel drain system. In *Proc of 21th JNC, JSSMFE*, pages 737–738, 1986.

H. Oishi and Y. Tanaka. Densification of surrounding soils due to the gravel drain construction. In *Proc., 4th U.S.-Japan Workshop on Earthquake Resistant Design of Lifeline Facilities and Countermeasures against Soil Liquefaction*, Buffalo, NY, 1993.

A. Onoue. Diagrams considering well resistance for designing spacing ratio of gravel drains. *Soils and Foundations*, 28(3):160–168, 1988.

A. Onoue, N. Mori, and J. Takano. In-situ experiment and analysis on well resistance of gravel drains. *Soils and Foundations*, 27(2):42–60, 1987.

L. Pedersen. Flexible shear beam container 2 features and limitations, 2004. <http://binders.cgm.ucdavis.edu/horizontal%20shaking%20table/Containers/FSB2.pdf>.

J. M. Pestana, C. E. Hunt, and R. R. Goughnour. FEQDrain: A finite element computer program for the analysis of the earthquake generation and dissipation of pore water pressure in layered sand deposits with vertical drains. Earthquake Engineering Research Center, Report No. EERC 97-15, College of Engineering, University of California, Berkeley, December 1997.

C. Phillips, Y. Hashash, S. Olson, and M. Muszynski. Significance of small strain damping and dilation parameters in numerical modeling of free-field lateral spreading centrifuge tests. *Soil Dynamics and Earthquake Engineering*, 42:161–176, 2012.

K. Pitilakis, E. Kirtas, A. Sextos, M. Bolton, G. Madabhushi, and A. Brennan. Validation by centrifuge testing of numerical simulations for soil-foundation-structure systems. In *Proc. 13th World Conference on Earthquake Engineering*, Vancouver, B.C., Canada, 2004.

G. I. Pokrovsky. Principles of the modelling of the foundations of structures. In *Technical Physics*, number 2, Moscow, 1934.

R. Popescu and J. H. Prevost. Centrifuge validation of a numerical model for dynamic soil liquefaction. *Soil Dynamics and Earthquake Engineering*, 12:73–90, 1993.

A. Rauch. *EPOLLS: An Empirical Method for Predicting Surface Displacements*

Due to Liquefaction-Induced Lateral Spreading in Earthquakes. PhD thesis, Virginia Tech, 1997.

K. M. Rollins, J. K. S. Anderson, A. K. McCain, and R. R. Goughnour. Vertical composite drains for mitigating liquefaction hazard. In *Proceedings of The Thirteenth International Offshore and Polar Engineering Conference*, pages 498–505, Honolulu, Hawaii, May 2003.

Y. Sasaki and E. Taniguchi. Shaking table tests on gravel drains to prevent liquefaction of sand deposits. *Soils and Foundations*, 22(3):1–14, 1982.

G. Saygili and E. Rathje. Probabilistically based seismic landslide hazard maps. *Engineering Geology*, 109(3-4):183–194, 2009.

A. N. Schofield. Cambridge geotechnical centrifuge operations. *Géotechnique*, 30(3):227–268, 1980.

A. N. Schofield. Geotechnical centrifuge development can correct a soil mechanics error, 1998. Report No. CUED/D-SOILS/TR308, Keynote lecture to the Tokyo Conference of TC2 "Centrifuge '98", 23 September 1998.

H. B. Seed and J. R. Booker. Stabilization of potentially liquefiable sand deposits using gravel drains. *ASCE Journal of the Geotechnical Engineering Division*, 103(GT7):757–768, 1977.

H. B. Seed, K. Mori, and C. Chan. Influence of seismic history on the liquefaction characteristics of sands. Earthquake Engineering Research Center, Report No. EERC 75-25, College of Engineering, University of California, Berkeley, 1975.

M. Seid-Karbasi and P. M. Byrne. Seismic liquefaction, lateral spreading and flow slides: a numerical investigation into void redistribution. *Canadian Geotechnical Journal*, 44:873–890, 2007.

M. K. Sharp and R. Dobry. Sliding block analyses of lateral spreading based on centrifuge results. *International Journal of Physical Modelling in Geotechnics*, 2(2):13–32, 2002.

V. Taboada and R. Dobry. Prediction of liquefaction-induced lateral spreading by dilatant sliding block model calibrated by centrifuge tests. In *Proc., 11th World Conference on Earthquake Engineering*, Acapulco, Mexico, 1996.

V. M. Taboada-Urtuzuastegui and R. Dobry. Centrifuge modeling of earthquake-induced lateral spreading in sand. *Journal of Geotechnical and Geoenvironmental Engineering*, 124(12), 1998.

U.S. Geological Survey. Lateral spread caused by the haiti earthquake, 2013. http://gallery.usgs.gov/photos/08_06_2010_g40Nfr5EDy_08_06_2010_3.

D. Wilson. *Soil-Pile-Superstructure Interaction in Liquefying Sand and Soft Clay*. PhD thesis, University of California, Davis, 1998.

Z. Yang, A. Elgamal, and E. Parra. Computational model for cyclic mobility and associated shear deformation. *Journal of Geotechnical and Geoenvironmental Engineering*, 129(12):1119–1127, 2003.

Z. Yang, J. L. Lu, and A. Elgamal. OpenSees soil models and solid-fluid fully coupled elements. User’s Manual 2008 ver 1.0, Department of Structural Engineering, University of California, San Diego, October 2008.

O. Zienkiewicz. *Computational geomechanics with special reference to earthquake engineering*. John Wiley, New York, 1999.

K. Ziotopoulou and R. Boulanger. Constitutive modeling of duration and overburden effects in liquefaction evaluations. In *Proc., Second International Conference on Performance-Based Design in Earthquake Geotechnical Engineering*, Taormina, Italy, 2012.